UNDERSTANDING DEFECT AND DOPANT MEDIATED OPTICAL PROPERTIES IN OXIDE MATRICES

By
NIMAI PATHAK
CHEM 01201304021

Bhabha Atomic Research Centre, Mumbai

A thesis submitted to the
Board of Studies in Chemical Sciences

In partial fulfillment of requirements
for the Degree of
DOCTOR OF PHILOSOPHY
of
HOMI BHABHA NATIONAL INSTITUTE

April 2018

Homi Bhabha National Institute

Recommendations of the Viva Voce Committee

As members of the Viva Voce Committee, we certify that we have read the dissertation prepared by **Mr. Nimai Pathak** entitled **"Understanding defect and dopant mediated optical properties in oxide matrices"** and recommend that it may be accepted as fulfilling the thesis requirement for the award of Degree of Doctor of Philosophy.

Chairman – Dr. P.K. Pujari		**Date:** 2/04/18
Guide / Convener – Dr. R.M. Kadam	RMKadam	**Date:** 02/04/2018
Examiner – Dr. V. Sivakumar	V. Sivakumar	**Date:** 02/04/2018.
Member 1- Dr. P.K. Mohapatra		**Date:** 02/4/2018
Member 2- Dr. P.A.Hassan		**Date:** 02/04/18
Member 3- Dr. V. Sudarsan	Sudarsan.V	**Date:** 02/04/18

Final approval and acceptance of this thesis is contingent upon the candidate's submission of the final copies of the thesis to HBNI.

I/We hereby certify that I/we have read this thesis prepared under my/our direction and recommend that it may be accepted as fulfilling the thesis requirement.

Date: 02/04/2018

Place: BARC

RMKadam

(Signature)
Guide

STATEMENT BY AUTHOR

This dissertation has been submitted in partial fulfillment of requirements for an advanced degree at Homi Bhabha National Institute (HBNI) and is deposited in the Library to be made available to borrowers under rules of the HBNI.

Brief quotations from this dissertation are allowable without special permission, provided that accurate acknowledgement of source is made. Requests for permission for extended quotation from or reproduction of this manuscript in whole or in part may be granted by the Competent Authority of HBNI when in his or her judgment the proposed use of the material is in the interests of scholarship. In all other instances, however, permission must be obtained from the author.

Nimai Pathak

Nimai Pathak

DECLARATION

I, hereby declare that the investigation presented in the thesis has been carried out by me. The work is original and has not been submitted earlier as a whole or in part for a degree / diploma at this or any other Institution / University.

Nimai Pathak

Nimai Pathak

List of Publications arising from the thesis

Journal

1. "Exploring Defect Induced Emission in $ZnAl_2O_4$: An Exceptional Color Tunable Phosphor Material with Diverse Lifetimes", **N. Pathak,** P.S. Ghosh, S. Saxena, D. Dutta, A. K. Yadav, D. Bhattacharyya, S. N. Jha and R.M.Kadam, *Inorganic Chemistry,* **2018**, *DOI: 10.1021/acs.inorgchem.8b00172*
2. "Defect induced ferromagnetism in MgO and its exceptional enhancement upon thermal annealing: a case of transformation of various defect states", **N. Pathak**, S. K. Gupta, C. L. Prajapat, S. K. Sharma, P. S. Ghosh, B. Kanrar , P.K.Pujari, R. M. Kadam, *Physical Chemistry Chemical Physics,* **2017**,*19*, 11975-11989.
3. "An Insight into the Various Defects Induced Emission in $MgAl_2O_4$ and Their Tunability with Phase Behavior: Combined Experimental and Theoretical Approach", **N. Pathak,** P. S. Ghosh, S. K. Gupta, S. Mukherjee, R. M. Kadam and A. Arya, *Journal of Physical Chemistry C,* **2016**, *120*, 4016–4031.
4. "Photoluminescence and EPR studies on Fe^{3+} doped $ZnAl_2O_4$: an evidence for local site swapping of Fe^{3+} and formation of inverse and normal phase", **N. Pathak,** S. K. Gupta, K. Sanyal, M. Kumar, R. M. Kadam and V. Natarajan, *Dalton Transactions*, **2014**, *43*, 9313–9323.
5. "Investigations on local structures in new $Bi_{2-2x}La_{2x}UO_6$ ($x = 0–0.05$) solid solutions: a combined XRD, EXAFS, PL and EPR study", K. Sanyal, **N. Pathak**, A. K. Yadav, B. Kanrar, R. M. Kadam, S. N. Jha, D. Bhattacharyac,andN. L. Misra, *Dalton Transactions,* **2016**, *45*, 7650–7664.
6. "Probing local site environments and distribution of manganese in $SrZrO_3$:Mn; PL and EPR spectroscopy complimented by DFT calculations", **N. Pathak,** S. K. Gupta, P. S. Ghosh, A. Arya, V. Natarajan and R. M. Kadam, *RSC Advances,* **2015**, *5*, 17501-17513.
7. "Defects induced changes in the electronic structures of MgO and their correlation with the optical properties: a special case of electron–hole recombination from the conduction band", **N. Pathak**, P.S.Ghosh, S. K. Gupta, R. M. Kadam and A. Arya**,** *RSC Advances,* **2016**, *6*, 96398–96415.
8. "EPR investigation on synthesis of Lithium zinc vanadate using sol–gelcombustion route and its optical properties", **N. Pathak** , S. K. Gupta , A.

Prince, R.M. Kadam and V. Natarajan, *Journal of Molecular Structure,* **2014**,*1056-1057*, 121–126.

9. “An efficient gel-combustion synthesis of visible light emitting barium zirconate perovskite nanoceramics: Probing the photoluminescence of Sm^{3+} and Eu^{3+} doped $BaZrO_3$”, S. K. Gupta , **N. Pathak**, R. M. Kadam , *Journal of Luminescence,* **2016**,*169*,106–114.
10. “On the photophysics and speciation of actinide ion in $MgAl_2O_4$ spinel using photoluminescence spectroscopy and first principle calculation: A case study with uranium”, S. K. Gupta, **N. Pathak**, P.S. Ghosh , R.M. Kadam, *Journal of Alloys and Compounds,* **2017**, *695*, 337-343.

Conferences

1. “Probing local site environments and distribution of Manganese in $SrZrO_3$: PL study”, **N. Pathak,** S. K. Gupta, V. Natarajan, International conference on luminescence and its application (ICLA-2015), Bangalore, Feb-2015.
2. “Photoluminescence Study Of Sol-gel Derived $ZnAl_2O_4$ Compound: A Potential Thermal Sensor And Colour Tuneable Novel Phosphor Material”, **N. Pathak** and R.M.Kadam, 60th DAE Solid State Physics Symposium 2015 (DAE-SSPS-2015), Amity University, Noida, December 21-25, 2015.
3. “Defect Induced Magnetism in MgO microcrystal”, **N. Pathak**, S.K.Sharma , S. K. Gupta, P. S. Ghosh, P. K. Pujari and R. M. Kadam, 6th DAE-BRNS Interdisciplinary Symposium on Materials Chemistry (ISMC-2016), BARC Training School**,** Mumbai, December 6-10, 2016
4. “Spectroscopic investigation on defects in MgO and $MgAl_2O_4$”, S. Saxena**, N. Pathak**, S. K. Gupta’ and R.M.Kadam, 8th International Conference on Advanced Materials Development and Performance 2017 (AMDP 2017), Savitribai Phule Pune University, Pune, July 11-15, 2017.
5. Defect mediated optical properties in ZnAl2O4 phosphor, **N. Pathak**, S. Saxsena, R. M. Kadam, 62nd DAE Solid State Physics Symposium-2017 (DAE-SSPS-2017), Bhabha Atomic Research Centre,Anushaktinagar, Mumbai, December 26 – 30, 2017.

Nimai Pathak

Nimai Pathak

DEDICATIONS

This work is dedicated to my beloved parents,
father
Gouranga Sundar Pathak
and mother
Tara Rani Pathak
for their resilience in insisting to educate me
amidst the absolute poverty in which they raised me.

ACKNOWLEDGEMENTS

Though only my name appears on the cover of this dissertation, a lot many people have contributed to its production. I owe my gratitude to all those people who have made this dissertation possible and because of whom my doctorate experience has been one that I will cherish forever.

My deepest gratitude is to my advisor, **Dr. R.M. Kadam**. I have been amazingly fortunate to have an advisor who gave me the freedom to explore on my own and at the same time the guidance to recover when my steps faltered. He taught me how to question thoughts and express ideas. I am deeply grateful to him for the long discussions that helped me sort out the technical details of my work. His patience and support helped me overcome many crisis situations and finish this dissertation.

I am thankful **Dr. P.K. Pujari**, Associate Director, RC&IG, BARC and Head, RCD, BARC for his constant encouragement, support and critical evaluation of the ongoing work during the course of Ph.D.

I would also like to thank other members of my doctoral committee; **Dr. P. K. Mohapatra, Dr. P.A.Hassan and Dr. V. Sudarsan,** for their valuable comments and suggestions during the course of Ph.D.

I am thankful to my former section head (Actinide Spectroscopy Section, RCD) **Dr. V. Natarajan** for his encouragement and support starting from registration to the end of thesis submission.

I would like to express my sincere gratitude to **Dr. S. K. Gupta** who has introduced me to the field of luminescence. His calm demeanor, logical way of guidance, help in crucial experiments, teachings about the writing of manuscript has helped to bring out the proper shape of this work.

I would like to thank my collaborator **Dr. P. Ghosh (MSD)** for Thoretical studies, **Mr. Kaushik Sanyal (FCD)** and **Mr. Buddhadev Kanrar (FCD)** for X-ray diffraction, **Dr. D. Dutta (RCD)** and **Dr. S. K. Sharma (RCD)** for PALS, **Dr. C. L. Prajapt (TPD)** for magnetic measurements**, Dr. S. K. Mukherjee (RCD)** for low temperature PL study and **Mr. Ashok Kumar Yadav (A&MPD)** for EXAFS study. They have contributed significantly to make my work complete in all respect. I am thankfull to **Dr. K. Sudarsan (RCD)** for his continued help and suggestions while writing the thesis and carrying out some of the experiemnts. I would also like to thank **Dr. Sabyasachi Patra (RCD)** and **Mr. Sankararao Chappa (RCD)** for UV-visible study, **Dr. Ruma Gupta (FCD), Mr. R. Agarwal (FCD)** and **Dr. S. Neogy (MMD)** for SEM, EDX and TEM measurements, and **Mr. Bal Govind Vats (FCD)** for FTIR study. Without their help, the thesis would not have been completed.

I am greatfull to all of my former and present colleagues at Actinide Spectroscopy section, Radiochemistry Division, for providing a stimulating academic environment to learn and grow. I am also indebted to many of my others colleagues at Radiochemistry Division for their continuous help and supports during the course of the present work.

I would like to thank **my parents** for their unconditional love, support, faith, encouragement and confidence in me. I thank my loving sisters **Mithu, Mousumi, Madhuri** and **Manasi** who have been supportive all the time. I sincerely thank my nephews **Babai, Kingshuk, Pratim** and **newly born Mivaan** for their love to me. I express my gratitude to my dearest brother in laws **Nareshda, Saileshda, Prabirda** and **Manik** for their endless love and support. I sincerely acknowledge the love and supports given to me by my **parent-in-laws**.

I run short of words in expressing my gratitude towards my wife **Suvra** who always stood by me and encouraged me up at every step of life. She has tried her best to keep me cheerful during all these days. She also stood by me through my weal and woe. I am indeed blessed to have her in my life.

During the course of my work, I received help from many, whose name I could not mention. I thank all of them.

CONTENTS

		Page No.
SYNOPSIS		13
LIST OF FIGURES		25
LIST OF TABLES		35
Chapter 1	**Introduction**	37
	1.1. General Introduction	38
	1.1.1. General introduction to the subject	38
	1.1.2. Transition metal , Rare earths and Actinides doped optical materials	41
	1.1.3. Defect related optical Materials	43
	1.2. Crystallographic Defects	44
	1.2.1. Point Defects	45
	1.2.2. Line defects	49
	1.2.3. Planar defects	50
	1.2.4. Surface defects	52
	1.3. Phosphor materials	53
	1.4. Photoluminescence (PL) in solid	55
	1.4.1. Intrinsic Photoluminescence	55
	1.4.2. Extrinsic Photoluminescence	55
	1.4.3. Type of Luminescence in Solid	55
	1.4.4. Luminescent Centres	58
	1.5. Scope of this work	76
Chapter 2	**Experimental**	80
	2.1. Synthesis of luminescent materials	81
	2.1.1. Conventional Solid state route	81
	2.1.2. Sol-gel Method	82
	2.1.3 .Sol-gel auto combustion technique	85
	2.2. Characterization Techniques	88
	2.2.1. X-ray diffraction	88
	2.2.2. Electron microscopy: SEM/TEM	92
	2.2.3. Positron annihilation spectroscopy (PAS)	99
	2.2.4. Electron paramagnetic resonance (EPR) spectroscopy.	101
	2.2.5. Photoluminescence spectroscopy (PL)	110
	2.3. DFT calculation methodology	119
Chapter 3	**Defects mediated optical properties in MgO, $MgAl_2O_4$ & $ZnAl_2O_4$**	122
	3.1. Introduction	123
	3.2. Synthesis, optical and magnetic properties of MgO	126
	3.2.1. Synthesis, characterization and morphology	126
	3.2.2. Absorption spectroscopy	129
	3.2.3. Excitation Spectroscopy	129
	3.2.4. Emission Spectroscopy	130

3.2.5. Lifetime Study 131
3.2.6. Time Resolved Emission Spectroscopy (TRES) 133
3.2.7. Electronic Structure and Band Gap Energy 138
3.2.8. Magnetic, EPR and PAS study 145
3.3. Synthesis and Optical properties of $MgAl_2O_4$ (MAS) 154
3.3.1. Synthesis and characterization 154
3.3.2. Excitation, emission and life time spectroscopy 156
3.3.3. Time Resolved Emission Spectroscopy (TRES) 163
3.3.4. Electronic Structure and Band Gap Energy. 165
3.3.5. Origin of the different colour components and their tunability with a proposed model. 166

3.4. Synthesis and Optical properties of $ZnAl_2O_4$ 173
3.4.1. Synthesis and characterization of $ZnAl_2O_4$ 173
3.4.2. Emission and life time spectroscopy 174
3.4.3. Time Resolved Emission Spectroscopy (TRES) 176
3.4.4. Positron annihilation lifetime spectroscopy. 179
3.4.5. EPR study 182
3.4.6. Electronic Structure and Band Gap Energy. 184
3.4.7. Discussion 184
Chapter 4 **Transition metal ions mediated optical properties in Fe^{3+}:$ZnAl_2O_4$, Mn^{2+}:$SrZrO_3$ & $LiZnVO_4$** 190
4.1. Introduction 191
4.2. Synthesis and Optical properties of Fe^{3+} doped $ZnAl_2O_4$ 195
4.2.1. Synthesis and Characterization 195
4.2.2. Emission, excitation and life time spectroscopy of Fe^{3+} doped $ZnAl_2O_4$ 198
4.2.3. EPR studies of paramagnetic Fe^{3+} in $ZnAl_2O_4$ 202
4.2.4. Transformation of inverse to normal phase: Tunable emission properties upon thermal annealing. 204
4.3. Synthesis and Optical properties of Mn doped $SrZrO_3$ 206

4.3.1. Synthesis and characterization 206
4.3.2. Photoluminescence: Emission, excitation and life time spectroscopy of Mn^{2+} doped $SrZrO_3$ 209
4.3.3. EPR study 214
4.4. Synthesis and optical properties of $LiZnVO_4$ 218
4.4.1 Synthesis, characterization and morphology 218
4.4.2 EPR study at various intermediate steps during synthesis. 221
4.4.3 Photoluminescence spectroscopy: Excitation and Emission spectroscopy, colour coordinates and lifetime study 223
Chapter 5 **Lanthanide and Actinide ions mediated optical properties in Sm^{3+}:$BaZrO_3$, Eu^{3+}:$BaZrO_3$, $Bi_{1.96}Eu_{0.04}UO_6$ & U:$MgAl_2O_4$** 225
5.1 Introduction 225
5.2. Synthesis and Optical properties of Sm^{3+} and Eu^{3+} doped $BaZrO_3$ nanocrystals 230
5.2.1. Synthesis, characterization and morphology 230
5.2.2. Defects induced photoluminescence in $BaZrO_3$ 232
5.2.3. Photoluminescence spectroscopy of Sm^{3+} doped $BaZrO_3$: Excitation and emission spectroscopy, colour coordinates and lifetime study. 223
5.2.4. Photoluminesence spectroscopy of Eu^{3+} doped $BaZrO_3$: Excitation and emission spectroscopy, colour coordinates, Stark splitting pattern, lifetime study and calculation of Ω_λ (Judd-Ofelt) parameters. 237
5.3 Synthesis and Local structure determination of $Bi_{2-2x}La_{2x}UO_6$ and $Bi_{1.96}Eu_{0.04}UO_6$ 242
5.3.1. Synthesis 242
5.3.2. XRD measurements and Rietveld refinement 243
5.3.3. EPR study 247
5.3.4. Photoluminescence study: Excitation and emission spectroscopy, lifetime study and time resolve emission spectra 250
5.4. Synthesis and optical properties of U:$MgAl_2O_4$ 255
5.4.1. Synthesis and Characterization 255
5.4.2. Excitation and Emission Characteristics, lifetime, local site occupancy, energy transfer and TRES study 256

Chapter 6 Summary, Conclusions and Future work 261

References 266

SYNOPSIS

The topic which was worked upon in this Ph.D. thesis is “Understanding defect and dopant mediated optical properties in oxide matrices”. The selected oxide matrices in present thesis are very important from photonics and optoelectronics point of view. Currently in the field of lighting, white light emitting diode (W-LED) or white phosphor-conversion (PC) light-emitting diodes (LEDs), a new generation solid source has been highlighted due to its high luminous efficiency, low power consumption and environmentally benign nature **[i, ii]**. In India, a goal has been set up to replace the conventional street and domestic lights with energy efficient LED lights across 100 cities in the country by lunching Street Light National Programme (SLNP) in January 2015 **[iii]**. This may help India to save Rs 5,500 crore or 9,000 million units of power annually if SLNP implemented properly. There is a tremendous growth in the development of LED worldwide due to its various scientific and technological applications viz. lighting, motor vehicle and backlight for mobile panel and liquid crystal displays **[iv-vi]**. Thus, there is an ongoing demand to develop new phosphors specifically for LEDs. Because of the ever-growing demand for advanced luminescent materials, huge scientific and technological efforts have been dedicated for improving existing phosphors and to develop new effective luminescent materials in the last few decades and so **[vii, viii]**.

Generally, phosphors are classified into two sub categories: activator based and non-activator based. In activator based phosphor, the luminescence property is governed by transitions between energy levels of metal activator ions **[vii-xi]**. Although there are numbers of advantages of using lanthanide doped phosphor because of its interesting optical properties such as high colour purity, narrow emission, large stoke shift, longer excited state lifetime, high photostability etc., but pure rare earth is facing serious shortage problem other than issues related with lack of recyclability and its higher cost. The other group of luminescent materials that is non activator based consist of semiconductors and defect-related materials **[xii]**. For most semiconductor, the luminescence normally results from band-to-band excitation between impurity states within the band gap. Since these non activator based materials do not contain any dopant ion, they seem to be promising alternatives to traditional phosphors in many applications because of their advantages such as low toxicity, stability, tunable emission colour, and low cost **[xiii-xv]**.

However in all the optical materials, irrespective of the fact whether it is doped or undoped, the local structures of the luminescence centres are directly linked with the luminescence phenomenon and therefore can have high impact on the luminescence efficiency. Here local structure of luminescence centre means its oxidation states, crystal field environment, coordination geometry, symmetry etc. Any change in the local structure will have serious consequences on the optical properties.

Over the past few decades material chemistry has experience tremendous evolution with regards to design, synthesis and controlling of properties of new functional materials with different size from micrometre to nanometre scale **[xvi]**. Such new materials are often structurally and chemically complex and often lack long range ordering and hence structurally disorder. Although design and synthesis of new materials is one of the challenges in materials chemistry, it is far from achieving this goal universally. Synthesis of new materials can be achieved but the success in controlling materials properties has been limited. The desire for novel functions or properties generate a vast demand for new materials which has to be fabricated with well defined aspect ratio, controllable properties and with well known morphology.

Presently used phosphors in CFLs and W-LEDs are activated with Lanthanide (Ln) and/or Transition metal (TM) ions **[vii, viii]**. In case of TM ions, the intra-shell d–d transitions are exploited while for Ln^{3+} ions, both parity-allowed 5d–4f (e.g. Ce^{3+}) and parity-forbidden 4f–4f (e.g. Tb^{3+}) transition occurs other than the charge transfer transition which arises due to host. Most of the TM ions have an incompletely filled d-shell (d^n, $0 < n < 10$). For example the 3d transition metal ions utilized in phosphors may have three electrons (Cr^{3+} and Mn^{4+}), or five electrons (Mn^{2+}) occupying the outermost 3d orbital, which in contrast to lanthanide ions, are not shielded from the host lattice. This is why the host lattice can influence the optical properties of TM ions. For lanthanides, the 4f-4f transitions result in sharp, "atomic-like" photoluminescence (PL) bands, which are insensitive to temperature and host lattice. Such doping enables to achieve light emission in a given spectral region. Lanthanide ions such Eu^{3+} ion is also extensively used as local probes for identifying local structures in crystalline material **[xvii, xviii]**, understanding the effect of chemical and thermal treatment on catalysts and probing the structure of biological molecules. In view of its non-degenerate emissive state $^5D_0$, Eu^{3+} ion is most appropriate as luminescent structural probe for the determination of the number of metal ion sites in a compound, their symmetry, and their respective population. In present thesis, we have given special emphasis on the local structure determination of lanthanide ions in matrices such as $BaZrO_3$ and $Bi_{2-2x}La_{2x}UO_6$, using Eu^{3+} as luminescent structural probe. Among the materials evaluated as hosts for TM ions in this thesis, our attention was mostly focused on perovskite and spinel based oxide materials such as $SrZrO_3$, $ZnAl_2O_4$. Since the crystal field environments surrounding the cation sites are different from each other, it is feasible to tune the emitting colour of TM ions by merely changing the site occupancy.

Actinides (5f block elements) exhibit much richer chemistry than lanthanide because of their tendency to exhibit variable oxidation states. Compared to 4f electron in lanthanides; 5f-electrons are relatively less shielded by outer lying electrons. As a result, they are more perturbed by local crystal field, which results in broad emission and absorption spectrum. Oscillator strength of 5f-5f transition is relatively larger than in iso-electronic lanthanide ions. Actinide chemistry is gaining new interest day by day because of stabilization of various unusual oxidation states, unique magnetic properties and chemical reactivity. They are also very important for various applications such as in radiation shielding and ceramics, as ballasts in ships and airplanes and as a heat and fuel source in space exploration and in terrestrial nuclear power production **[xix]**. Among actinides, uranium displays unique photophysical characteristics. Uranium is known to exist in various oxidation states, such as +3, +4, +5 and +6 **[xx-xxii]**. Each one of them exhibit characteristics optical fingerprint. The fascinating uranyl luminescence has been explored in various glasses and ceramic based matrices. Some of the applications are internal actinometers in biological chemistry, as luminescent sensors and in uranium detection assays **[xxiii].** Other than being a constituent of high-level radioactive wastes, uranium is also one of the daughter products in α-decay of plutonium. In this context, it is of paramount importance to examine the chemical environment (coordination and oxidation state) of uranium in important nuclear waste host. In present thesis a special emphasize has been given on photoluminescence properties of Uranium in $MgAl_2O_4$. $MgAl_2O_4$ is proposed candidate for minor actinide transmutation because of its favorable high temperature properties and high radiation stability **[xxiv]**.

There are several investigations going on throughout the world to explore rare earth free phosphor. In this series, alkaline earth metal oxides, such as CaO, BeO, MgO, and SrO **[xxv]**, have been gaining considerable attention in material science as an inorganic phosphor for optoelectronics devices, sensors, and solid-state lighting applications due to their defect-induced luminescence properties. Various activator free materials such as ZnO, TiO_2, SnO_2, CuI, Al_2O_3, MgO **[xxvi-xxxi]** etc. are reported to show defect induced photoluminescence (PL) characteristics. When the defects induced optical properties in oxides matrices are considered, different types of electronic states within the band gap of the material are found to be responsible for the emission behavior. Although the roots of defect-related luminescent materials can be traced to 1986 **[xxxii],** the remarkable growth was observed after Sailor *et al.,* reported the white phosphors from a silicate-carboxylate sol–gel precursor **[xiii]**.The origins of photoluminescence in this kind of materials are complex in nature and not yet entirely understood. However there is mounting evidence that the emission arises due to presence of various defects such as vacancies, impurities, radical, donor–acceptor pairs, etc., **[xii]**. This results in a charge imbalance at these defect sites which must be compensated by localization of electrons and electron hole pairs or give rise to impurity states within the band gap. Therefore, the defect sites are apparently the precursors for various luminescence centres in defect-related luminescent materials and impart them with excellent emission characteristics. Here in present thesis, we have chosen various activator free oxide matrices such as MgO, $MgAl_2O_4$ and $ZnAl_2O_4$. Although several reports on defects induced emission properties in MgO are available, a proper understanding about the correlation of the defect structure with the emission colours is still lacking in the literatures. We have considered a special electron-hole recombination process to understand the defects induced characteristics in MgO. Very few reports exist in literature about the defects induced emission characteristics in $MgAl_2O_4$ and $ZnAl_2O_4$. In present thesis, using a combine experimental and theoretical investigation a detail analysis about the defect structure and their respective emission has been presented.

Various synthesis techniques were explored to synthesize the materials of interest such as solid-state, sol-gel, combustion etc. Characterization of the materials was carried out by various physical and chemical methods. For structure, phase purity and crystallite size, X-Ray Diffraction has been used. For morphology and average particle size, scanning electron microscopy (SEM) and transmission electron microscopy (TEM) have been used. Energy dispersive X-ray Spectrometry (EDX or

EDS) and inductively coupled plasma atomic emission spectroscopy (ICP-AES) have been used for impurity analysis. Positron annihilation lifetime spectroscopy (PALS) was used to understand the nature of defects in some of the materials. Time resolved emission spectroscopy (TRES) has been extensively used in this thesis work for recording emission and excitation spectra along with the luminescence lifetimes. Electron paramagnetic resonance (EPR) spectroscopy has been used to characterize the paramagnetic defects centres and to understand the local structure of the TM ions. Extended X-ray absorption fine structure (EXAFS) was used to understand the local environment around Ln^{3+} ion in various inorganic hosts. For better understanding of the electronic structure, Density Functional Theory (DFT) based calculation has been carried out for different matrices. The present thesis is divided into 6 chapters. A brief description of the different chapters is given below.

Chapter 1: Introduction

In this chapter, the fascinating photophysics of lanthanides, actinides and transition metal ions and their origin have been discussed. The choice of dopant ions and the host have been explained in details. Characteristics difference in photophysics of 3d, 4f and 5f block elements have been discussed thoroughly to make audience appreciate the quantum of work done in this thesis. This chapter gives a brief introduction about various crystallographic defects centres and the mechanism of defects induced optical properties in oxide-based matrices. A detail insight about the electron-hole recombination process inside the band gap has also given in this chapter. This chapter also explains about the choice of host and luminescent dopant to synthesize the phosphor. With respect to the energy gap requirement, it is obvious that Eu^{3+} , Gd^{3+}, and Tb^{3+} are the best ions, with ΔE = 12 300 ($^5D_0 \rightarrow {}^7F_6$), 32 200 ($^6P_{7/2} \rightarrow {}^8S_{7/2}$) and 14 800 ($^5D_4 \rightarrow {}^7F_0$) cm^{-1}, respectively. However, Gd (III) emits in the UV and therefore it is not very useful as luminescent probe for bioanalyses, because its luminescence interferes with either emission or absorption processes in the organic part of the complex molecules. Lanthanide photophyics, Judd-Ofelt Theory, information gained from lanthanide luminescence, luminescence quenching, energy transfer, multiphonon emission etc. are also discussed in this chapter.

Chapter 2: Experimental

The synthesis techniques adopted in preparation of different micro/nano luminescent materials and the experimental techniques used for characterization of these materials have been presented in Chapter 2. Brief description on various synthesis methodology and their characteristics has been discussed for the researcher who wants to repeat the experiments and do some other analysis. Sol-gel route and combustion method adopted for preparation of MgO, $MgAl_2O_4$, $ZnAl_2O_4$, $SrZrO_3$, $BaZrO_3$, $LiZnVO_4$ matrices (both undoped and doped) has been elaborated. Solid state method which was used for the preparation of $Bi_{2-2x}La_{2x}UO_6$ and $Bi_{1.96}Eu_{0.04}UO_6$, has also been discussed. Phase evolution of synthesized powders after calcination was characterized by X–ray diffraction. Particle morphologies were studied using SEM and TEM. Impurity analysis in MgO was carried out using ICP-AES and EDX techniques. Local environment/ site symmetry around TM, Ln ion, and defect centres in a particular host was investigated using time resolved fluorescence spectroscopy (TRFS). EPR technique is used to study the local structure of paramagnetic defect centres e.g. singly charged oxygen vacancies in various matrices like MgO, $MgAl_2O_4$, $ZnAl_2O_4$, $SrZrO_3$, $BaZrO_3$. EPR also helped to understand the local structure of TM ions in matrices such as Fe^{3+}:$ZnAl_2O_4$, Mn^{2+}:$SrZrO_3$ & $LiZnVO_4$.Positron annihilation lifetime spectroscopy (PALS) has been carried out to probe the nature of defects in MgO and $ZnAl_2O_4$. Local environment/ site symmetry around La^{3+},Bi^{3+} and U^{6+} ion in $Bi_{2-2x}La_{2x}UO_6$ host was investigated using time resolved fluorescence spectroscopy (TRFS) and extended x-ray absorption fine structure (EXAFS) measurement employing synchrotron. DFT based calculations were carried out to understand the electronic structure due to various defect centres in MgO, $MgAl_2O_4$ & $ZnAl_2O_4$ and to understand the local site occupancy of Mn^{2+} in $SrZrO_3$ and that of U^{6+} in $MgAl_2O_4$.

Chapter 3: Defects mediated optical properties in MgO, $MgAl_2O_4$ & $ZnAl_2O_4$

This chapter discusses about the defect induced optical properties in binary compound MgO and in spinels such as $MgAl_2O_4$ and $ZnAl_2O_4$ .We have characterized various defect centres in these matrices and established a correlation with the multicolour emission behaviors. Generally defects induced emission phenomena is very complex in nature, which often results in very broad emission spectra consisting of different kind of defect centres. Thus it is very much essential to isolate each and individual defect emission from the complex spectra which has been done by lifetime and TRES measurements. We have also monitored the changes of these individual emission profiles with varying synthesis conditions, which helped to control the emission profiles. The lifetime values of the defect centres could also be controlled by controlling the annealing temperature.

MgO is known to display defect induced optical and magnetic properties. However proper understanding for the same is completely lacking in the literature. An effort was taken to understand the origin of various defect induced emission and ferromagnetism in MgO. A combined EPR and PALS study helped in a great deal in understanding the defect structures in MgO. With the help of DFT calculation, a proper summery about the various defects induced electronic structure inside the band gap was obtained. In MgO, a photo ionization process of the F centre is involved at an excitation wavelength of 250 nm, followed by the equation $F + h\upsilon \leftrightarrow F^{+} + e$. The released electron in this process may prompt into the conduction band and thereby behaves as a free carrier. Being free, the electron may recombine with different types of positively charged defect centres in addition to the newly formed F^{+} centres. Thus different electronic transitions from the conduction band (CB) to the empty ground electronic states of positively charged F- and F_2-type centres could be correlated with the observed emission components. Low temperature EPR study also helped to identify the paramagnetic defect centres responsible for ferromagnetism behavior in MgO.

In $MgAl_2O_4$, we have observed defect induced tunable emission from blue-green-yellow to red and near-infrared region (NIR) upon thermal annealing of the compound. With varying excitation wavelength, a photo conversion process of F to F^{+} centres at λ_{ex} = 250 nm was observed for the first time. The thermally tunable emission characteristic is attributed to the change in the phase behavior of the spinel. Further low temperature tunable emission characteristics render $MgAl_2O_4$ to be a potential optical based thermal sensor material. In another aluminates based spinel compound i.e. $ZnAl_2O_4$, it has been found that the compound obtained at lower annealing temperature is a blue emitting phosphors while that obtained at higher annealing temperature is near white emitting phosphor. Interestingly for both $MgAl_2O_4$ and $ZnAl_2O_4$ compounds obtained after synthesising at lower annealing temperature, the lifetime of the defect centres were found to be high (of the order of millisecond) while at higher annealing temperature the life times were significantly reduced (of the order of μs). This makes the phosphors more variant i.e. either long persistent or short persistent. From the DFT calculated density of states (DOS), we have successfully established a clear understanding about the electronic structures inside the band gap due to different defect states and their correlation with the emission.

Chapter 4: Transition metal ions mediated optical properties in Fe^{3+}:$ZnAl_2O_4$, Mn^{2+}:$SrZrO_3$ & $LiZnVO_4$

This chapter discusses about the optical properties of TM ion doped oxide materials and their tunable emission characteristics with crystal field variation. By changing the crystal field environment surrounding the transition metal ion, one can induce a large diversity in optical properties in the transition metal doped oxide materials. For a d^5 system such as for Fe^{3+} and Mn^{2+} ion, the emission is due to $^4T_1 \rightarrow {}^6A_1$ transition which is very much dependent on the crystal field strength **[xxxiii]**. At higher crystal field strength, the transition energy gap is small while it is large for low crystal filed environment.

For all the $Zn_{1-X}Fe_XAl_2O_4$ (x = 0.005, 0.010, 0.025 or 0.050) compounds which were prepared at 700 ^{0}C through sol-gel combustion method, we have observed two different emission bands in the blue and red region respectively. The blue band is attributed to the Fe^{3+} in tetrahedral geometry (low crystal field) while the red band is due to Fe^{3+} in octahedral geometry (high crystal field). When these compounds were annealed at higher temperatures (such as 800 ^{0}C & 900 ^{0}C), a reverse trend in the two respective bands was observed; the intensity of the blue band was found to decrease while that of the red band was increased. This crystal field dependent photoluminescence property of Fe^{3+} ion also helped to probe the inverse to normal phase transition in $ZnAl_2O_4$ spinel. Through a combined XRD, PL and EPR study in Fe^{3+} doped $ZnAl_2O_4$, it has been established that in $ZnAl_2O_4$ which was obtained at low annealing temperature, the percentage of inverse spinel is more while heating this compound at higher temperature led to a transformation of the inverse phase to normal.

In Mn: SrZrO3, the emission due to Mn^{2+} was found to be varied depending on its substitution at different cation site. Mn^{2+} ion substituted at Zr-site faces a strong crystal field environment, while at Sr-site it faces a weak crystal field. Thus at Sr-site, Mn^{2+} emits green colour while at Zr-site it gives red emission. We have also observed an enhancement of the red emission at higher doping level, indicating more substitution of Mn^{2+} at Zr-site at higher concentration. Further these Mn- substitutions at Sr & Zr- sites were also found to influence the shallow and deep defects related emissions, which was further supported by DFT calculation.

In $LiZnVO_4$ an intense green emission was observed due to oxygen vacancy and charge transfer transition of the VO_4^{3-} host. The compound was synthesised through sol-gel combustion route. Usually phosphor materials obtained via this route often show low quantum yield due to agglomeration of the particles at higher annealing temperature. In present case, vanadium exists as VO^{2+} ($3d^1$ and EPR active) in the sol and gel form during the synthesis procedure whereas in the final product $LiZnVO_4$, it exists as V^{5+} ($3d^0$ and EPR inactive). Thus monitoring the EPR spectra at different intermediate steps during the synthesis process helped to conclude that 600 ^0C is the optimum temperature for synthesis of $LiZnVO_4$ phosphors. Further, the calculated EPR parameters at various intermediate steps suggested that there is a change in co-ordination surrounding vanadium atom from octahedral to tetrahedral geometry, which confirmed that tetrahedral VO_4^{3-} is the main luminescence centres. Thus transition metal ions can be used in colour tunable phosphor materials and also as a local structural probe.

Chapter 5: Lanthanide and Actinide ions mediated optical properties in Sm^{3+}:$BaZrO_3$, Eu^{3+}:$BaZrO_3$, $Bi_{1.96}Eu_{0.04}UO_6$ & U: MgAl2O4

This chapter discusses about the photoluminescence properties of lanthanide and actinide ions in different oxide matrices. Here, we had introduced both Sm^{3+} & Eu^{3+} ions in nanocrystalline $BaZrO_3$ and Eu^{3+} in Bi_2UO_6. $BaZrO_3$ nanoceramics (both doped and undoped) were synthesized using gel-combustion route. Intense blue and green emission was observed in undoped sample due to the presence of oxygen vacancy. Both Sm^{3+} and Eu^{3+} doped $BaZrO_3$ compounds were found to be red emitting phosphors. Based on PL spectroscopy, it was inferred that majority of Sm^{3+} ion stabilizes at Ba^{2+} site without inversion symmetry where as majority of Eu^{3+} ion occupies Zr^{4+} site. The actual site symmetry for Eu^{3+} ion in barium zirconate was also evaluated based on stark splitting pattern, which was found to be C_6.

In $Bi_{2-2x}La_{2x}UO_6$, doping of La^{+3}creates oxygen vacancies in the matrix which leads to ionic conductivity due to the migration of oxide ions through the oxygen vacancies. Now in order to understand the local structure of La, Eu^{3+} had doped in place of La^{+3}, since La^{+3} is a non-activator ion. In iso-structural $Bi_{1.96}Eu_{0.04}UO_6$ compound, it was observed that majority of Eu^{3+} ions are occupying the Bi^{3+} site.

Thus Eu^{3+} can be used as a spectroscopic probe for site occupancy of La^{3+} having similar charge and size. Emission due to oxygen vacancies was also observed in this compound, which in combine study with EXAFS was concluded to be due to La substitution at Bi site, which leads to distortion in the matrix. These oxygen vacancies were also detected by EPR technique and their concentration was found to increase up to a certain percent of La doping followed by decay.

Considering the fact that this $MgAl_2O_4$ is one of the probable candidates to be used for transmutation of actinide; speciation study of uranium ion in this particular matrix holds high significance for nuclear scientist. Time resolved photoluminescence (TRPL) is used extensively in uranium speciation in doped solid.The compounds were synthesised through sol-gel combustion method. From excitation and emission spectroscopy, it was observed that uranium stabilizes in +6 oxidation state in the form of UO_2^{2+} ion. On doping uranium in $MgAl_2O_4$, complete energy transfer from host to uranium ion was observed which is explained using DFT. Based on luminescence lifetime it was inferred that U in the form of uranyl exist in two different chemical environments in $MgAl_2O_4$.

Chapter 6: Conclusions and future scope

The conclusions drawn from the work carried out have been described in the last chapter of the thesis. The future scopes of research in this rapidly growing area have also been highlighted. The present work describes various defect and doping induced optical properties in different oxide matrices such as spinel compounds ($ZnAl_2O_4$, $MgAl_2O_4$ etc.), perovskite ($SrZrO_3$ & $BaZrO_3$), MgO, $Bi_{2-2x}La_{2x}/Eu_{2x}UO_6$ and $LiZnVO_4$. The different type of defect centres such as oxygen vacancy, cationic vacancy, interstitial defect create different electronic states inside the wide band gap, which are responsible for multicolour emission of the undoped compounds. Defect centres such as Mg and O-vacancies in MgO are also responsible for magnetism behavior. Additionally tuning of emission profile of these defects related materials was also possible by means of thermal annealing. In case of doped materials, optical properties of various dopant ions such as transition metal ion (Fe^{3+}:$ZnAl_2O_4$, Mn:$SrZrO_3$, $LiZnVO_4$), lanthanide (Sm^{3+} and Eu^{3+} doped $BaZrO_3$) and actinide (U:$MgAl_2O_4$ and $Bi_{2-2x}La_{2x}/Eu_{2x}UO_6$) were investigated. For transition metal ions, the optical properties can be tuned in the blue and red regions by changing the crystal field environment surrounding the metal ion while in case of lanthanides, the emission profile is very much dependent on the site symmetry. For actinides such as U, the optical properties vary with the oxidation state. Different spectroscopic techniques such as Photoluminescence (PL), Electron Paramagnetic Resonance (EPR), Extended X-ray Absorption Fine Structure (EXAFS), UV-visible , Positron annihilation lifetime spectroscopy (PALS) etc. were used throughout the thesis work. The findings of these studies were further corroborated with the Density Functional Theory (DFT) calculations. The chapter is concluded by outlined the directions for future research related to the topic of the thesis.

References:

I. N. Kimura, K. Sakuma, S. Hirafune, K. Asano, N. Hiroski and R.J. Xie, *Applied Physics Letter*, **2007**, *90*, 051109.

II. E.F. Schubert and J.K. Kim, *Science*, **2005**,*308*,1274.

III. http://www.indiatimes.com/news/india-will-save-9k-million-of-units-of power-rs-5500-cr-annually-if-slnp-is-implemented-properly-263400.html

IV. R.F. Wang, J.L. Zhang, X.M. Xu, Y.L. Wang, L.Y. Zhou and B. Li, *Materials Letters*, **2012**, *84*, 24.

V. S. D. Jee, J. K. Park and S. H. Lee, *Journal of materials science*,**2006**, *41*, 3139.

VI. H.J. Yang, H.R. Xu, G.S. Zhu, L. Yuan, C. Zhang, F.S. Li and A.B. Yu, *Materials Letter,* **2013***, 92,* 161.

VII. C. Feldmann, T. Justel, C. R. Ronda and P. J. Schmidt, *Adv. Funct. Mater.*, **2003**, *13*,511.

VIII. A. A. Setlur, *The Electrochemical Society Interface*,Winter, 2009,32

IX. V. P. Tuyen, T. Hayakawa, M. Nogami, J. R. Duclere and P. Thomas, *J. Solid State Chem.,***2010**,*183*,2714.

X. P. A. Tanner, Z. Pan, N. Rakov and G. S. Maciel, *J. Alloys Compd.,* **2016**, *424*, 347.

XI. W. C. Ke, C. C. Lin, R. S. Liu and M. C. Kuo, *J. Electrochem. Soc.,***2010**, *157*, 307.

XII. C. Zhang and Jun Lin, *Chem. Soc. Rev.,* **2012**, *41*, 7938.

XIII. W. H. Green, K. P. Le, J. Grey, T. T. Au and M. J. Sailor, *Science*, **1997**, *276*, 1826.

XIV. K. P. Loh, Q. Bao, G. Eda and M. Chhowalla*, Nat. Chem.,* **2010**, *2*, 1015.

XV. V. Bekiari and P. Lianos, *Chem. Mater.*, **1998**, *10*, 3777.

XVI. S.D. Haa and S. Ramanathan, *J. Appld. Phys.,* **2011**, *110*, 071101.

XVII. S. K. Gupta, C. Reghukumar and R. M. Kadam, *RSC Adv.,* **2016**, *6*, 53614.

XVIII. S. K. Gupta, P. S. Ghosh, N. Pathak and R. M. Kadam, *RSC Adv.,* **2016**, *6*, 42923.

XIX. L.S. Natrajan, *Coord. Chem. Rev*. **2012**, *256*, 1583.

XX. M. Sobczyk, J. Drozdzynski, R. Lisiecki, W. R. Romanowski, *J. Lumin.*, **2008**, *128* ,185.

XXI. B. Ordejon, V. Vallet, J.P. Flament, L. Seijo and Z. Barandiara, *J. Lumin.,* **2007**,*126* ,779.

XXII. S. K. Gupta, A.K. Yadav, Sandeep Nigam, S.N. Jha, C. Mazumder, D. Bhattacharya and S.K. Thulasidas, *Spectrochim. Acta A*, **2015**,*151*, 453.

XXIII. L.S. Natrajan, *Coord. Chem. Rev*., **2012,** *256*,1583.

XXIV. L. Thome and F. Garrido ,*Vacuum,* **2001**,*63*,619.

XXV. Y. Chen , M. M. Abraham , T. J. Turner, C. M. Nelson, *Philosophical Magazine,***1975**, *32*, 99.

XXVI. C. Park, J. Lee and W.S. Chang, *J. Phys. Chem. C,* **2015**, *119*, 16984.

XXVII. J. Li, Z. Wang, A. Zhao, J. Wang, Y. Song and T.K. Sham, *J. Phys. Chem. C,* **2015***, 119*, 17848.

XXVIII. A. Kar, S. Kundu and A. Patra, *J. Phys. Chem. C*, **2011**, *115*, 118.

XXIX. S. Saha, S. Das, D. Sen, U.K Ghorai, N. Mazumder, B.K. Gupta and K.K. Chattopadhyay, *J. Mater. Chem. C*, ***2015***, *3*, 6786.

XXX. S. Ikeda, T. Uchino, *J. Phys. Chem. C*, **2014**,*118*, 4346.

XXXI. P. V. Pikhitsa, C. Kim, S. Chae, S. Shin, S. Jung, M. Kitaura, S. Kimura, K. Fukui and M. Choi, *Appl. Phys. Lett*., **2015**, *106*, 83106.

XXXII. S. Angelov, R. Stoyanova, R. Dafinova and K. Kabasanov, *J. Phys. Chem. Solids*, **1986**, *47*, 409.

XXXIII. P. D. Fleischauer, P. Fleischauer, *Chem. Rev.,* **1970**,*70*, 199.

List of Figures

Chapter 1

1. Figure 1.1. Schematic involves in materials study
2. Figure 1.2. Local structure in material
3. Figure 1.3. Schematic of activator doped emission
4. Figure 1.4. Schematic activator free (defect) related emission.
5. Figure 1.5. Flow chart of various points defects in solid
6. Figure 1.6. Pictorial representation of various stoichiometric defects
7. Figure 1.7. Schottky and Frenkel defect
8. Figure 1.8. Edge dislocation.
9. Figure 1.9. Screw dislocation
10. Figure 1.10. Grain Boundaries
11. Figure 1.11. Tilt Boundaries.
12. Figure 1.12. Twin Boundaries
13. Figure 1.13. Origin of stacking faults. Different stacking sequences of close-packed crystals
14. Figure 1.14. Schematic diagram of phosphors.(a) Activator in the host lattice. (b) Energy transfer from a sensitizer to an activator. A. activator; S. sensitizer; EXC. excitation; EM. emission; ET. energy transfer
15. Figure 1.15. Energy band diagram of fluorescent phosphor
16. Figure 1.16. An energy band diagram representing a phosphorescent phosphor.
17. Figure 1.17. Configurational coordinate diagram
18. Figure. 1.18. Energy level diagram of a d5 configuration
19. Figure 1.19. Configurational coordinate diagram. After absorption the system reaches a high vibrational level of the excited state. Subsequently it relaxes to the lowest vibrational level from where the emission occurs.
20. Figure 1.20. The dashed curve shows the PL spectrum of Mn^{2+} in $LiBaF_3$, excited at 255 nm.
21. Figure 1.21. The periodic table of elements. The lanthanides are highlighted in green.

22. Figure 1.22. Splitting of the 4f energy levels of Eu^{3+} as a result of electronic repulsion, spin-orbit coupling, and the ligand field

23. Figure 1.23. Energy diagram of the 4f levels responsible for the lanthanide luminescence

24. Figure 1.24. Electronic transitions in lanthanide ions. (a) absorption/excitation, (b) excited state absorption, (c) direct excitation into a higher excited state, (d) ‘‘conventional’’ emission from the lowest luminescent state, (e) non-radiative relaxation, (f) radiative transition between excited states, (g) emission from a higher excited state.

25. Figure 1.25. Graphical representation of the number of vibrational quanta of four high frequency oscillators that is required to match the energy gap between the lowest luminescent state and the highest non-luminescent state of the lanthanide ion (the dashed line is merely a guide to the eye).

Chapter 2

1. Figure 2.1. Various steps in the sol-gel process to control the final morphology of the product
2. Figure 2.2. Acid and base catalyzed hydrolysis step
3. Figure 2.3. Simplified representation of the condensation of TEOS in sol gel process
4. Figure 2.4. Scattering of x-rays from atoms and Bragg’s law. The incoming beam (coming from upper left) causes each scatterer to re-radiate a small portion of its intensity as a spherical wave. When the scatterers are arranged symmetrically with a separation d, these spherical waves will be in constructive interference or sync (add constructively) only in some directions, where their path-length difference 2d sin θ equals an integer multiple of the wavelength λ. Thus part of the incoming beam is deflected by an angle 2θ and produce a reflection spot in the diffraction pattern.
5. Figure 2.5. Continuous and characteristic x-rays for copper.
6. Figure 2.6. Using a Nickel filter for Cu X-rays
7. Figure 2.7. X-ray diffractometer.
8. Figure 2.8. Typical range of light and electron microscope

9. Figure 2.9. Schematic of scanning electron microscope
10. Figure 2.10. Various electron and photon emitted in SEM and information’s gathered from them.
11. Figure 2.11. Schematic of transmission electron microscope.
12. Figure 2.12. Schematic representation of positron annihilation indicating the basis for the three experimental techniques of positron annihilation spectroscopy (PAS). lifetime, angular correlation, and Doppler broadening.
13. Figure 2.13. The conventional positron lifetime measurement system
14. Figure 2.14. Separation between the lower and the upper state for unpaired free electrons in EPR
15. Figure 2.15. Pascal's triangle
16. Figure 2.16. Simulated EPR spectrum of the •CH3 radical.
17. Figure 2.17. Simulated EPR spectrum of the H2C(OCH3) radical.
18. Figure 2.18. Triangle for I=1
19. Figure 2.19. Comparison of absorption spectrum and EPR spectrum.
20. Figure 2.20. Block diagram of typical EPR spectrometers
21. Figure 2.21. Photograph of Bruker ESP-300 EPR spectrometer
22. Figure 2.22. A Jablonski diagram shows the possible relaxation processes in a molecule after the molecule has absorbed a photon (A). IC = internal conversion, ISC= intersystem conversion, F= fluorescence, P= phosphorescence
23. Figure 2.23. Parameters affecting fluorescence emission
24. Figure 2.24. Block diagram of spectrofluorometer.
25. Figure 2.25. Photograph of the time resolved fluorescence spectrometer
26. Figure 2.26. a) TCSPC - A fast stopwatch with two inputs b) TCSPC Measurement Principal .
27. Figure 2.27. The main components for signal processing in TCSPC.
28. Figure 2.28. CIE xy Chromaticity diagram

Chapter 3
1. Figure 3.1. XRD patterns of different temperature annealed MgO compounds. MgO-600, MgO-800 and MgO-1000.
2. Figure 3.2. (a1) SEM images of MgO-600 and (a2) corresponding

size distribution histogram.(b1) SEM images of MgO-1000 compounds and (b2) corresponding size distribution histogram.

3. Figure 3.3. UV–Visible spectrum (in reflectance mode) of a) MgO-600, b) MgO-800 and c) MgO-1000.
4. Figure 3.4. a) Excitation spectra of Mg-600 at λ_{em} = 540 nm and b) Emission spectra of MgO-600 at different excitation wavelengths (viz. λ_{ex} = 210 nm, 250 nm, 290 nm & 310 nm) [57]
5. Figure 3.5. Emission spectra of a) MgO-600, b) MgO-800 and c) MgO-1000 at λ_{ex} = 250 nm. Arrows show the peak position of different emitting components which may slightly shift towards right hand or left hand side at different annealing temperature.
6. Figure 3.6. Decay profiles of the MgO-600 compound at λ_{ex} = 250 nm and at different emission wavelength viz. a) 390 nm, b) 450 nm, c) 490 nm & d) 540 nm
7. Figure 3.7. TRES at different time interval.
8. Figure 3.8. TRES due to different colour components.
9. Figure 3.9. TRES at 2-20 μs and 20-40 μs time interval.
10. Figure 3.10. TRES at 100-300 μs and 300-600 μs time interval.
11. Figure 3.11. a) TRES at 800 μs & b) Gaussian Fit of TRES in the Figure 3.8f.
12. Figure 3.12. Gaussian fit of the emission profile of MgO-600, MgO-800 and MgO-1000 compound.
13. Figure 3.13. Overall summary of the location of the oxygen defect states arises due to $V_O^0(F^0)$, V_O^{+1} (F^+) and V_O^{+2} (F^{+2}) as well as Mg defect states arises due to V^0_{Mg}, V^{-1}_{Mg} and V^{-2}_{Mg}. Distribution of defect states for vacancy clusters F_2 centre and P centre are also summarized. Colour filled bands filled with electrons and white bands are empty.
14. Figure 3.14. Possible free electron model for different transitions of the emission components in MgO. The bold circles represent filled electronic states while the white ones represent vacant electronic state. The white circles in the VB represent positively charged holes. All the electronic states inside the band gap represent the ground state

configuration. At 250 nm excitation wavelength a photo conversion process of F centre is involved followed by the equation F + hυ ↔ F^+ + e. The released electron in this process becomes free after prompting into the conduction band and may recombine with different types of positively charged defect centres in addition to the newly formed F^+ centres. Thus different electronic transitions from the conduction band (CB) to the empty ground electronic states of positively charged F- and F_2-type centres can be correlated with the observed emissions.

15. Figure 3.15. Room temperature and low temperature (77 K) Emission spectra of MgO-600 compound at different excitation wavelengths (λ_{ex} = 250 nm & 290 nm).
16. Figure 3.16. FC and ZFC M vs T plots showing for MgO-600, MgO-800 & MgO-1000.
17. Figure 3.17. Hysteresis plots for a) MgO- 600, b) MgO- 800 and c) MgO-1000 after diamagnetic correction. Inbox represents the enlarge view of the hysteresis loop near origin.
18. Figure 3.18. Typical PALS spectrum for MgO-1000 compound.
19. Figure 3.19. Room temperature EPR spectra of MgO-600, MgO-800 and MgO-1000.
20. Figure 3.20. Simulation of the EPR spectra (a) MgO-600 & (b) MgO-1000.
21. Figure 3.21.Temperature dependent EPR spectra of a) MgO-600 & b) MgO-1000.
22. Figure 3.22.Temperature dependencies of (a) line width, $\Delta H_{1/2}$, of the S_{II} signal in MgO-600 (b) resonance field, H_R of the S_{II} signal in MgO-600 and (c) resonance field, H_R of the S_I signal in MgO-1000.
23. Figure 3.23. Temperature dependencies of the inverse of EPR integral intensity i.e.$1/I_{EPR.}$
24. Figure 3.24. XRD patterns of MAS after annealed at (a) 600 ^{0}C (MAS-600). (b) 800 ^{0}C (MAS-800) and (c) 1000 ^{0}C (MAS-1000) and with Mg/Al composition ratio (d) $\frac{0.98}{2.00}$ and (e) $\frac{1}{1.96}$.

25. Figure 3.25. Excitation spectra of MAS compound observed after annealing at 600 ^{0}C with different emission wave length.
26. Figure 3.26. Emission spectra of the MAS compounds obtained after annealed at a) MAS-600, b) MAS-800 and c) MAS-1000 temperature with λ_{ex}= 250 nm.
27. Figure 3.27. CIE chromaticity diagram for the MAS phosphor at different temperature with λ_{ex} =250 nm.
28. Figure 3.28. Emission spectra of MAS -1000 at a) different excitation wavelengths and b) the enlarge version.
29. Figure 3.29. Temperature variation Emission spectra of MAS-1000.
30. Figure 3.30. Emission spectra of the MAS compounds with different Mg/Al composition (a) $\frac{\mathrm{Mg}}{\mathrm{Al}} = \frac{1}{1.96}$, (b) $\frac{\mathrm{Mg}}{\mathrm{Al}} = \frac{0.98}{2}$ and (c) $\frac{\mathrm{Mg}}{\mathrm{Al}} = \frac{1}{2}$ with λ_{ex}= 250 nm.
31. Figure 3.31. Emission spectra of the MAS compounds observed after annealing in different atmospheres (vacuum and air).
32. Figure 3.32. PL decay curves of MAS compound prepared at 600 ^{0}C with λ_{ex} = 250 nm and λ_{em} = (a) 410, (b) 460, (c) 530 and (d) 720 nm.
33. Figure 3.33. Time Resolved Emission Spectra (TRES) at different delay time.
34. Figure 3.34. Time Resolved Emission Spectra of the respective species.
35. Figure 3.35. Overall summary of the location of the defect states arises due to V_O^{0}, V_O^{+1} and V_O^{+2} in the normal and inverse spinel of $MgAl_2O_4$. Light grey coloured bands are filled with electrons and white bands are empty.
36. Figure 3.36. EPR spectra of MAS samples at different annealing temperature.
37. Figure 3.37. Proposed model for trapping de trapping mechanism.
38. Figure. 3.38. Rietveld fittings of XRD patterns of the $ZnAl_2O_4$.
39. Figure 3.39. (a)Emission spectrum of ZA annealed at different temperature with λ_{ex} =250 nm and (b) CIE chromaticity diagram for the ZA phosphor at different temperature which shows a tuning of

colour coordinate from bluish to near-white
40. Figure 3.40. Gaussian fitting of emission spectrum of ZA-750
41. Figure 3.41. Time Resolved Emission Spectra (TRES) of (a) ZA-750 and (b) ZA-1300 at different delay time.
42. Figure 3.42. Time Resolved Emission Spectra (TRES) of ZA-750 in (a) 5-500 μs region and b) 500 μs -5 ms time interval
43. Figure 3.43. Time Resolved Emission Spectra (TRES) at a) 60 ms delay and b) in the 5ms -60 ms time interval
44. Figure 3.44. Time Resolved Emission Spectra (TRES) of ZA-1300 in the 2μs-75 μs time interval.
45. Figure 3.45. Time Resolved Emission Spectra (TRES) at (a) 400 μs delay and (b) at 1.7 ms delay
46. Figure 3.46 . Typical PALS spectra for ZA-750, ZA-1000 and ZA-1200
47. Figure 3.47 . Room temperature EPR spectra for ZA-750, ZA-1000, ZA-1200 and ZA-1300
48. Figure 3.48 . Room temperature EPR spectra for ZA 1000 and ZA-1200
49. Figure 3.49. Room temperature EPR spectra for ZA 750 and ZA-1000
50. Figure 3.50. Overall summary of the location of the defect states arises due as O vacancy (V_O^0, V_O^{+1} and V_O^{+2}), Al vacancy (V_{Al}^{3-}), Zn vacancy (V_{Zn}^0,V_{Zn}^{2-}), interstitial Zn (Zn_i^+), antisite defects (Al_{Zn}^+ & Zn_{Al}^-) etc in $ZnAl_2O_4$. Light gray coloured bands are filled with electrons and white bands are empty.
51. Figure 3.51. Probable electron transition of various colour components a) 375 nm, b) 420 nm, c & d) 450 nm, e& f) 490 nm
52. Figure 3.52. Probable electron transition of various colour components a) 530 nm, b & c) 600 nm
53. Figure 3.53. Probable electron transition of various colour components a & b) 720 nm, c) 780 nm & d) 850 nm

Chapter 4

1. Figure 4.1. a) XRD pattern of the $ZnAl_2O_4$ powder samples annealed at 600°C and standard ICDD stick patterns with file No-5-669, b) Rietveld fittings of XRD patterns undoped $ZnAl_2O_4$ system & c) Expanded XRD pattern corresponding to 2θ value of 36.835.
2. Figure 4.2. Excitation spectra of 0.5 mol% Fe^{3+} doped $ZnAl_2O_4$ with λ_{em}= 693 nm.
3. Figure 4.3. Emission spectra of a) 0.5 mol% Fe^{3+} doped $ZnAl_2O_4$ where Inset shows vibronic sidebands FeO_4, b) 5.0 mol% Fe^{3+} doped $ZnAl_2O_4$with λ_{ex}= 280 nm and c) Energy level diagram of a d^5 configuration .
4. Figure 4.4. Luminescence decay time profile of the 0.5 mol % Fe^{3+} doped $ZnAl_2O_4$ at λ_{ex}= 280 nm with a) λ_{em}= 445 nm and b) λ_{em}= 693 nm.
5. Figure 4.5. a) Room-temperature X-band EPR spectra of $Zn_{0.975}Fe_{0.025}Al_2O_4$ (a) Experiment (blue) and (b) numerical simulation (red).
6. Figure 4.6. a) Simulations (red) of experimental EPR spectra (a) and its components (b-g) for $Zn_{0.975}Fe_{0.025}Al_2O_4$.
7. Figure 4.7. EPR spectra of different mol % Fe^{3+} doped $ZnAl_2O_4$.
8. Figure 4.8. (a) Emission and (b) EPR spectra of 1.0 mol% Fe^{3+} doped $ZnAl_2O_4$ at different annealing temperature.
9. Figure 4.9. (i) XRD pattern of the undoped and Mn doped $SrZrO_3$ powder samples annealed at 600 °C with dopant mol % of (a) 0, (b) 0.1, (c) 0.5, (d) 1.0, (e) 2.5, (f) 5.0 and the standard ICDD stick patterns with file no. 44-0160 and (ii) Schematic crystal structure of $SrZrO_3$
10. Fig. 4.10. Excitation spectra of a) Pure SZO & b) 0.1mol% Mn^{2+}doped SZO with λ_{em} =430 nm.
11. Figure 4.11. Room temperature emission spectrum of a) pure SZO and b) 0.1 mol% Mn^{2+}doped SZO with λ_{ex} =255 nm.
12. Figure 4.12. Variation of intensity ration of peak P_5 to P_3 and P_4 to P_1 with different mol % of Mn^{2+} ion.
13. Figure 4.13. Pictorial representation for the origin of the different peaks of $SrZrO_3.Mn^{2+}$ and their variation with doping level.

14. Figure 4.14. Luminescence decay time profile of the a) SZO and b) 0.1 mol% Mn^{2+}doped SZO.
15. Figure 4.15. Room-temperature EPR spectra of a) SZO & b) 0.1 mol% Mn^{2+} doped SZO.
16. Figure 4.16. (a) First & (b) Second harmonic EPR spectra of 0.1 mol% Mn^{2+} doped SZO samples (blue) and their simulated signals S_I, S_{II}, S_{III} and $S_{Total}= S_I+ S_{II}+ S_{III.}$
17. Figure 4.17. The EPR spectra recorded for the $Sr_{1-x}Mn_xZrO_3$ samples with concentration. a) x = 0.001, b) x = 0.005, c) x = 0.01, d) x= 0.025 and e) x = 0.05..
18. Figure 4.18. Latimer Diagram.
19. Figure 4.19. (a) XRD pattern of the lithium zinc vanadate (LZV) powder samples annealed at 600°C and Standard ICDD stick patterns with file No-38-1332 , (b) Crystal structure of $LiZnVO_4$ and (c)SEM image of LZV
20. Figure 4.20. (a)EPR spectra of vanadium at different stages during sol-gel chemistry and (b) Comparison of $A_{||}$ value of VO^{2+} in different stages of annealing
21. Figure 4.21. (a) Excitation and(b) Emission spectra of $LiZnVO_4$ (c) and its decay profile.
22. Figure 4.22 . CIE chromaticity diagram for the $LiZnVO_4$ phosphor at 359 nm excitation

Chapter 5

1. Figure 5.1. XRD Pattern of undoped and Sm and Eu doped $BaZrO_3$ nanocrystal. This figure also consists of standard pattern corresponding to JCPDS No. 060399.
2. Figure 5.2. (a) TEM (b) HRTEM image and (c) SAED pattern of BZO nanoparticles.
3. Figure 5.3. (a) PL and (b)EPR spectra of $BaZrO_3$ at room temperature.
4. Figure 5.4. (a) Excitation (b) Emission spectra of $BaZrO_3.Sm^{3+}$ under 643 nm (λ_{em}) and 240 nm (λ_{ex}) (c) CIE diagram showing the co-ordinates and representing the colour emitted by $BaZrO_3.Sm^{3+}$.
5. Figure 5.5. PL decay profile for (a) $BaZrO_3.Sm^{3+}$ under excitation of

240 nm and emission of 643 nm and (b) for $BaZrO_3.Eu^{3+}$ under excitation of 255 nm and emission of 616 nm

6. Figure 5.6. (a) Excitation (b) Emission spectra of $BaZrO_3.Eu^{3+}$ under 616 nm (λ_{em}) and 255 nm (λ_{ex}) (c) CIE diagram showing the co-ordinates and representing the colour emitted by $BaZrO3.Eu^{3+}$.
7. Figure 5.7. Stark splitting pattern of Eu^{3+}emission peak in $BaZrO_3$.
8. Figure 5.8. (a) Rietveld fitting of XRD pattern of Bi_2UO_6 (dotted line, observed pattern; continuous line, best fitted theoretical curve after Rietveld refinement)and (b) Crystal structure of Bi_2UO_6.
9. Figure 5.9. (a)XRD patterns of $Bi_{2-2x}La_{2x}UO_6$ with X= 0.00, 0.02, 0.05, 0.06, 0.08 respectively and (b) XRD patterns of the enlarged portion of Fig.5.9a (in the 2 theta range of 14-24°) as shown above.
10. Figure 5.10. EPR spectra of $Bi_{2-2x}La_{2x}UO_6$ (x=0.02 to 0.08) recorded at room temperature.
11. Figure 5.11. PL excitation spectra of $Bi_{1.96}Eu_{0.04}UO_6$ at different emission wavelengths (530 nm & 615 nm) . a) Charge Transfer Bands (CTB) and b) Different characteristic excitation lines of Eu^{3+} and U^{6+}.
12. Figure 5.12. PL emission spectrum of $Bi_{1.96}Eu_{0.04}UO_6$ at a) λ_{ex}=245 nm and b) λ_{ex}=270 nm
13. Figure 5.13. PL decay curves corresponding to 2 atom % Eu^{3+} doped Bi_2UO_6 ($Bi_{1.96}Eu_{0.04}UO_6$) with different emission wavelengths (λ_{em} = 430, 537 and 615 nm) at an excitation wavelength of λ_{ex} = 245.
14. Figure 5.14. TRES spectra of 2 atom % Eu^{3+} doped Bi_2UO_6 ($Bi_{1.96}Eu_{0.04}UO_6$) at two different delay time (20 & 200 μs).
15. Figure 5.15. Powder X-ray diffraction pattern of $MgAl_2O_4$. U
16. Figure 5.16. Emission spectrum of $MgAl_2O_4$ under excitation of 230 nm.
17. Figure 5.17. Excitation spectrum of $MgAl_2O_4$.U (λ_{em}-501 nm)
18. Figure 5.18. Emission spectra of $MgAl_2O_4$.U in the excitation range (a) 230-300 and (b) 300-400
19. Figure 5.19. Emission spectra of $MgAl_2O_4$.U and uranyl fluoride

crystals under identical conditions
20. Figure 5.20. (a)Luminescence decay profile of Uranyl ion in $MgAl_2O_4$ under λ_{ex}-250 nm and λ_{em}-501 nm & (b) Time resolved emission spectra of short and longer lived uranyl ion in MA

List of Tables

Chapter 1

1. Table 1.1. Classification of Defects
2. Table 1.2 .The various types of luminescence.
3. Table1.3.Electronic configuration of lanthanide atoms and trivalent ions as well as the radii of the trivalent ions.
4. Table 1.4. Selection rules for f–f transitions between spectroscopic levels.

Chapter 2

1. Table 2.1. Advantages and disadvantages of electron microscope
2. Table 2.2. Comparison between light optical microscope and electron microscope
3. Table 2.3. Comparison between SEM and TEM
4. Table 2.4. Bio transition metal nuclear spins and EPR hyperfine patterns.
5. Table 2.5. Bio ligand atom nuclear spins and their EPR hyperfine patterns.
6. Table 2.6. List of fields for resonance for a g = 2 signal at microwave frequencies commonly available in EPR spectrometers.

Chapter 3

1. Table 3.1. Lifetime values of MgO-600 at different emission wavelength and their respective contributions.
2. Table 3.2. Colour components and their respective recombination process.
3. Table 3.3. Saturation Magnetisation value for different temperature annealed MgO compound obtained from Brillouin function fitting of the experimental data.
4. Table 3.4 . Positron lifetimes of MgO compounds annealed at different temperature.
5. Table-3.5. Lifetime values of MAS compounds obtained at different annealing temperature
6. Table-3.6. Lifetime values for different emission components at 250 nm excitation wavelength.
7. Table 3.7. Positron lifetimes of $ZnAl_2O_4$

(ZA) compounds annealed at different temperature.

8. Table 3.8. The average lifetime τ_{av} and the bulk lifetime τ_B for different ZA compounds

Chapter 4

1. Table-4.1. Structural parameters of Fe doped $ZnAl_2O_4$ synthesized through the sol-gel-combustion route .
2. Table-4.2. Percentage and Lifetime values of T_1 (Short lived) and T_2 (Long lived) at different mol% of Fe^{3+}.
3. Table 4.3. Structural parameters of manganese doped $SrZrO_3$ synthesized through the sol–gel-combustion route.
4. Table-4.4. Principal values of g and hyperfine (A) tensors for paramagnetic vanadyl complexes at different temperatures

Chapter 5

1. Table 5.1. J-O intensity parameters and radiative properties for Eu^{3+} in $BaZrO_3$.
2. Table.5.2. Cell parameters and reliability factors (chi-square, R-factor) obtained after the Rietveld refinement.
3. Table. 5.3 . Bond distances at different doping concentration
4. Table 5.4. Lifetime values at different emission wavelength

Chapter 1

Introduction

1.1. Introduction

1.1.1 General introduction to the subject

For the past two decades solid state material chemistry has become a most fascinating area of research globally because of its application in all facets of human life. It encompasses an interface between chemistry, physics, engineering and biological sciences. It basically involves processing of material, its systematic characterization, property optimization and finally evaluation of its performance which can be seen in schematic shown in Figure 1.1. Synthesis and processing involves the creation of a material with the desired material's properties. From an engineering standpoint, a material cannot be used in industry until an economical production method has been developed for it. In this step, chemistry plays a major and challenging role for economical development of a material with its optimum performance. In order to find or discover newer properties in materials the best way is to developed new kind of materials. Therefore the most imminent challenges of modern materials chemist are not only to develop new materials but also to develop novel materials that have comparable or better functionalities **[1]** than those existed in the present market. Again in exploring new material, structural-property correlation is very important for optimum and efficient performance of the designed materials. Thus a systematic structure-property correlation study is very much essential in developing any kind of multifunctional materials with properties such as optical, magnetic, electrical, catalytic etc. [2]

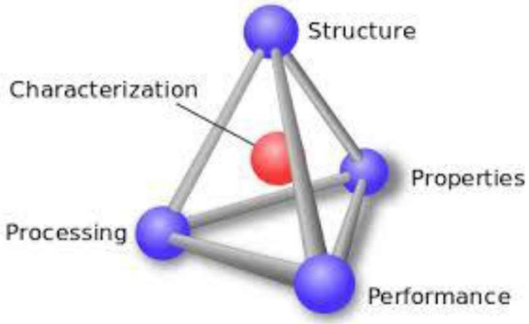

Figure 1.1: *Schematic involves in materials study*

One such astounding area of materials research encompasses phosphor material related research. Because of the ever-growing demand for advanced luminescent materials, huge scientific and technological efforts have been dedicated to improve the existing phosphors and to develop new effective luminescent materials **[3]**. In general, phosphors are classified into two sub categories: activator based and non-activator based. In activator based phosphor, the luminescence property is governed by transitions between energy levels of metal activator ions such as rare earth and transition metal ions (e.g. f–f transitions of Eu^{3+} in $Y_2O_3:Eu^{3+}$) **[4 -7]** or complex ions e.g. $[WO_4]^{2-}$ in $CaWO_4$ where the emission is due to charge-transfer transition **[8,9]**. However these luminescent materials are sometimes expensive and contain non-environment friendly elements, such as Ag (in ZnS:Ag) **[3]**. Though there are several advantages of lanthanide doped phosphor because of its interesting optical properties such as high colour purity, narrow emission, large stoke shift, longer excited state lifetime, high photostability etc., but pure rare earth is facing some serious problems such as shortage problem, lack of recyclability and its high cost. On the other hand, it is also necessary for most metal-activator-based phosphors to be excited by short wavelength ultraviolet (UV) light for operation, which results in the extensive use of a mercury vapour plasma in fluorescent lighting products **[3]**. The excess usage of mercury vapour will give rise to environmental contamination and technical difficulties. Mercury is extremely hazardous chemical and can have serious ill effect on humans.

The other group of luminescent materials is non-activator based luminescence materials, which consists of semiconductors and defect-related materials **[10]**. For most semiconductors, the luminescence normally results from band-to-band excitation involving the impurity states within the band gap. Since these non activator based materials do not contain any activator ion, they seem to be promising alternatives to the traditional phosphors in many applications because of their advantages of low toxicity, stability, tunable emission colour, and low cost **[11-13]**.

However in all the optical materials, irrespective of the fact whether it is doped or undoped, the local structure of the luminescence centres (activator or the defect canter) is directly linked with the luminescence phenomenon and therefore highly influences the luminescence efficiency. Here local structure of luminescence centres means its oxidation states or charge, crystal field environment, co-ordination, symmetry etc., as shown in Figure 1.2. Any change in these parameters will have serious consequences on the optical and magnetic properties.

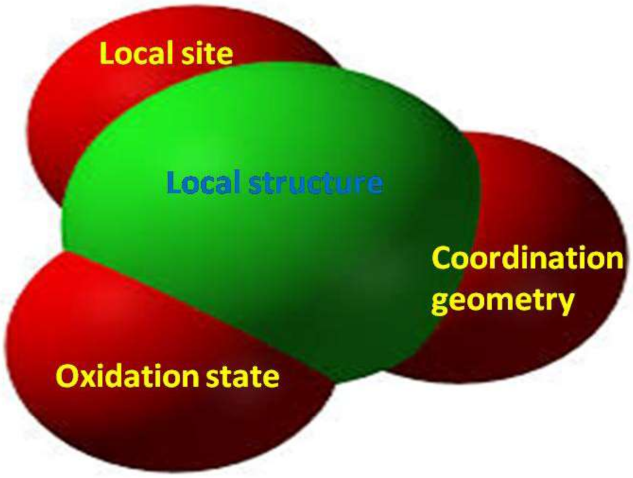

Figure 1.2: *Local structure in material*

Although there is a tremendous evolution in material chemistry with regards to design, synthesise and controlling of properties of new functional materials with different sizes from micro to nanometre scale **[14]**, such new materials are often structurally and chemically complex and often lack long range ordering or structurally disorder, which may degrade its performance. Therefore though the synthesis of new materials can be achieved but the successes of developing an efficient performing material have been limited. The desire for efficient novel functions or properties generate a vast demand for new materials which have to be fabricated with well defined size of the particle, controllable properties and with well known structures. In oxide based materials, tremendous interest has been generated in tailoring the properties on the molecular and nanoscale level, which either shows characteristics in between the precursor oxide phases or even new properties. Tailoring of specific properties such as magnetic, optical, electronic etc. is very important for the material to be utilized. To accomplish the target properties, the right structure and composition have to be achieved. Mounting evidences suggest that their structure, defects and interaction on nanometre length scale are intimately connected to their remarkable properties. Therefore in order to optimise or enhance the material's properties, precise structural determination on atomic scale i.e. local structure determination for those materials is essential. The present thesis is organised based on a systematic study on different doped and undoped oxide based phosphor materials, which involves their synthesis with different sizes, characterisation, structure-property correlation and finally tailoring of the optical properties for optimum performance of the material.

1.1.2. Transition metal (3d configuration), Rare earth (4f configuration) and Actinide (5f configuration) doped optical materials:

Presently used phosphors in CFLs and w-LEDs are activated with rare earth (RE) and/or Transition metal (TM) ions. Such doping enables to achieve light emission in a given spectral region, which has some advantages (for example temperature insensitivity), but also imposes some limitations.

Especially RE ions show very attractive properties for applications as emission activators. Their 4f-4f transitions result in sharp, atomic-like photoluminescence (PL) bands, which are temperature and host insensitive. As mentioned earlier that use of intra-shell transitions of RE ions also imposes some limitations. In particular, the intra shell 4f-4f transitions of RE ions are difficult to excite under the host excitation, which is due to the screening of electrons from the 4f shell by electrons in the external and filled 5s and 5p shells. Consequently, host excitation is inefficient and 4f-4f transitions are excited only upon 4f-5d or charge transfer (CT) excitation **[15, 16]**. Moreover, the 4f-4f transitions are parity forbidden and thus show rather low rates of radiative decay. The above reason imposes serious limitations on host materials for RE ions. Their band gap must be large enough to allow for either 4f-5d or CT excitation **[16].** Moreover, we must select materials in which one of these excitation processes exactly fits to the energy of emission of mercury vapours or LED emission. These limitations can be avoided if RE emission could be excited by band-to-band excitation of the host material. On the other hand, the d electrons of TM ions are not shielded and hence their emission is host sensitive.

In modern solid state optical technology, lanthanide ions play a great role with applications ranging from solid state lasers for industry, medicine and environmental monitoring, to active optical fibers for telecommunication purposes, phosphors for cathode ray tubes, displays, plasma monitors and lightning applications **[3,16]**. From the scientific point of view, lanthanide doped materials attract increasing interest due to their specific physical properties. Indeed their electron configuration involving *f*-electrons and the exceptional time and space coherence properties led to the observation of new and fascinating phenomena. Lanthanide ion, such Eu^{3+} ion is extensively used as local probes for identifying local structures in crystalline material **[17, 18]**, understanding the effect of chemical and thermal treatment on catalysts and probing the structure of biological molecules. In view of its non-degenerate emissive state i.e. $^5D_0$, Eu^{3+} ion is most appropriate as luminescent structural probe for the determination of the number of metal ion sites in a compound, their symmetry, and their respective population. Other lanthanide ions have transitions that are usually the mixtures of electric dipole transition (EDT) and magnetic dipole transition (MDT) and the effects of symmetry are less pronounced.

Actinide elements (5f-ions) exhibit much richer chemistry than lanthanide because of their tendency to exhibit variable oxidation states. Among actinides, uranium displays unique photophysical characteristics. Other than being a constituent of high level radioactive wastes, uranium is also one of the daughter products in α-decay of plutonium. In this context, it is of paramount importance to examine the chemical environment (coordination and oxidation state) of uranium in important nuclear waste host.

Uranium exists in various oxidation states such as +3, +4, +5 and +6 **[19-21]**. Each one of them exhibit characteristics optical fingerprint. Interestingly the +6 oxidation state of uranium can exhibit different molecular forms such as UO_4^{2-}, UO_6^{6-} or UO_2^{2+} species depending upon the host crystal field, synthesis method, thermal treatment etc. Each one of them exhibit distinct emission characteristics. The fascinating uranyl luminescence has been explored in various glasses and ceramic based matrix. Some of the related applications are internal actinometers in biological chemistry, as luminescent sensors and in uranium detection assays **[22]**. Schematic of activator emission is schematically presented in Figure 1.3.

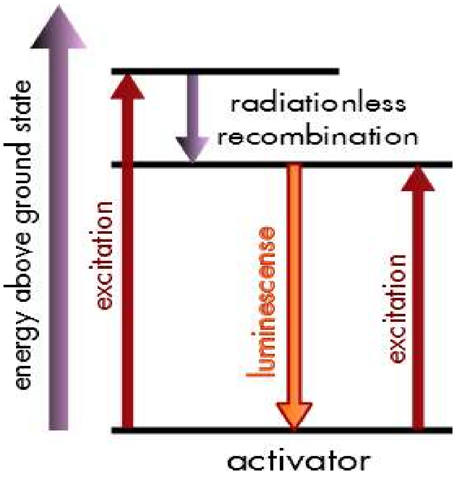

Figure 1.3: *Schematic of activator doped emission*

1.1.3. Defect related optical Materials:

Over the past few decades, enormous amounts of different luminescent nonmaterial have been studied globally. Several discoveries have emerged to provide alternate solutions for overcoming solid-state lighting problems in our daily life. Although, there are well-known materials that can easily emit light, such as semiconductor nanomaterials (CdS, ZnS), quantum dots, and rare earth based nanomaterials (Y_2O_3:Eu^{3+}, YAG:Ce) **[23]** and even though these luminescent materials have found numerous applications, such as luminescent security ink, optoelectronic devices, solar cell, biological fluorescence labelling, light harvesting devices, and optical imaging, **[24]** they have some disadvantages. For instance, semiconductor materials, like sulphides, have issues of toxicity, low efficiency, and require the use of harmful solvents and additives **[25].** Similarly quantum dots require a low temperature to control their size. Though, the rare earth materials have sharp transitions, anti-stokes emission, and better stability, they also suffer from some obvious drawbacks such as inconsiderate synthesis conditions, high cost, and limited availability on earth. There are several investigations going on throughout the world to address these issues. In this series, alkaline earth metal oxides, such as CaO, BeO, MgO, and SrO, have been gaining considerable attention in material science as an inorganic phosphor for optoelectronics devices, sensors, and solid-state lighting applications due to their defect-induced luminescence properties.

Although the roots of defect-related luminescent materials can be traced to 1986, **[26],** the remarkable growth was observed after Sailor *et al.,* reported the white phosphors from a silicate-carboxylate sol–gel precursor **[27]**. Since then, these materials without containing any transition metal or rare earth activators appear to be promising alternatives to traditional phosphors in many applications because of their advantages of low toxicity, stability, tunable emission colour, and low cost **[10 -13]**. The origins of photoluminescence (PL) in this kind of materials are complex in nature and not yet entirely understood. However there is mounting evidence that emission arises from special defects such as vacancies, impurities, radical impurities, donor–acceptor pairs, etc. **[10]**. This results in a charge imbalance at these defect sites which must be rectified by localization of electrons and electron-hole pair or give rise to impurity states within the bandgap. Therefore, the defect sites are apparently the precursors for various luminescent centres in defect-related luminescent materials and impart them with excellent emission characteristics. A schematic diagram of activator free emission is presented in Figure 1.4.

In addition to various attractive luminescence properties in defect related materials, detection of low level defect-induced ferromagnetism (DIFM) at room temperature has also got a substantial attention in several diamagnetic oxides such as ZnO, **[28]** HfO_2, **[29]** CaO, **[30]**, and MgO **[31]** and some of them can be used as spintronics devices for the manipulation of charges and spins **[32]**. The origin of ferromagnetism in these nano size oxide particles, which are otherwise non-magnetic in bulk size, is also a controversial topic till date. In some oxides such as ZnO, HfO_2, TiO_2, In_2O_3, CeO_2, Al_2O_3, SnO_2 etc. the observed ferromagnetism behavior is widely attributed to the oxygen vacancies at the surface of the particles **[33-36]**. On the contrary some other studies attributed this behavior to metal-deficient centres and formation of ferromagnetic clusters **[37-39]**.

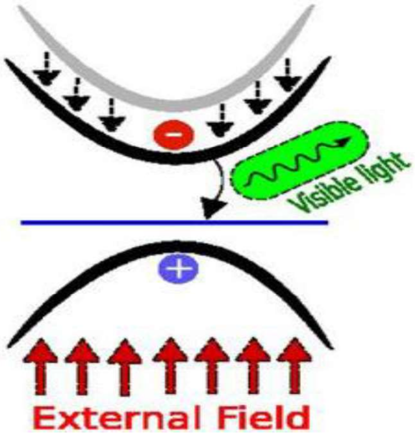

Figure 1.4: *Schematic activator free (defect) related emission* ***[40]***

1.2. Crystallographic Defects [41]

Perfect crystals exist only in theory – in reality, materials have defects. Defects in materials constitute a wide and interesting subject, important in many fields such as material engineering, metallurgy, physics and chemistry.Usually a solid consists of an aggregate of large number of small crystals. These small crystals have defects in them. This happens when crystallization process occurs at fast or moderate rate. Single crystals are formed when the process of crystallization occurs at extremely slow rate. Even these crystals are not free of defects **[41]**. The defects are basically irregularities in the arrangement of constituent particles. The defects can be of various types viz. Point defects, Line defects, Planar defects and Surface defects.

Defects are classified by their spatial extent: Point defects have no spatial extent, as their name suggests, line defects are one-dimensional and two-dimensional defects include planar defects and surfaces. The classification is displayed in Table 1.1 **[42]**.

Table 1.1: Classification of Defects

Type of Defect	Spatial Extent	Some Examples	Definition
Point Defects	0 Dimensional	A missing atom	Vacancy
		An extra atom	Interstitial impurity
		A 'wrong' atom in the lattice	Substitutional impurity
Line Defects	1 Dimensional	Linear discontinuity in the lattice	Dislocation
Planar Defects	2 Dimensional	A missing/ extra sheet of atoms	Stacking fault
		Boundaries between crystals	Grain boundaries
Surfaces	2 Dimensional	Most common '2D-defect'	

1.2.1. Point Defects

Point defects are the irregularities or deviations from ideal arrangement around a point or an atom in a crystalline substance. Point defects can be classified into three types: stoichiometric defects, impurity defects and non-stoichiometric defects. A flow chart of different point defects is given below in Figure 1.5.

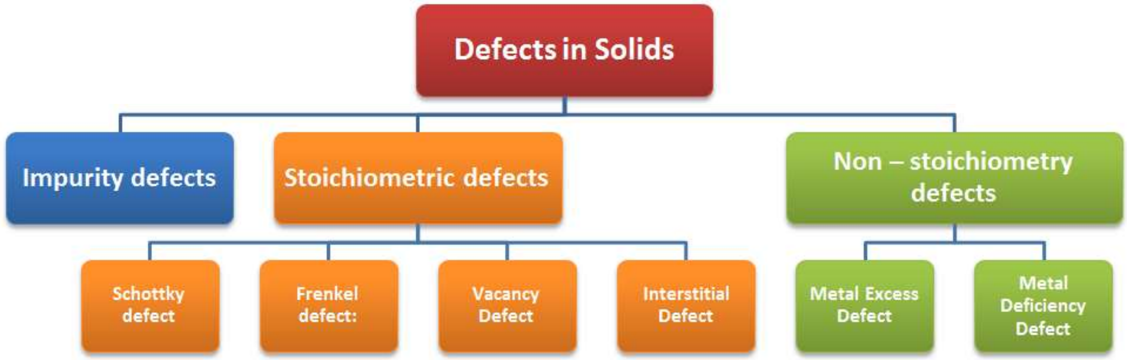

Figure 1.5: *Flow chart of various points defects in solid*

1.2.1.1. Stoichiometric defects

These point defects do not disturb the stoichiometry of the solid. They are also called intrinsic or thermodynamic defects. They are of four types namely vacancy, interstitial, Frenkel and Schottky defects. Vacancy and interstitial defects can be shown by non-ionic solids whereas ionic solids must always maintain electrical neutrality. Rather than simple vacancy or interstitial defects, they show these defects as Frenkel and Schottky defects. These are pictorially represented in Figure 1.6.

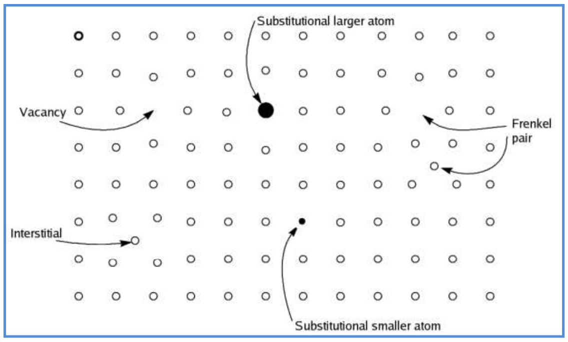

Figure 1.6: *Pictorial representation of various stoichiometric defects*

[Figure courtsey: https://en.wikipedia.org/wiki/Crystallographic_defect]

1.2.1.1 a: Vacancy defects:

When some of the lattice sites are vacant, the crystal is said to have vacancy defect. Vacancies are empty spaces where an atom should be, but is missing.This results in decrease in density of the substance. This defect can also develop when a substance is heated. These are known as vacancy defects. There are different types of vacancies **[42-44]**: F_m^n centre – an electron trapped at an anion vacancy. Vacancy aggregates of ***F*** centres are stable in ionic solids in units of two (called ***M*** centres), three (called ***R*** centres) and four (called ***N*** centres). V_m^n centre - a hole trapped at a cation vacancy. In ***F*** centres the electrons are localized by the net positive charge of the missing anion and vice versa for the ***V***, where *n* are the ion charge that has been removed and *m* is the number of ***F** and **V*** centres that are coupled. Irradiation of simple halide crystals at low temperature with ionizing radiation produces ***F*** centres and trapped holes centres. Pictorial representation of vacancy defects is given in Figure 1.6.

1.2.1.1 b :Vacancy defects*:* Interstitial defects:

When some constituent particles (atoms or molecules) occupy an interstitial site, the crystal is said to have interstitial defect **[45]**. This defect increases the density of the substance. They are of two types; Self-interstitials and Impurity interstitials. Pictorial representation of interstitial defects is given in Figure 1.6

(i) Self-interstitials: Self-interstitial defects are interstitial defects, which contain only atoms which are the same as those already present in the lattice. Self interstitial atoms occur only in low concentrations in metals because they distort and highly stress the tightly packed lattice structure.

(ii) Impurity interstitials: Interstitial impurity atoms are much smaller than the atoms in the bulk matrix and they fit into the open space between the bulk atoms of the lattice structure.

1.2.1.1 c: Schottky defects:

It is a vacancy defect in ionic solids. In order to maintain electrical neutrality, the number of missing cations and anions are equal. Schottky defects decrease the density of the substance. Ionic substances in which the cation and anion are of almost similar sizes **[45]** show Schottky defect. Few examples include NaCl, KCl, CsCl and AgBr. It may be noted that AgBr shows both Frenkel as well as Schottky defects. They are also called ***P*** centre i.e. vacancy of both cations and anions. Pictorial representation of schottky defects is given in Figure 1.7.

1.2.1.1 d: Frenkel defects:

Ionic solids show this defect. The smaller ion (usually cation) is dislocated from its normal site to an interstitial site. It creates a vacancy defect at its original site and an interstitial defect at its new location. Frenkel defect is also called dislocation defect **[45]**. It does not change the density of the solid. Frenkel defect is shown by ionic substance in which there is a large difference in the size of ions, for example, ZnS, AgCl, AgBr and AgI due to small size of Zn^{2+} and Ag^{+} ions. Pictorial representations of Frenkel defects are given in Figure 1.6 and Figure 1.7.

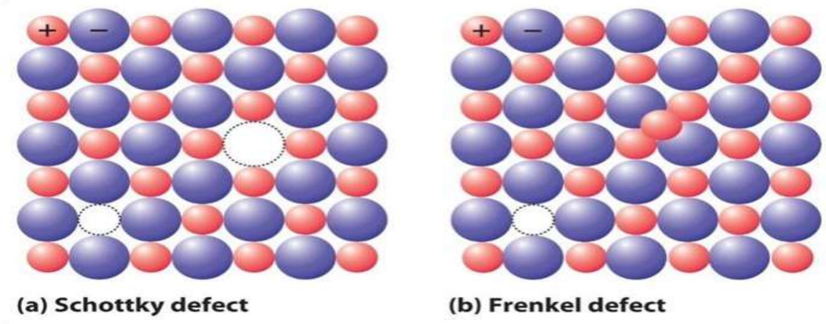

Figure 1.7: *Schottky and Frenkel defect.*

[Figure courtsey: https://www.majordifferences.com/2013/02/difference-between-schottky-defect-and.html#.Wrs95rvkK4g]

1.2.1.2: Impurity Defects

If molten NaCl containing a little amount of $SrCl_2$ is crystallized, some of the sites of Na^+ ions are occupied by Sr^{2+}. Each Sr^{2+} replaces two Na^+ ions. It occupies the site of one ion and the other site remains vacant. The cationic vacancies thus produced are equal in number to that of Sr^{2+} ions **[45]**. Such defects are known as impurity defects. Another example is the solid solution of $CdCl_2$ and AgCl. Pictorial representation of such impurity defects due to substitution is given in Figure 1.6.

1.2.1.3: Non-stoichiometric defects

Impurity and stoichiometric defects do not disturb the stoichiometry of the crystalline substance. However, a large number of non-stoichiometric inorganic solids are known which contain the constituent elements in non-stoichiometric ratio due to defects in their crystal structures. These are of two types: metal excess and metal deficient defects.

1.2.1.3a: Metal excess defects:

(i) Metal excess defects due to anion vacancies: A compound may have excess metal cation if a negative ion is absent from its lattice site, leaving the hole, which is occupied by an electron to maintain electrical neutrality. These kinds of defects are found in the crystals which are likely to possess the "Schottky defects". The Anion vacancies in the alkali metal halides are reduced by heating up the alkali metal halides crystals in an atmosphere of alkali metal vapours. The "holes" occupy by electrons are called "F-centres" (or colour centres).

(ii) Metal excess defects due to interstitial cations: Another way in which metal excess defects might occur is, if the extra positive ion is present in an interstitial site. Electrical neutrality is maintained by the presence of an electron in the interstitial site.

1.2.1.3b: Metal deficiency defects:

There are many solids, which are difficult to prepare in the stoichiometric composition and contain less amount of the metal as compared to the stoichiometric proportion. A typical example of this type is FeO, which is mostly found with a composition of $Fe_{0.95}O$. It may actually range from $Fe_{0.93}O$ to $Fe_{0.96}O$. In crystals of FeO some Fe^{2+} cations are missing and the loss of positive charge is made up by the presence of required number of Fe^{3+} ions.

1.2.2. Line defects

When the deviation from the perfect arrangement is present in the entire row of lattice points, then the defect is known as line defect. These are commonly called as dislocation. This can be further divided into two types: Edge dislocation and Screw dislocation.

1.2.2.1. Edge Dislocation

The edge defect exists due to the presence of an extra half plane of atoms in the crystal lattice. This dislocation is a line defect because distortion is present only in the immediate vicinity of the dislocation line. This area is called dislocation core or area. Dislocation lines are along the top of extra half plane. This type of dislocation can distort the perfect crystal with a small stress. This dislocation moves parallel to the direction of stress. Pictorial representation of Edge Dislocation is given in Figure 1.8**.**

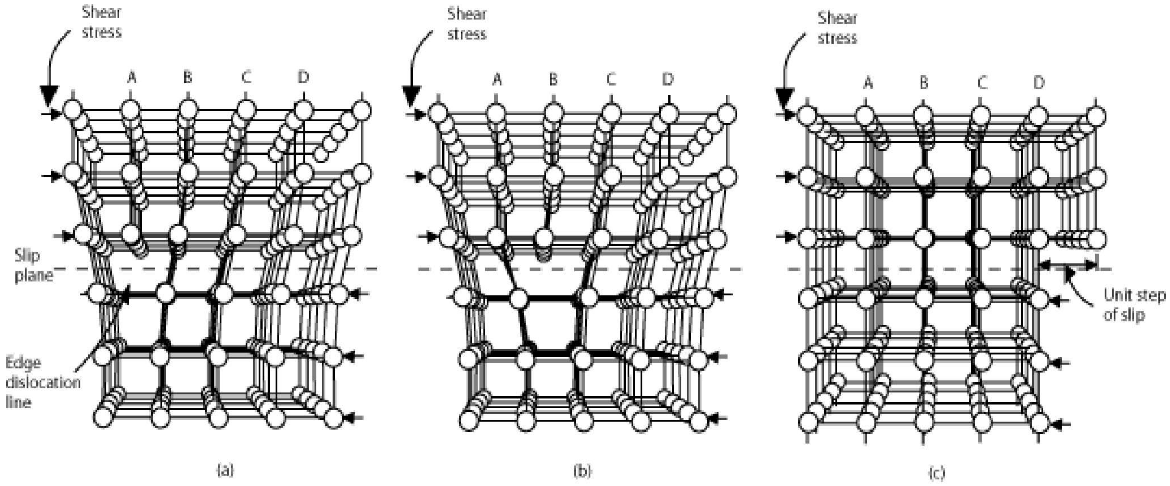

Figure 1.8: *Edge dislocation* **[41]**

As shown in the set of images above, the dislocation moves a small amount at a time. The dislocation in the top half of the crystal is slipping one plane at a time as it moves to the right from its position in image (a) to its position in image (b) and finally image (c). In the process of slipping one plane at a time the dislocation propagates across the crystal. The movement of the dislocation across the plane eventually causes the top half of the crystal to move with respect to the bottom half. However, only small fractions of the bonds are broken at any given time. Movement in this manner requires a much smaller force than breaking all the bonds across the middle plane simultaneously.

1.2.2.2. Screw Dislocation

The movement of screw dislocation is a result of shear stress but the defect moves in perpendicular direction of the stress of the atom displacement. This can be explained with a metal block by applying shear stress. If a shear stress (τ- stress which is applied parallel or tangential to a face of a material as opposed to a normal stress, which is applied perpendicularly) is applied to the block of metal, the plane of atoms of top side will not move from their original position. The atoms of the bottom side have moved to their new position in the lattice and have re-established metallic bonds. The middle side atoms are in the process of moving. In this, only small portions of the bonds are broken at a time. This movement requires a much smaller force than breaking all the bonds across the middle plane and edge dislocation. The atoms will continue the movement with increasing shear stress. Pictorial representation of Screw Dislocation is given in Figure 1.9.

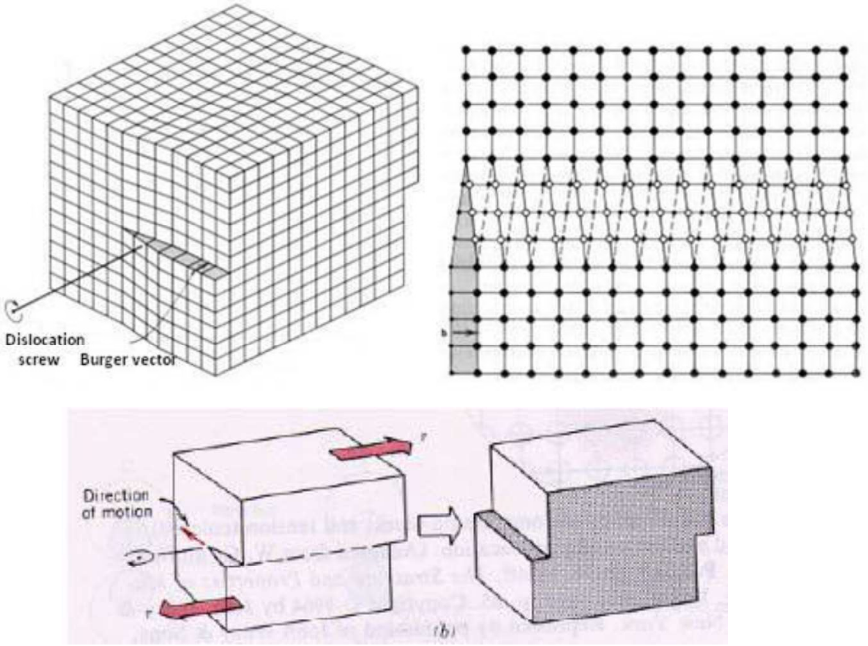

Figure 1.9: *Screw dislocation* **[41]**

1.2.3. Planar defects: A Planar Defect is a discontinuity of the perfect crystal structure across a plane. There are different types of planner defects

1.2.3.1 Grain Boundaries:

A Grain Boundary is a general planar defect that separates regions of different crystalline orientation (i.e. grains) within a polycrystalline solid. The lattice in each grain is identical but the lattices are oriented differently. The atoms are so close at some locations in the grain boundary that they cause a region of compression, and in other areas, they are so far apart that they cause a region of tension.The atoms in the grain boundary will not be in perfect crystalline arrangement. Grain boundaries are usually the result of uneven growth when the solid is crystallising. Grain sizes vary from 1 μm to 1 mm. Pictorial representation of Grain Boundaries is given in Figure 1.10**.**

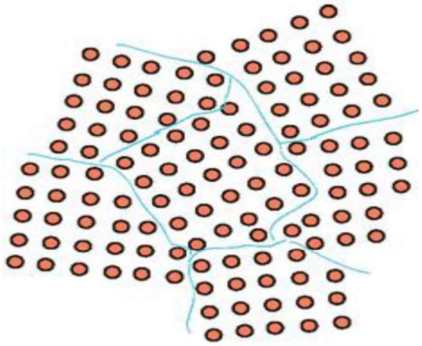

Figure 1.10: *Grain Boundarie. [Figure courtsey: http://moisespinedacaf.blogspot.in/2010/06/planar-defects-and-boundaries.html]*

1.2.3.2 Tilt Boundaries:

A Tilt Boundary, between two slightly misaligned grains appears as an array of edge dislocations. Pictorial representation of Tilt Boundaries is given in Figure 1.11**.**

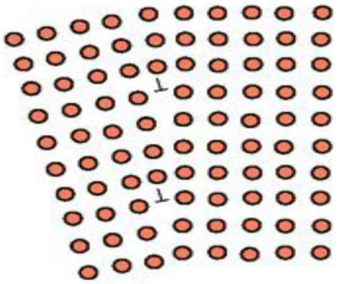

Figure 1.11*:* *Tilt Boundarie. [Figure courtsey: http://moisespinedacaf.blogspot.in/2010/06/planar-defects-and-boundaries.html]*

1.2.3.3 Twin Boundaries:

A Twin Boundary happens when the crystals on either side of a plane are mirror images of each other. The boundary between the twinned crystals will be a single plane of atoms. There is no region of disorder and the boundary atoms can be viewed as belonging to the crystal structures of both twins. Twins are either grown-in during crystallisation, or the result of mechanical or thermal work. Pictorial representation of Twin Boundaries is given in Figure 1.12**.**

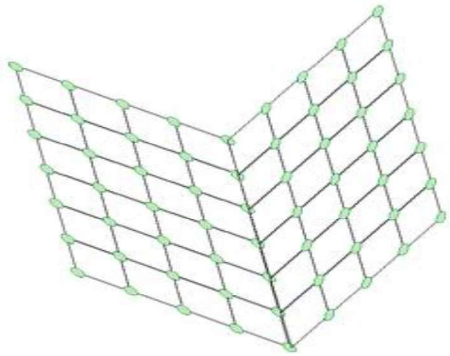

Figure 1.12: *Twin Boundaries [Figure courtsey: http://moisespinedacaf.blogspot.in/2010/06/planar-defects-and-boundaries.html]*

1.2.3.4 Stacking faults:

It occurs in a number of crystal structures, but the common example is in close-packed structures. They are formed by a local deviation of the stacking sequence of layers in a crystal. An example would be the ABABCABAB stacking sequence. Pictorial representation of Twin Boundaries is given in Figure 1.13**.**

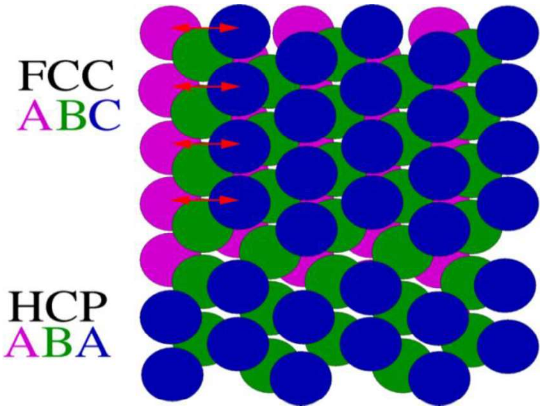

Figure 1.13: *Origin of stacking faults: Different stacking sequences of close-packed crystals. [Figure courtsey: https://en.wikipedia.org/wiki/Crystallographic_defect]*

1.2.4. Surface defects:

Surface defects are the boundaries, or planes, that separate a material into regions, each region having the same crystal structure but different orientations. Surface defects determine much of the material's reaction abilities. There are different kinds of surface defects, some of which are described:

a. Material Surface

The exterior dimensions of the material represent surfaces at which the lattice abruptly ends. Each atom at the surface no longer has the proper coordination number and atomic bonding is disrupted. The exterior surface may also be very rough, may contain tiny notches, and may be much more reactive than the bulk of the material.

In order to minimize the energy of the crystal, the defects will diffuse to the grain boundaries **[46]**. There are two types of diffusion creeps (a diffusion creep is the deformation of crystalline solids by the diffusion of vacancies through their crystal lattice):

Nabarro-Herring creep – the movement of vacancies inside the crystal. In this type of diffusion creep chemical bonds are broken and formed. Activation energy is needed for the diffusion, which strongly varies with the temperature.

Coble creep- which is the movements of the vacancies along the grain boundaries, the activation energy for this type is lower than the first type of diffusion creep.

Dislocations do not diffuse to the grain boundary. When stress is applied the dislocation will move to the grain boundary. The difference is that diffusion is random and the movement of the dislocation is not random and happens only when stress is applied. When the term dislocation "diffusion" is used in this work, it should be the dislocation movement to the grain boundaries due to stress in the grain.

1.3. Phosphor materials:

The science and technology for understanding, controlling and exploiting the interaction of light and matter is broadly defined as Photonics, which furnishes enabling technologies for telecommunications, solar energy, lighting, displays, biotechnology, medical diagnostics, bio-imaging etc. Luminescence is a phenomenon of emission of electromagnetic radiation by a physical system in excess of energy following excitation by electrons/photons **[16, 47]**. Phosphor (luminescent materials) is an example of such a physical system, which essentially emits light by converting one type of energy into another. They can be crystalline or non-crystalline **[16, 48]**. Generally a phosphor is a combined system of a host lattice and one or more activators with concentration ranging from parts per million to a few mole percent. The luminescent properties of phosphor materials can be determined by any of them i.e. either by the host or by the activator ions. Such as in zinc sulphide/cadmium sulphide: silver (ZnS:Ag/CdS:Ag) phosphor, the emitted colours can be varied with varying the Cd content. At zero cadmium, the emitted colour is blue and then it can be changed through green, to yellow and into red as the Cd content is increased. The phosphors are generally powders having average particle sizes ranging from micro to nano-scale **[49]**.

Generally phosphors are inorganic solid materials consisting of a host lattice, usually intentionally doped with impurities such as rare earth ions or transition metal ions **[3, 16, and 50]** with relatively low concentration. At higher concentrations the efficiency of the luminescence process usually decreases due to concentration quenching effects. A white body colour is an essential feature for most of the phosphors since it prevents absorption of visible light by the phosphors **[16, 50]**. Ultraviolet (UV) energy can be used as an excitation source. The excitation energy can be absorbed either by the host lattice first and then transferred to luminescent centres (usually intentionally introduced rare earth ions or transition metal ions or defects) or it can be absorbed by an impurity ion and then transfer to another impurity ion identical to the former. In general, the emission takes place on the impurity ions, and when these impurity ions are used to generate the desired emission, they are referred to as activators **[50]**. Again if the absorption efficiency displayed by an activator is too low, a second kind of impurity called sensitizer can be added, which will absorb the energy and subsequently transfer it to the activators. A pictorial representation has been given in Figure 1.14.

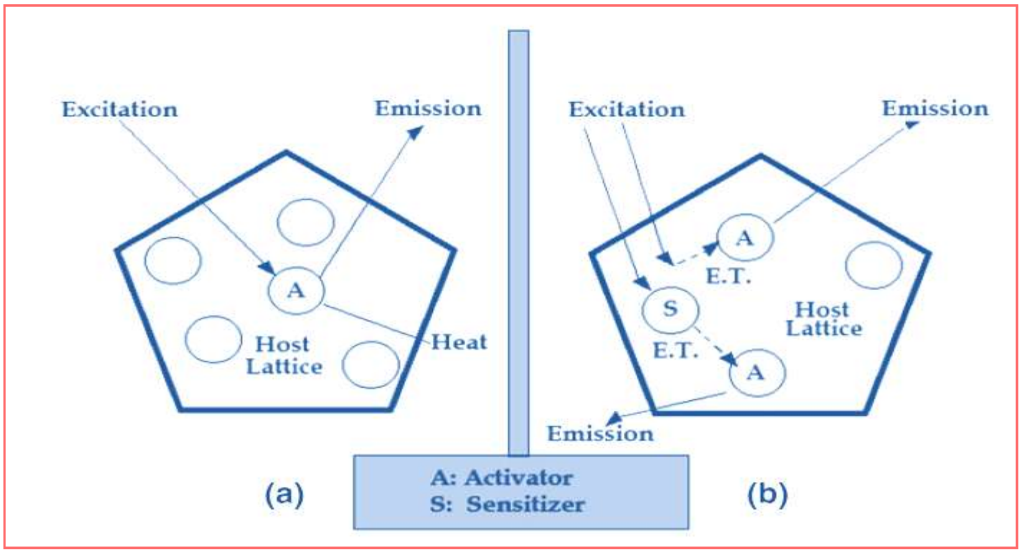

Figure 1.14. *Schematic diagram of phosphors.(a) Activator in the host lattice. (b) Energy transfer from a sensitizer to an activator. A: activator; S: sensitizer; EXC: excitation; EM: emission; ET: energy transfer* ***[50]***

In most cases, we can adjust the emission colour by choosing the proper impurity ion, without changing the host lattice in which the impurity is incorporated. It is well known that the emission of light exhibited by the luminescent materials is due to the excited electrons whose quantum state is above the minimum ground state. Based on excitation source by which electrons can be excited in luminescent in materials there are various types of luminescence processes **[51, 52]** and corresponding excitation mechanisms as listed in Table 1.2.

Table 1.2 -The various types of luminescence **[51]**

Type of Luminescence	**Source of excitation**	**Examples**
Bioluminescence	Biochemical reactions in living organisms	fireflies
Chemiluminescence	Chemical reaction	Luminol ($C_8H_7N_3O_2$)
Photoluminescence	Absorption of electromagnetic radiation (photons)	Phosphor material such as YAG:Ce^{3+} , $NaYF_4$:Eu, $NaGdF_4$:Eu, Y_2O_3:Eu etc.
Crystalloluminescence	Crystallization, the process in which solid crystals precipitate from a solution, a melt or more rarely deposited directly from a gas	NaCl
Electrochemiluminescence	Resulting from electrochemical reactions	ZnS:Mn
Mechanoluminescence	Mechanical action on a solid	Quartz glass, KBr and LiF
Radioluminescence	Bombardment by ionizing radiation	YBO_3:Eu
Thermoluminescence	Emission as a result of heating	ZnS:Cu

1.4. Photoluminescence (PL) in solid

As stated in Table 1.2, in case of PL, the electronic states of the solids are excited by a photon, and the excitation energy is released in the form of light **[52]**.Since the generation of light by luminescence is initially tied up with the energy relaxation mechanism in the solid, the emission process is more complicated than the absorption process. The shape of the emission spectrum is also affected by the thermal distribution of the electrons and holes within their bands **[52]**. Again based on the nature of the electronic transitions, the PL emission in solids, i.e. in inorganic insulators and semiconductors can also be classified such as intrinsic and extrinsic luminescence. **[52]**

1.4.1. Intrinsic Photoluminescence

In case of intrinsic photoluminescence, the luminescence arises due to the presence of variety of defects in a crystal structure **[52, 53].** This type of luminescence does not involve impurity atoms. Intrinsic photoluminescence are of three kinds namely: band to band, excitons and cross luminescence. The important factors that may influence intrinsic photoluminescence are (1) non-stoichiometry (a state of a material not having exactly the correct elemental proportion), (2) Structural imperfections –owing to poor ordering, 3) radiation damage etc.

1.4.2. Extrinsic Photoluminescence

Extrinsic photoluminescence is defined as the luminescence that results due to intentionally incorporated impurities in the crystal structure or doping of external luminescence active ion **[54]**. These impurity ions also known as activators with energy levels in the band gap (forbidden zone) provide additional energy levels for excitation and relaxation processes **[54]**.

1.4.3. Type of Luminescence in Solid

Two different kinds of luminescence phenomena can be observed in luminescent materials: fluorescence and phosphorescence. They are distinguished by whether the transition to emit light is allowed or forbidden by spin selection rules. Fluorescence is observed where the light emission is an allowed singlet-singlet transition while phosphorescence is observed due to a forbidden transition such as singlet-triplet transition, which usually shows long afterglow **[55]**.

1.4.3.1 Fluorescence

In Fluorescence the valence electrons are raised to the conduction band and return immediately via the luminescence centre to fill the holes in the valance band and there are no traps but many luminescent centres **[52, 56]**. When the excited electrons return to the ground state, their surplus energy will be emitted in a form of visible light and the process is instantaneous. If in the time interval 10^{-6} sec the excited electrons return back to the ground state, the resulting emission is described as fluorescence **[57]**. The emitted energy is always less than the excitation energy. If phosphors are exited with UV light then it will result in emission in the visible region. A pictorial representation of electronic transition of an excited electron to the conduction band followed by its return to the valance band via a luminescence centre is given in Figure 1.15 **[56]**. In this case the emitted photon has an energy that is equivalent to the energy difference across the luminescence centre.

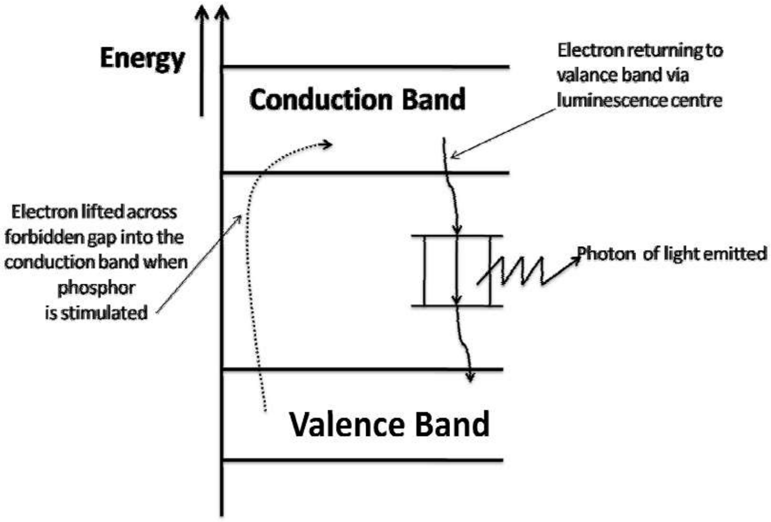

Figure 1.15: *Energy band diagram of fluorescent phosphor* ***[56]***

1.4.3.2. Phosphorescence

Phosphorescence in a luminescent material is observed when the recombination of the photogenerated electrons and holes is significantly delayed. For example when one of the excited states of a luminescent centre is a quasistable state i.e., with very long life time the recombination process may get delayed. Again the excited electrons and holes in the conduction and valence bands of a phosphor can often be captured by impurity centres or crystal defects before they are captured by emitting centres. When an electron (or hole) captured by an impurity or defect centre and thereby the probability of recombine with a hole (electron) becomes negligible and the electron has to be reactivated into the conduction band (valence band), then the defect centres are known as traps **[57]**.

Figure 1.16 gives a representation of the electrons (holes) captured by traps which are responsible for phosphorescence. These trapped electrons are thermally reactivated into the conduction band (valence band) and radiatively recombined at an emitting centre. Due to trapping of these electron or holes, the decay time of phosphorescence can be as long as several hours and also results in photoconductive phenomena **[56]**. Unlike others simple exponential function cannot represents the decay curve of the long afterglow due to traps. The form of a decay curve depends on various factors such as the concentration of the traps, electron capture cross-sections of the traps and the emitting centre and also on the excitation intensity **[56]**.

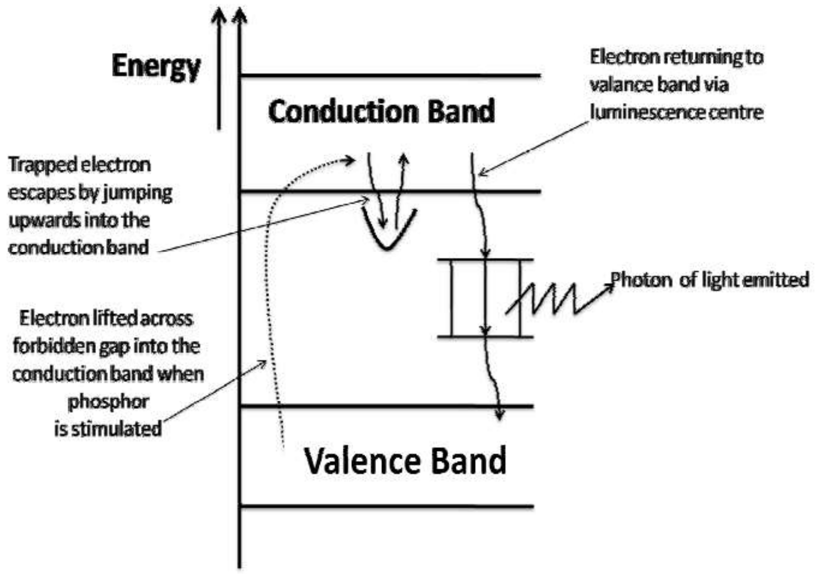

Figure 1.16: *An energy band diagram representing a phosphorescent phosphor* ***[56]***

1.4.4. Luminescent Centres

There are wide variety of centres which give rise to luminescence in semiconductors and insulating materials. Examples are rare earth ions, transition metal ions, excitons, donor-acceptor pairs, and ions with a d^{10} or s^2 electronic configuration state **[58]**. The resulting characteristic luminescence can be comprised of either relatively sharp emission lines or a broad band in the visible part of the electromagnetic spectrum **[50]**. The sharp emission lines that are usually illustrated by most of the rare earth ions arise from purely electronic transitions and the effect of the environment is felt mainly through their effects on the lifetimes of the excited states **[58]**. The broad emission bands arise from the interaction between the electronic system of the luminescent centre and the vibrations of the atoms or ions, which surround it. This is due to the simultaneous transitions of both electronic and vibrational systems **[58]**. Furthermore the broad band spectra are observed when the character of the chemical bonding in the ground and excited states differs considerably. This process goes hand in hand with a change in equilibrium distance between the emitting ion and its immediate environment and is commonly explained with the configuration coordinate diagram, shown in Figure 1.17 **[50]**.

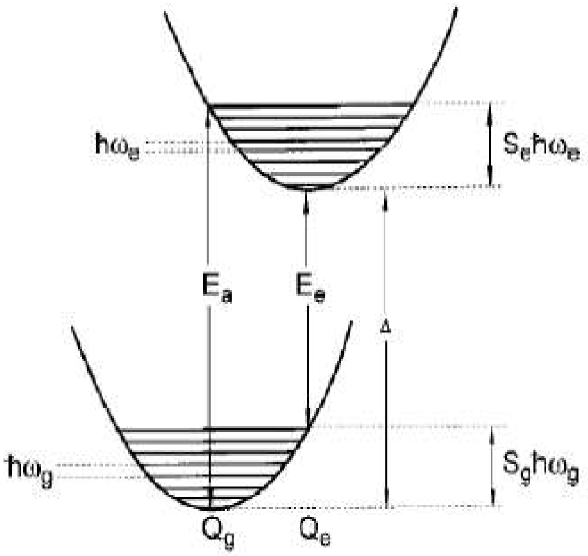

Figure 1.17: *Configurational coordinate diagram **[50]**.*

Figure 1.17 represents the configurational coordinate diagram where Qg and Qe represent the metal-ligand distances in the ground and excited state, respectively. Ea and Ee are the energies at which the absorption and the emission bands have their maximum intensity, respectively. The zero phonon energy given by Δ is the transition which involves the completely relaxed excited and ground states, and no excited photon states are involved- hence the name of this kind of transitions. The ħωg and ħωe are the phonon energies in the ground and the excited states, respectively. The relaxation energies in the ground and excited states can be expressed as a product of the phonon energy and the Huang-Rhys factors. The Huang-Rhys factors Sg and Se in the ground and the excited state, respectively give the mean number of phonons involved in the absorption and emission processes, respectively **[50]**. According to the harmonic approximation the curvature of the parabolic bands, the phonon frequencies and the Huang-Rhys factors are the same in the ground and excited state **[50]**. This diagram is very elementary, in the sense that it does not describe the thermal expansion of the lattice. However it does give a lot of insight, for example, it can be used to illustrate that a larger Stokes Shift is expected on increasing lattice relaxation and also in the description of thermal quenching of the emission **[50]**.

1.4.4.1 Optical Transition of Transition metal ions:

I. Photoluminescence of Mn^{2+} & Fe^{3+}:

In this section the electronic structure of Mn^{2+} and Fe^{3+} will be explained for a better understanding of their optical properties. Both Mn^{2+} & Fe^{3+} have an incompletely filled d shell and have similar electron configuration which is d^5. The energy levels originating from this configuration have been calculated by Tanabe and Sugano considering the interaction between the d electrons and the crystal field **[59]**. The energy levels of a free ion are given on the left hand side of the Tanabe- Sugano diagrams in Figure 1.18**.** For a crystal field 10Dq ≠ 0, many of these levels split into two or more levels. The ground state is represented by the x axis. The free ion levels are marked ^{2S+1}L, where S presents the total spin quantum number, and L the total orbital angular momentum. The degeneracy of these levels is 2L + 1 and can be lifted by the crystal field. Crystal field energy levels are marked ^{2S+1}X, where X may be A for no degeneracy, B for a twofold degeneracy and T for a threefold degeneracy. In Figure 1.18**,** the ground state terms of this d^5 configuration are $^6A_{1g}$ (^6S) for octahedral and ^6A_I (^6S*)* for tetrahedral coordination respectively where g stands for gerade in case of centrosymmetric octahedral ion. All the electronic transitions are spin forbidden since ground state term is the only sextet of d^5 configuration. Since these energy levels are all within the d shell, all transitions from the ground state to excited levels are spin and parity forbidden. However, the Mn^{2+} transitions can still be observed. It was suggested that the selection rule is relaxed through a spin-spin interaction and a vibronic mechanism, where the electronic transitions are coupled with vibrations of suitable symmetry **[60]**. The first excited state for octahedral coordination is $^4T_{Ig}$ (^4G*)* and ^4T_I for tetrahedral coordination respectively. Phosphorescence of Fe^{3+} for octahedral coordination is attributed due to the transition $^4T_{lg}(t_{2g}{}^4,e_g) \rightarrow {}^6A_{lg}(t_{2g}{}^3,e_g{}^2)$*,* while for tetrahedral coordination, the phosphorescence is due to $^4T_l(e^3, t_2{}^2) \rightarrow {}^6A_l(e^2, t_2{}^3)$ transition. The emission peaks are broadened due to difference in occupancy of e and t_2 orbitals in ground and excited states. Thus, the transition energies depend on the crystal field parameter l0*Dq.* In a cubic field approximation the free electron term ^4G splits into $^4T_1(^4G)$, $^4T_2(^4G)$ and the degenerate $^4A_1$,$^4E(^4G)$. Generally, those energy terms, which give horizontal lines, are independent of the crystal field splitting. The ground state free-ion term $^6A_1(^6S)$ is a horizontal line. Other terms giving horizontal lines are ^4E (^4G), $^4A_1$ (^4G), ^4E (^4D) and $^4A_2$ (^4D) and hence their energies are independent of the crystal field. Thus, transitions from ground state to these four states should give rise to sharp peaks. By the same reasoning, the transitions from states with appreciable slope such as $^4T_1$ and $^4T_2$ to $^6A_1$ give broader bands.

Exciting a system with UV light brings an electron of Mn^{2+} in a high vibrational level of the excited state, as shown in Figure 1.19. The electron falls to the lowest vibrational level of the excited state giving up the excess energy to the surrounding. Another way to describe this process is to say that the nucleus adjusts its position to the excited state, so the interatomic distance varies from the distance it has in equilibrium. The configurational coordinate changes by ΔR. This process is called relaxation. From the lowest vibrational level the electron can return to the ground state spontaneously under emission of radiation. From this it can be seen, that the emission has a lower energy than the excitation of the same excited level. This effect is called Stokes Shift.

If the ground-state energy is zero then that of the first excited state, $^4T_1$ is $-10Dq + 10B + \mathbf{6C}$, and therefore decreases in energy as $10Dq$ increases and ***B*** and ***C*** remain constant **[61]** as shown in Figure 1.18. Thus the emission spectra of d^5 ion vary with varying the crystal field. A typical excitation bands from Mn^{2+} are presented in Figure 1.20 **[63]**. The PL arises from the radiative return to the ground state via the $^4T_{1g}(G) \rightarrow {}^6A_{1g}(S)$ transition. The excitation bands are marked with their corresponding energy level. The interesting feature in this excitation spectrum is that there is a different width for the different excitation maxima. Such as the degenerate states $^4A_{1g}$ (G) and $^4E_g(G)$ have a narrow band while that of the $^4T_{2g}(G)$ and $^4T_{1g}(G)$ states have rather broad. The band-width resulted due to coupling with vibrations. Tanabe-Sugano diagrams can predict the width of the band due to the crystal field strength, which varies during the vibration. When the energy level runs parallel to the ground state level, influence of Δ on the transition energy will be very small and a narrow band can be expected as observed for $^4A_{1g}(G)$ and $^4E_g(G)$. Because of this reason for most systems these energy levels show their excitation band at about 400 nm. However if the excited levels has a slope relative to the ground state, a variation of Δ will influence the transition energy resulting a broad transition band. That is why the $^4T_{1g}$ (G) state is most sensitive to the crystal field Δ.

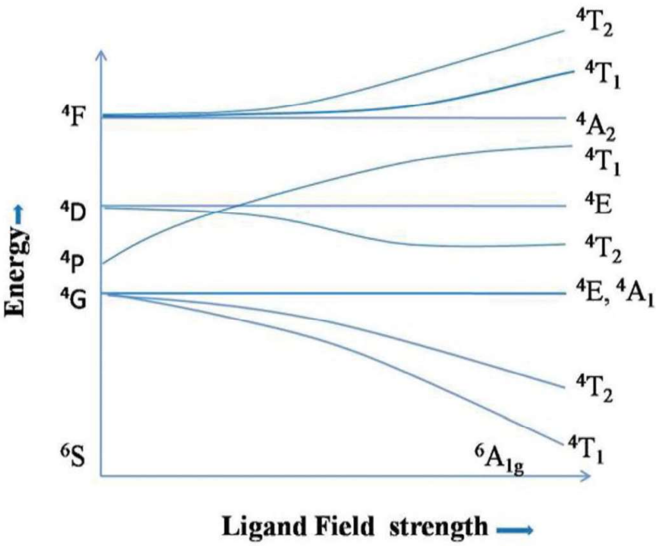

Figure 1.18. *Energy level diagram of a d^5 configuration.*

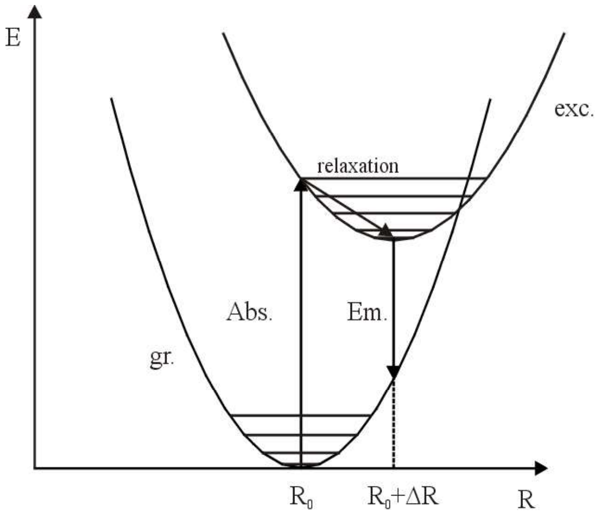

Figure 1.19: *Configurational coordinate diagram. After absorption the system reaches a high vibrational level of the excited state. Subsequently it relaxes to the lowest vibrational level from where the emission occurs* **[62]**.

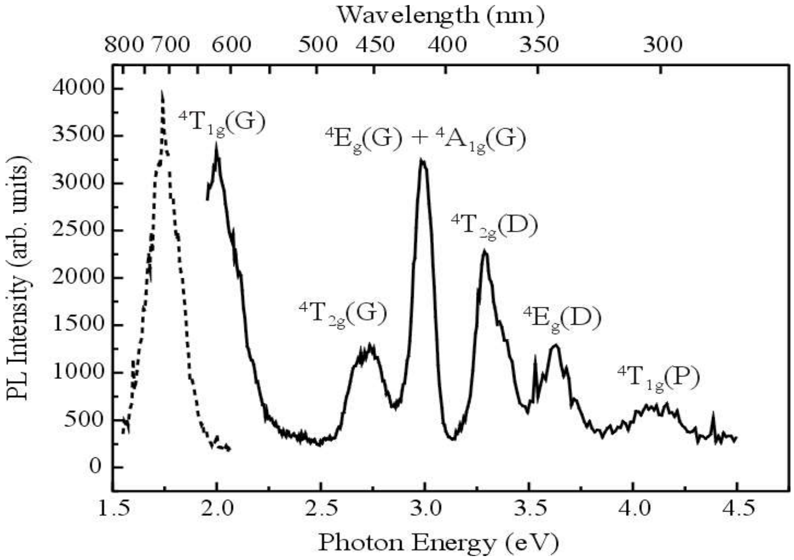

Figure 1.20: *The dashed curve shows the PL spectrum of Mn^{2+} in $LiBaF_3$, excited at 255 nm. The solid curve presents the excitation bands for this transition and the PL was detected at 712 nm* ***[62]***.

1.4.4.2 Optical transition of rare earth ions:

Lanthanides are the group of atoms ranging from lanthanum (atomic number 57) to lutetium (atomic number 71) in the periodic table of elements as shown in Figure 1.21. They are characterized by gradual filling of the 4f electron shell and are therefore called f- block elements.

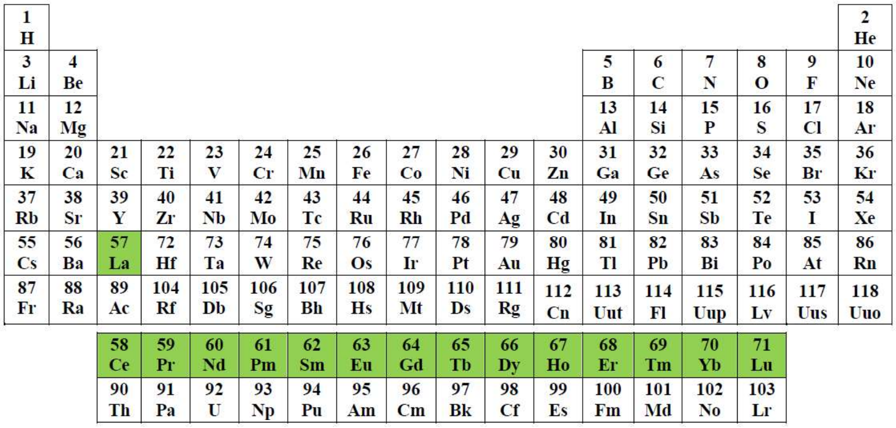

1 H																	2 He
3 Li	4 Be											5 B	6 C	7 N	8 O	9 F	10 Ne
11 Na	12 Mg											13 Al	14 Si	15 P	16 S	17 Cl	18 Ar
19 K	20 Ca	21 Sc	22 Ti	23 V	24 Cr	25 Mn	26 Fe	27 Co	28 Ni	29 Cu	30 Zn	31 Ga	32 Ge	33 As	34 Se	35 Br	36 Kr
37 Rb	38 Sr	39 Y	40 Zr	41 Nb	42 Mo	43 Tc	44 Ru	45 Rh	46 Pd	47 Ag	48 Cd	49 In	50 Sn	51 Sb	52 Te	53 I	54 Xe
55 Cs	56 Ba	57 La	72 Hf	73 Ta	74 W	75 Re	76 Os	77 Ir	78 Pt	79 Au	80 Hg	81 Tl	82 Pb	83 Bi	84 Po	85 At	86 Rn
87 Fr	88 Ra	89 Ac	104 Rf	105 Db	106 Sg	107 Bh	108 Hs	109 Mt	110 Ds	111 Rg	112 Cn	113 Uut	114 Fl	115 Uup	116 Lv	117 Uus	118 Uuo
		58 Ce	59 Pr	60 Nd	61 Pm	62 Sm	63 Eu	64 Gd	65 Tb	66 Dy	67 Ho	68 Er	69 Tm	70 Yb	71 Lu		
		90 Th	91 Pa	92 U	93 Np	94 Pu	95 Am	96 Cm	97 Bk	98 Cf	99 Es	100 Fm	101 Md	102 No	103 Lr		

Figure 1.21: *The periodic table of elements. The lanthanides are highlighted in green* ***[16].***

Since lanthanides have very similar chemical behaviors, their properties can be discussed in a general way. They are most frequently found in the trivalent (3+) oxidation state (see Table 1.3), however tetravalent (4+) cerium/terbium and divalent (2+) europium/ytterbium also occur. Since the f-orbitals are shielded by the 5s and 5p orbitals, the f-electrons do not participate in chemical bonding so that the predominant interactions in lanthanide complexes are electrostatic ones. This shielding of the spectroscopically active 4f-electrons by filled 5s and 5p orbital result in the lanthanide f-f electronic transitions to be very narrow lines in the luminescence and absorption spectra compared to the broad band observed for transition metal ions. Since changes in the local environment of the lanthanide ion has a negligible influence on the 4f-electrons, coordination will only affect the fine structure of the absorption and emission bands and there will be hardly any shifts in the peak position. Lanthanide ions can show emission in the near-UV, visible, near-infrared and infrared spectral regions. Each lanthanide ions has a characteristic absorption and emission spectra.

Table 1.3: Electronic configuration of lanthanide atoms and trivalent ions as well as the radii of the trivalent ions **[16]**

Element	**Atomic electron configuration (all begin with [Xe])**	**Ln^{3+} electron configuration (all begin with [Xe])**	**Ln^{3+} radius (pm) (6-coordinate)**
La	$5d^1 6s^2$	$4f^0$	103
Ce	$4f^1 5d^1 6s^2$	$4f^1$	102
Pr	$4f^3 6s^2$	$4f^2$	99
Nd	$4f^4 6s^2$	$4f^3$	98.3
Pm	$4f^5 6s^2$	$4f^4$	97
Sm	$4f^6 6s^2$	$4f^5$	95.8
Eu	$4f^7 6s^2$	$4f^6$	94.7
Gd	$4f^7 5d^1 6s^2$	$4f^7$	93.8
Tb	$4f^9 6s^2$	$4f^8$	92.3
Dy	$4f^{10} 6s^2$	$4f^9$	91.2
Ho	$4f^{11} 6s^2$	$4f^{10}$	90.1
Er	$4f^{12} 6s^2$	$4f^{11}$	89
Tm	$4f^{13} 6s^2$	$4f^{12}$	88
Yb	$4f^{14} 6s^2$	$4f^{13}$	86.8
Lu	$4f^{14} 5d^1 6s^2$	$4f^{14}$	86.1

The trivalent rare earth or lanthanide cations both in solution and in the solid state have characterized narrow emission bands with relatively long luminescence lifetimes values up to milliseconds **[16, 63]**. This characteristic shape of the bands can be explained by the fact that the ground and excited states of these transitions have the same equilibrium geometry, since excitation only involves rearrangement of the electrons within f-orbitals. Except for lanthanum (La^{3+}) and lutetium (Lu^{3+}), each lanthanide ion has its specific emission bands: for example, the lanthanide ions europium (Eu^{3+}) and samarium (Sm^{3+}) emit red light, terbium (Tb^{3+}) green light, gadolinium (Gd^{3+}) UV-light and neodymium (Nd^{3+}), ytterbium (Yb^{3+}), and erbium (Er^{3+}) near-infrared light. These characteristics have led to the application of lanthanide ions as probes in fluoroimmunoassays (Eu^{3+} and Tb^{3+}) **[16, 64, 65]**, laser systems (e.g. Nd^{3+}) **[16, 66]**, and optical amplifiers (Er^{3+} and Pr^{3+}) **[16, 67]**.

1.4.4.2.1 The 4f energy levels and selection rules

The different energy levels to a same configuration are a result of several interactions within the ion. The degeneracy of the energy levels of 4f orbital is lifted due to the electronic repulsion, spin-orbit coupling, and (in a coordination environment) the ligand field, as shown in Figure 1.22. The electronic repulsion among the electrons, which is the strongest columbic interaction, disrupts the degeneracy of the 4f energy levels into various energy terms with separations in the order of 10^4 cm^{-1}. Each of these terms are further split into several J-levels owing to the spin-orbit coupling in the order of 10^3 cm^{-1}, which is relatively large in lanthanide ions, because of their heavy nuclei. Spin-orbit coupling is defined as the interaction between the magnetic moments of the electrons due to their spin (spin angular momentum) and the magnetic moments due to their movement around the nucleus (orbital angular momentum). Now let us consider the free ion levels that are described by the term symbols $^{(2S+1)}L_J$. 2S+1 represent the total spin multiplicity; L is the total orbital angular momentum and J is the total angular momentum of the f electrons. When present in a coordinating environment, such as a crystal or an organic ligand, the individual J-levels are split up further by the electric field of the matrix, which is usually referred to as the crystal field. These splitting are usually small (10^2 cm^{-1}) and, depending on the spectral resolution of the spectrometer, appear as fine structure on the individual bands. Often this fine structure is ignored, although it may be used to gather information about the symmetry of the coordination environment.

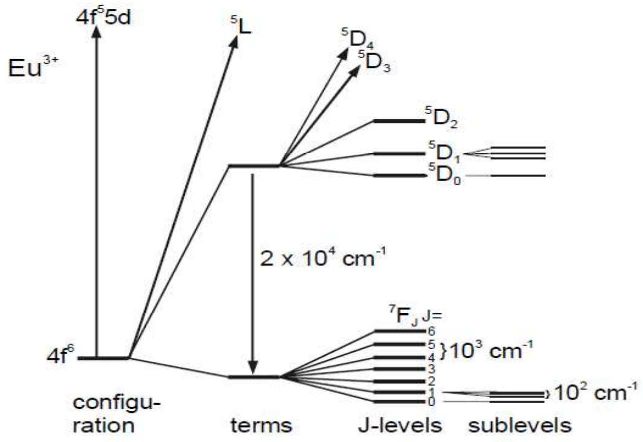

Figure 1.22: *Splitting of the 4f energy levels of Eu^{3+} as a result of electronic repulsion, spin-orbit coupling, and the ligand field* ***[16]***

According to the Russell-Saunders coupling scheme the term symbol of the J-states is written as $^{(2S+1)}L_J$ **[68]**. The 2S+1 is the spin multiplicity, where S is the total spin-impulse momentum of the system gives the maximum of possible spin orientations and denotes the degeneracy of the J-states. L is the total orbital angular momentum and its value is represented by the symbols S (L=0), P (L=1), D (L=2), F (L=3), G (L=4) etc. The value of L is obtained by coupling the individual orbital angular momenta l_i: $L = (l_1+l_2+\ldots+l_i), (l_1+l_2+\ldots+l_{i-1}),| (l_1- l_2-\ldots-l_i)|$. J is total angular momentum and it indicates the relative orientation of the spin and the orbital momenta: $J = L+S, L+S-1, L+S-2\ldots, |L-S|$.

The energy levels of some of the trivalent lanthanide ions are depicted in Figure 1.23.

The following selection rules have to be obeyed for an atomic spectrum in general:

- $\Delta S = 0$, since light does not affect the spin and thus the overall spin is not allowed to change.
- $\Delta L = 0, \pm1$, with $\Delta l = \pm1$, the orbital angular momentum of an individual electron must change.
- $\Delta J = 0, \pm1$, but $J = 0$ to $J = 0$ is forbidden.
- The Laporte rule or the parity selection rule, which forbids electric dipole transitions between levels with the same parity, examples are electronic transitions within the d-shell, within the f- shell, and between d and s shells.

In quantum mechanics the basis for a spectroscopic selection rule is the value of the transition moment integral (Equation 1.1)

$$\int \psi_1^* \mu \psi_2 d\tau \qquad (1.1)$$

where $\psi_1$and ψ_2 are the wave functions of the two states involved in the transition and μ is the transition moment operator. If the value of this integral is zero the transition is forbidden. In practice, the integral itself does not need to be calculated to determine a selection rule. It is sufficient to determine the symmetry of transition moment function, $\psi_1^*\mu\psi_2$. If the symmetry of this function spans the totally symmetric representation of the point group to which the atom or molecule belongs then its value is (in general) not zero and the transition is allowed. Otherwise, the transition is forbidden.

The transition moment integral is zero if the transition moment function, $\psi_1^*\mu\psi_2$, is anti-symmetric or odd, i.e. $y(x) = -y(-x)$ holds. The symmetry of the transition moment function is the direct product of the parities of its three components. The symmetry characteristics of each component can be obtained from standard character tables. Rules for obtaining the symmetries of a direct product can be found in texts on character tables.

The Laporte selection rule formally stated as follows: In a centrosymmetric environment, transitions between like atomic orbitals such as s-s, p-p, d-d, or f-f, transitions are forbidden. The Laporte rule applies to electric dipole transitions, so the operator has u symmetry (meaning ungerade, odd). p orbitals also have u symmetry, so the symmetry of the transition moment function is given by the triple product u×u×u, which has u symmetry. The transitions are therefore forbidden. Likewise, d orbitals have g symmetry, so the triple product g×u×g also has u symmetry and the transition is forbidden

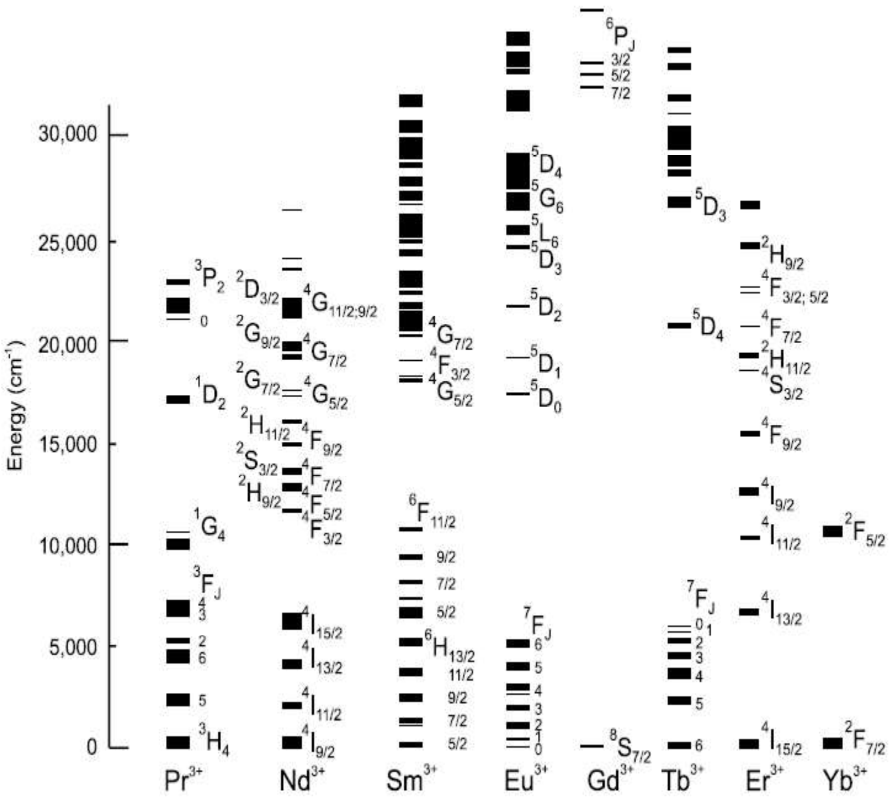

Figure 1.23: *Energy diagram of the 4f levels responsible for the lanthanide luminescence* ***[16, 69]***.

On the other hand Magnetic dipole (MD) transitions obey the selection rule ΔJ = 0, ±1 and are allowed (except for J = 0 to J = 0), but have low oscillator strengths. In case of the electric dipole intra-4f transitions, which are parity forbidden, the transitions that do not occur within the ground multiplets are also spin-forbidden ($\Delta S \neq 0$). However in an asymmetric environment, by mixing of opposite parity wave functions (primarily the 5d wave functions) into the 4f wave functions, the ED f-f transitions become weakly allowed (with oscillator strength of 10^{-6}) or we can say that the parity forbidden intra-4f transitions 'steal' some intensity from the allowed 4f-5d transitions. Since the heavy atoms have large spin-orbit couplings, the spin selection rule is relaxed in this case. Again since the oscillator strengths of these induced ED transitions are in the same order of magnitude as those of MD transitions, both transitions can be observed in lanthanide absorption and emission spectra. However due to forbidden character of intra-4f transitions, those transition have low absorptivities, with absorption coefficients in the visible spectral range of less than 10 M^{-1} cm^{-1} and relatively long luminescence lifetimes (in the range of μs to ms).

For certain induced electric dipole transitions that have $|\Delta J| < 2$, $|\Delta L| < 2$, and $\Delta S = 0$, the intensities are much more sensitive to complexation than other transitions, and have been termed as *hypersensitive transitions*. The intensities of these transitions may be up to 200 times larger than the corresponding transition in the hydrated ion, whereas the intensities of the other transitions are generally approximately the same. Table 1.4 included the other selection rules applying to S, L and J quantum numbers for f–f transitions between spectroscopic states. While deriving them it was assumed that the wave functions of the 4f electrons are described by $f^n[SL]J$ functions (i.e. that Russell–Saunders spin–orbit coupling scheme is valid).

Table 1.4: Selection rules for f–f transitions between spectroscopic levels **[70]**

Operator	**Parity**	**ΔS**	**ΔL**	**ΔJ***
ED	Opposite	0	≤6	≤6 (2,4 6 if J or J' =0)
MD	Same	0	0	0, ±1
EQ	Same	0	0, ±1, ±2	0, ±2
*** J=0 to J'=0**	always forbidden			

Several hypotheses are considered to derive the selection rules, which are not always completely fulfilled in reality (in particular 4f wave functions are not totally pure). Thus the terms ''forbidden'' and ''allowed'' transitions cannot be taken too rigidly. Therefore, a more correct wording would be that a forbidden transition has a low probability and an allowed transition a high probability of occurring.

1.4.4.2.2 Radiative and Non-radiative transitions in lanthanide

In the hypothetical free lanthanide ion, only magnetic dipole (MD) transitions are allowed followed by the selection rules ΔJ = 0, ±1 (but J = 0→J = 0 is forbidden). They are practically independent of the surrounding matrix and their probability is relatively easily calculated **[71]**. The $^5D_0 \rightarrow {}^7F_1$ emission line of Eu^{3+} is an example of a purely MD transition. In a coordinating environment, electric dipole (ED) transitions are induced, as the ligand field mixes odd parity configurations slightly into the [Xe] $4f^n\ 5d^0$ configuration.

Most of the absorption and emission lines are such induced ED transitions. In some cases, such as the emission spectrum of Tb^{3+} is dominated by mixed ED/MD transitions. Here transitions acquire strength both by MD and ED schemes. Since ED transitions in lanthanide ions are induced by the ligand field, the transition probabilities are quite sensitive to it. In case of strong asymmetric or interacting ligand fields, ED transitions become relatively more intense. The intensities of some ED transitions are extremely sensitive to coordinating environment and in those cases the transitions are either completely absent or very intense, depending on the ligand field.

Symmetry of the surroundings has pronounced influence on the emission spectrum of the Eu^{3+}. The main emissions of this ion occur from the $^5D_0$ to the ^7F_J (J = 0-6) levels. The $^5D_0 \rightarrow {}^7F_1$ transition is a pure magnetic dipole (MD) transition, it is practically independent of the symmetry of the surroundings, and the strength can be calculated theoretically. The transitions to the $^7F_{0,\,3,\,5}$ levels are forbidden both in magnetic and electric dipole schemes and are usually very weak in the emission spectrum. The remaining transitions to the $^7F_{2,\,4,\,6}$ levels are pure electric dipole (ED) transitions and they are strongly dependent on the symmetry of the environment. In a crystal site with inversion symmetry, the electric dipole transitions are strictly forbidden and the $^5D_0 \rightarrow {}^7F_1$ transition is usually the dominant emission line. In a site without inversion symmetry, the strength of the electric dipole transition is higher. The $^5D_0 \rightarrow {}^7F_2$ transition is usually the strongest emission line in this case, because transitions with $\Delta J = \pm 2$ are hypersensitive to small deviations from inversion symmetry. The symmetry around the lanthanide ion can thus be obtained from the shape of the emission spectrum of the Eu^{3+} ion. The other lanthanide ions have transitions that are usually mixtures of electric and magnetic dipole transitions and the effects of the symmetry are less pronounced. The symmetry also has an influence on the radiative lifetime of the $^5D_0$ level. The radiative lifetime is the time for the luminescence to drop to 1/e in intensity in absence of quenching. In the case of Eu^{3+} ion without inversion symmetry, the rate of the forced electric dipole transition is higher than in the case of a Eu^{3+} ion with inversion symmetry. This automatically means that the radiative lifetime of a Eu^{3+} ion in a site with inversion symmetry is longer. Radiative lifetimes of lanthanide ions have been calculated with several methods, of which the Judd-Ofelt theory is the most popular **[72]**. In this theory, the strength of the electric dipole transitions are calculated from the absorption spectrum and these strengths can be related to the radiative lifetime. Werts *et al.,* have formulated an equation to calculate the radiative lifetime of the Eu^{3+} ion from the shape of the emission spectrum (Equation 1.2) **[73]**.

$$\frac{1}{\tau_R} = A_{MD,0} n^3 \left(\frac{I_{tot}}{I_{MD}}\right) \qquad (1.2)$$

In this equation, the strength of the magnetic dipole transition (MD) is compared to the intensity of the total spectrum (I_{tot}). $A_{MD,0}$ is the spontaneous emission probability of the $^5D_0 \rightarrow {}^7F_1$ transition in vacuum and n^3 is a correction for the refractive index. $A_{MD,\,0}$ could be calculated and was found to be 14.65 s^{-1}.

Both MD and induced ED transitions of lanthanide ions are weak compared to the 'fully allowed' transitions found in organic chromophores. In the case of luminescence, this gives rise to radiative lifetimes of the order of milliseconds, depending on the lanthanide ion and its matrix. This is 6 orders of magnitude as long as the radiative lifetimes of organic fluorophores. On the other hand, the absorption bands are also weak, typically resulting in extinction coefficients of the order of 1 $M^{-1}cm^{-1}$ with bandwidths less than 0.2 nm. This makes the long-lived photoluminescence of lanthanide ions difficult to excite. Figure 1.24 schematizes the types of electronic transitions in lanthanide ions, both of radiative and non-radiative nature. If highly excited lanthanide ions could only decay radiatively, their emission spectra would become extremely rich in lines, since in principle radiative transitions between any two states can take place. Under favourable conditions, emission from 'higher' excited states is indeed observed. Such processes are the basis of upconversion (UC) **[71]**, in which an already excited ion is excited into a higher lying luminescent state, converting two low-energy photons into one high-energy photon, and quantum cutting (QC) **[74]**, in which a highly excited ion emits sequentially two photons. Both UC and QC have important technological implications. UC can convert a flux of near-infrared light into visible light, whereas QC offers the prospect of highly energy-efficient conversion of ultraviolet light into visible light.

The excited states of lanthanide ions, however, do not decay solely by radiative processes. In glasses and crystals, the electronic excitation energy can be dissipated by vibrations of the surrounding matrix, a process known as multiphonon relaxation (MPR) **[75]**. MPR is inversely proportional to number of vibrational quanta needed to bridge the gap between given energy level and the next lower one. A similar process occurs also in complexes with organic ligands and is even of bigger importance in such systems, since in organic media, suitable high-energy vibrations are more common. The efficiency of matrix vibration mediated nonradiative relaxation is inversely proportional to the number of vibrational quanta that are needed to bridge the gap between a given energy level and the next-lower one. This energy gap law is a result of the overlap between the vibronic wave functions. A semi-quantitative treatment was given by Haas and Stein **[76]**.

The rate of phonon emission, ω, depends on the number of phonons emitted simultaneously to bridge the energy gap and is expressed by equation 1.3:

$$\boldsymbol{\omega} \propto \left(\frac{-\mathbf{k}\Delta\mathbf{E}}{\mathbf{h}\boldsymbol{\vartheta}_{\mathbf{max}}}\right) \tag{1.3}$$

Where, ΔE is the energy gap to the nearest lower level and h_{vmax} is the maximum energy of phonons coupled to the emitting states. The phonon emission rate, ω, decreases rapidly with an increase in ΔE, so that the competitive light emission or radiative process becomes dominant.

The nonradiative decay rate does not depend exclusively on the energy gap and the number of matrix vibrations that fit this gap. Multiphonon relaxation still involves electronic transitions in the ion without a change in parity. Weber **[75]** has pointed out that for this process also; selection rules apply, although they affect only a few transitions, such as $^5D_1 \rightarrow ^5D_0$ in Eu^{3+} (and Tb^{3+}). Indeed even in organic media, weak luminescence from the 'higher excited' $^5D_1$ state can be observed. As a result of vibration (or phonon)-mediated nonradiative (NR) decay, luminescence of a given lanthanide ion occurs mainly from one state, which is the state that has a large gap with the next lower lying level. More highly excited states are quickly deactivated to this state, since the higher states form a 'ladder' consisting of relatively small gaps that efficiently undergo multiphonon relaxation. Especially in organic media and in aqueous solution, where matrix vibrations of high energy are ubiquitous **[77, 78]** the emission of lanthanide ions stems (almost) exclusively from one level and therefore the number of emission lines is limited.

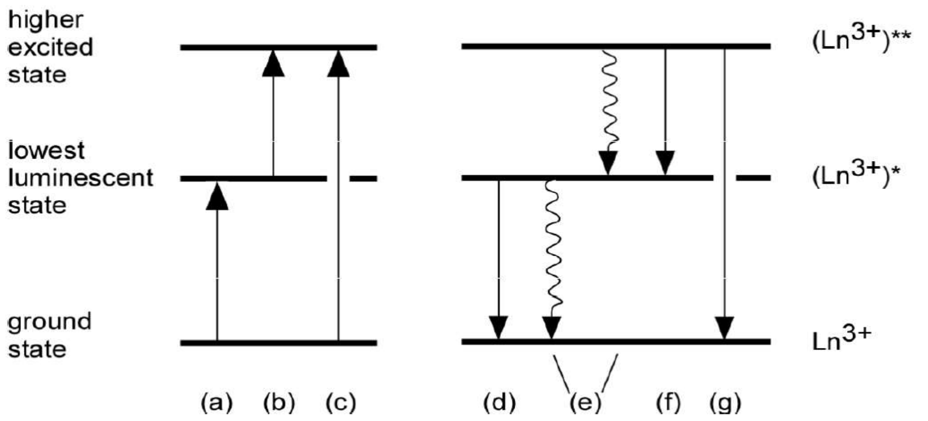

Figure 1.24: *Electronic transitions in lanthanide ions: (a) absorption/excitation, (b) excited state absorption, (c) direct excitation into a higher excited state, (d) ''conventional'' emission from the lowest luminescent state, (e) non-radiative relaxation, (f) radiative transition between excited states, (g) emission from a higher excited state [16]*

In most cases, the decay of the lanthanide luminescent level is not controlled by the radiative rate constant, which is the rate constant of spontaneous emission, but by non-radiative processes. For lanthanide ions, the most important nonradiative processes are those that emerge from interaction of the lanthanide 4f electronic states with suitable vibrational modes of the environment. The *luminescent* trivalent rare earth cations can be classified into two groups: The first group of lanthanides consists of praseodymium, neodymium, holmium, erbium, thulium, and ytterbium, and this group exhibits only weak luminescence in the visible and/or the near-infrared region. The main reason for this is that the energy difference between the lowest luminescent state and the highest non-luminescent state is relatively small. This small energy gap makes the competing radiationless decay more likely to occur, i.e. vibronic quenching by high frequency oscillators. The second group of lanthanides consists of samarium, europium, terbium, and dysprosium, which exhibit strong luminescence. These lanthanide ions have large energy gaps between the lowest luminescent state and the highest non-luminescent state (as shown in Figure 1.23), and are therefore less sensitive towards vibronic quenching by high frequency oscillators. These energy gap considerations are known as the energy gap law theory. The lanthanide ions lanthanum, lutetium and gadolinium do not exhibit any luminescence. Because the 4f subshells are completely empty or completely filled in La^{3+} and Lu^{3+} respectively, no intra-4f transitions are possible. Luminescence is rarely observed for Gd^{3+}, because of the large energy gap between the ground and the first excited state (as shown in Figure 1.23).

The measured lifetimes of luminescent species are generally shorter than the natural lifetimes, because non-radiative processes compete with the radiative decay. High frequency O-H and C-H vibrations in the local environment and the size of the energy gap between the excited and the ground state of the lanthanide ion, play an important role in removing energy non-radiatively from the lanthanide excited state **[79,80]**. The deactivation arises from a weak vibronic coupling between the f-electronic states of the lanthanide ions and the vibrational states of O-H and C-H. To provide an efficient deactivation route, the energy gap between the excited and the ground state of an excited lanthanide ion must be bridged by these vibrational states. According to the theory of the energy gap law **[76]** the smaller the harmonic number of vibrational quanta that is required to match the energy gap between the lowest luminescent state and the highest non-luminescent state of the lanthanide ion, the more effective the vibronic quenching will be. The harmonic number of vibrational quanta (ν) of several vibrations that is required to match the energy gap in Tb^{3+}, Eu^{3+}, Yb^{3+}, Er^{3+}, and Nd^{3+} are indicated in Figure 1.25.

The Tb^{3+} ion, which has a large energy gap (as shown in Figure 1.23), is the least sensitive towards quenching by high frequency oscillators, and as a result has a higher luminescence quantum yield than for example, Eu^{3+}. It can furthermore easily be seen from Figure 1.25 that the near-infrared luminescent lanthanide ions (such as Nd^{3+}) are more prone to quench by vibrations in their environment than the visible emitting lanthanide ions. Indeed, the observed lifetimes of Eu^{3+} and Tb^{3+} complexes in solution are in the ms range, whereas the observed lifetimes of the near-infrared luminescent lanthanide complexes are in the μs range. It has been shown that by replacing the C-H bonds in the ligands by C-D bonds the luminescence lifetimes of the complexed lanthanide ions are increased **[81, 82].**

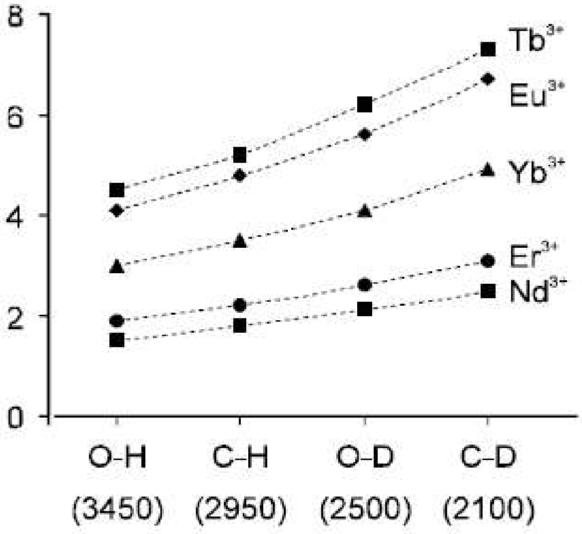

Figure 1.25: *Graphical representation of the number of vibrational quanta of four high frequency oscillators that is required to match the energy gap between the lowest luminescent state and the highest non-luminescent state of the lanthanide ion (the dashed line is merely a guide to the eye). [16]*

1.4.4.3 Optical transition of actinide ions (U^{+3}, U^{+4}, $U^{+5}$and U^{+6}):

Compared to 4f electron in lanthanides; 5f-electrons are relatively less shielded by outer lying electrons. As a result, they are more perturbed by local crystal field, which results in broad emission and absorption spectrum. Oscillator strength of 5f-5f transition is relatively larger than in iso-electronic lanthanide ion. The fact that U^{+3}, U^{+4}, U^{+5} and U^{+6} are all luminescence active ions and stabilize under different conditions. L. S. Natrajan [22] gives a detail description of luminescence properties of various actinides ions including U.

U^{3+} ($5f^3$) exhibits luminescence in the near-IR region (1400-1600 nm) which is suitable for high power laser materials and amplifiers. The main transitions observed are $^4F_{3/2} \rightarrow$ $^4I_{11/2}$ and $^4I_{9/2}$.

In the case of uranium (IV) ($5f^2$), doped in solid state matrices with cubic geometry or symmetry, (e.g. U^{4+} in doped systems of $LiYF_4$, $ThBr_4$, $ThCl_4$, $ThSiO_4$ and Cs_2ZrBr_6,Cs_2GeBr_6 and in Cs_2UCl_6) [22], both the charge transfer emission bands in the UV–VIS and the relatively less intense broad emission bands in the visible region, have been assigned to $5f^16d^1 \rightarrow 5f^2$ electronic transitions. These transitions arise from a redistribution of valence electrons in the 5f sub-shell. For example, in single crystals of $LiYF_4$:U^{4+}, the observed emission bands at 262, 282, 304, 328 and 334 nm (and the weaker bands at 438 and 492 nm) were assigned to transitions between the $^3F_2$ excited state derived from the $5f^16d^1$ configuration and the ground state $^3H_4$ ($5f^2$) manifold. Following excitation at 240 nm (the $5f^2 \rightarrow 5f^16d^1$ absorption band), the UV and near visible emission bands possessed radiative lifetimes of approximately 17 ns at both 300 and 77 K. Similarly, computed and experimental spectra of the doped system $Cs_2GeF_6:U^{4+}$ consist of several broad, intense bands in the ultraviolet and a number of broad weaker bands in the visible and near infrared region. All these emission bands were associated with $5f^16d^1 \rightarrow 5f^2$. The luminescence properties of U^{4+} is suitable for tunable UV solid state laser material

Pentavalent uranyl (U^{5+}) has a $5f^1$ electronic configuration, which is unstable in protic media, and it undergoes rapid disproportionation to U^{+4} and UO_2^{2+}. The first solution luminescence study of uranyl (V) was followed by photo-reduction of uranyl(VI) under ambient conditions where a broad emission band with a maxima at 440 nm was observed [22].

Hexavalent Uranium depending on the synthesis conditions and thermal treatment, can have different molecular species such as tetrahedral uranate (UO_4^{2-}), hexagonal uranate (UO_6^{6-}) or uranyl (UO_2^{2+}) species. The stabilization of U(VI) in the octahedral (UO_6^{6-}) / tetrahedral (UO_4^{2-}) uranates is reported in solids only, whereas UO_2^{2+} moiety is stable both in solutions and solids. Both UO_2^{2+} and octahedral UO_6^{6-} give emission in the green region owing to ligand-to-metal charge transfer (LMCT) transition, but UO_2^{2+}emission can be distinguished from that of the latter on the basis of its characteristic vibronic structure exhibiting a set of six characteristic equidistant bands around 460, 480, 500, 520, 546 and 572 nm. While characteristic emission of UO_4^{2-} species was reported to be in the red region **[21]**. Such fascinating uranyl luminescence has been explored for various applications such as photocatalysis, bio-remediation , chemosensor, internal actinometers in biological chemistry.

1.5. Scope of the Thesis:

The subject of this Ph.D. thesis is the synthesis and characterization of the photoluminescence properties of various oxide based compounds of interest in photonics and optoelectronics. In this context, both undoped and doped oxide matrices were investigated. The main focus was on understanding various kind of fascinating optical properties which arise due to presence of various intrinsic defect centres or due to doping of metal activators such as transition metal, lanthanide and actinide ions. The peculiarity of 4f, 5f and 3d orbital in terms of their photophysical characteristics were highlighted. Various multifunctional oxide based matrices were studied, starting with simple MgO to complicated $Bi_{2-2x}La_{2x}/Eu_{2x}UO_6$. A great emphasis was given on understanding thermally tunable defect induced optical properties in matrices such as $MgAl_2O_4$ and $ZnAl_2O_4$ spinel. Even a system as old as MgO was taken to explain the unexplained dimension in its defect induced luminescence and ferromagnetism. Site selective luminescence spectroscopy was investigated in perovskite matrices using TM and RE ion as a dopant. Extra efforts were made to explain the experimental data using density functional theory calculations.

A variety of inorganic matrices (undoped and doped) starting from binary magnesium oxides (MgO) to aluminates ($ZnAl_2O_4$, $Fe:ZnAl_2O_4$, $MgAl_2O_4$ & $U:MgAl_2O_4$), zirconate ($SrZrO_3$, $Mn:SrZrO_3$, $BaZrO_3$, $Sm:BaZrO_3$ & $Eu:BaZrO_3$), uranate ($Bi_{2-2x}La_{2x}/Eu_{2x}UO_6$) and vanadate ($LiZnVO_4$) were synthesised in present thesis work. These compounds exhibit broadband absorption and emission spectra covering deep ultraviolet (DUV) (300-440 nm), visible (400-700 nm) and near-infrared (NIR) spectral range (700-900nm), which are of scientific and technological importance due to their valuable applications in the field of broadband photodetectors, solar cells, and bioimaging.

MgO is known to display defect induced optical and magnetic properties. But Proper understanding for the same is lacking in the literature. An effort was taken to understand the reason for defect induced emission and ferromagnetism in MgO. The data were explained by Photoluminescence (PL), Positron annihilation spectroscopy (PAS) or Positron annihilation lifetime spectroscopy (PALS), Superconducting quantum interference device (SQUID) and Density functional theory (DFT) studies. For the first time in $MgAl_2O_4$, we have observed defect induced tuneable photoluminescence characteristics, from blue-green-yellow to red-NIR region, upon thermal annealing of the compound. This tunable emission characteristic was attributed to the change in the phase behavior of the spinel. Further low temperature tunable emission characteristics render $MgAl_2O_4$ to be a potential optical based thermal sensor material. In another aluminates based spinel compound i.e. $ZnAl_2O_4$ (ZA), it has been found that the compound obtained at lower annealing temperature is a blue emitting phosphors while that obtained at higher annealing temperature is near white emitting phosphors. Interestingly for both $MgAl_2O_4$ and $ZnAl_2O_4$ compounds synthesised at lower annealing temperature, the lifetime of the defect centres were found to be high (of the order of ms) while at higher annealing temperature the life times were significantly reduced (of the order of μs). This makes the phosphors more variant i.e. either long persistent or short persistent.

The photoluminescence property of Fe^{3+} ion was used to probe the inverse to normal phase transition in ZnAl2O4 spinel. The emitting colour can be tune in between blue and red depending on the site selectivity of Fe^{3+}. Through a combined XRD, PL and EPR study on Fe^{3+} doped $ZnAl_2O_4$, it has been established that in $ZnAl_2O_4$ which was obtained at low annealing temperature, the percentage of inverse spinel is more while at higher annealing temperature majority of the phase is normal spinel. In Mn: $SrZrO_3$, the emission due to Mn^{2+} was found to vary depending on its substitution at different cation site. These substitutions again lead to creation of shallow and deep defects in $SrZrO_3$, which is also reflected in their respective emissions. In sol-gel combustion derived $LiZnVO_4$ an intense green emission was observed which renders the compound as a potential rare earth free green emitting phosphor. In order to make the synthesis procedure cost effective, EPR study was also carried out to monitor the progress of the reaction at different steps, so that a optimum synthesis temperature can be derived.

Special effort was given to understand the photoluminescence characteristics of $SrZrO_3$ and $BaZrO_3$ perovskite in the visible region. These undoped matrices emits in the blue and green regions due to various intrinsic defect centres while on doping Sm^{3+} and Eu^{3+}, the compounds (Sm^{3+}:$BaZrO_3$ & Eu^{3+}:$BaZrO_3$) become red emitting phosphors. Stark splitting pattern of Eu^{3+} emission also help to determine its actual site symmetry. The PL characteristics of $Bi_{1.96}Eu_{0.04}UO_6$ indirectly help to understand the local structure of La in $Bi_{2-2x}La_{2x}$ UO_6, which shows fascinating conductivity properties with respect to temperature. Considering the fact that $MgAl_2O_4$ is one of the probable candidates to be used for transmutation of actinide; speciation study of uranium ion in $MgAl_2O_4$ holds high significance for nuclear scientist. In present thesis the local site occupancy, valence state and coordination geometry behavior of U was determined using PL technique.

The thesis may be helpful in opening up new avenues for researcher working in the field of optoelectronics. The thesis provides a great deal of understanding particularly for defects and dopant mediated tunable optical properties. A great effort has been devoted to understand the local structure of the luminescence centre which enables us to control the optical properties of the material. In some cases the characteristics photoluminescence also enable us to get an insight about other material properties. The outcome of the thesis will be interesting for young researcher to take such problems and investigate the fundamentals to application.

Chapter 2

Experimental

2.1. Synthesis of luminescent materials:

2.1.1 Conventional Solid-state route:

The most widely used method for the preparation of polycrystalline solids from a mixture of solid starting materials is solid-state reaction route. In this method, since the precursor solids do not react together at room temperature over normal time scales, the precursors need to be heated at much higher temperatures, often to 1000 to 1500 °C in order for the reaction to occur at an appreciable rate. The factors which decide the feasibility and rate of a solid state reaction depend are structural properties of the reactants, their reactivity, surface area of the solids, reaction conditions and the thermodynamic free energy change associated with the reaction. Further repeated grinding and repeated heating are required in this method since the mechanism of solid-state reactions is diffusion control.

Following are the consequences of high reaction temperatures

- Ions that readily form volatile species (i.e. $Ag+$) are difficult to incorporate
- Low temperature, metastable (kinetically stabilized) products are not possible to access
- At high temperature, higher (cation) oxidation states are often unstable because of the thermodynamics of the following reaction:

$2MO_n(s) = 2MO_{n-1}(s) + O_2(g)$

Since the entropy increases due to the release of a gaseous product (O_2), the forwards reaction is favored. Positive entropy leads to negative free energy and thus forward reaction becomes increasingly important as the temperature increases.

It is difficult to obtain single-phase compound by the conventional solid-state method. Hence, doping a low concentration (of the order of 1–3%) of activator has always been delicate. Following are the limitations of conventional solid-state route:

1. Products are inhomogeneous.
2. Large particles with low surface area are obtained and hence mechanical particle size reduction is required, which may introduce impurity and defects.

This problem of inhomogeneity of the products could be mitigated by preparing them through non-conventional methods (wet-chemical), which do not comprise of the normal mixing, calcinations and grinding operations. Various wet-chemical methods such as sol-gel, combustion, polymeric precursor etc have been employed to synthesize both undoped and activator doped phosphors. These wet-chemical methods facilitate doping of activators uniformly. However, calcination is required to get crystalline (required) phosphor.

2.1.2 Sol-gel Method:

Solid state method, which is the most widely used synthetic technique for bulk metal oxides is based on the direct reaction of powder mixtures and the reactions are completely controlled by the diffusion of the atomic or ionic species through the reactants and products. Thus, these solid-state processes always require high temperature and small particle sizes of the reactants in order to bring the reaction partners sufficiently close together and to provide high mobility. Although this approach gave access to a large number of new solid compounds and thereby enabled the development of structure-properties relationships, the ceramic method is a rather crude approach in comparison to organic chemistry, where highly sophisticated synthetic pathways are employed to make and break chemical bonds in a controlled way. It is therefore no surprise that liquid-phase routes represent the most promising alternatives for the size- and shape-controlled synthesis of nanoparticles. In this approach, synthesis of nanoparticles with well-defined and uniform crystal morphologies and with superior purity and homogeneity is achievable due to possibility to control the reaction pathways on a molecular level during the transformation of the precursor species to the final product **[83]**. In this context, sol-gel procedures were particularly successful in the preparation of bulk metal oxides (e.g., ceramics, glasses, films and fibers) among the various soft-chemistry routes **[84, 85]** and therefore they have also been applied for nanoparticle synthesis.

The sol-gel process may be described as formation of an oxide network through polycondensation reactions (where molecules join together, losing small molecules as by-products such as water or methanol) of a molecular precursor in a liquid. Sol-gel is a chemical solution process used to make ceramic and glass materials in the form of thin films, fibres, or powders. A sol is a colloidal (the dispersed phase is so small that gravitational forces do not exist; only Van der Waals forces and surface charges are present) or molecular suspension of solid particles of ions in a solvent and a gel is a semi-rigid mass that forms when the solvent from the sol begins to evaporate and the particles or ions left behind begin to join together in a continuous network.

In general, the precursor or starting compound is either an inorganic (no carbon) metal salt (chloride, nitrate, sulfate etc) or a metal organic compound such as an alkoxide.

Metal alkoxides are the most widely used precursors, because they react readily with water and are known for many metals. Some alkoxides, which are widely used in industry, are commercially available at low cost (Si, Ti, Al, Zr), whereas other ones are hardly available or only at very high costs (Mn, Fe, Co, Ni, Cu, Y, Nb, Ta ...). These metal alkoxides and metal chlorides undergo hydrolysis (Hydrolysis is a chemical reaction or process in which a chemical compound is broken down by reaction with water) and polycondensation reactions. This leads to the formation of a colloid, a system composed of solid particles (size ranging from 1 nm to 1 μm) dispersed in a solvent. The sol evolves then towards the formation of an inorganic network containing a liquid phase (gel).Formation of a metal oxide involves connecting the metal centres with oxo (M-O-M) or hydroxo (M-OH-M) bridges, therefore generating metal-oxo or metal-hydroxo polymers in solution. The *drying* process serves to remove the liquid phase from the gel thus forming a porous material, then a thermal treatment (*firing*) may be performed in order to favour further polycondensation and enhance mechanical properties. The precursor sol can thus be used for various purposes including synthesis of powders.

The overall sol-gel process can be presented as below:

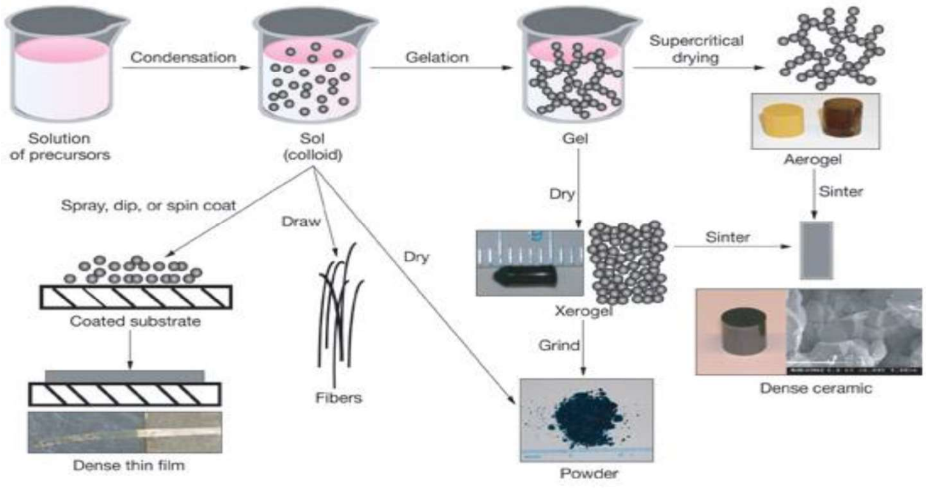

Figure 2.1: *Various steps in the sol-gel process to control the final morphology of the product* ***[86].***

In case of metal alkoxides precursors, the sol-gel conversion of involves two main reaction types: hydrolysis and condensation (Scheme 2.1). During hydrolysis, the metal ion undergoes a nucleophilic substitution reaction where the alkoxide groups (-

OR) are replaced by the nucleophilic attack of the oxygen atom of a water molecule followed by release of alcohol and the formation of a metal hydroxide. As shown in Figure 2.2, in most cases the hydrolysis step requires a catalyst. When two hydroxylated metal species undergoes condensation reactions a M-O-M bond is formed under release of water (oxolation) while the condensation reaction between a hydroxide and an alkoxide also leads to format M-O-M bonds under release of an alcohol (alkoxolation). Figure 2.3 represents the steps involved in the condensation of tetra ethyl orthosilicate (TEOS) during sol-gel process. Hydrolysis (Eq. 2.1) and condensation, involving oxolation (Eq. 2.2) and alkoxolation (Eq. 2.3)

$$\equiv M{-}OR + H_2O \longrightarrow \equiv M{-}OH + ROH \tag{2.1}$$

$$\equiv M{-}OH + HO{-}M\equiv \longrightarrow \equiv M{-}O{-}M\equiv + H_2O \tag{2.2}$$

$$\equiv M{-}OR + HO{-}M\equiv \longrightarrow \equiv M{-}O{-}M\equiv + ROH \tag{2.3}$$

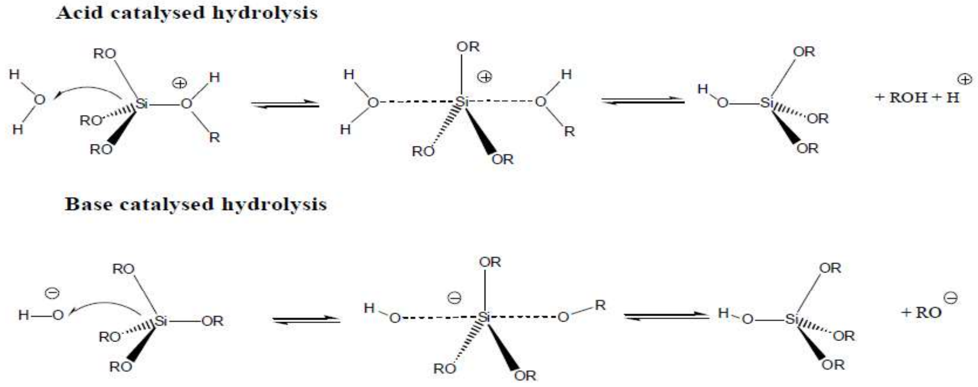

Figure 2.2: *Acid and base catalyzed hydrolysis step*

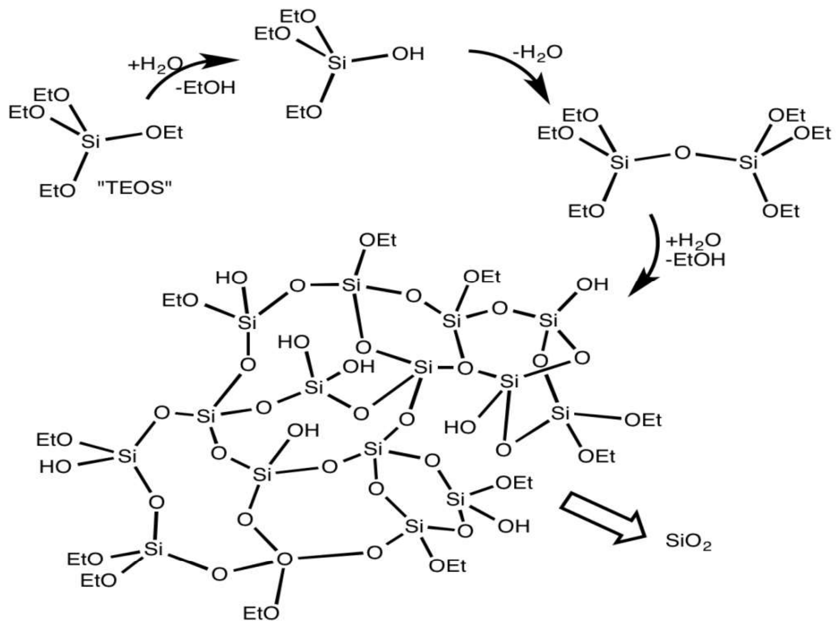

Figure 2.3: *Simplified representation of the condensation of TEOS in sol gel process*

Following are the advantage and disadvantages of sol-gel methode\

Advantages of Sol-Gel Technique:

1. It can easily shape materials into complex geometries in a gel state.
2. It can produce high purity products because the organo-metallic precursor of the desired ceramic oxides can be mixed, dissolved in a specified solvent and hydrolyzed into a sol, and subsequently a gel, the composition can be highly controllable.
3. Can have low temperature sintering capability, usually 200-600°C.
4. It can create very fine powders.

Disadvantages of Sol-Gel Technique:

Despite its advantages, sol-gel technique never arrives at its full industrial potential due to some limitations, e.g. weak bonding, low wear-resistance, high permeability, and difficult controlling of porosity

2.1.3 Sol-gel auto combustion technique

The Sol-gel auto combustion method, which is also known as self-propagating high-temperature synthesis (SHS), has been proved to be extremely facile, time saving and energy-efficient route for low-cost production of various industrially useful bulk/ nano-crystalline powders of oxide ceramics, at a lower calcination temperature.

Principle:

This gel combustion technique comprises of two-step process viz. (i) formation of a precursor (viscous liquid or gel) and (ii) auto-ignition. In a typical reaction, the precursor (mixture of water, metal nitrates and fuel) on heating decomposes, dehydrates and ruptures into a flame. The resultant product is a voluminous, foamy powder, which occupies the entire volume of the reaction vessel. As starting materials, oxidizing metal salts, such as metal nitrates, and a combustion agent (fuel), such as citrate acid, polyacrylic acid or urea are used **[87]**. Generally, Citric acid is suited for obtaining precursors of transition metal oxides due to the good capability of chelating metallic ions and low decomposition temperatures. Since during the initial step of the preparation process, this method uses a solution, the reactants are well-dispersed and are in a much higher reactive state and thereby providing a homogeneous reaction mixture. The combustion agent or organic fuel plays an important role in preventing the precipitation of hydroxilated compounds by forming complexes with metal ions **[88]**. The combustion process can be considered as a thermally induced redox reaction. The chemical energy released from the exothermic reaction between the metal nitrates and fuel can rapidly heat the system to high temperatures without an external heat source. Compared to the powders obtained by conventional solid-state methods, nanomaterials synthesized through combustion route are generally homogeneous, contain fewer impurities, and have higher surface areas. Nature of fuel, fuel to oxidizer ratio, ignition temperature and water content of the precursor mixture are the important parameters, which influence the reaction.

For an intimate blending of the starting constituents and preventing the random redox reaction between a fuel and an oxidizer, the formation of the precursor (viscous liquid or gel), is a primary condition. The process is termed as auto-ignition process since the high exothermicity generated during combustion manifests in the form of either a flame or a fire. For getting a transparent viscous gel without any phase separation or precipitation, the nature of the fuel and its amount, are some of the important process parameters **[89]**. Thus, the fuel should have some basic characteristics such as it should be able to maintain the compositional homogeneity among the constituents and undergo combustion with an oxidizer at a low ignition temperature. Most common used fuels are citric acid, urea, glycine, ascorbic acid etc. During the combustion process, the two events, which occur, are (i) generation of heat of combustion, and (ii) gas evolution. The flame temperature generated during the first event helps in crystallization and formation of the desired phase. However, a very high flame temperature always leads to increase in the crystallite size, formation of hard agglomerates which inturn reduce the surface area and sinterability. The second event i.e evolution of gaseous products during the combustion plays an important role in dissipating the heat of combustion and thereby limits the rise of temperature. This step thus reduces the possibility of premature local partial sintering among the primary particles. Hence, the heat of combustion and gas evolution steps in this process primarily govern the powder characteristics, which themselves are dependent on nature of the fuel and oxidant-to-fuel ratio **[90]**.

The self combustion synthesis (SCS) may occur as either volume or layer-by-layer propagating combustion modes depending on the type of the precursors, as well as on conditions used for the process organization. Through this process not only yield of nanosize oxide materials is possible but also a homogeneous doping of trace amounts of activator ions in a single step is also possible. Literature survey revealed that among the gamut of papers published in recent years on SCS, synthesis of various luminescent materials and catalysts occupy the lion share. Most of the latest developments in SCS technique are discussed based on the materials applications. Currently synthesis of nanophosphors is a hot topic in the field of self-combustion synthesis.

There are various advantages and disadvantages of gel-combustion method over other routes as mentioned below

Advantages of Sol-gel auto combustion process:

Sol-gel combustion methods show advantages over the other processes mainly due to the following important facts,

1. Low cost and low temperature process.
2. Better control of stoichiometry.
3. Crystalline size of the final oxide products is invariably in the nanometer range.
4. Exothermic reaction makes product almost instantaneously.
5. Possibility of multicomponent oxides with single phase and high surface area.

Limitations of Sol-gel auto combustion process:

1. Contamination due to carbonaceous residue, particle agglomeration, poor control on particle morphology.

2. Understanding of combustion behavior is needed to perform the controlled combustion in order to get final products with desired properties.
3. Possibility of violent combustion reaction which needs special production.
4. Synthesis of non-oxide ceramic is difficult.
5. Scaling up is an issue

2.2. Characterization Techniques:

2.2.1. X-ray diffraction:

X-ray diffraction (XRD) technique is used to determine the structural properties of materials and it can give information to the researchers about phase identification, the lattice parameters, degree of crystallinity and grain size. In 1912, Von Laue first suggested the use of the diffraction of waves from the periodic arrangement of atoms in solids to determine the crystal structure, which was then developed by Bragg in 1913 and is now a well-developed science. Since in solids, the typical interatomic distances are a few angstroms, waves with approximately this wavelength are required to explore this structure. X-rays are used to produce the diffraction pattern because their wavelength λ is typically the same order of magnitude (1–100 angstroms) as the spacing d between planes in the crystal. The commonly applied x-rays for x-ray diffraction are having wavelengths in between 0.7 and 2.3 Å, which is close to the interplanar spacings of most crystalline materials.

2.2.1.1. Principle:

Crystals are regular arrays of atoms, and X-rays can be considered waves of electromagnetic radiation. Electrons in atom are mainly responsible for scattering of X-ray waves. Just as an ocean wave striking a lighthouse produces secondary circular waves emanating from the lighthouse, so an X-ray striking an electron produces secondary spherical waves emanating from the electron. This phenomenon is known as elastic scattering, and the electron (or lighthouse) is known as the scatterer. A regular array of scatterers produces a regular array of spherical waves. Although these waves cancel one another out in most directions through destructive interference, they add constructively in a few specific directions. Since in a crystal, the atoms have a periodic arrangement, at certain angles, the scattering produces a diffraction pattern with sharp maxima (peaks). These peaks in the x-ray diffraction pattern are directly related to the interatomic distances. In Figure 2.4, an incident x-ray beam interacting with the atoms arranged in a periodic manner is shown in two dimensions (2-D) where the atoms can be viewed as forming different sets of planes in the crystal. The condition for a diffraction (peak) to occur for a given set of lattice plane with an interplanar distance of d can be written as

$$2d \sin \theta = n\lambda \qquad (2.4)$$

This is known as Bragg's law, after W.L. Bragg, who first proposed it. In this equation λ is the wavelength of the x-rays, θ is the Bragg angle, which is half of the scattering angle and n is an integer representing the order of the diffraction peak .

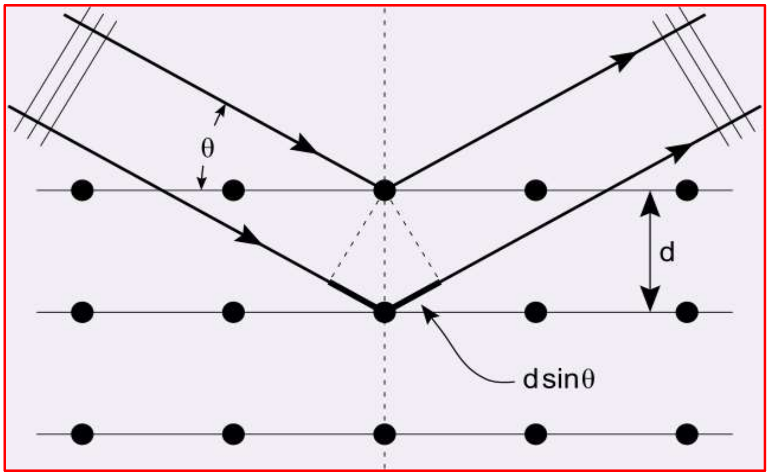

Figure 2.4: *Scattering of x-rays from atoms and Bragg's law. The incoming beam (coming from upper left) causes each scatterer to re-radiate a small portion of its intensity as a spherical wave. When the scatterers are arranged symmetrically with a separation d, these spherical waves will be in constructive interference or sync (add constructively) only in some directions, where their path-length difference 2d sin θ equals an integer multiple of the wavelength λ. Thus part of the incoming beam is deflected by an angle 2θ and produce a reflection spot in the diffraction pattern.[Figure courtesy-Wikipedia].*

2.2.1.2. X-ray production:

X-rays is a form of electromagnetic radiation in the region between ultraviolet and gamma rays. X-rays have a wavelength between 10.0 and 0.1 Å. X-ray wavelengths are shorter than those of UV rays and typically longer than those of gamma rays. When fast-moving electrons of sufficient energy are decelerated, X-rays are produced. Whenever charged particles (electrons or ions) of sufficient energy hit a material, x-rays are produced. X-rays can be generated by an X-ray tube, a vacuum tube where a high voltage is maintained to accelerate the electrons released by a hot cathode to a high velocity [91].

The high velocity electrons then collide with a metal target called anode, creating the X-rays. Thus X-rays are produced at the point of impact, and radiated in all directions. The kinetic energy of the electrons is transformed into electromagnetic energy (x-rays). Since energy must be conserved, the energy loss results in the release of x-ray photons of energy equal to the energy loss. This process generates a broad band of continuous radiation (called Bremsstrahlung, or braking radiation) as shown in Figure 2.5.

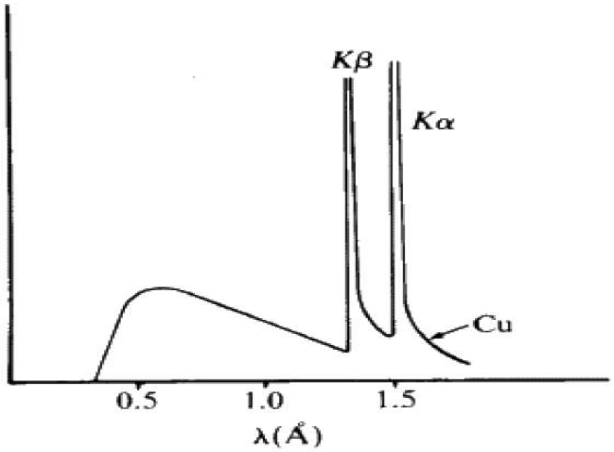

Figure 2.5: Continuous and characteristic x-rays for copper ***[92]***

X-rays are created by two different atomic processes, when the electrons hit the target:

Characteristic X-ray emission (X-ray fluorescence): Characteristic x-rays can be produced when the moving electron interacts with an inner-shell electron of the target atom. When this moving electron ionizes the target atom by removal of a K-shell electron, transition of an outer orbital electron to the vacant inner shell will occur, accompanied by the emission of an x-ray photon. The emitted x-ray photon will have an energy equal to the difference in the binding energies of the orbital electrons in outer and inner shell involved. Thus if an L-shell electron moves to the vacant position a K-shell electron , a Kα x-ray is produced (with wavelength 1.54178 Å for Cu). Similarly when an M-shell electron moves to replace a vacanmt position of a K-shell electron, a K_{β} x-ray is produced (with wavelength 1.39217 Å for Cu). These characteristic x-rays are presented in Figure 2.5 and are suitable for diffraction experiments. A suitable metal filter is used to obtain monochromatic x-rays. Such as Nickel strongly absorbs x-rays below 1.5 Å and thus it can be used to filter the K_{β} x-rays from Cu, as represented in Figure 2.6 **[93]**.

Bremsstrahlung: This is radiation given off by the electrons as they are scattered by the strong electric field near the high-Z (proton number) nuclei. These X-rays have a continuous spectrum. The intensity of the X-rays increases linearly with decreasing frequency, from zero at the energy of the incident electrons, the voltage on the X-ray tube.

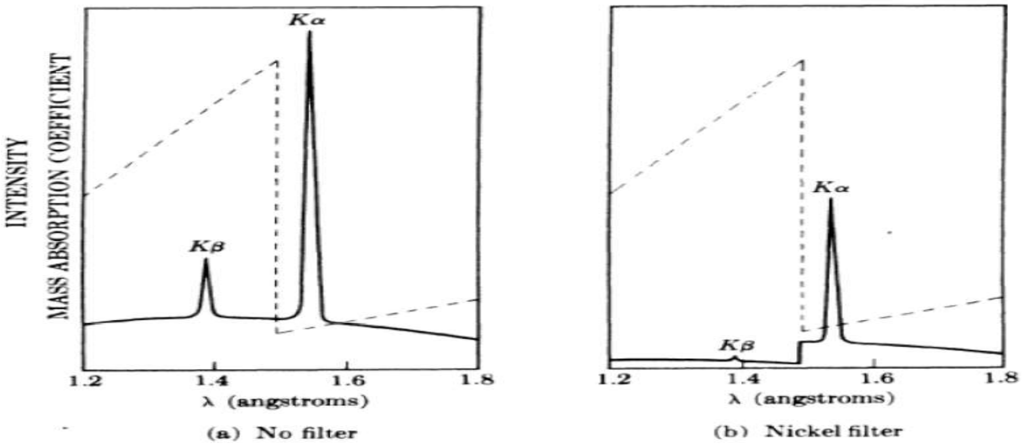

Figure 2.6: *Using a Nickel filter for Cu X-rays* ***[93]***

2.2.1.3. XRD diffractometer:

Diffraction pattern of a sample is recorded in a diffractometer. Figure 2.7 gives the schematical representation of the essential features of a diffractometer. The diffractometer consists of an x-rays source (usually an x-ray tube) which produces monochromatic x-rays of known wavelength, a sample stage, a detector, and a way to vary the angle. The x-rays are focused at some angle of θ on the sample while the detector reads the intensity of the diffracted x-rays it receives at the scattering angle 2θ.

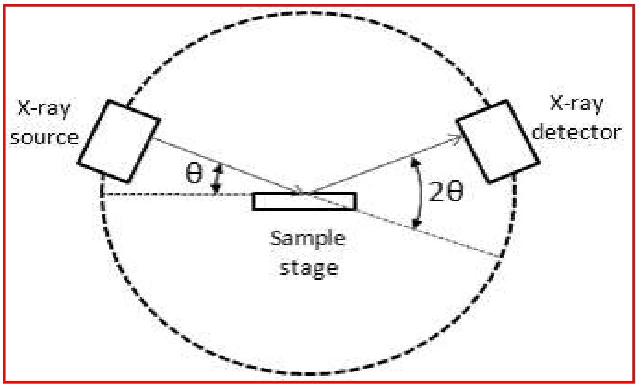

Figure 2.7: *X-ray diffractometer* **[94].**

2.2.1.4. XRD applications: phase purity and crystallite size:

From the XRD pattern, identification of an unknown crystalline material becomes possible. With the help of Bragg’s law (Equation 2.4), the angles where peaks occur can be converted to interplanar spacings (d-spacings). In the Powder Diffraction Files

(PDF) of the International Centre for Diffraction Data (ICDD), for comparison files of d-spacings for hundreds of thousands of inorganic compounds are available there.

For lower crystallite size (less than 100 nm), appreciable broadening in the x- ray diffraction reflections will occur. From the broadening of the diffracted beam, the grain size can be calculated using the Scherer's formula:

$$\mathbf{t = K\lambda / B\cos\theta} \qquad (2.5)$$

Where, t = Diameter of the grain, K = Scherer's constant and its value is the order of unity for usual crystals. Normally, K = 0.9 is used. λ = Wavelength of the X-ray (for Cu-Kα, λ = 1.5418 Å), B = Full width at half maximum (FWHM) of a diffraction peak, θ = Bragg angle or diffraction angle, Hence,

$$\mathbf{t = 0.9\lambda / B\cos\theta} \qquad (2.6)$$

The line broadening B is measured from the Warren's formula:

$$\mathbf{B^2 = B_M{}^2 - B_S{}^2} \qquad (2.7)$$

Where, B_M = Full width at half maximum of the sample, B_S = Full width at half maximum of a standard sample of grain size of around 2 μm. The reflections were chosen such that the standard and sample had closest possible 2θ values and the operations carried out on two reflections were identical. Quartz was used as the standard.

In the present study, all the Powder X-ray diffraction measurements were carried out at room temperature using a Rigaku Miniflex-600 diffractometer using Cu Kα X-rays. The instrument operates in Bragg-Brentano focusing geometry. Graphite monochromator was used to get monochromatic X-rays and NaI (Tl) scintillation detector was used for detection of X-rays. To obtain accurate lattice constants, the $K_{\alpha2}$ reflections were removed by a stripping procedure. The goniometer was calibrated for correct zero position using silicon standard. Before recording the samples are well grounded and made in the form of a slide. As all the micro crystals are randomly oriented, at any point on the sample different planes from crystals will be exposed to X-ray

2.2.2. Electron microscopy: SEM/TEM

Micro-structural characterization, which gives substantial information about the structure-property correlation, has now become very much important for all types of materials. Micro-structural characterization helps to ascertain the morphology, to estimate the particle size and to identify of crystallographic defects and composition of phases etc.

The most extensively used techniques for this purpose is electron microscopy, which is based on the interaction between electrons (matter wave) and the sample.

A beam of highly energetic electrons is used in these scientific instruments (Electron microscopes) to examine objects on a very fine scale. These instruments are widely used as tools for research, quality assurance and failure analysis in the field of material science. In the field of biological and life sciences, they are indispensable implements. In electron microscopy, since wavelength of electron beam is much shorter than light, it results much higher resolution image. The advantages and disadvantages of electron microscope are given in Table 2.1 shows while comparison between light optical microscope and electron microscope are presebted in Table 2.2. The range of optical and electron microscope is depicted in Figure 2.8.

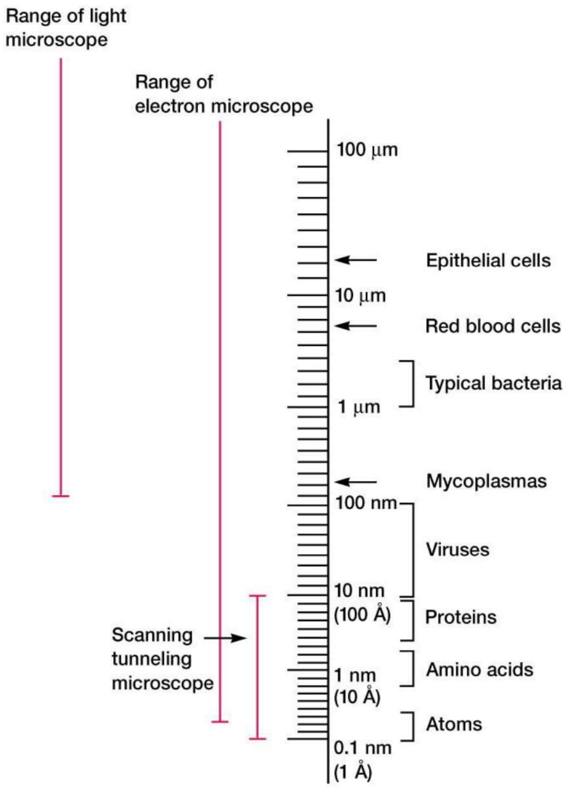

Figure 2.8: *Typical range of light and electron microscope*

Table 2.1: Advantages and disadvantages of electron microscope

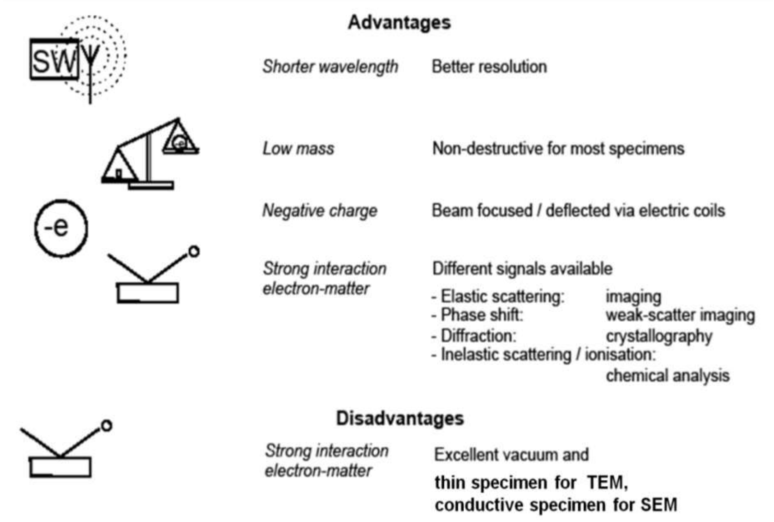

Advantages

Shorter wavelength	Better resolution
Low mass	Non-destructive for most specimens
Negative charge	Beam focused / deflected via electric coils
Strong interaction electron-matter	Different signals available - Elastic scattering: imaging - Phase shift: weak-scatter imaging - Diffraction: crystallography - Inelastic scattering / ionisation: chemical analysis

Disadvantages

Strong interaction electron-matter	Excellent vacuum and **thin specimen for TEM,** **conductive specimen for SEM**

Table 2.2: Comparison between light optical microscope and electron microscope

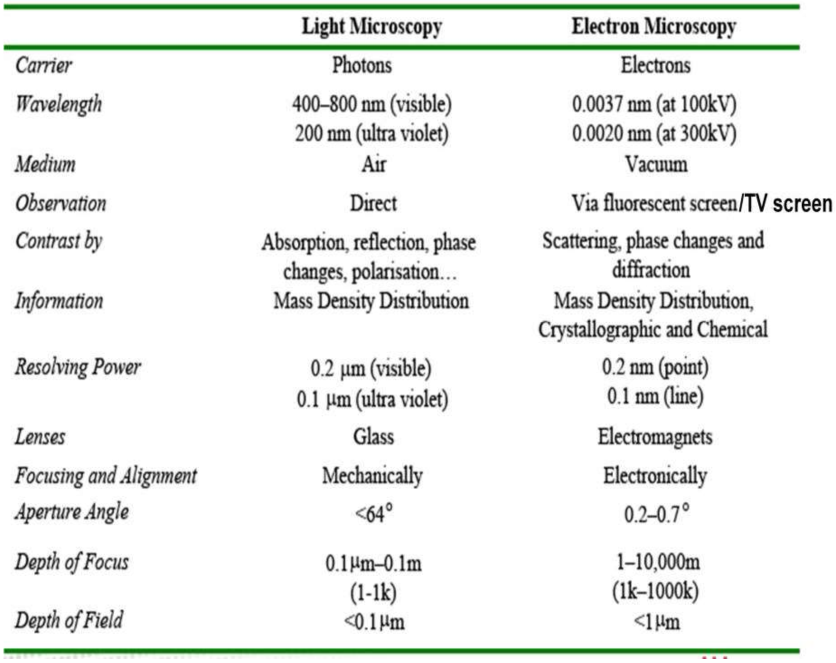

	Light Microscopy	Electron Microscopy
Carrier	Photons	Electrons
Wavelength	400–800 nm (visible) 200 nm (ultra violet)	0.0037 nm (at 100kV) 0.0020 nm (at 300kV)
Medium	Air	Vacuum
Observation	Direct	Via fluorescent screen/TV screen
Contrast by	Absorption, reflection, phase changes, polarisation…	Scattering, phase changes and diffraction
Information	Mass Density Distribution	Mass Density Distribution, Crystallographic and Chemical
Resolving Power	0.2 μm (visible) 0.1 μm (ultra violet)	0.2 nm (point) 0.1 nm (line)
Lenses	Glass	Electromagnets
Focusing and Alignment	Mechanically	Electronically
Aperture Angle	<64°	0.2–0.7°
Depth of Focus	0.1μm–0.1m (1-1k)	1–10,000m (1k–1000k)
Depth of Field	<0.1μm	<1μm

In the present work, Scanning Electron Microscopy (SEM) and Transmission Electron Microscopy (TEM) have been used to characterize the nano and micron sized particles. The basic principle and experimental details of these two techniques are listed below.

In Material Science, following informations about the materials can be obtained by studying these two techniques:

- Morphology - describes the size and shape of the particles making up the object. There is a direct relation between the morphology and material’s properties such as ductility, strength, reactivity etc.
- Topography - describes the surface features of an object or ` how it looks’, its texture. There is a direct relation between the topography and material’s properties such as hardness, reflectivity etc.
- The composition of the specimen - the relative amounts of the elements and compounds that the specimen is composed of. Electron microscope is used to evaluate the homogenicity or the uniformity of composition and their correlation with properties like melting point, mechanical properties etc.
- Crystallographic information - About the arrangement of atoms in the specimen of the object. A direct relation between the atomic arrangements and the properties like conductivity, electrical characteristics, strength etc., of the material under investigation can be obtained.

Therefore a complete *structure – property* correlation understanding is possible with electron microscopy study.

2.2.2.1. Scanning Electron Microscopy (SEM):

An SEM produces Difffenr types of signals, which include secondary electrons (SE), reflected or back-scattered electrons (BSE), photons of characteristic X-rays and light (cathodoluminescence) (CL), absorbed current (specimen current) and transmitted electrons. Secondary electron detectors are standard equipment in all SEMs and single machine with detectors for all other possible signals is rare. The signals are resulted due to the interactions of the electron beam with atoms at various depths within the sample. In secondary electron imaging or SEI which is the most common or standard detection mode, since the secondary electrons are emitted from very close to the specimen surface, SEM produces very high-resolution images of a sample surface and thereby revealing details less than 1 nm in size. Back-scattered electrons (BSE) are nothing but a beam of electrons that are reflected from the sample due to elastic scattering. Since BSE emerge from deeper locations within the specimen, the resolution of BSE images is generally poorer than SE images. However, since the intensity of the BSE signal is strongly related to the atomic number (Z) of the specimen, these signals are often used in analytical SEM along with the spectra made from the characteristic X-rays. Information regarding the distribution of different elements in the sample can be obtained from BSE images. Characteristic X-rays are emitted when an inner shell electron is removed from the sample and causing a higher-energy electron to fill the shell and release energy. In order to identify the composition and to measure the abundance of respective elements in the sample, these characteristic X-rays are used.

In a typical SEM, a well-focused electron beam is incident and scanned over the sample surface by two pairs of electro-magnetic deflection coils. The signals generated from the surface by secondary electrons are detected and fed to a synchronously scanned cathode ray tube (CRT) as intensity modulating signals. Thus, the specimen image is displayed on the CRT screen. Any changes in the brightness represent changes of a particular property within the scanned area of the specimen. The large depth of field in SEM allows a large amount of the sample to be in focus at one time. The high resolution image in SEM also allows to examine closely spaced features at a high magnification. In SEM analysis, the sample must be vacuum compatible (~ 10-6 Torr or more) and electrically conducting. By coating with a thin film of gold or platinum or carbon, the surfaces of non-conductive materials are generally made conductive.

A schematic representation of SEM is given in Figure 2.9 . Image formation in a SEM depends on the acquisition of signals produced from the interaction of the specimen and the electron beam. A pictorial representation of information that can be obtained from SEM are given in Figure 2.10.

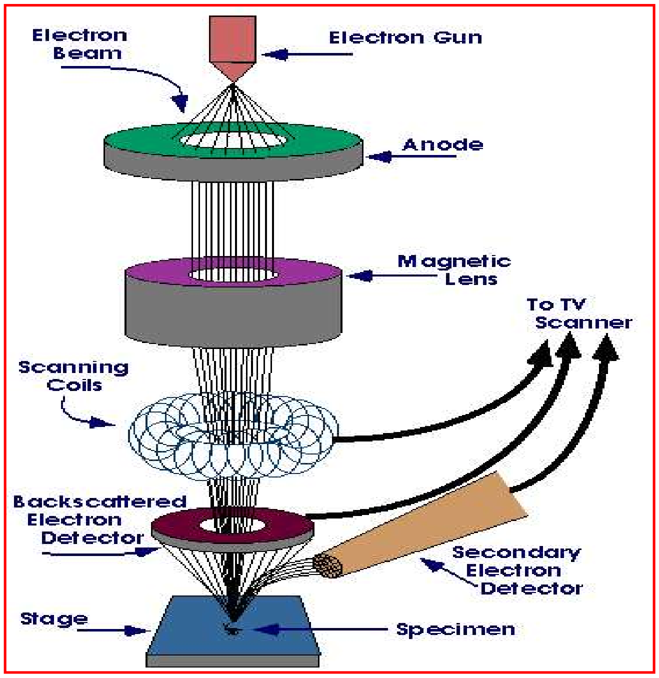

Figure 2.9: *Schematic of scanning electron microscope*

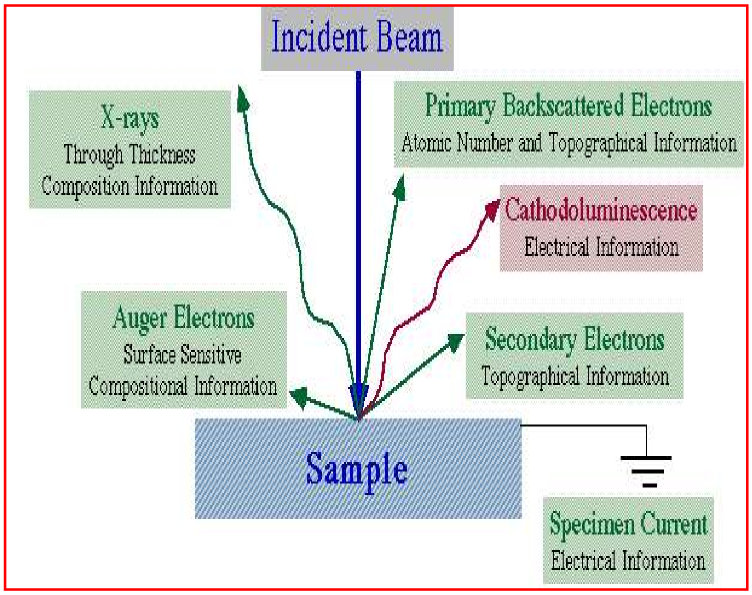

Figure 2.10: *Various electron and photon emitted in SEM and information gathered from them.*

2.2.2.2. Transmission electron microscopy (TEM):

Transmission electron microscopy (TEM) is a microscopy technique in which a beam of electrons is transmitted through an ultra-thin specimen, interacting with the specimen as it passes through. An image is formed from the electrons transmitted through the specimen, magnified and focused by an objective lens and appears on an imaging screen, a fluorescent screen in most TEMs, plus a monitor, or on a layer of photographic film, or to be detected by a sensor such as a CCD camera. TEMs are capable of imaging at a significantly higher resolution than light microscopes, owing to the small de Broglie wavelength of electrons. This enables the instrument's user to examine fine detail—even as small as a single column of atoms, which is thousands of times smaller than the smallest resolvable object in a light microscope. Electrons are usually generated in an electron microscope by a process known as thermionic emission from a filament, usually tungsten, in the same manner as a light bulb, or by field emission. The electrons are then accelerated by an electric potential (measured in V, or volts) and focused by electrostatic and electromagnetic lenses onto the sample. The transmitted beam contains information about electron density, phase and periodicity; this is used to form an image. A TEM can be modified into a scanning transmission electron microscope (STEM) by the addition of a system that rasters the beam across the sample to form the image, combined with suitable detectors. An analytical TEM is one equipped with detectors that can determine the elemental composition of the specimen by analysing its X-ray spectrum or the energy-loss spectrum of the transmitted electrons. Schematic representation of TEM is shown in Figure 2.11. Table 2.3 represents the comparison between SEM and TEM.

Table 2.3: Comparison between SEM and TEM

SEM	TEM
Electrons scan the surface	Electron is transmitted through the specimen
Bulk sample can be done	Extremely thin sample
Larger depth of field	Comparatively less
Resolution-10 nm	Resolution-0.1 nm

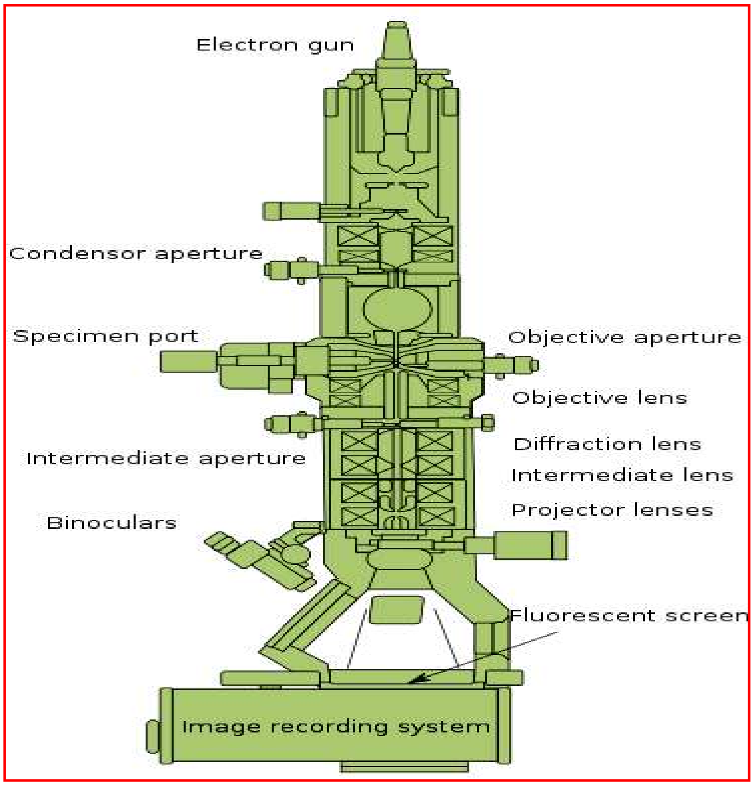

Figure 2.11: *Schematic of transmission electron microscope.*

2.2.3. Positron annihilation spectroscopy (PAS):

Positron annihilation spectroscopy (PAS) which is sometimes specifically referred as Positron annihilation lifetime spectroscopy (PALS) is a non-destructive spectroscopy technique used to study voids and defects in solids. In the field of material science PAS is a well established technique to study the electronic structure and defects in materials **[95-98]**. The basic principle of PALS is that a positron or positronium will annihilate through interaction with electrons and thus the lifetime of positrons depends on the electron density at the annihilation site. This annihilation process resulted release of gamma rays that can be detected. Thus, the time between emission of positrons from a radioactive source and detection of gamma rays due to annihilation corresponds to the lifetime of positron or positronium. After being injected into a solid body, positrons interact in some manner with the electrons in that species. In case of solids containing free electrons such as metals or semiconductors, the implanted positrons annihilate rapidly. However if voids are available in the material, positrons will reside in them and annihilate less rapidly than in the bulk of the material, on time scales up to ~ 1 nanosecond. In the presence of defects the electron density experienced by positron is reduced which leads to increase in its lifetime value and thus positrons have high affinity for open volume defects. This way positron lifetime spectroscopy is capable of giving information about the size, type and relative concentration of various defects/vacancies even at ppm level concentration. On the other hand, Doppler broadening technique measures the momentum distribution of the annihilating electrons. The low momentum part of the Doppler spectrum (511 keV gamma line) arises mainly from the annihilation with the valence electrons while the high momentum part the spectrum arises from annihilation with core electrons that can be taken as signature of an element. However, due to the repulsion of positron by the positively charged nucleus a very small fraction of positrons annihilate with core electrons. Therefore, the amplitude of the high momentum or core electron component is low and it is buried in the Compton background in conventional Doppler spectrum. Coincidence Doppler broadening (CDB) technique using two HPGe detectors **[99]**, is capable of eliminating the background to a great extent, e.g., peak to background ratio of ~ 10^6 can be obtained as compared to a few hundreds in conventional Doppler technique. This enables unambiguous extraction of the shape and magnitude of the high momentum part of the Doppler spectrum. Information regarding chemical surrounding of the annihilation site or elemental specification is obtained from the shape/magnitude of the high momentum core component, which carry the signature of the element. Again since the physical or chemical state of the element does not influence the core electron momentum distribution, the CDB technique is capable of identifying the elements at the annihilation site irrespective of its physical or chemical state in the sample. Therefore, valuable information about the vacancy structure can be obtained by a combined study of lifetime spectroscopy (LTS) and CDB technique. Figure 2.12 shows a schematic representation of positron annihilation while Figure 2.13 shows the schematic of instrument used in positron lifetime measurement.

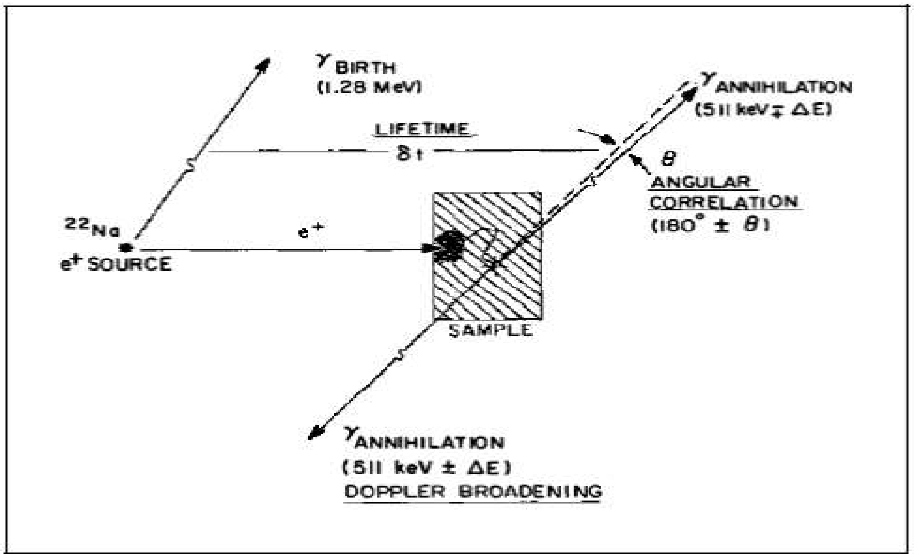

Figure 2.12: *Schematic representation of positron annihilation indicating the basis for the three experimental techniques of positron annihilation spectroscopy (PAS): lifetime, angular correlation, and Doppler broadening.*

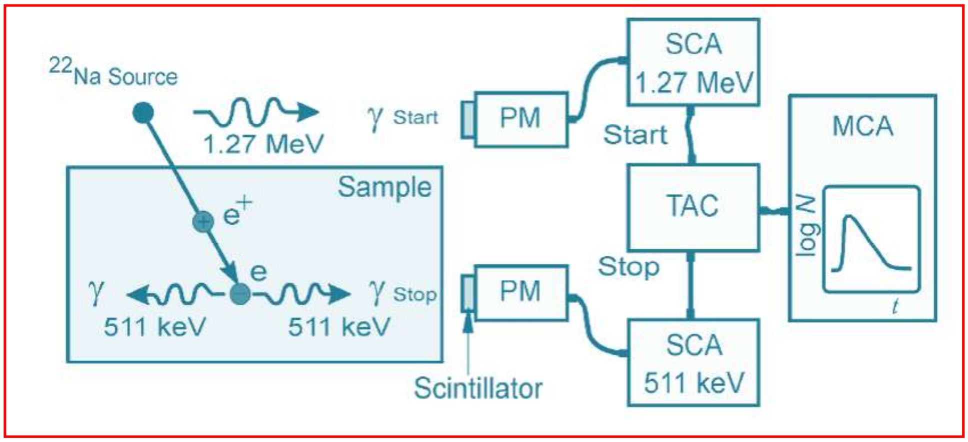

Figure 2.13: *The conventional positron lifetime measurement system*

2.2.4. Electron paramagnetic resonance (EPR) spectroscopy:

Electron paramagnetic resonance spectroscopy (EPR), also called electron spin resonance (ESR), is a technique used to study chemical species with unpaired electrons. EPR was first observed by Soviet physicist Yevgeny Zavoisky in 1944 in Kazan State University, **[100]** and was developed independently at the same time by Brebis Bleaney at the University of Oxford.

Very surprisingly, there are large numbers of materials that have unpaired electrons such as free radicals, many transition metal ions, defects in materials etc. Short-lived free electrons play crucial roles in many processes such as photosynthesis, oxidation, catalysis, and polymerization reactions. Therefore, EPR crosses several disciplines including chemistry, physics, biology, materials science, medical science and many more.

The basic concepts of EPR are analogous to those of nuclear magnetic resonance (NMR), but it is electron spins that are excited instead of the spins of atomic nuclei. Like a proton, the electron has spin, which gives it a magnetic property known as a magnetic moment and makes the electron behaves like a tiny bar magnet.

Every electron has a magnetic moment and spin quantum number s = 1/2, with magnetic components $m_s = + 1/2$ and $m_s = - 1/2$. In the presence of an external magnetic field with strength H , the electron's magnetic moment aligns itself either parallel ($m_s = - 1/2$) or antiparallel ($m_s = + 1/2$) to the field, each alignment having a specific energy due to the Zeeman effect: $E = m_e g_e \beta H$

where g_e is the electron's so-called g-factor (see also the Landé g-factor), $g_e = 2.0023$ for the free electron and β is the Bohr magneton. Therefore, the separation between the lower and the upper state is $\Delta E = g_e \beta H$ for unpaired free electrons. This equation implies that the splitting of the energy levels is directly proportional to the magnetic field's strength.

An unpaired electron can have transition between the two energy levels by either absorbing or emitting a photon of energy hν obeying the resonance condition, $h\nu = \Delta E$. Hence the fundamental equation of EPR spectroscopy is $h\nu = g_e \beta H$. Although this equation permits a large combination of frequency and magnetic field values experimentally, but the great majority of EPR measurements are made with microwaves in the 9000–10000 MHz (9–10 GHz) region, with fields corresponding to about 3500 G (0.35 T). Furthermore, EPR spectra can be generated by either varying the photon frequency incident on a sample while holding the magnetic field constant or doing the reverse. The usual practice is to keep the frequency fixed and the paramagnetic centres are exposed to microwaves at a fixed frequency. With increasing the external magnetic field, the gap between the $m_s = + 1/2$ and $m_s = - 1/2$ energy states becomes widened until it matches the energy of the microwaves, as represented by the bold arrow in Figure 2.14. The condition where the magnetic field and the microwave frequency are "just right" to produce an EPR resonance (or absorption) is known as the resonance condition and is described by the equation shown in the above

Figure 2.14. At this point, the unpaired electrons can move between their two spin states. Since there will be more electrons in the lower energy level (i.e., parallel to the field) than in the upper level (antiparallel), due to the Maxwell–Boltzmann distribution (see below), there is a net absorption of energy, and it is this absorption that is monitored and converted into a spectrum.

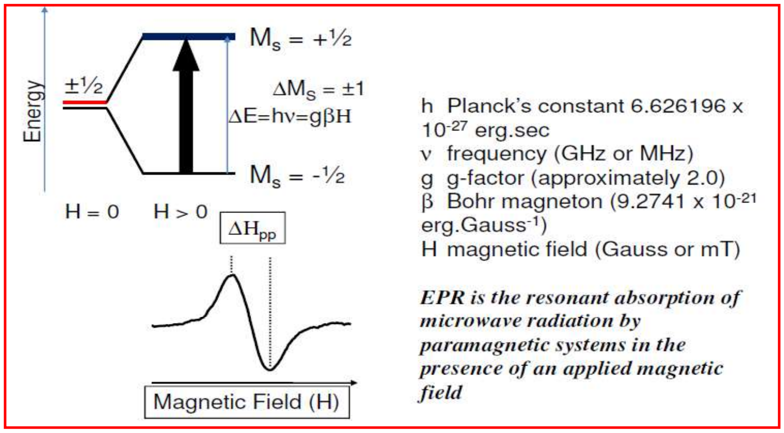

Figure 2.14: *Separation between the lower and the upper state for unpaired free electrons in EPR*

g- factor:

The factor g can provide information about a paramagnetic centre's electronic structure. The unpaired electron of a paramagnetic species not only responds to the spectrometer's applied magnetic field H, but also to any local magnetic fields of atoms or molecules. The effective field H_{eff} experienced by an electron is thus written as $H_{eff} = H(1- \sigma)$, where σ includes the effects of local fields and it can be positive or negative. Therefore, the $h\nu = g_e\beta H_{eff}$ resonance condition cab be rewritten as follows:

$h\nu = g_e\beta H_{eff} = g_e\beta H(1- \sigma)$

Here the quantity $g_e(1- \sigma)$ is denoted as g and called simply the g-factor. Therefore the final resonance equation becomes $h\nu = g\beta H$

From this equation, g-factor can be determined in an EPR experiment by measuring the field and the frequency at which resonance occurs.

The factor g is the measure of the total magnetic moment associated with the paramagnetic molecule and it is represented by the following equation.

$$\mathbf{g = 1+ [J (J +1) + S (S+1) - L (L + 1)]/ [2 J (J + 1)]} \qquad (2.8)$$

For free electron, S =1/2, L = 0, J = S = ½. This gives g = 2.0. The g factor is a dimensionless constant. For most of the free radicals, g value is very close to 2.0000.

This is because in case of free radicals the unpaired electron is not confined to a localized orbital but can move freely over the orbital resulting in the quenching of the orbital contribution (L=0). In case of transition metal complexes, on the other hand, the unpaired electron is confined in a particular orbital. Because of the loss of orbital degeneracy and the spin orbit coupling the g value of the complex is different from 2.0000. The g value of the transition metal complexes depends on the relative magnitude of the spin orbit coupling and the crystal field splitting. The spin orbit contribution makes "g" as a characteristic property of a transition metal ion and its oxidation state. The g factor is an anisotropic quantity i.e. its value depends on the direction of observation (orientation dependent). From the g value of a transition metal complex, one can obtain important information about the structure of the complex. In solids, the movement of the molecule is restricted and thus one can have different g values for different direction of observations. In a cubic crystal field, the metal ligand bond lengths are same along three crystallographic axes and hence g value remains the same (isotropic), that is $g_x = g_y = g_z$.

If the crystal field is tetragonal, the metal - ligand distance along the x and y axis are the same but different from the metal ligand distance along the z direction. The g value for such complex is anisotropic and they are expressed as $g_z = g_{||}$ and $g_x= g_y = g_{\perp}$. This is because it is always assumed that, the principal axis (along which the magnetic field if aligned) is along the z-axis. Whereas if the symmetry of the complex is orthorhombic, all the three g values will be different, that is $g_x \neq g_y \neq g_z$.

However, for most systems in solution or gas phase, the g value is averaged over all the orientations because of the free motion of the molecules. In this case, the

$$\mathbf{g_{av} = (g_x+g_y+g_z)/3}. \qquad (2.9)$$

Hyperfine Interactions:

Hyperfine interactions are another very important factor in EPR spectroscopy. In addition to the applied magnetic field H, the unpaired electrons in a compound are also sensitive to their local environment. This allows to draw additional conclusions or information from the so called hyperfine interaction. When the nuclei of the atoms in a molecule or complex have their own fine local magnetic moments and if the moment is intense enough, can affect the electron. Such interaction between the local magnetic field of the nuclei and electron is called the *hyperfine interaction*. Then the energy level of the electron can be expressed as

$$E = g\beta H M_S + aM_sI_s \tag{2.10}$$

Here a is the hyperfine coupling constant, m_I is the nuclear spin quantum number. Hyperfine interactions can provide a wealth of information about the sample such as the number and identity of atoms in a molecule or compound, as well as their distance from the unpaired electron. The rules for interacting nuclei are same as for NMR. Isotopes, which have even atomic and even mass numbers and the ground state nuclear spin quantum number, I, is zero, will have no EPR (or NMR) spectra. While isotopes with odd atomic numbers and even mass numbers, the values of I are integers e.g. for ^2H is 1. For isotopes with odd mass numbers, the values of I are half integer. For example the spin of ^1H is 1/2 and the spin of ^{23}Na is 7/2. Here are more examples from biological systems given in Table 2.4 and Table 2.5:

Table 2.4. Bio transition metal nuclear spins and EPR hyperfine patterns **[101]**

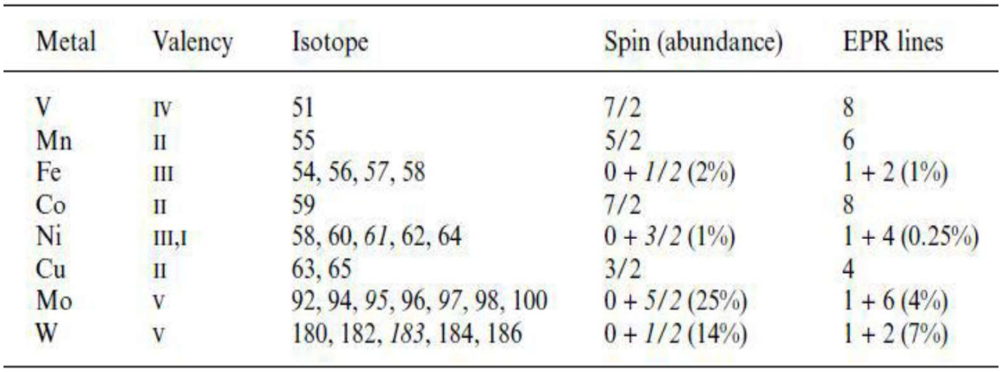

Metal	Valency	Isotope	Spin (abundance)	EPR lines
V	IV	51	7/2	8
Mn	II	55	5/2	6
Fe	III	54, 56, *57*, 58	0 + *1/2* (2%)	1 + 2 (1%)
Co	II	59	7/2	8
Ni	III,I	58, 60, *61*, 62, 64	0 + *3/2* (1%)	1 + 4 (0.25%)
Cu	II	63, 65	3/2	4
Mo	V	92, 94, *95*, 96, *97*, 98, 100	0 + *5/2* (25%)	1 + 6 (4%)
W	V	180, 182, *183*, 184, 186	0 + *1/2* (14%)	1 + 2 (7%)

Table 2.5. Bio ligand atom nuclear spins and their EPR hyperfine patterns **[101]**

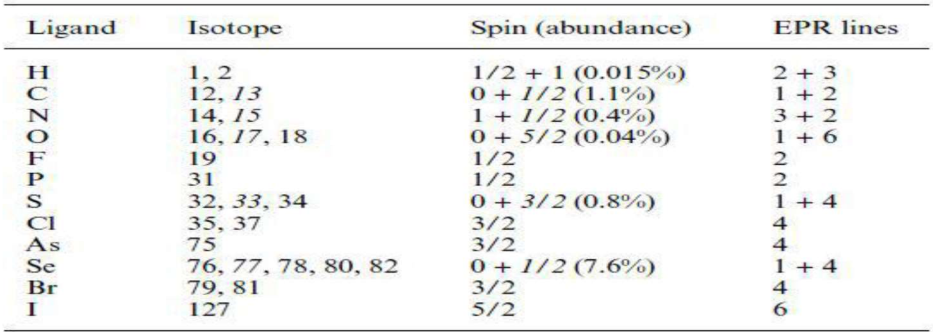

Ligand	Isotope	Spin (abundance)	EPR lines
H	1, 2	1/2 + 1 (0.015%)	2 + 3
C	12, *13*	0 + *1/2* (1.1%)	1 + 2
N	14, *15*	1 + *1/2* (0.4%)	3 + 2
O	16, *17*, 18	0 + *5/2* (0.04%)	1 + 6
F	19	1/2	2
P	31	1/2	2
S	32, *33*, 34	0 + *3/2* (0.8%)	1 + 4
Cl	35, 37	3/2	4
As	75	3/2	4
Se	76, *77*, 78, 80, 82	0 + *1/2* (7.6%)	1 + 4
Br	79, 81	3/2	4
I	127	5/2	6

The number of lines from the hyperfine interaction can be determined by the formula: $2NI + 1$ where N is the number of equivalent nuclei and I is the spin. For example, an unpaired electron on a V^{4+} (I=7/2) will give 8 lines in the EPR spectrum. In case of coupling to a single nucleus, each line has the same intensity while coupling to more than one nucleus, the relative intensity of each line is determined by the number of interacting nuclei. For the most common *I*=1/2 nuclei, the intensity of each line follows Pascal's triangle, which is shown below in Figure 2.15 :

1
1 1
1 2 1
1 3 3 1
1 4 6 4 1
1 5 10 10 5 1

Figure 2.15: *Pascal's triangle*

For example, for •CH3, the radicals signal is split to 2N*I*+1= 2*3*1/2+1=4 lines, the ratio of each lines intensity is 1:3:3:1. The spectrum looks like this in Figure 2.16:

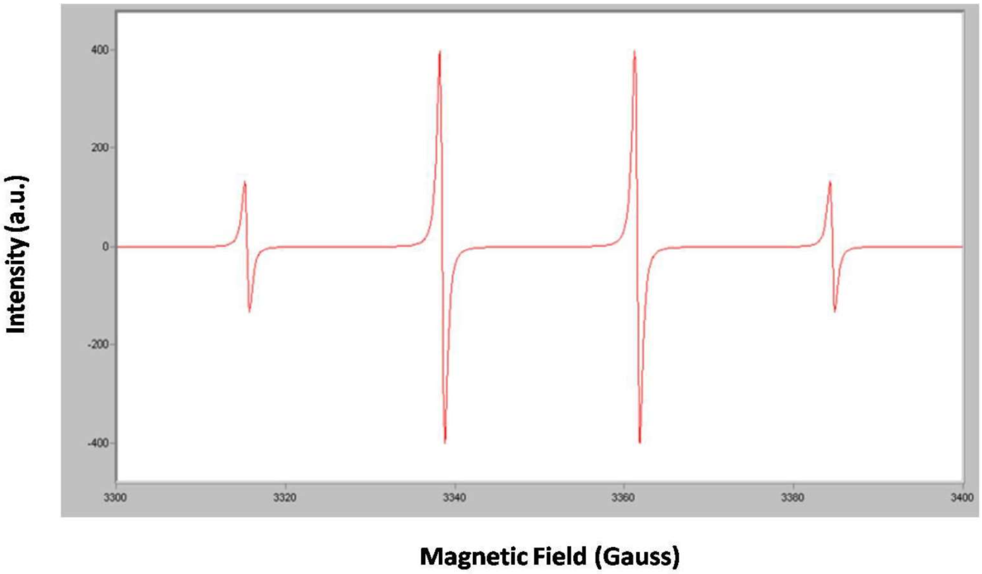

Figure 2.16. *Simulated EPR spectrum of the •CH3 radical.* ***[102]***

If an electron couples to several sets of nuclei, first one can apply the coupling rule to the nearest nuclei, then we split each of those lines by the coupling them to the next nearest nuclei, and so on. For the methoxymethyl radical, H2C(OCH3), there are (2*2*1/2+1)*(2*3*1/2+1)=12 lines in the spectrum, the spectrum looks like this in Figure 2.17:

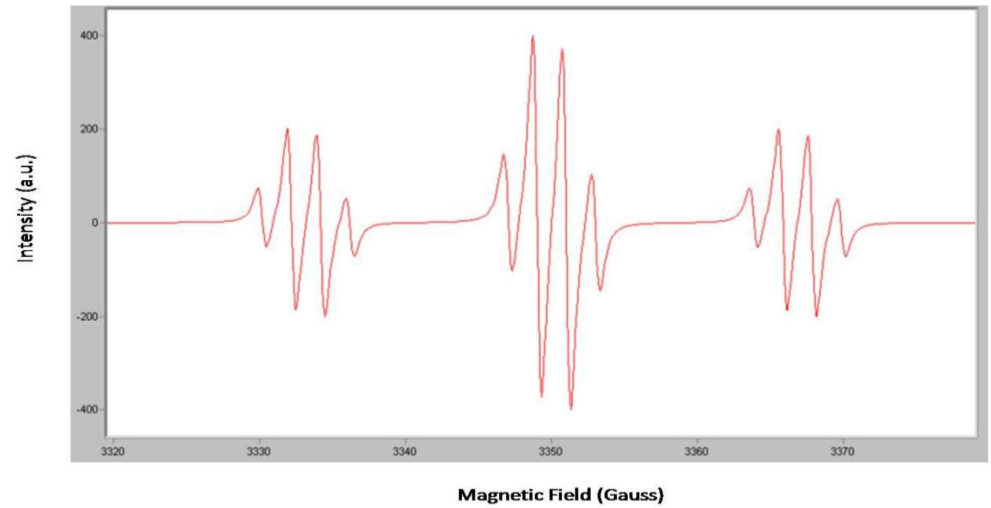

Figure 2.17. *Simulated EPR spectrum of the $H_2C(OCH_3)$ radical.**[103]***

For I=1, the relative intensities follow this triangle in Figure 2.18:

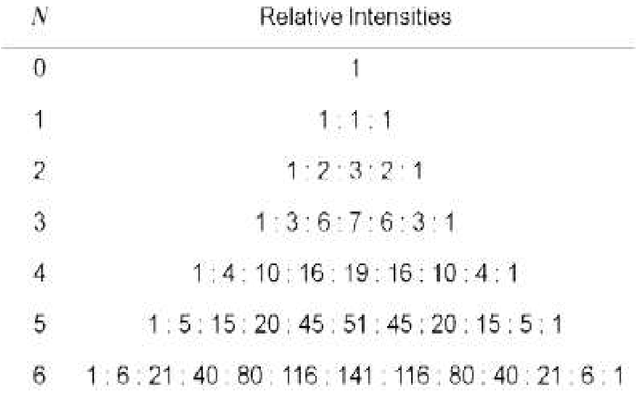

N	Relative Intensities
0	1
1	1 : 1 : 1
2	1 : 2 : 3 : 2 : 1
3	1 : 3 : 6 : 7 : 6 : 3 : 1
4	1 : 4 : 10 : 16 : 19 : 16 : 10 : 4 : 1
5	1 : 5 : 15 : 20 : 45 : 51 : 45 : 20 : 15 : 5 : 1
6	1 : 6 : 21 : 40 : 80 : 116 : 141 : 116 : 80 : 40 : 21 : 6 : 1

Figure 2.18: *Triangle for I=1*

The three essential components for any spectroscopic technique has are a source of electromagnetic radiation (EMR), a sample, and a detector. To acquire a spectrum, we can vary the frequency of the EMR and measure the amount of radiation that passes through the sample with a detector to observe the spectroscopic absorptions. In an EPR spectrometer, the source of the microwave radiation is a Klystron or a Gunn-diode. The source provides a limited range of variable frequency. The microwave source and the detector are in a box called the microwave bridge.

To measure the EPR spectrum of a paramagnetic sample, the sample is placed in a magnetic field of a resonator cavity in which microwave power is concentrated. The sample is so positioned inside the resonator cavity that the electrical component of the EMR is at its minimum and the magnetic component is at its maximum.

At the sample, the static magnetic field (H) is perpendicular to the microwave magnetic field. The interaction of magnetic spins with the oscillating magnetic field of the electromagnetic radiation leads to the EPR transitions. Either varying the magnetic field strength or the microwave frequency can record the EPR spectrum. As it is easier to vary the magnetic field than the frequency due to restriction in the electronics, usually the magnetic field H is varied over a wide range and the frequency is kept constant.

An electromagnet having sweep width ranging from 5000 G to 15000 G can be used. The microwave energy is modulated and the microwave power absorbed by the sample at the resonance is measured by the phase sensitive detector, the signal is amplified and fed to a computer for data processing. A semiconductor silicon-tungsten diode is used as a detector. Earlier, the EPR spectrum used to be recorded as a function of absorption intensity against magnetic field. Such a curve often produces broad absorption bands. In modern instrument, the first derivative of the absorption intensity (dA/dH, i.e. slope) is plotted against H as shown in Figure 2.19. This type of plot gives more accurate g values. It may be noted that the resonance field H is not a unique fingerprint for identification of the paramagnetic species because spectra can be acquired at different frequencies. The g-factor, $g = h\nu/\beta H$ being independent of the microwave frequency, is much better for that purpose. Notice that higher values of ‘g’ occur at low magnetic fields and vice versa. A list of fields for resonance for a g= 2 signal at microwave frequencies commonly available in EPR spectrometers is presented in the Table 2.6. Figure 2.20 shows the block diagram of typical EPR spectrometers. Figure 2.21 shows the photographs of EPR spectrometer used in current studies.

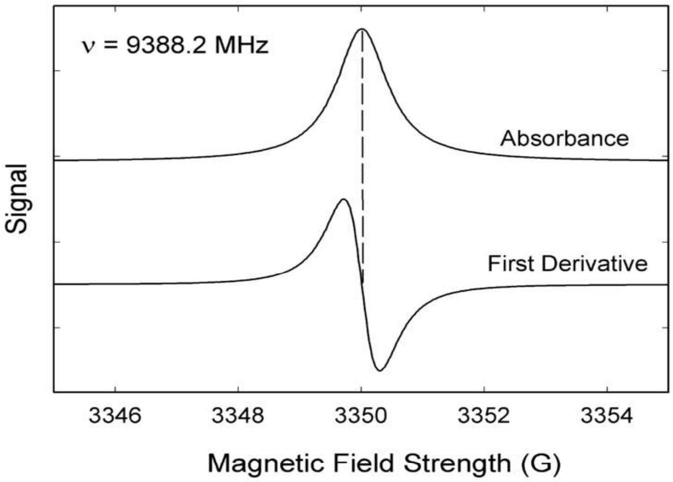

Figure 2.19. *Comparison of absorption spectrum and EPR spectrum* ***[104]***.

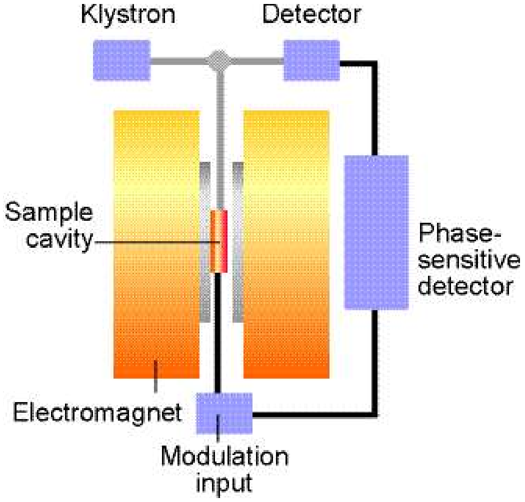

Figure 2.20: *Block diagram of typical EPR spectrometers*

Figure 2.21: *Photograph of Bruker ESP-300 EPR spectrometer*

Table 2.6: List of fields for resonance for a g = 2 signal at microwave frequencies commonly available in EPR spectrometers

Designation	**ν/GHz**	***$H_{(electron)}$/ Tesla***
L	1.1	0.0392
S	3.0	0.107
X	9.5	0.339
K	23	0.82
Q	35	1.25
W	95	3.3

The most widely used EPR spectrometer is the X-band spectrometer operating in the frequency range 9-10 GHz. The sensitivity of an EPR spectrometer is directly proportional to the square of the frequency, and a high frequency is preferred for a better resolution of the EPR signal. The sensitivity of the Q band spectrometer is fifteen times than that of X band spectrometers.

In the present work, a Bruker ESP-300 EPR spectrometer was used to record the EPR spectra. In order to calibrate the g-values of the paramagnetic species, Diphenyl picrylhydrazyl (DPPH) was used as a standard. The spectrometer operates at X-band frequency (9.5 GHz) equipped with 100 kHz field modulation and phase sensitive detection in order to obtain the first derivative signal. Simulation of the experimental spectra were carried out using Bruker WinEpr SymFonia programme

2.2.5. Photoluminescence spectroscopy (PL):

Photoluminescence spectroscopy is uded to study the emission and excitation behaviours of various luminescence centres and their lifetimes. Here the sample is excited by photons (generally in UV range) and the excess energy of the excited state is released through the emission of light which can be detected and recorded for different modes, i.e. excitation, emission and luminescence decay lifetime. A spectrofluorometer is an instrument, which is capable of recording the emission spectrum or both the excitation and emission spectra. The wavelength distribution of an emission measured at a single constant excitation wavelength is an emission spectrum while the dependence of emission intensity, measured at a single emission wavelength, upon scanning the excitation wavelength is the excitation spectrum. The spectrofluorometer can record the luminescence lifetime decay curve with the help of a pulsed excitation source and a fast detector. The fluorescence decay time is obtained by measuring the fluorescence signals at fixed wavelength as a function of time. A decay curve is a spectrum measured within a narrow time-window during the decay of the fluorescence of interest. A pulsed excitation source (pulse duration short in comparison with the excited-state lifetime of the molecule) and a fast detector are the two main requirements for lifetime measurements.

2.2.5.1. Physical principle:

In photoluminescence spectroscopy, at first the species is excited from its ground electronic state to one of the various vibrational states in the excited electronic state by absorbing a photon. Collisions with other molecules cause the excited molecule to lose vibrational energy until it reaches the lowest vibrational state of the excited electronic state. From there the molecule can then drops down to one of the vibrational levels in the ground electronic state. This process will result in the emission of a photon. Since the molecules can drop down into any of the several vibrational levels in the ground state, the emitted photons may have different energies. These processes are often visualised with the Jablonski diagram as shown in Figure 2.22. There are several factors, which can affect the fluorescence intensity. A pictorial representation is given Figure 2.23.

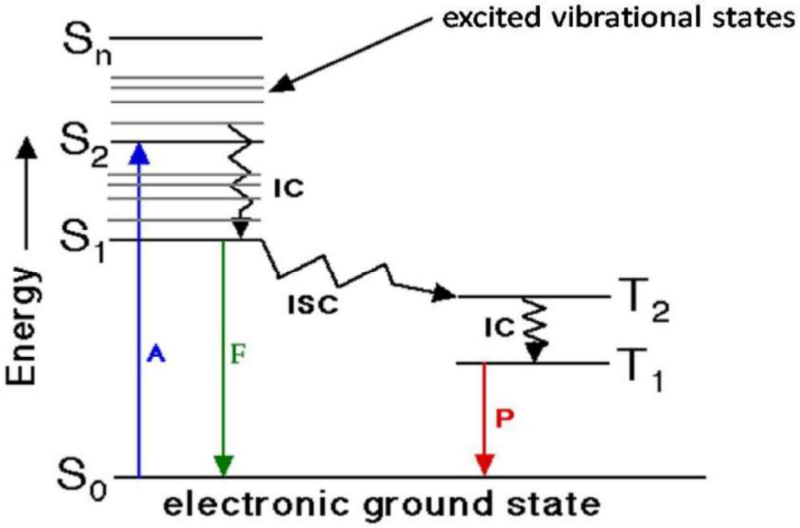

Figure 2.22: A Jablonski diagram shows the possible relaxation processes in a molecule after the molecule has absorbed a photon (A): IC = internal conversion, ISC= intersystem conversion, F= fluorescence, P= phosphorescence

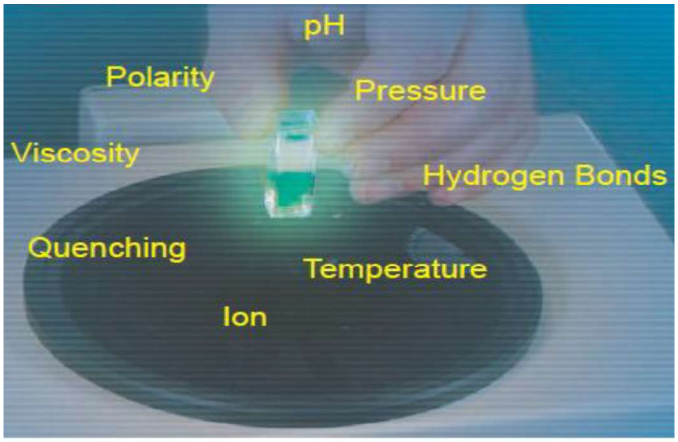

Figure 2.23: *Parameters affecting fluorescence emission*

2.2.5.2. Instrumentation: Excitation and emission spectroscopy

Various light sources may be used as excitation sources including lasers, photodiodes, lamps etc, which produce light photons. At first, the photons impinge on the excitation monochromator. This monochromator selectively transmits light in a narrow range around the specified excitation wavelength. For laser excitation sources, filters may be used instead of a monochromator, or with a monochromator to give high quality monochromatic light. The transmitted light is then allowed to pass through adjustable slits, which control intensity and resolution by further limiting the range of transmitted light. In this way, the filtered light passes into the sample. The emitted light from the excited samples again goes through a filter to prevent the excitation light entering the detector, which results second order peaks. The filtered light then enters the emission monochromator, positioned at a 90º angle from the excitation light path. This setting help to eliminate background signal and minimize noise due to stray light. Again, emitted light is transmitted in a narrow range centred on the specified emission wavelength and exits through adjustable slits, finally entering the photomultiplier tube (PMT). A schematic diagram of a general-purpose spectrofluorometer is given in Figure 2.24. It is possible to record both excitation and emission spectra with most spectrofluorometer. An emission spectrum can be described as the wavelength distribution of an emission measured at a single constant excitation wavelength. Conversely, the dependence of emission intensity, measured at a single emission wavelength, upon scanning the excitation wavelength is described as an excitation spectrum. For an ideal instrument, the directly recorded emission spectra would represent the photon emission rate or power emitted at each wavelength, over a wavelength interval determined by the slit widths and dispersion of the emission monochromator. Similarly, the excitation spectrum would represent the relative emission of the fluorophore at each excitation wavelength. Xenon lamp is used as a source of exciting light in this instrument. Such lamps have high intensity at all wavelengths ranging upward from 250 nm and are very useful. As shown in Figure the instrument is equipped with monochromators to select both the excitation and emission wavelengths. As shown in this schematic, the excitation monochromator contains two gratings, which decreases stray light i.e. light with wavelengths different from the desired one. In addition, Again use of concave gratings, produced by holographic means, in these monochromators further decreases stray light. In order to allow automatic scanning of wavelength both monochromators are motorized. The fluorescence is detected with photomultiplier tubes followed by quantification with the appropriate electronic devices. The output is usually presented in graphical form and stored digitally. Figure 2.25 shows the fluorescence spectrometer used in current studies.

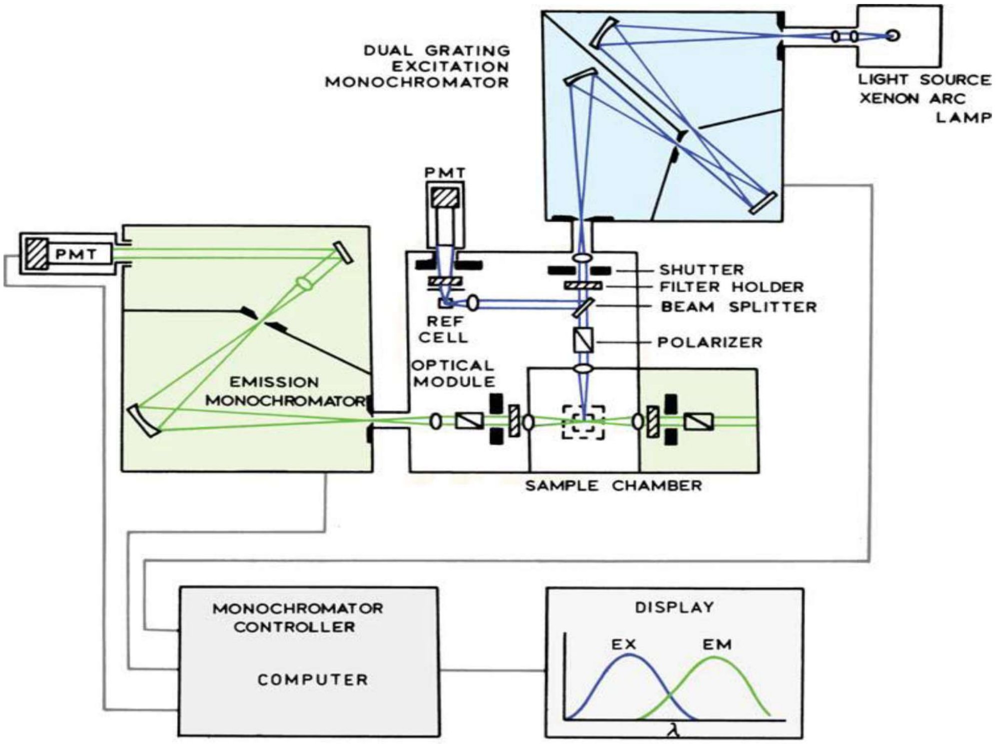

Figure 2.24: *Block diagram of spectrofluorometer* ***[105].***

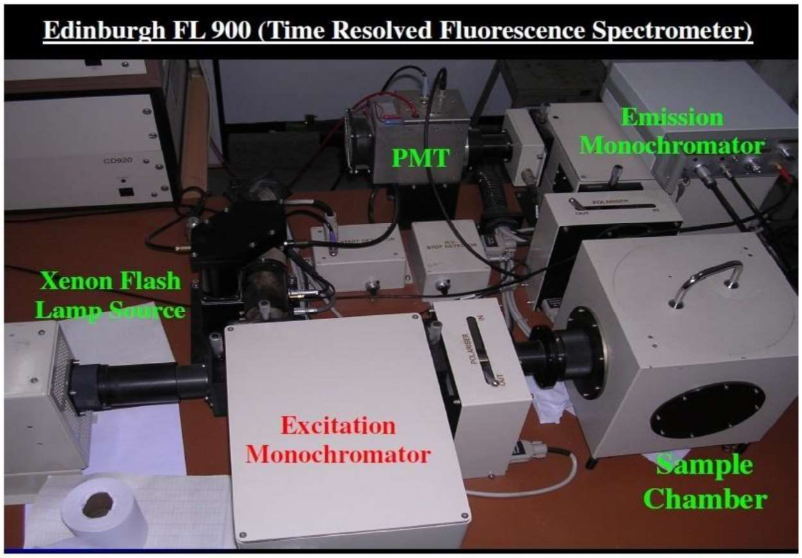

Figure 2.25: *Photograph of the time resolved fluorescence spectrometer*

2.2.5.3. Instrumentation: Luminescence lifetime

Time-correlated single-photon counting (TCSPC) is a well established and a common technique for fluorescence lifetime measurements, it is also becoming increasingly important for photon migration measurements, optical time domain reflectometry measurements and time of flight measurements.

The principle of TCSPC is the detection of single photons and the measurement of their arrival times in respect to a reference signal, usually the light source. TCSPC is a statistical method requiring a high repetitive light source to accumulate a sufficient number of photon events for a required statistical data precision. TCSPC electronics can be compared to a fast stopwatch with two inputs (Fig 2.26a). The clock is started by the START signal pulse and stopped by the STOP signal pulse. The time measured for one START – STOP sequence will be represented by an increase of a memory value in a histogram, in which the channels on the x-axis represent time. With a high repetition rate light source millions of START – STOP sequences can be measured in a short time.

The detector signal consists of a train of randomly distributed pulses due to the detection of the individual photons. There are many signal periods without photons; other signal periods contain one photon pulse. Periods with more than one photons are very rare. When a photon is detected, the time of the corresponding detector pulse is measured. The events are collected in a memory by adding a '1' in a memory location with an address proportional to the detection time. After many photons, in the memory the histogram of the detection times, i.e. the waveform of the optical pulse builds up. The resulting histogram counts versus channels will represent the fluorescence intensity versus time as shown in Figure 2.26b.

Generally, one of the inputs to the TCSPC electronics (either START or STOP) will be a pulse generated by a single photon. Single photons can be detected by photodetectors with intrinsically high gain. The majority of those photodetectors are photomultipliers or micro-channel plate photomultipliers, but also single photon avalanche photodiodes. For statistical reasons it is important to ensure no more than one single photon event per light flash is detected. Multi-photon events will affect the histogram statistics and will yield to erroneous measurement results. (This is known in literature as the "pulse pile-up problem".) In order to ensure that only one photon per light flash is detected; the photon rate is kept low in comparison to the rate of the exciting lamp; usually 5% or lower.

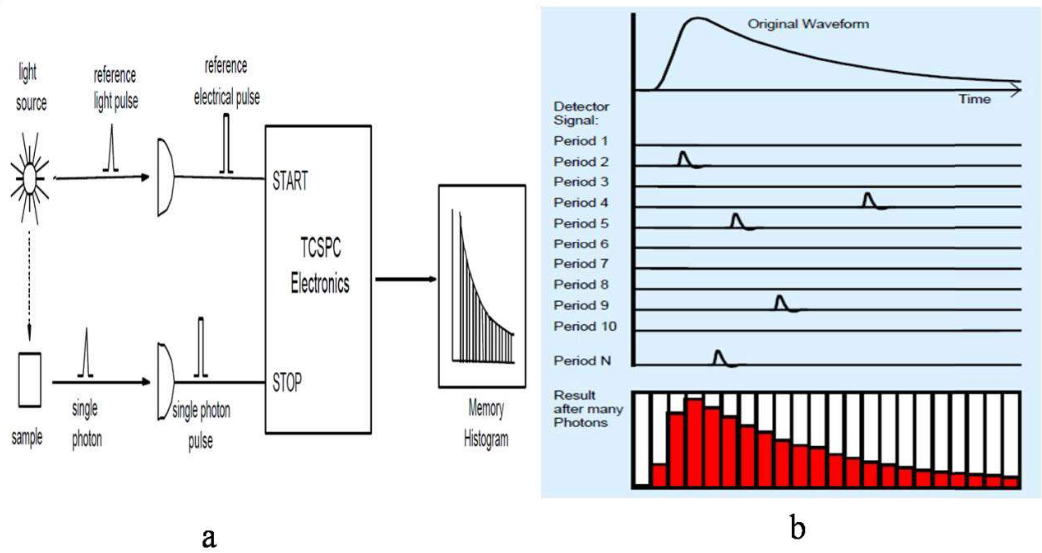

Figure 2.26: ***a)*** *TCSPC - A fast stopwatch with two inputs* ***b)*** *TCSPC Measurement Principal* ***[106]***

The main components for signal processing in TCSPC as shown in Figure 2.27 are constant fraction discriminators (CFD), electrical delays (DEL), the Time-to-Amplitude Converter (TAC), Amplifier (between the TAC and ADC), Analogue to Digital Converter (ADC) and digital memory (Mem).

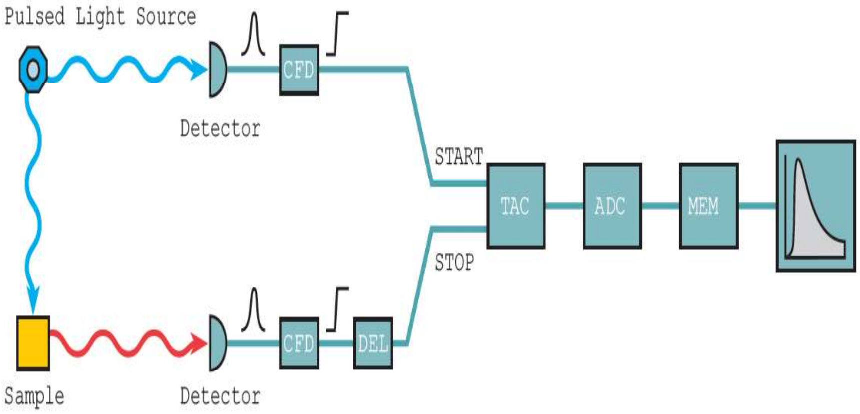

Figure 2.27: *The main components for signal processing in TCSPC* ***[106]***

At the input of the electronics, incoming pulses are evaluated with respect to pulse height. Only pulses higher than a given threshold will be accepted for further signal processing. Thus small amplitude noise pulses are readily eliminated. The constant fraction discriminators on both the START and the STOP input then analyse the pulse shape of the individual pulses. The portion of the incoming (generally negative) pulses with the steepest slope on the leading edge is taken as a criterion for the temporal position. Which portion of the slope is taken will depend on the fraction, the constant fraction delay (or shaping delay), and the zero crossing level. Threshold, fraction, constant fraction delay, and zero crossing level will depend on the type of detector used and need to be matched to the individual detector. At the output of the CFD, pulses are re-shaped to a standard height and shape. They then can be delayed by an electronic shifting delay. This delay will later result in a left or right shift of the entire measurement on the time axis. The TAC is the fast clock, started by the START and stopped by the STOP pulse. The START pulse initiates the growth of a ramp signal. Depending on the arrival time of the STOP pulse the ramp will have a lower or higher height. Once the growth of the ramp has been stopped, the level will remain constant for a defined period. The TAC output pulse can then be amplified, thus effectively stretching the time axis. Minimum and maximum available (amplified) TAC amplitude determine the time range. The amplified TAC output pulse is effectively an analogue pulse of a height corresponding to a measured time of a single START – STOP sequence. For further processing the pulse height will be measured by a digital pulse height measure devise, the ADC. The ADC resolution determines how many discrete time values are possible. All possible measured TAC pulse amplitudes will therefore put into different time bins. The width of the time bin is the ratio of the full time range and the resolution of the ADC in channels. It is the time resolution, usually given in picoseconds / channel or nanoseconds / channel.

The PL data were recorded on an Edinburgh CD-920 unit equipped with M 300 monochromator. The data acquisition and analysis were done by F-900 software provided by Edinburgh Analytical Instruments, UK. A Xenon flash lamp with frequency range of 10–100 Hz was used as the excitation source. Emission spectra for a particular sample were recorded with a lamp frequency of 100 Hz. Multiple scans (at least five) were taken to minimize the fluctuations in peak intensity and maximize S/N ratio. Luminescence lifetime measurements were based on well established Time-Correlated Single-Photon Counting (TCSPC) technique.

2.2.5.4. The C.I.E. Color Space

The CIE 1931 color spaces were the first defined quantitative links between distributions of wavelengths in the electromagnetic visible spectrum, and physiological perceived colors in human color vision. The mathematical relationships that define these color spaces are essential tools for color management, important when dealing with color inks, illuminated displays, and recording devices such as digital cameras. The International Commission on Illumination (CIE) created the CIE 1931 RGB color space and CIE 1931 XYZ color space in 1931. They resulted from a series of experiments done in the late 1920s by William David Wright and John Guild. The experimental results were combined into the specification of the CIE RGB color space, from which the CIE XYZ color space was derived. The CIE 1931 color spaces are still widely used, as is the 1976 CIELUV color space.

Since the human eye has three types of color sensors that respond to different ranges of wavelengths, a full plot of all visible colors is a three-dimensional figure. However, the concept of color can be divided into two parts: brightness and chromaticity. For example, the color white is a bright color, while the color grey is considered to be a less bright version of that same white. In other words, the chromaticity of white and grey are the same while their brightness differs.

CIE tristimulas values X, Y, Z are product of data values for illuminant, reflectance/transmittance of object and sensitivity functions and integration over all wavelengths in visible region .The CIE XYZ color space was deliberately designed so that the Y parameter is a measure of the luminance of a color. The chromaticity of a color is then specified by the two derived parameters x and y, two of the three normalized values being functions of all three tristimulus values X, Y, and Z. The derived color space specified by x, y, and Y is known as the CIE xyY color space and is widely used to specify colors in practice.

$$x = \frac{X}{X+Y+Z}, \; y = \frac{Y}{X+Y+Z}, \; z = \frac{Z}{X+Y+Z} = (1\text{-}x\text{-}y)$$

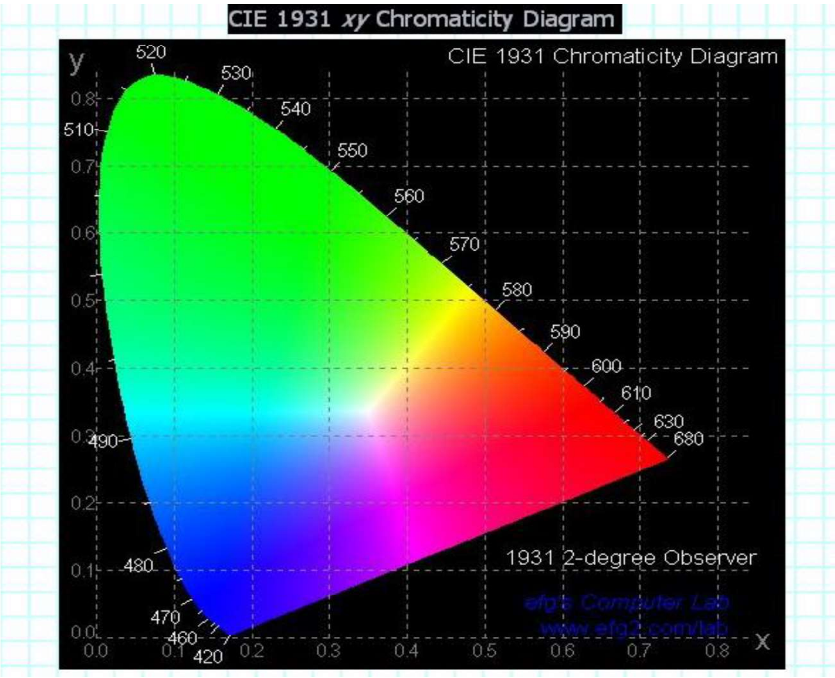

Figure 2.28: CIE xy Chromaticity diagram

Figure 2.28 represents the CIE xy Chromaticity diagram. Following are the features of this diagram

1. Edge marks the wavelengths of visible light and is 'pure' spectral light colors.
2. Other colors are developed by mixing varying amounts of different wavelengths.
3. Purples at the bottom do not have a wavelength associated with them. These purples are non-spectral colors, that is they can only be seen by mixing wavelengths from the two ends of the spectrum.
4. White light is perceived when all three cones are stimulated

Note: Few of the contents on C.I.E. Color Space are taken from Wikipedia.

2.3. DFT calculation methodology

Mn: $SrZrO_3$:

The calculations were performed using the density functional theory (DFT) with the plane wave pseudopotential formalism as implemented in Vienna Ab-initio Simulation Package (VASP). We imposed the generalized gradient approximation (GGA) for the exchange and correlation potentials as parameterized by Perdew, Burke and Ernzerhof (PBE). The projector augmented wave (PAW) potentials were used for the ion-electron interactions including the valence states of Sr (4s, 4p, 5s - 10 valence electrons)), Zr (4s, 4p, 5s, 4d – 12 valence electrons), Mn (3p, 4s, 3d - 13 valence electrons) and O (2s, 2p – 6 valence electrons). In our calculations, the Kohn-Sham single particle wave functions were expanded in a plane wave basis with kinetic energy cutoff 500 eV and it was shown that the results were well converged at this cut off. For orthorhombic $SrZrO_3$ (SZO) structure, optimization was carried out with respect to E_{cut} and k-point meshes to ensure convergence of total energy to within a precision 0.1 meV/atom. The Brillouin-zone (BZ) integrations were performed on an optimized Monkhorst-Pack k-point grid of 12x12x8 for SZO and 4x8x8 for 2x1x1 supercell of SZO. We studied three systems, namely pure $SrZrO_3$, $Sr_{1-x}Mn_xZrO_3$ (SMZO) and $SrZr_{1-x}Mn_xO_3$ (SZMO). For SMZO, one or two Sr^{2+} ions were replaced by Mn^{2+} ions while for SZMO one or two of Zr^{4+} were replaced. We performed spin polarized GGA calculations for Mn doped structures. The total energy of SZO, SMZO and SZMO were optimized with respect to volume (or lattice parameter), b/a, c/a ratio and atomic positions. The structural relaxations (b/a, c/a ratio and atomic positions) were performed for each structure using the conjugate gradient algorithm until the residual forces and stress in the equilibrium geometry were of the order of 0.005 eV/Å and 0.01GPa, respectively. The final calculation of total electronic energy and density of states (DOS) were performed using the tetrahedron method with Blöchl corrections. The strong on-site Coulomb repulsion among the Mn 3d electrons has been considered by employing a rotationally invariant method proposed by Dedarev *et al.* along with PBE form of GGA (GGA+U). In this method, the total energy depends on the difference between the Coulomb, U, and exchange, J, parameters. The U_{eff} which is known as U-J parameter, adjusts the electron correlation contribution (on-site columbic effects), was set at 5.04 eV for Mn-3d electrons.

$MgAl_2O_4$:

The $MgAl_2O_4$ face-centered cubic normal and inverse spinel phases are studied using the Vienna ab initio simulation package (VASP), which calculates the Kohn–Sham eigenvalues within the framework of DFT. The calculations have been performed with the use of the generalized gradient approximation (GGA) while the exchange and correlation energy per electron have been described by the Perdew-Burke-Ernzerhof (PBE) parametrization[40]. The interaction between electrons and atoms are described by means of the projector augmented-wave (PAW) method using Mg (3s – 2 valence electrons), Al (3s, 3p - 3 valence electrons) and O (2s, 2p – 6 valence electrons) as implemented in the VASP package. For normal and inverse cubic spinel unit-cell as well as structures comprises of oxygen vacancy (neutral and charged), optimization was carried out with respect to E_{cut} and k-point meshes to ensure convergence of total energy within a precision 0.1 meV/atom. A Monkhorst-Pack k-space sampling of 13x13x13 for normal spinel and 7x7x7 for inverse spinel in reciprocal space for the brillouin zone integration and a cutoff energy (E_{cut}) of 500 eV for the plane wave basis set was used. The total energy of normal and inverse cubic spinel unit-cell as well as structures comprises of oxygen vacancy (neutral and charged) were optimized with respect to volume (or lattice parameter) and atomic positions. Conjugate gradient algorithm was used for the unit-cell relaxations until the residual forces and stress in the equilibrium geometry were of the order of 0.005 eV/Å and 0.01GPa, respectively. The final calculation of total electronic energy and density of states (DOS) were performed using the tetrahedron method with Blöchl corrections.

MgO:

All the electronic structure calculations of various defects in MgO are performed by spin-polarized plane wave based density functional theory (DFT) as implemented in Vienna Ab-intio Simulation package (VASP). The interaction between electrons and ions is described using projector augmented wave (PAW) method which includes the valence states of Mg (3s – 2 valence electrons) and O (2s, 2p – 6 valence electrons). Generalized gradient approximation (DFT-PBE) is used for the exchange-correlation potential in the form of Perdew-Burke-Ernzerhof (PBE). A 2×2×2 supercell (64 atoms) is employed to study defect formation in MgO. For calculations of the unit cell (8 atoms) and 2×2×2 supercell (64 atoms), the integration over the Brillouin zone is carried out on 16×16×16 and 8×8×16 k-point meshes generated using the Monkhorst–

Pack method, which are both proven to be sufficient for energy convergence of less than 0.1 meV/atom. A cutoff energy (E_{cut}) of 500 eV for the plane wave basis set is used. For cubic MgO unit-cell, optimization of E_{cut} and k-point meshes are carried out to ensure convergence of total energy to within a precision 0.1 meV/atom. The total energy of MgO unit cell as well as supercells are optimized with respect to volume, shape and atomic positions as permitted by the space group symmetry of the crystal structure. The structural relaxations are performed for each defect structure using the conjugate gradient algorithm until the residual forces and stress in the equilibrium geometry were of the order of 0.005 eV/Å and 0.01GPa, respectively. The final calculation of total electronic energy and density of states (DOS) were performed using the tetrahedron method with Blöchl corrections.

Chapter 3

Defects mediated optical properties in MgO, $MgAl_2O_4$ & $ZnAl_2O_4$

3.1. Introduction

In an inorganic matrix, although defects are often considered as imperfections and may degrade various material properties, sometimes they may also lead to some attractive materials properties such as optical, magnetic, catalytic, energy conversion etc. [**107-111**]. It is now widely accepted that defects play great roles in determining the optical properties of wide band gap crystalline materials, which have various potential technological applications such as adsorbents, sensors, catalysis, refractory material, paint, fluoride remover, optoelectronics and luminescence devices **[112-115]**. Defect induced properties in material have now become hot research areas. Examples are photocatalysis properties in TiO_2 **[116]**, electronic and magnetic properties in graphene [**117,118**], opto-electronic properties in indium sulfide **[119]**, plasmonic properties in silicon nanocrystal and CdO:Dy **[120,121]**, electrochemical properties in $LiFePO_4$ **[122]**, optical properties in activator free Ag_2Se, and MoS_2 **[123,124]**, electric and ferroelectric properties in CuO:Fe **[125]** etc. When the defects induced optical properties in oxides matrices is considered, different types of electronic states within the band gap of the material are found to be responsible for the emission behavior, while for the magnetic properties, paramagnetic vacancies such as F^+ centres, V^- centres etc. are mainly responsible. Various activator free materials such as ZnO, TiO_2, SnO_2, CuI, Al_2O_3, MgO **[126-131]** etc. are reported to show defect induced photoluminescence (PL) characteristics. Recently, alumina has been found to show various kinds of optical properties such as photoluminescence (PL), thermo luminescence (TL) and optically stimulated luminescence (OSL), both in pure and doped α-Al_2O_3 **[130,132-135]**. In these entire luminescence phenomenon, presence of defect centres e.g. F centres (oxygen vacancies occupied by two electrons), F^+ centres (oxygen vacancies occupied by one electron), their aggregates such as F_2 centres (two associated oxygen vacancies occupied by four electrons) and the F_2^+ centres (two associated oxygen vacancies occupied by three electrons) are reported to be mainly responsible and sometimes they are also inter-convertible using light irradiation.

Another wide band gap insulator MgO with band gap energy of 7.8 eV has shown some exceptional optical, magnetic and electronic properties in recent years **[131,136-138]**. Various structural defects such as oxygen vacancies, Mg vacancies (F-centre defects and V centre defects) and interstitials defects are reported to be responsible for the Photoluminescence (PL) properties of MgO nanomaterials

[**135,139, 140**]. In spite of being a wide band gap material [**141**], presence of these intrinsic/extrinsic defects create various electronic states within the band gap, which reduces the photon excitation energy of the material significantly well below the band gap energy **[142]**. Uchino group recently **[143]** has reported a more detailed investigation on the trapping and recombination processes of the F-type centres (F & F+ centre) and their lasing property in MgO microcrystals. However, there is still some controversy about these defects regarding their position within the band gap and interaction with the excitation **[144, 145]**. In this context, Rinke *et al.,* have shown an agreement between the calculated and the experimentally observed absorption and emission spectra of F^0 and F^+ centres in MgO **[146]**. However, various other defects e.g. doubly charged oxygen vacancies (F^{2+} or V_O^{+2}), cluster of F^+ centres such as F_2^{2+}, F_2^{1+}[pair of adjacent F and F^+ centres such as ($F^+ + F^+$) or ($F + F^+$)], cationic vacancies (V_{Mg}^{-2}), hole trap at cationic vacancies [$V_{Mg}^{-1} = V_{Mg}^{-2} + h(+)$], interstitial oxygen ($O_i^0$,O_i^{-1} & O_i^{-2}) and Schottky defects (forms when oppositely charged Mg^{2+} and O^{2-} ions leave their lattice sites and form MgO molecule) etc. also exist in MgO. Information regarding their electronic structures and correlation with the optical properties is still missing in literature. Thus, a correlation study of the observed optical properties with the DFT calculated electronic states due to various defect centres in MgO would be very much helpful to understand the defect induced optical properties.

ZnO is another wide-band gap semiconductor, which has also attracted the attention of researchers for several decades due to its many important applications, especially in optics and optoelectronics **[147,148]**. The compound showed emission bands both in the ultraviolet (UV) and visible (green, yellow, blue and violet) regions in the photoluminescence (PL) spectroscopy. The UV emission is generally considered as the characteristic emission of ZnO,**[149,150]** and attributed to the band–edge transition or the exciton combination **[151].** On the other hand, various intrinsic or extrinsic defects such as oxygen vacancies **[152,153]**, Zn interstitial etc. **[154]** are universally considered to be responsible for the bands in the visible regions in ZnO.

$MgAl_2O_4$ and $ZnAl_2O_4$ may be assumed as a combination of MgO &Al_2O_3 and ZnO & Al_2O_3. The emission characteristic will therefore be always a complex one. In $MgAl_2O_4$ various factors such as stoichiometry, structural disorder, impurities, thermal/mechanical treatment and sintering or annealing conditions can lead to creation of various kinds of defects **[155]**. For example in pure stoichiometric $MgAl_2O_4$, three types of intrinsic defects can be present which are misplaced atoms, Schottky and Frenkel defects and approximately uo to 30% of cation antisite disorder **[156,157]**.

The antisite defects can be expressed according to Kroger–Vink as:

$$\left[Mg_{Mg}^{X}\right] + [Al_{Al}^{X}] = \left[Al_{Mg}^{\bullet}\right] + [Mg_{Al}^{'}] \qquad (3.1)$$

Because of cation disorder few other defects also exist and can be described by following equation **[156]**:

$$\left[Mg_{Mg}^{X}\right] + [V_{Al}^{'''}] = [Mg_{Al}^{'}] + \left[V_{Mg}^{''}\right] \qquad (3.2)$$

$$[Al_{Al}^{X}] + \left[V_{Mg}^{''}\right] = \left[Al_{Mg}^{\bullet}\right] + [V_{Al}^{'''}] \qquad (3.3)$$

Now in order to charge neutrality of the samples due to these antisite defects formation of various kinds of defect centres viz. V-centre, F-centre and F^+ centre is also possible. All of these defects may act as a colour centres and give rise to various attractive optical properties. Specially defects induced optical properties in insulators are of renewed interest because of the emergence of colour centre lasers. As far as defect related optical properties in $MgAl_2O_4$ (MA) spinel is concerned report due to cations disorder and oxygen vacancy (F^+ centre) is present in literature **[158]**. However, emissions due to F, F_2^{2+}, F^+ centre surrounding each of the cations and due to different shallow and deep states in the visible and near infrared (NIR) region are yet to be explored.

Optical properties of another aluminates based spinel compound i.e. $ZnAl_2O_4$ (ZA) spinel with different band gap energy (3.8 eV) is also yet to be explored elaborately. As far as optical properties of undoped $ZnAl_2O_4$ is concerned, very few reports exist in the literature. In this context, Wang *et al.,* have reported ZA to be blue emitting phosphors prepared from different aluminum salt **[159]**. Cornu *et al.,* have observed a change in the emission profile of ZA compound when annealed at higher temperature through the co-precipitation synthetic route and showed ZA to be a potential sensor material **[160]**. Although these emission profiles are attributed to different oxygen vacancies, antisite defects and interstitial Zn, concrete evidence is still lackingin literature and a detailed investigation of various defects induced emission behavior is much needed in ZA to understand its optical properties.

In present thesis, we have chosen various activator free oxide matrices such as MgO, $MgAl_2O_4$ and $ZnAl_2O_4$. In this chapter, the main focus will be on characterization of various defect centres in these matrices and their correlation with the multicolour emission behaviors. Generally, defects induced emission phenomena are very complex in nature, which often result very broad emission spectra consisting of different defects related emission components. Therefore, it is very much essential to isolate each and individual defect related emission component from the complex spectra. This has been done by lifetime and Time Resolved Emission Spectra (TRES) study. Monitoring these individual emission profiles with changing synthesis condition was also carried out in order to optimize the luminescence intensity. From the DFT calculated density of states (DOS) we have successfully established a correlation between the electronic structures inside the band gap and various emitting colour components arising due to different defect states.

3.2. Synthesis, optical and magnetic properties of MgO

3.2.1. Synthesis, characterization and morphology

MgO compounds were synthesized by the thermal decomposition of magnesium oxalate (MO) precursor [**161**]. At first MO was synthesized through sol-gel method using magnesium nitrate hexa hydrate [$Mg(NO_3)_2.6H_2O$] (98%, AR grade) and oxalic acid (98%, AR grade) as precursors in 1:1 molar ratio. Two clear solutions of [$Mg(NO_3)_2.6H_2O$] and oxalic acid were prepared by dissolving them separately in ethanol in separate beakers. These two solutions were then mixed in another beaker with continuous stirring for 2 hours until a thick white gel was obtained. This gel was then heated at 100 ^{0}C for 8h followed by grinding when a fine powder of magnesium oxalate was obtained. This oxalate product was then allowed to decompose at 600 ^{0}C for 6 h in a furnace after which the desired product magnesium oxide (MgO-600) was obtained followed by characterization using XRD and SEM. The compound was further annealed at higher temperature such as 800 ^{0}C (MgO-800) and 1000 ^{0}C (MgO-1000).

Figure 3.1 represents the XRD patterns of different MgO compounds viz. MgO-600, MgO-800 & MgO-1000, prepared after annealing at different temperatures. The XRD patterns correspond to cubic (NaCl-type) periclase phase of MgO with known lattice parameter a = 4.211Å [JCPDS 45-946]. The diffraction peaks of MgO-600 are somewhat broader and when the annealing temperature increased, they become sharper.

We have also determined the crystallite size from the X-ray line broadening technique using the Debye–Scherrer formula: $\boldsymbol{t} = \frac{\boldsymbol{k\lambda}}{\sqrt{(B_S^2 - B_M^2)}\,\cos\boldsymbol{\theta}}$ (3.4)

where t is the crystallite size, $\boldsymbol{\lambda}$ is the used wavelength of Cu Kα_1 radiation (1.5418 Å), $\boldsymbol{\theta}$ is the angle of the corresponding Bragg reflection, which was considered to calculate the FWHM. The full width at half maximum (FWHM) of the peaks at 2θ = 42.94 and 2θ = 62.39 were calculated after fitting them by employing the standard pseudo Voigt function. B_S and B_M are the FWHM (in radians on the $2\boldsymbol{\theta}$ scale) of selected diffraction peaks from the sample and reference (silicon), respectively, and k is a Scherrer constant, whose value is 0.94 when the crystallites are spherical and for non spherical crystallites the value of k is 0.89 as given by Klug and Alexander [**162**]. To calculate the value of B_M from the FWHM, the highest-intensity peak of pure silicon at $2\boldsymbol{\theta}$ = 28.41 is considered. The instrumental broadening was taken care of by subtracting the contribution from silicon most intense peak from the one due to sample. The average crystallite sizes determined from the two peaks are 27.5±0.2 nm for MgO-600, 33.7±0.4 nm for MgO-800 and 65.4±0.3 nm for MgO-1000. Thus with increasing annealing temperature, the average crystallite sizes were found to increase. Figure 3.2-a1 and 3.2-b1 represent the two SEM micrographs of MgO-600 and MgO-1000 compounds respectively, which showed flake like morphology oriented in clustered vertical geometry and each particle is an agglomerate of crystals. At higher annealing temperature (i.e. MgO-1000) the flakes start disintegrating into crumbled powder and agglomerating in random orientation. Image J software was used to measure the average particle size of the samples. The particle size distributions histogram of the two different thermally annealed compounds viz. MgO-600 and MgO-1000 are shown below their corresponding SEM images as represented by Figure 3.2-a2 and Figure 3.2-b2. The histograms clearly show that for MgO-600, majority of the particles have size in the range of 0.5-0.7 μm while in case of MgO-1000, the size of the particles becomes bigger with higher frequency in the range of 1.0-1.4 μm. The larger size of the particles observed in SEM compared to that calculated from XRD data is due to agglomeration of several crystallites. In true sense a crystallite is considered as a single crystal and in a particle several such crystallites are arranged in a random fashion in the sense of different lattice panes. This agglomeration of randomly oriented crystallites is called the particle or grain. Since XRD sees only the lattice planes, it gives information about crystallite size only.

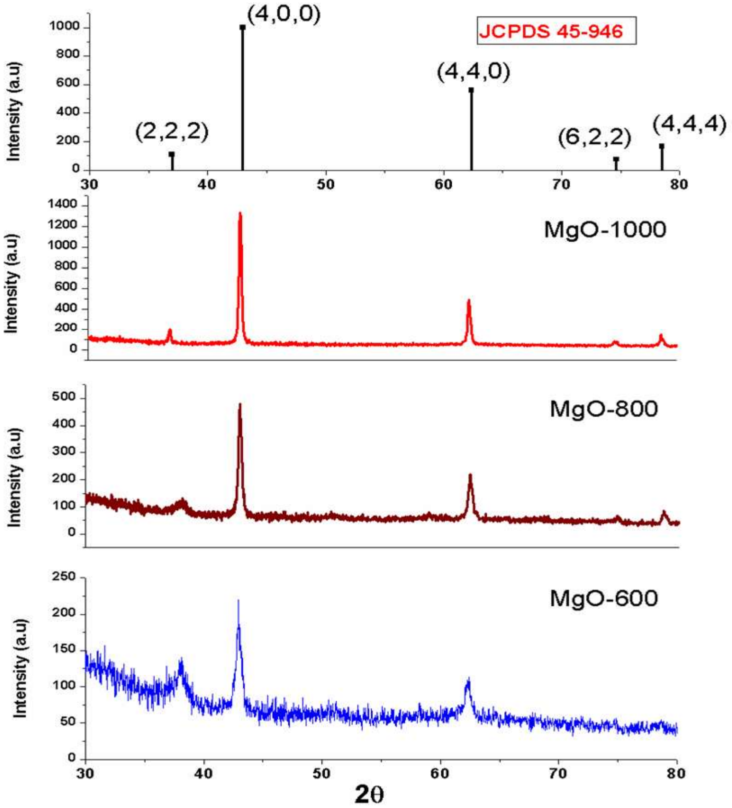

Figure 3.1. *XRD patterns of different temperature annealed MgO compounds: MgO-600, MgO-800 and MgO-1000* ***[161]***.

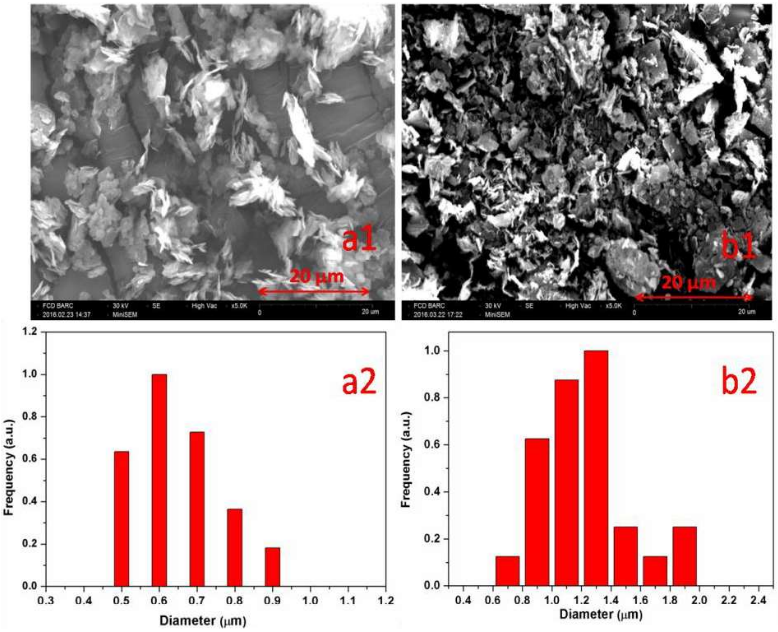

Figure 3.2. *(**a1**) SEM images of MgO-600 and (**a2**) corresponding size distribution histogram.(**b1**) SEM images of MgO-1000 compounds and (**b2**) corresponding size distribution histogram **[163]**.*

3.2.2. Absorption spectroscopy

Figure 3.3 represents the UV–Visible spectrum of MgO-600, MgO-800 and MgO-1000 in the reflectance mode. Due to restriction of the lower spectral detection limit of the UV–vis spectrophotometer, any absorption or reflectance below 200 nm cannot be detected. Presence of several absorption peaks in the UV and visible region indicates the existence of several defects and low coordinated cations and anions on the surface, interface, etc. [**140**]. For example the excitation at ~240 nm and ~ 250 nm are attributed to F$^+$ and F centre while the absorption at 207 nm is due to the excitation of 5 coordinated surface anions while s respectively [**164,165**]. The absorption peak at 313 nm can be ascribed to the F$_2^{2+}$ centres [**164**] while that at 450 nm is due to the transition of a four-coordinated F centre [**166**]. Annealing of the defect centres with increasing the annealing temperature is reflected in the net decrease in absorbance of the concerned defect centres. The negative value of absorbance is due to error associated with the instrument during the base line correction. However, since the all the datas are collected in the same set up, we can compare the data to each other for any changes.

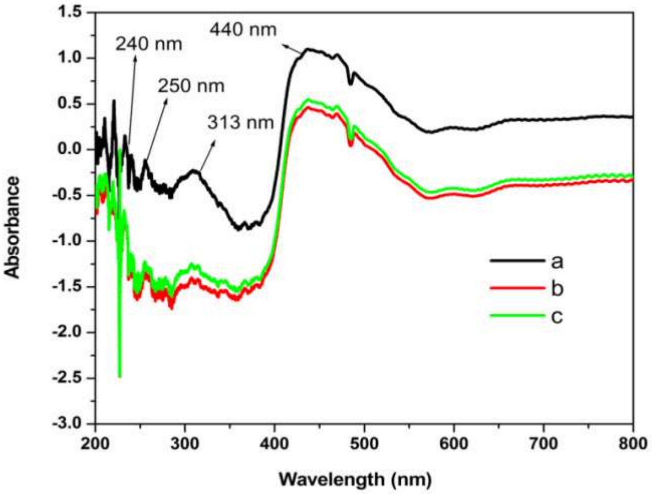

Figure 3.3. *UV–Visible spectrum (in reflectance mode) of a) MgO-600, b) MgO-800 and c) MgO-1000* ***[161]***

3.2.3 Excitation Spectroscopy

Figure 3.4-a represents the photoluminescence excitation (PLE) spectrum of MgO-600 at λ_{em}= 540 nm. Various intense lines near about 230, 247, 258, 271, 285, 297, 310 and 345 nm are found in the spectra which clearly indicates presence of different type of defect states inside the band gap. The peaks in the 230-270 nm range are assigned to different type of F and F^+ centre **[165, 166]** while peaks at 285, 310 and 340 nm can be attributed to their aggregates such as $F_2$and F_2^{2+} centres [**165**].

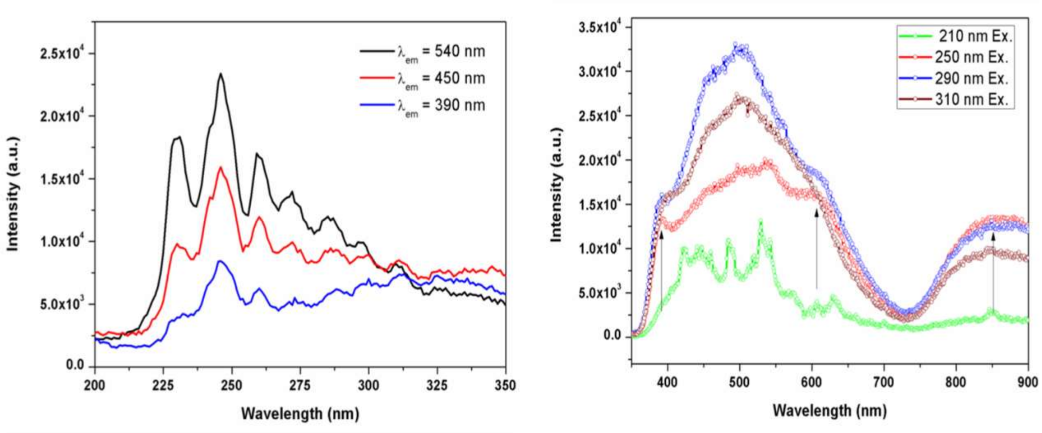

a

b

Figure 3.4. a) *Excitation spectra of Mg-600 at λ_{em} = 540 nm and b) Emission spectra of MgO-600 at different excitation wavelengths (viz. λ_{ex} = 210 nm, 250 nm, 290 nm & 310 nm)* ***[161]***

3.2.4 Emission Spectroscopy

The emission spectra at different excitation wavelength are presented in **Figure 3.4-b**. The higher intensity of the emission spectra at 250 nm excitation was due to photo conversion process of the F centre followed by the equation F + hυ ↔ F^+ + e , as reported earlier **[139-141].** The detail explanation will be given later in this report. Now in present case since the excited state is energetically close to the conduction band **[146]**, the released electron in this process may prompt into the conduction band and thereby behaves as a free carrier. Being free, the electron may recombine with different types of positively charged defect centres in addition to the newly formed F^+ centres **[146]**. Thus different electronic transitions from the conduction band (CB) to the empty ground electronic states of positively charged F- and F_2-type centres can be correlated with the observed emission components. Recombination of a hole in the valence band (VB) with the filled electron in the electronic states may also responsible for some emission behaviors. Therefore, an understanding about all the emitting colour components due to various defect centres in MgO might is achievable by considering those special recombination processes and may also help to remove the long standing contradiction regarding their origin.

Therefore since in present case our main interest is on the photo conversion process of the F centre at and its consequence on the different defect induced emission characteristics, all the emission spectra are recorded at excitation wavelength of λ_{ex}= 250 nm (≈ 247 nm). Figure 3.5 shows the room temperature PL spectra of MgO-600, MgO-800 and MgO-1000 compounds where the intensity in some regions was found to be decreased when the samples were annealed at higher temperatures due to decrease in concentration of the defect states responsible for the emission at those wavelength regions. More decay in intensity was observed in the near infrared (NIR) region (750-900 nm) and orange-red (605 nm) region while intensity of the blue region (450 nm) was found to decrease for MgO-800 followed by increase in case of MgO-1000. The broad emission profiles of the compounds clearly indicate the existence of several colour centres in the MgO matrix, each having individual emission maxima and in combination give rise to a broad profile. In Figure 3.5, such emission peaks with their λ_{max} around 390 nm, 450 nm, 490 nm, 540 nm, 605 nm, 680 nm and 850 nm are shown by arrows. To get a clear picture of these emission components, life time measurement and time resolved emission spectroscopy (TRES) studies were carried out.

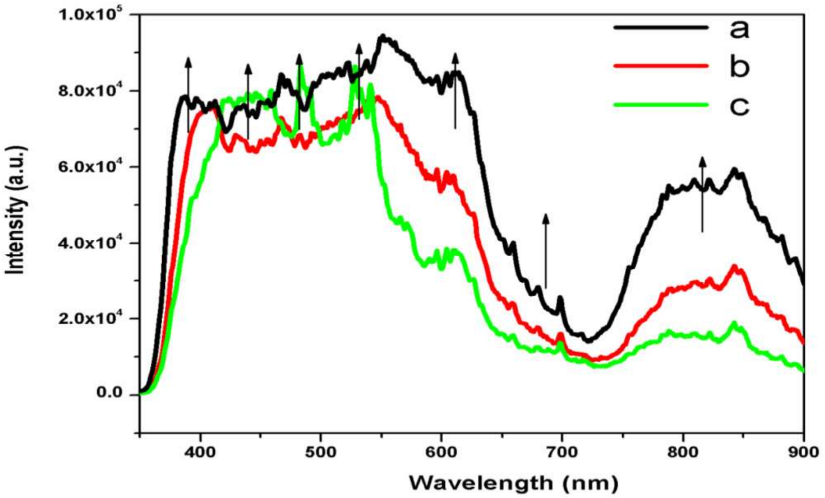

Figure 3.5. *Emission spectra of a) MgO-600, b) MgO-800 and c) MgO-1000 at λ_{ex} = 250 nm. Arrows show the peak position of different emitting components, which may slightly shift towards right hand or left hand side at different annealing temperature.* ***[161]***

3.2.5 Lifetime Study

Fig. 3.6 shows some of the luminescence decay profiles of MgO-600, recorded at different emission wavelengths viz., λ_{em} = 390, 450, 490, 540 nm at an excitation wavelength of λ_{ex} = 250 nm. Decay profiles at λ_{em} = 605, 680 and 850 nm are given in reference **[161]**. Most of the decay curves were fitted into a mono or multi-exponentials using the following decay equations 3.5, 3.6 & 3.7

$$I(t) = A_0 + A_1 \exp(-t/\tau^1) \tag{3.5}$$
$$I(t) = A_0 + A_1 \exp(-t/\tau^1) + A_2 \exp(-t/\tau^2) \tag{3.6}$$
$$I(t) = A_0 + A_1 \exp(-t/\tau^1) + A_2 \exp(-t/\tau^2) + A_3 \exp(-t/\tau^3) \tag{3.7}$$

Where t is the time, and τ^1, τ^2 and τ^3 are decay time values for exponential components and A_0, A_1, A_2 , A_3 are scalar quantities obtained from the decay curve fitting. The multi-exponential behavior of some of the decay profiles indicates that there might be an overlap to the λ_{em} either by the preceding or by the next emission band or by both bands, which leads to multi exponential decay equation instead of mono exponential. In those cases we have considered only that life time value, which has the highest percentage of contribution. Thus, the decay times for various colour components are given in Table 3.1

Table 3.1: Lifetime values of MgO-600 at different emission wavelength and their respective contributions. **[161]**

Wavelength (nm)	**τ** (μs)
390	11.22
450	13.54
490	212.2
540	82.48
605	15.09
680	362
850	13.23

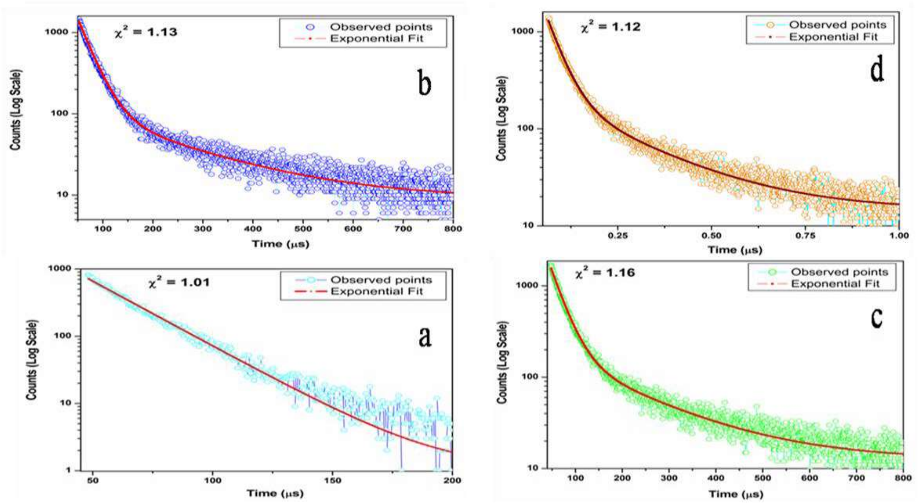

Figure 3.6. *Decay profiles of the MgO-600 compound at λ_{ex} = 250 nm and at different emission wavelength viz. a) 390 nm, b) 450 nm, c) 490 nm & d) 540 nm*

3.2.6 Time Resolved Emission Spectroscopy (TRES)

Figure 3.7 represents the TRES spectra at different delay times such as 2 μs, 20 μs, 40 μs, 100 μs, 200 μs, 500 μs and 900 μs, with a constant integration time of 1 ms while Figure 3.8 shows the TRES spectra of individual emission components derived from Figure 3.7. Mostly the excited species are fully decayed at an average time that is approximately three times of their respective lifetime (3τ). Therefore, at the very initial of the decay i.e. at low delay time such as at 2 μs, it is assumed that none of the colour components will be completely decayed since none of them have lifetime below 2 μs as given in Table-3.1. However, at higher delay time, the short-lived components were decayed first followed by the long-lived ones. From Table 3.1, the different colour components can be arranged in the increasing order of their lifetime as 11.22 µs (390 nm), < 13.23 µs (850 nm) < 13.54 µs (450 nm) < 15.09µs (605 nm) < 82.48 µs (540 nm) < 212.2 µs (490 nm) < 362 µs (680 nm) etc. Hence in the time interval of 2 -20 µs, the species with lifetime values 11.22 µs, 13.23 µs, 13.54 µs and 15.09 µs will start to decay. The observed decay in intensity in the 390 nm, 450 nm, 605nm and 850 nm regions also support this as we increase the delay time from 2 µs to 40 µs, as shown by Figure 3.7. Again in the time interval of 2 -20 µs, the 390 nm colour component will be decayed more compared to others since due to its lowest lifetime i.e. 11.22 µs. On contrary, in the next time interval i.e. 20-40 µs, the other components such as 450, 605 and 850 nm that have comparatively higher lifetime will be the prominent decaying components. This is also reflected in the Figure 3.8a, where we have subtracted the TRES spectra at 2 µs delay time with that at 20 µs and in Figure 3.8b where the TRES spectra at 20 µs delay time was subtracted with that at 40 µs delay time. For further understanding, gaussian fitted spectra of Figure 3.8a and Figure 3.8b are provided in Figure 3.9.

From Figure 3.9, we can see that in the time interval of 2-20 µs, the P_1 (~390 nm) component was decaying more in comparison to the P_2, P_5 and P_7 while in the time interval of 20-40 µs, the contribution of P_1 was negligible and the main decaying components are P_2, P_5 and P_7. The next long-lived colour component is 540 nm (82.48 µs) and in the time interval of 100 -300 µs, we have seen a comparatively more decrease in intensity in this wavelength region, as shown in Figure 3.8. The next colour component with higher lifetime is 490 nm (212.2 µs) and in the time interval of 300 - 600µs, we can see a decrease in intensity in the respective wavelength region in Figure 3.8. Here it is necessary to mention that in the 100 -300 µs time interval, along with 540 nm, the 490 nm species are also decaying and the resulting TRES will compose of both the 490 and 540 nm with the major contribution from the latter. This is shown by the Gaussian fitted spectra in Figure 3.10, which showed that P_3 (~ 490 nm), P_4 (~ 540 nm) and P_5 (~605nm) are major decaying component in the 100-300 µs time interval and the major contribution is coming from P_4 (~ 540 nm). However, in the higher decay time interval such as in the 300 -600 µs, the TRES spectra will have major contribution from P_3 (~ 490 nm) emission as shown by Gaussian fitted spectra in Figure 3.10. Along with $P_{3,}$ rest of the P_4 (~ 540 nm) components have also been found to be decayed in this time interval. No P_6 (~680nm) component was found to decay due to its highest lifetime value. Now at higher delay time such as at 900 µs, a constant decrease in intensity of the P_3 (~ 490 nm) emission component compare to that of P_6 (~680nm) component can be seen in Figure 3.7g. One Gaussian fit TRES spectra at 800 μs is presented in Figure 3.11a which clearly shows presence of two components P_3 (~ 490 nm) and P_6 (~ 680 nm) at higher delay time with the major contribution coming from P_6 (~ 680 nm). Gaussian fit of Figure 3.8f is shown in Figure 3.11b which showed the TRES spectra of 540 nm emission. Thus, all these Gaussian fitted spectra support those emitting components.

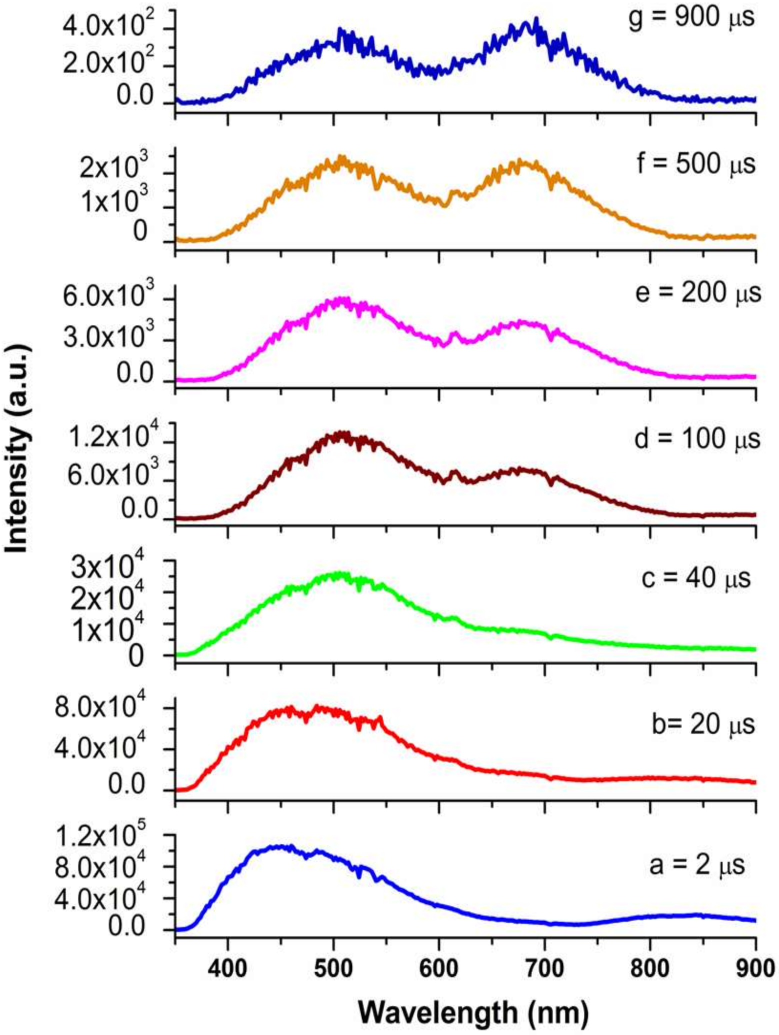

Figure 3.7. *TRES spectra at different time interval* ***[161]***

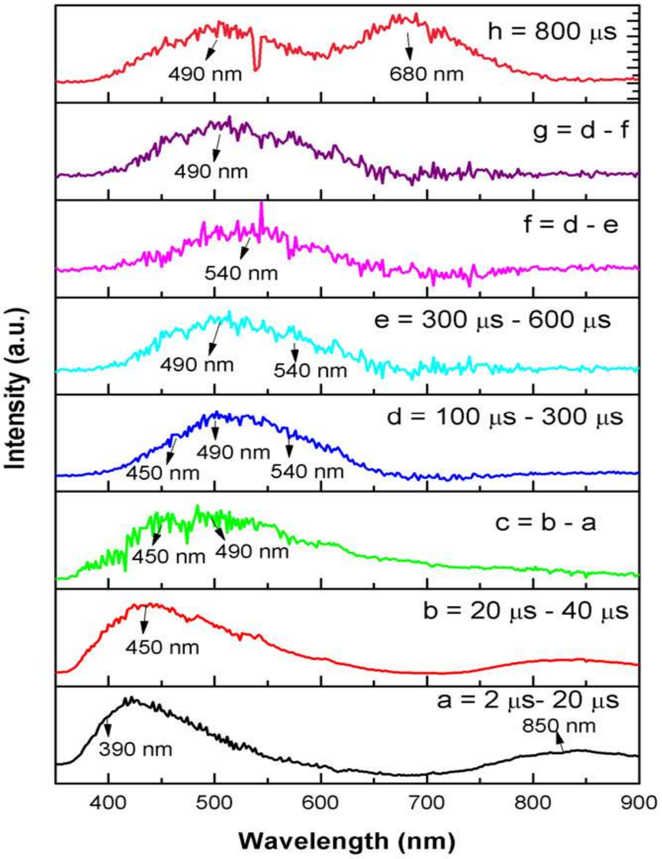

Figure 3.8. *TRES spectra due to different colour components.* ***[161]***

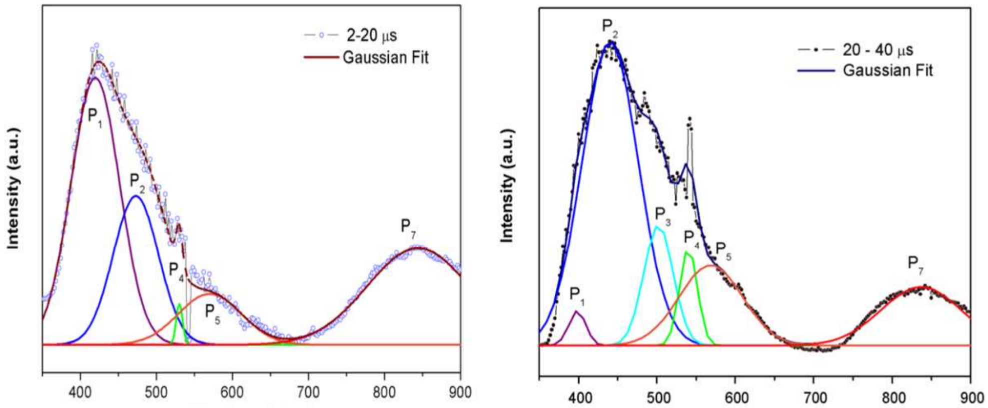

Figure 3.9. *Gaussian Fitted TRES spectra at 2-20 μs and 20-40 μs time interval* ***[161]***

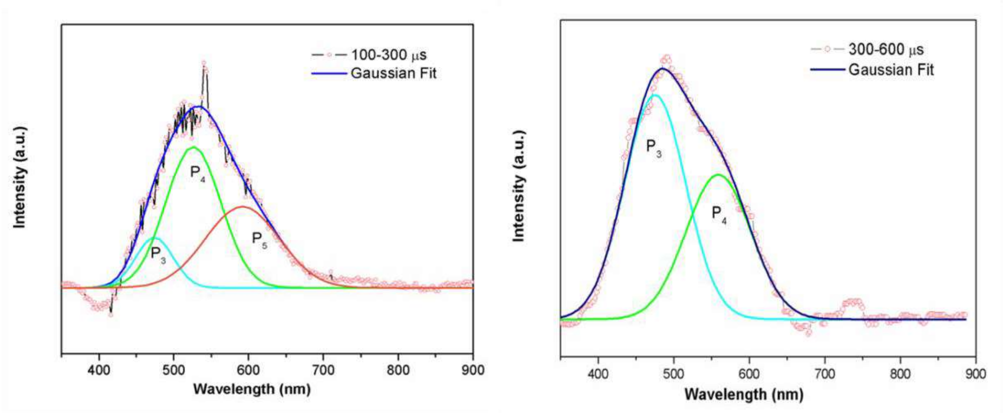

Figure 3.10. *TRES at 100-300 μs and 300-600 μs time interval* ***[161]***

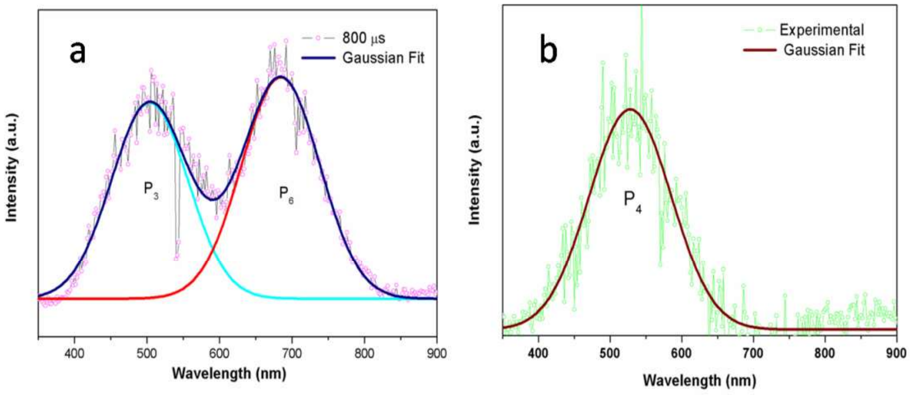

Figure 3.11. ***a)*** *TRES at 800 μs &* ***b)*** *Gaussian Fit of TRES in the Figure 3.8f* ***[161]***

Thus from the TRES study, we have successfully isolate the different colour components viz. 390, 450, 490, 540, 605, 680 and 850 nm from the complex emission spectra. Since the luminescence processes involve Gaussian line broadening mechanism, the emission curves of MgO-600, MgO-800 and MgO-1000 compounds were deconvoluted and decomposed to different colour components, which are violet at $\lambda_{max} \approx 390$ nm (P_1), indigo at $\lambda_{max} \approx 450$ nm (P_2), blue at $\lambda_{max} \approx 490$ nm (P_3), green at $\lambda_{max} \approx 540$ nm (P_4), Orange at $\lambda_{max} \approx 605$ nm (P_5) , orange-red at $\lambda_{max} \approx 680$ nm (P_6) and NIR region at $\lambda_{max} \approx 850$ nm (P_7), as shown in Figure 3.12. From the deconvoluted spectra in Figure 3.12, several observations can be made on these individual emission components. The intensity of the P_1 band was found to decrease while that of P_2 to increase compared to each other. Later in this chapter, we will show that this increase in P_2 intensity will be very much useful to draw a conclusion on defect induced magnetism behavior. The other colour components where a prominent decrease in peak intensity was found are P_3, P_5 and P_7 respectively. Now to understand the origin of all these defects induced colour components we have to consider the electronic structures inside the band gap of MgO.

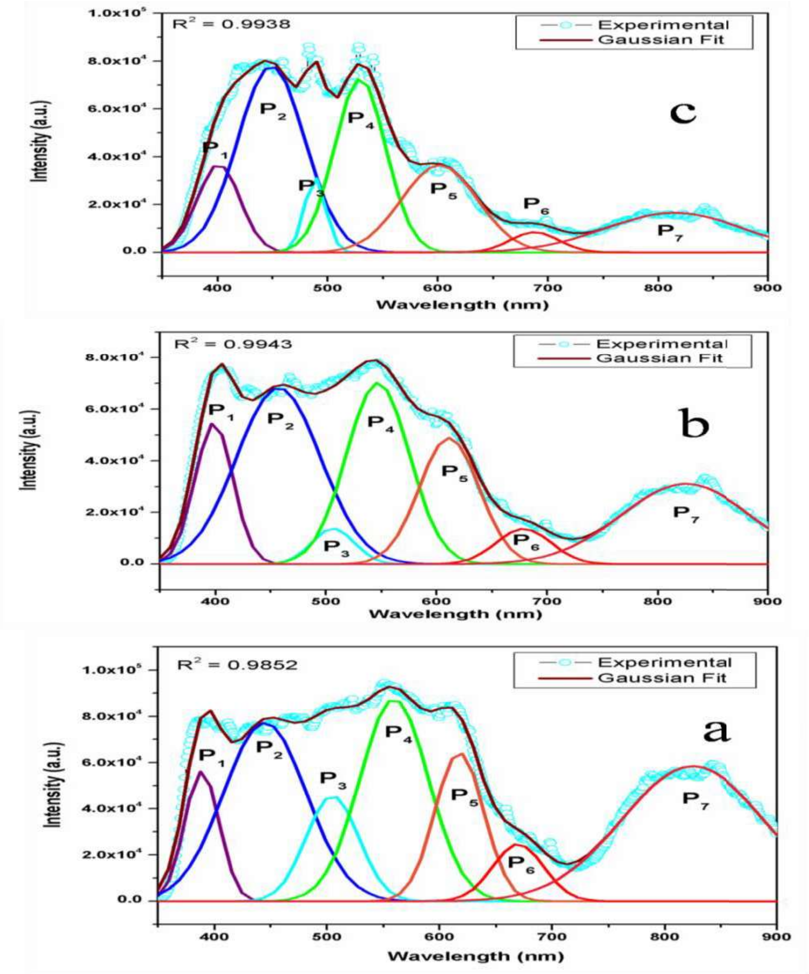

Figure 3.12: *Gaussian fit of the emission profile of MgO-600, MgO-800 and MgO-1000 compound.* ***[161]***

3.2.7 Electronic Structure and Band Gap Energy

As stated earlier, that the multicolour emission of pure MgO compound indicates the presence of various electronic states inside the band gap of the material and these electronic states may be originated from various defect states; otherwise in a wide band gap material like MgO (band gap ≈ 7.8eV), multiple colour components in the visible region would not have been possible. In present case the individual electronic states of various neutral and charged defect centres are calculated using DFT calculation where we have considered most of the possible neutral and charged single anionic vacancies (F- type centres) and their cluster (F_2-type centres) **e.g.** F (or V_O^0), F^+ (or V_O^{+1}), F^{2+} (or V_O^{+2}), F_2^{2+} (or V_O^{+1}+ V_O^{+1}), F_2^{1+} (or V_O^{+1}+ V_O^0), F_2^{3+} (or

V_O^{+1}+ V_O^{+2}); cationic vacancies e.g V_{Mg}^0,V_{Mg}^{-1},V_{Mg}^{-2}, Schottky defect (V_{Mg}^0 + V_O^0) ; interstitial oxygen e.g. O_i^0, O_i^{-1},O_i^{-2} etc. The details of the DFT based calculation methodologies are given in our published report **[161]**. The overall summary of the electronic structures for different kind of charged and uncharged vacancies as obtained from the respective density of states (DOS) is pictorially represented in Figure 3.13. All the electronic states represent the ground state configuration. From this figure, different filled (represented by bold) and unfilled (represented by white colour) electronic states inside the band gap can be seen, which are arising due to different kind of vacancies in the matrix. Thus, the excitation of the electron will be from the filled electronic state of these ground state configurations and the emission will be due to the transition of an electron from the excited state to the unfilled electronic state. Although in the present case, the DFT study does not deal with the excited states due to some restriction, fortunately the excited states of F and F^+ centres lie very closely to the conduction band and a photo conversion process of F to F^+ centres is involved at 250 nm following the equation $F + h\upsilon \leftrightarrow F^+ + e^-$ **[139-141]**. Since the absorption bands of F to F^+ centres are energetically close **[164,168],** it is difficult to excite any of them without exciting the other. The F^+ centre is thus considered as the ionized state of the F. The released electron in this photo ionization process becomes free and behaves as a free carrier. This means that the recombination process of the free electron with the hole does not need to occur at the same site where they have been created. Other positively charged defect centres such as F^+ , F^{2+} , F_2^{1+}, F_2^{2+}, F_2^{3+} centres etc (which might be created by bleaching process or were already present in the compound) will naturally attract the free electron and the recombination process may occur with them also as predicted by Rinke *et al.,* for F^+ centre [**146**]. The free electron can also be trapped into different trap state (vacant electronic state) within the band gap. The F centre emission can therefore be realized by a recombination process of the free electron in the conduction band with the vacant spin state of the F^+ centre in the ground state, following the equation $F^+ + e \leftrightarrow F + h\upsilon$ **[139,146]**. Similarly if the electron in the filled electronic state of F^+ centre is photo excited to the conduction band, the resulted ground state will be like F^{2+} centre and on encounter with the free electron in the conduction band, the F^+ centre emission can be realized by the equation $F^{2+} + e \leftrightarrow F^+ + h\upsilon$ as reported by Kumar *et al.,*[**169]**. In the same manner we can also say that by considering the recombination process of the free electron in the conduction band with the unfilled ground state of $F_2^{2+}$and F_2^{3+} , emission of the F_2^{1+} and F_2^{2+}centre can be realized, following the equations F_2^{2+}+ e ↔ F_2^{1+}+ hυ and F_2^{3+}+ e ↔ F_2^{2+}+ hυ , respectively, since these vacancies are nothing but cluster of F and F^+ centres. Thus the energy of the radiative emission of F centre will be the energy difference between the bottom of the conduction band and the unfilled electronic state of F^+. Similarly, the energy difference between the unfilled electronic state of F^{+2}, F^{+2}_2 and F^{+3}_2 and the CB will be emitted in the form of radiative emission due to F^+, F^{+1}_2 and F^{+2}_2 centres respectively. The reverse recombination process i.e. a free hole in the valence band with the electron in the filled state of F centre is also possible (positively charged F centre will be repealed by the hole). For this recombination process to occur, some electrons have to be knocked out from the VB to the upper unfilled states,at 250 nm excitation wavelength. In this way, Figure 3.13 will help in a great deal to find a correlation of the observed emission components with the different defects induced electronic states inside the band gap.

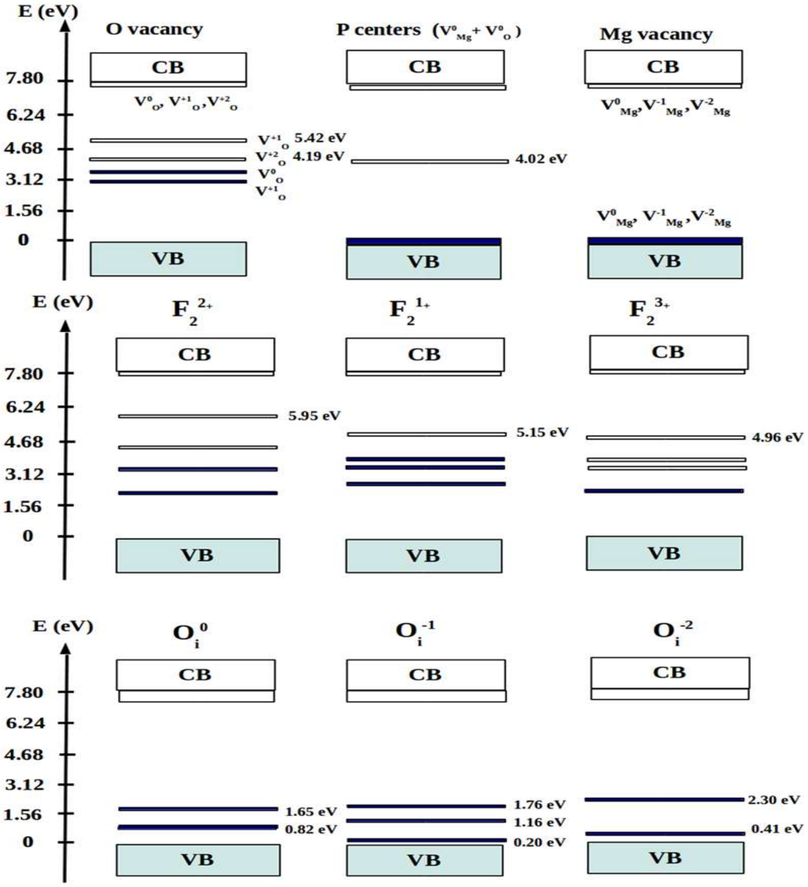

Figure 3.13: *Overall summary of the electronic structures arise due to various defects centres. Colour bands filled with electrons and white bands are empty.* ***[161]***

Now let us propose a model in Figure 3.14, to explain all the colour components present in the emission profile and their correlation with electronic structure inside the band gap. In Table 3.2, all the recombination processes of the respective emissions are listed and they are pictorially presented in the proposed model Figure 3.14**.** In this model a photo conversion process at 250 nm is shown followed by release of an electron. Now the electron being free can go to the conduction band as marked by green arrow and thus behaving as a free carrier. Being free the electron can now recombine with different positively charged F and F_2 type centres at their ground states. At the bottom of the model, a recombination process of a free hole in the VB with the electron in the filled states of negatively and neutral interstitial oxygen atom is also shown. Now to justify our proposed model of electronic transitions, we have also compared the emission energies for some of the defect centres obtained through present calculations and experiments with that previously reported in literature. In literature, the violet emission (P_1) at $\lambda_{max} \approx 390$ nm is assigned to the F^+ centre while the green emission (P_4) at $\lambda_{max} \approx 540$ nm is attributed to F centre **[139,140]**. In our present case, we can see that in Figure 3.13 there are two vacant empty states for F^+ (V_O^{+1}) and F^{+2} (V_O^{+2}) centres and the energy difference of these two states with the conduction band are ~ 2.4 eV and ~ 3.5 eV respectively. Although these theoretically obtained energy differences do not exactly match to the experimental value 2.3 eV (~540 nm) & 3.2 eV (~390 nm), but fall very well into the very broad experimental peak. Thus the Violet emission (P_1) at $\lambda_{max} \approx 390$ nm is assigned to the F^+ centre owing to the encounter of the free electron in the conduction band with the F^{+2} centre as represented by violet colour in the model Figure 3.14 following the equation $F^{2+} + e \leftrightarrow F^+ + h\upsilon$ (390nm) in Table 2. Similarly the green emission (P_4) at $\lambda_{max} \approx 540$ nm can be assigned to the F centre following the recombination $F^+ + e \leftrightarrow F + h\upsilon$ (540 nm) which is represented by green colour in the model. Similarly for the indigo (P_2) emission at $\lambda_{max} \approx 450$ nm (2.81 eV), we have observed that the energy difference between the CB and the higher vacant state of F_2^{3+} state i.e. ~ 2.8 eV is closely resembling. Therefore this indigo (P_2) emission can be assigned to the F_2^{2+} centres which is also supported by the literature survey **[142]**, following the equation $F_2^{3+} + e \leftrightarrow F_2^{2+} + h\upsilon$ (450 nm), as marked by indigo colour in the model. For other emissions such as 490 nm (P_3), 605 nm (P_5), 680 nm (P_6) and 850 nm (P_7) we have compared the energy difference between the vacant electronic states of different defect centres with the observed emission in similar way and successfully correlated them with various defect centres, shown by different transition in the model. The corresponding electron-hole recombination processes are also included in Table 3.2. However any transition of the free electron from the CB or from trap state to the vacant spin states of the defects cannot explain the broad emission in NIR region with $\lambda_{max} \approx 850$ nm (P_7) (1.45 eV) since none of the energy difference match with this low energy emission (1.3 eV -1.6 eV). In this case a reverse combination process i.e. a hole at the VB and an electron in the defect states may explain this broad band emission **[146]**. The hole at 250 nm excitation wavelength may be created by knocking out one electron to vacant excited states inside the band gap or it may be created by a two photon excitation phenomenon. From Figure 3.13, we can see that there are various filled electronic states present for the neutral and negatively charged interstitial oxygen atoms (O_i) which are present 0.2 - 1.8 eV above the valance band. Being neutral and negatively charged, they will attract these positively charged holes. Thus recombination of a free hole at the VB with the filled spin states of different interstitial oxygen atom is mostly responsible for the broad NIR emission. The detail explanation is given in reference **[161]**.

Table- 3.2: Colour components and their respective recombination process **[161]**

Colour Components (nm)	**Recombination Process**
390 (P_1)	$F^{2+} + e \leftrightarrow F^{+} + h\upsilon$
450 (P_2)	$F_2^{3+} + e \leftrightarrow F_2^{2+} + h\upsilon$
490 (P_3)	$F_2^{1+} + e \leftrightarrow F_2 + h\upsilon$
540 (P_4)	$F^{+} + e \leftrightarrow F + h\upsilon$
605 (P_5)	F^{+} + e (shallow trapped) $\leftrightarrow F + h\upsilon$
680 (P_6)	$F_2^{2+} + e \leftrightarrow F_2^{1+} + h\upsilon$
850 (P_7)	h^{+} (VB) + e (filled states of O_i) $\leftrightarrow$ $h\upsilon$

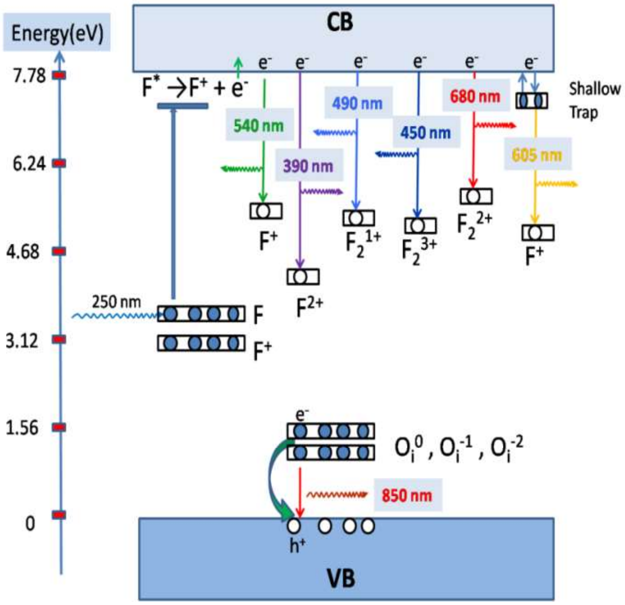

Figure 3.14: *Possible free electron model for different transitions of the emission components in MgO. The bold circles represent filled electronic states while the white ones represent vacant electronic state. The white circles in the VB represent positively charged holes. All the electronic states inside the band gap represent the ground state configuration. At 250 nm excitation wavelength a photo conversion process of F centre is involved followed by the equation F + hυ ↔ F^+ + e. The released electron in this process becomes free after prompting into the conduction band and may recombine with different types of positively charged defect centres in addition to the newly formed F^+ centres. Thus different electronic transitions from the conduction band (CB) to the empty ground electronic states of positively charged F- and F_2-type centres can be correlated with the observed emissions.* ***[161]***

Now let us explain the emission map in Figure 3.4b**,** at different excitation wavelength.From the spectra it is observed that when the excitation wavelength was increased to 250 nm, there was an increase in the intensity of the overall spectra. The enhancement of intensity was more pronounced in the 390, 600 and 850 nm regions as shown by arrows. The overall intensity of the spectrum was further increased as we tune the excitation wavelength to 290 nm, while tuning it to 310 nm led to decay in intensity. Now this enhancement of intensity at 390 nm region at 250 nm excitation can be explained only on the basis of photo ionization process of F centre followed by the equation F + hυ ↔ F^+ + e^-. Since at this excitation wavelength, the F centre is converted to the F^+ centre, there should be an increase in intensity of its characteristic emissions. By same logic, a decrease in intensity of the F centre emission [540 nm (P_4)] would have also observed against the current trend. However, since 250 nm is the excitation wavelength of F centre, the emission intensity will always be more at this wavelength and also there is a chance of the F^+ centre to recombine with the free electron, which might be the reason for not observing the expected result. The enhancement in intensity in the 605 nm region can be explained based on our proposed model in Figure 3.14 where the 605 nm emission is shown to be associated with shallow trap electron, which comes from the conduction band. Thus there is a direct link with the photo conversion process since at 250nm excitation wavelength the released electron will be prompted into the conduction band and being free they can also be trapped at shallow level. At 290 nm excitation, the further increase in intensity both at 390 nm and 605 nm region (Figure 3.4b) indicates that some other photo conversion process such as F_2 + hυ ↔ F_2^{1+} (or $F+F^+$) + e might also be involve at this wavelength. As seen from Figure 3.4b, at 290 nm excitation the emission at 490 nm region is highest which corresponds to the F_2 centres, which are nothing but a pair of adjacent F centre. Hence if a photo conversion process is at all involved at this excitation wavelength (290 nm), there will be an enhancement in intensity of the F^+ centre too, similar to 250 nm excitation.

For further support of our argument about the photo ionization process and the recombination process involving a free electron, the low temperature emission spectra both at 250 nm and 290 nm excitation were recorded, which is shown in **Figure 3.15**. The figure shows that at both of these excitation wavelengths, there is a decay in intensity around the 390, 605 and 850 nm regions. Therefore, it can be argued that at low temperature (77 K), the electron released in the photo conversation process i.e. F + hυ (250 nm) ↔ $F^+ + e^-$, might not be able to move into the conduction band and rather it will recombine with the newly formed F^+ centres. This is what reflected in the in decay in intensity in the 390 nm &605 nm wavelength region.

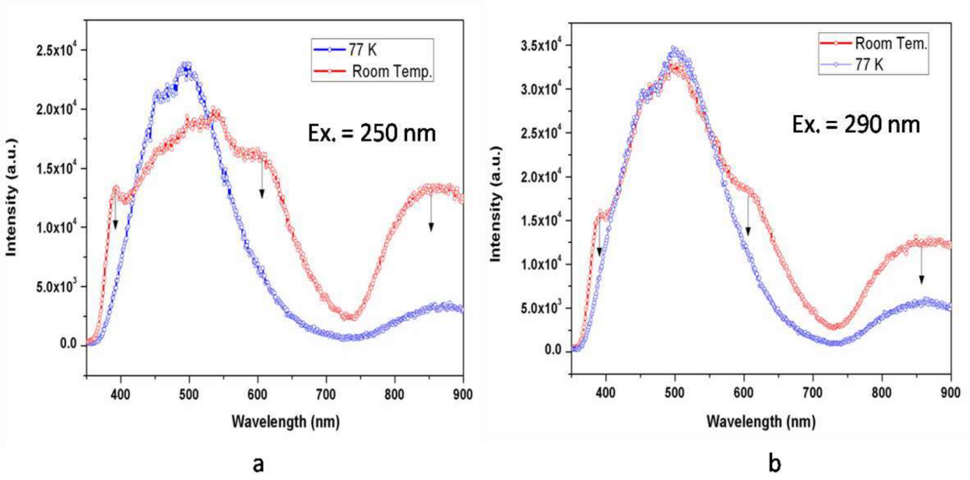

Figure 3.15. *Room temperature and low temperature (77 K) Emission spectra of MgO-600 compound at different excitation wavelengths* (λ_{ex} *= 250 nm & 290 nm)* ***[161]***

3.2.8. Magnetic, EPR and PAS study:

3.2.8.1. Magnetization studies [163]

Figure 3.16 shows the temperature dependent field cooled (FC) and zero field cooled (ZFC) measurements under an applied field of 1000 Oe for different annealed compounds viz. MgO-600, MgO-800 & MgO-1000. Here a paramagnetic (PM) to ferromagnetic (FM) transition at a Curie temperature (T_C) around 65 K (±10 K) was observed for all of the compounds, where the FC and ZFC curve are getting bifurcated. Figure 3.17-a, b & c represent the M (magnetisation) vs H (applied field) curves at 5K over a field 50kOe, for MgO-600, MgO-800 and MgO-1000 compounds. Now the S-shaped nature of the M vs. H plot indicates existence of weak ferromagnetic ordering at low temperature, which is further supported by the enlarge view of the hysteresis loop near origin as shown in the inbox of Figure 3.17. In order to calculate the saturation magnetization, these M vs H curves were fitted using Brilluin function **[170-172]** given in Equation 3.8.

$$M = Ng_J J\mu_B \left[\frac{2J+1}{2J}\coth\left(\frac{2J+1}{2J}y\right) - \frac{1}{2J}\coth\left(\frac{y}{2J}\right)\right] \quad \textbf{(3.8)}$$

Here the saturation magnetization value is$(M_s) = Ng_J J\mu_B$, $y = \frac{g_J J\mu_B H}{k_B T}$, $H = H_{app} + H_{mol}$ where H_{app} and H_{mol} are the applied and Weiss molecular magnetic field. Assuming $g_J = 2$, the Brillouin function was fitted for MgO-600, MgO-800 and MgO-1000 compounds with various J values ranging from 1/2 to 5/2 and it was found that the best fittings were obtained for J = 1 or 3/2 values. The saturation magnetization (M_s) values with J = 1 or 3/2 are included in Table 3.3 which shows that for both the J values, the M_s was increased when MgO was annealed at higher temperature. This present trend of saturation magnetization with annealing temperature is exceptional since in most of the cases of MgO nanoparticles, a decrease in the M_s with annealing temperature was reported due to the decrease in the surface defect concentration, which are mainly responsible for the magnetism behavior **[137,138]**. However in present case the surface to volume ratios play hardly any role in determining the magnetism trend since the MgO particles are in the micron size and some other things must be responsible as discussed later.

Table-3.3: Saturation Magnetization values for different temperature annealed MgO compounds obtained from Brillouin function fitting of the experimental data. [**163**]

Compound	Saturation Magnetization (M_s) (emu/g)	
	For J = 1	For J = 3/2
MgO-600	0.49	0.43
MgO-800	0.64	0.55
MgO-1000	0.80	0.69

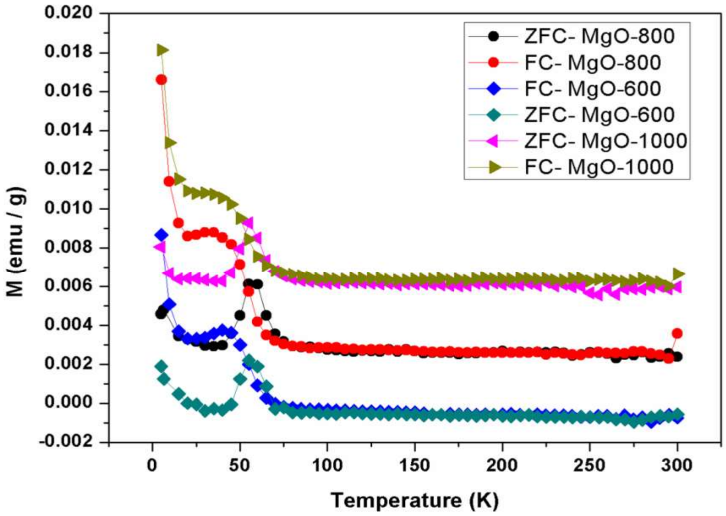

Figure 3.16. *FC and ZFC M vs T plots showing for MgO-600, MgO-800 & MgO-1000* [**163**]

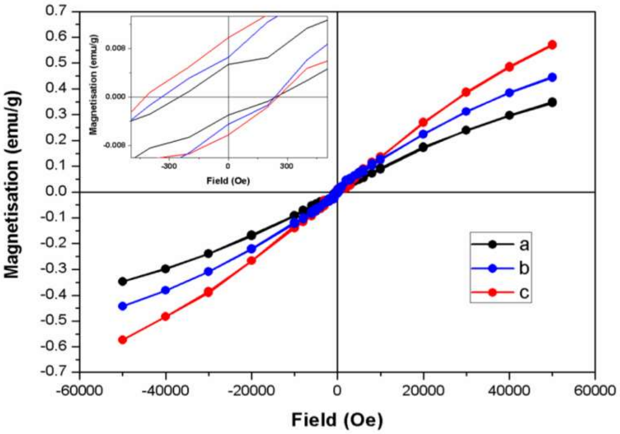

Figure 3.17. *Hysteresis plots for a) MgO- 600, b) MgO- 800 and c) MgO-1000 after diamagnetic correction. Inbox represents the enlarge view of the hysteresis loop near origin.* [**163**]

3.2.8.2. Positron annihilation lifetime spectroscopy (PALS) measurements [163]

Figure 3.18 shows typical PALS spectrum for MgO-1000 compound. PALSFIT program was used to analyze the PALS spectra into discrete positron lifetime components. For the analysis, after source correction and back ground (B) subtraction, the PALS spectrum, N (t) is fitted to sum of exponentials convoluted with a Gaussian resolution function (R) through equation 3.9.

$$N(t) = R \otimes [\sum_{i=1}^{i=k+1} (\frac{I_i}{\tau_i}) \exp(-t/\tau_i) + B] \qquad \textbf{(3.9)}$$

Where the index *i* stands for different positron lifetime components τ_i with its corresponding intensity I_i. The index *k* stands for the number of positron trapping sites available in the samples. Table 3.4 includes various positron lifetimes and their corresponding intensity values in MgO compounds. The third lifetime component which is in the nanosecond range is due to the *orhto*-positronium(o-Ps) *pick-off* annihilation. It was found that in case of metal oxide powder samples, a fraction of positron diffuses to the particle surface and form positronium [**173**]. Generally, the o-Ps lifetime depends on the open volume (local structure) at the grain boundary whereas its corresponding intensity (I_3) depends on their concentration in the sample. In present case, the o-Ps lifetime (τ_3) and I_3 do not vary significantly among the studied samples which indicates that the variation in the local structure as well as the concentration of grain boundaries as a result of annealing is non-significant and would not be considered for its role of magnetic properties of the samples. For MgO-600, the first two lifetime components viz. 237.0 ps(picosecond) and 445.0 ps are attributed to open volume defects as both these values are higher compared to the bulk positron lifetime in MgO, which is reported to be 160 ps [**174**], also supported by theoretical calculations [**175**]. The open volume defects can be present either in bulk or at the surface of the samples. The 237 ps lifetime component in MgO-600 samples is close to the calculated positron lifetime value (244 ps) of Mg monovacancy while the 445 ps lifetime component can be ascribed to the vacancy clusters consisting of $2V_{Mg}$ and $2V_O$ or $2(V_{Mg} + V_O)$ (calculated lifetime 414 ps) [**175,176**].

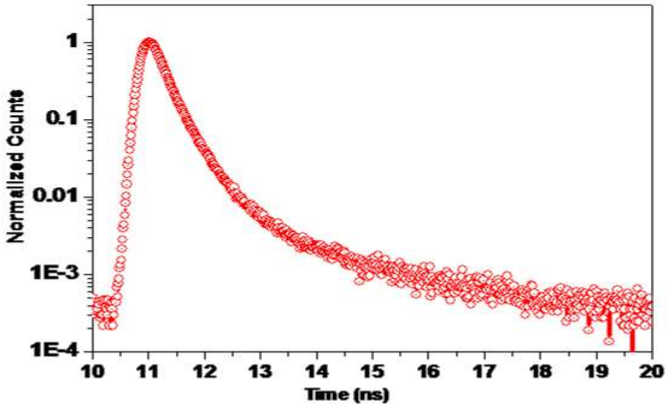

Figure 3.18. *Typical PALS spectrum for MgO-1000 compound* [**163**]

Table 3.4 : Positron lifetimes of MgO compounds annealed at different temperature.

Sample	**τ_1(ps) / I_1(%)**	**τ_2 (ps) / I_2(%)**	**τ_3 (ns) / I_3(%)**
MgO-600	237.0±7.0/ 67.3±6.3	445.0±4.7/26.9±5.2	1.16±0.11/5.17±1.28
MgO-800	145.5±6.1/45.64±4.0	291.0±8.0/51.82±3.81	1.06±0.05/2.53±0.27
MgO-1000	115.9±5.2/30.78±2.08	279.0±4.0/64.9±1.90	1.03±0.03/4.22±0.25

Since the isolated positively charged oxygen vacancy do not trap positrons,their presence cannot be ascertained by the PALS measurements. From Table 3.4, it can be found that on annealing, both the lifetime values are reduced indicating the reduction in the size of the defects. On annealing, the second lifetime value was reduced from 445 ps to 291 ps which suggests that the large vacancy cluster undergo dissociation and reduced to smaller size of vacancy defects. On comparison with theoretically calculated lifetime, the second component for MgO-800 sample can be ascribed to the di vacancy of V_{Mg} + V_O [**176**]. Here the first lifetime was found to reduced to 145 ps, which is lower than the bulk lifetime (160 ps) indicating unsaturated trapping at the defects sites. On further annealing the compound at 1000 ^{o}C, the second component was further reduced to 279 ps, which does not match with any characteristic lifetime value of any plausible monovacancy defects in MgO. Thus, it appears that the di vacancies present in the MgO-800 sample undergo dissociation leading to creation of isolated mono vacancies of Mg and O along with the residual di vacancies. In such a case, the observed lifetime of 279 ps is the average of positron annihilation from combination of V_{Mg} and V_{Mg}+V_O. It is to be noted that isolated V_O cannot be indexed using positron due to their positive charge. The first lifetime component is further reduced in this sample, which is consistent with the creation of V_{Mg} in this sample. The trapping constant for V_{Mg}, which is negatively charged, is much higher compared to neutral $V_{\mathrm{Mg}}+V_{\mathrm{O}}$. Thus from positron annihilation lifetime measurements we can conclude that for low temperature annealed compound such as MgO-600, the prominent defects are Mg vacancies ($\mathrm{V_{Mg}}$) and vacancy cluster consisting of $\mathrm{2V_{Mg}}$ and $\mathrm{2V_{O}}$ or $\mathrm{2(V_{Mg} + V_{O})}$. However, at higher annealed samples this cluster undergoes dissociation, forming mono vacancies of Mg and O along with the residual di vacancies [**163**].

3.2.8.3. Electron Paramagnetic Resonance (EPR) spectroscopy [163]

The EPR spectra of MgO-600, MgO-800 and MgO-1000 are shown in Figure 3.19, where we have not observed any characteristic lines due to paramagnetic metal impurity such as transition metal impurities viz. V, Fe, Mn etc.[**177-179**]. This indicates that the observed spectra must be originating from some kind of intrinsic defect states in the compound. From the spectra, it is clearly visible that more than one paramagnetic species or defect centres are present in the system. When the compound was annealed at higher temperature such as in case of MgO-1000, the spectra showed an increase in intensity on lower field side. Figure 3.20 represents the simulation of the EPR spectra for MgO-600 & MgO-1000. As seen the spectra are composed of four different signals at $g \approx 1.96$ ($\mathrm{S_{IV}}$), 1.98 ($\mathrm{S_{III}}$), 2.03 ($\mathrm{S_{II}}$) and 2.07 ($\mathrm{S_{I}}$). These strong intense resonance signals must be contributed from some type of intrinsic defects, such as oxygen and Mg vacancies, since both $\mathrm{Mg^{2+}}$ and $\mathrm{O^{2-}}$ do not contribute to the EPR spectrum. Among different possible oxygen vacancies, only $\mathrm{F^{+}}$ centres and their aggregate such as $\mathrm{F_2^{2+}}$, $\mathrm{F_2^{1+}}$ centres are paramagnetic and hence they are EPR sensitive while for Mg- vacancies, when a hole traps at the Mg vacancy ($\mathrm{V_{Mg}^{//}}$), it becomes paramagnetic ($\mathrm{V_{Mg}^{/}}$) and EPR active. Here the broad peaks of $\mathrm{S_I}$ ($\Delta \approx 730$ Gauss) and $\mathrm{S_{II}}$ ($\Delta \approx 1400$ Gauss) in Figure 3.20, indicate that the spins in the system are strongly coupled and may form spin clusters [**137**] . This $\mathrm{S_{II}}$ signal is attributed to the $\mathrm{F^{+}}$ centre [**180-182**] while the $\mathrm{S_{III}}$ and $\mathrm{S_{IV}}$ signals are due to trapping of superoxide ($\mathrm{O_2^{-1}}$) radicals in the air-annealed MgO **[137,181-183]**. On the other hand the broad $\mathrm{S_I}$ signal can be attributed to $\mathrm{V^{-}}$ centre or hole trap at Mg vacancy i.e $\mathrm{V_{Mg}^{\ 1-}}$ **[184]**. From Figure 3.20, it can be concluded that when MgO compound was annealed at higher temperature, the intensity of the $\mathrm{S_I}$ signal was increased which is responsible for the higher intensity in lower field region of the EPR spectra for MgO-1000 shown in Figure 3.19. This also supports the observation from positron annihilation study that at higher annealing temperature the concentration of cationic vacancies increases due to thermal dissociation of 2(V_{Mg} + V_O) cluster. However, $V_{Mg}{}^{1-}$ cannot be solely responsible for the increased magnetization value as we go from MgO-600 to MgO-1000 since during thermal dissociation along with $V_{Mg}{}^{1-}$, paramagnetic oxygen vacancies are also another product, which cannot be characterized by positron annihilation study. Again it is not known whether these paramagnetic species are ferromagnetically coupled or not and thereby increasing the magnetization value.

In this context, EPR spectroscopy plays a great role where by measuring line position, line width and integral intensity of EPR spectra at different temperature, information about magnetic ordering in a ferromagnetic material can be easily obtained [**185-195**]. Figure 3.21 represents the temperature dependence of EPR spectra of the MgO-600 and MgO-1000 compounds. In Figure 3.21a, in case of MgO-600, a continuous increase in intensity and broadening of the S_{II} signal and shifting of the resonance field position to the lower field was observed as the temperature is lowered, which are the characteristic of ferromagnetic resonance spectra [**185-195**]. For MgO-600, since the intensity of S_I signal is very less, information regarding ordering of those spins is difficult. However in case of MgO-1000, since the S_I signal has significant contribution to the EPR spectra, such information about the S_I signal can be easily obtained in addition to that of S_{II} signal. As shown in Figure 3.21b, as the temperature is lowered, the magnetic field positions of both the S_I and S_{II} signal are shifted to the lower field side.

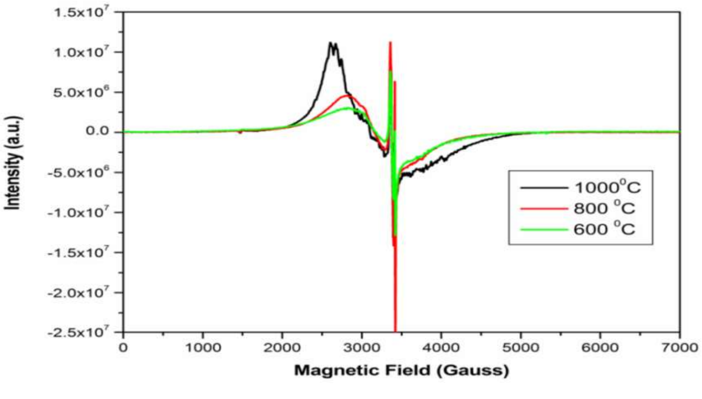

Figure 3.19. *Room temperature EPR spectra of MgO-600, MgO-800 and MgO-1000* [**163**]

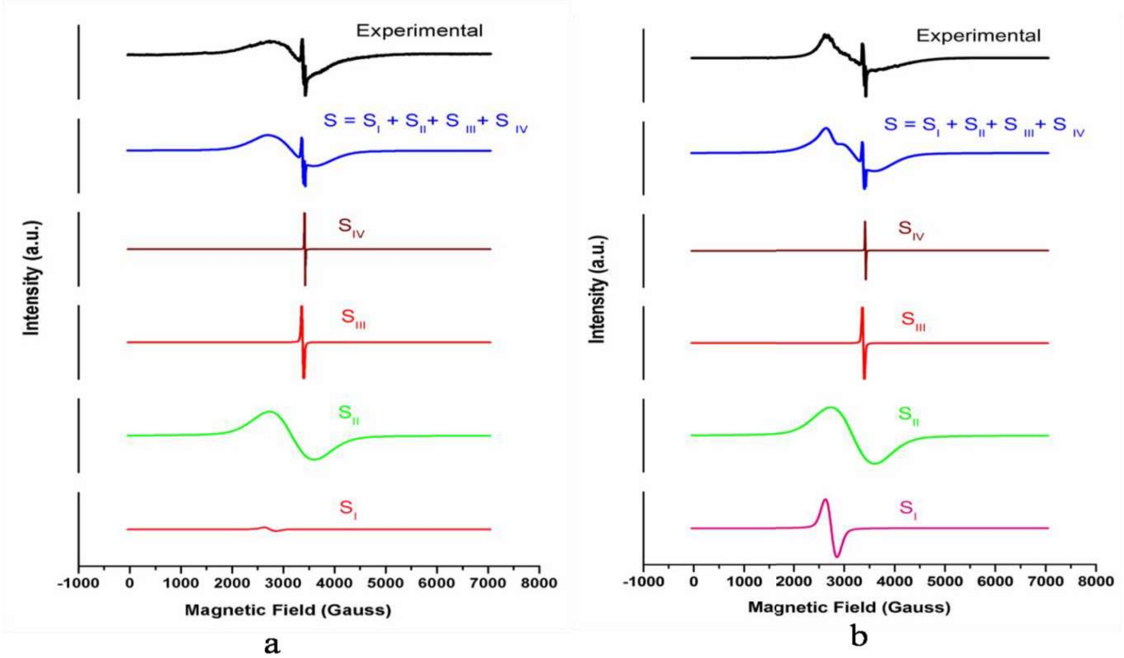

***Figure 3.20**: Simulation of the EPR spectra (a) MgO-600 & (b) MgO-1000* [**163**]

The temperature dependence of the resonance field position and line width of the S_{II} signal for MgO-600 are presented in Figure 3.22a & 3.22b. For MgO-1000, the temperature dependence plot of resonance field position of S_{II} signal is given in Figure 3.22c. Since in this case both the S_I and S_{II} signal has significant contribution and both are broad in nature, the line width and intensity measurement will be more erroneous and hence we have avoided such plot. However, the change in resonance field position is enough to explain its magnetic ordering. In the paramagnetic state, such temperature- dependent changes in the line width and line position of the resonance signal would not occur. This behavior is attributed to the presence of a non-homogeneous local magnetic field, which modifies both the resonance *H* and the line shape of the signal in the ferromagnetic state [**188-190**]. Therefore, from these T-dependence spectra we can conclude that both the S_I and S_{II} signals are ferromagnetically coupled and we can denote both these signals as ferromagnetic resonance (FMR) signals. Hence, the observed ferromagnetism in MgO compounds must have originated from either the $V_{Mg}{}^{1-}$ or $V_O{\bullet}$ or F^+ centres. The relatively large linewidth of the S_{II} signal compare to the S_I signal implies that paramagnetic oxygen vacancies i.e $V_O^{\bullet}$ or F^+ centres are strongly coupled compared to the paramagnetic cationic vacancies i.e V_{Mg}^{-1}.

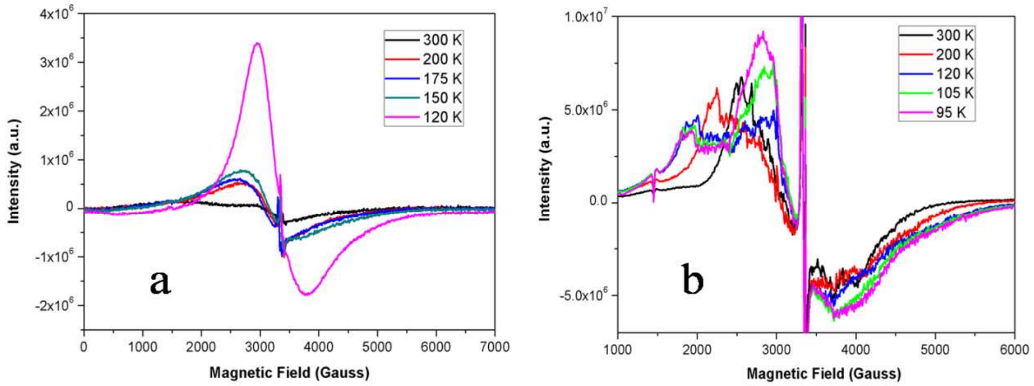

Figure 3.21: *Temperature dependent EPR spectra of a) MgO-600 & b) MgO-1000*[**163**]

Direct information about the magnetic state can also be obtained from the variation of the integral intensity of the FMR signals (S_I & S_{II}) from temperature dependent EPR spectrum [**188-190**]. Generally in the high temperature range, the temperature variation of $I_{EPR}(T)$ can be represented by equation 3.10

$$I_{EPR}(T) \propto \frac{C}{T-T_{\theta}} \qquad \textbf{(3.10)}$$

where C stand for Curie constant, T for recording temperature and T_{θ} is the Curie–Weiss temperature. This Integral intensity I_{EPR} (T) is proportional to the spin susceptibility of the paramagnetic species taking part in resonance. In present case we have plotted the temperature dependence of $1/I_{EPR}$ of the FMR (S_{II}) signal in MgO-600 as shown in Figure 3.23. The numerical value of T_{θ} can be obtained from the linear extrapolation of the high temperature part of $1/I_{EPR}$ and the value of T_{θ} is ~ 75 K. The positive sign of the Curie–Weiss temperature (T_{θ}) indicates that the spins are ferromagnetically coupled **[188,191,193]**. A detailed explanation for the change of EPR parameters such as resonance filed, intensity etc. is given in the published report [**163]**on the basis of electronic phase separation (EPS) where some parts of the spins are involved in ferromagnetic (FM) coupling while others remain as paramagnetic (PM) state.

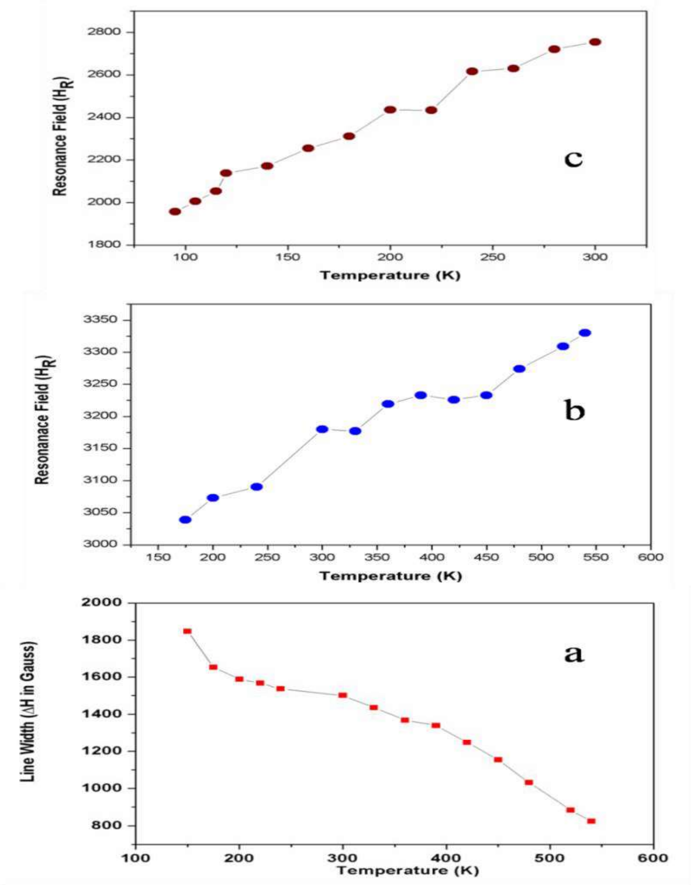

Figure 3.22: *Temperature dependencies of (a) line width,* $\Delta H_{1/2}$*, of the* S_{II} *signal in MgO-600 (b) resonance field,* H_R *of the* S_{II} *signal in MgO-600 and (c) resonance field,* H_R *of the* S_I *signal in MgO-1000* [**163**].

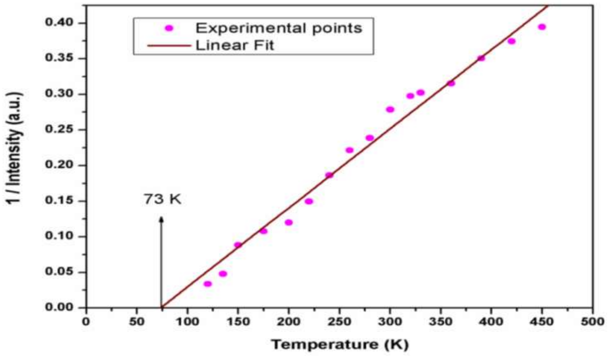

Figure 3.23: *Temperature dependencies of the inverse of EPR integral intensity i.e.* $1/I_{EPR}$ [**163**]

3.2.8.4. Explanation of origin of ferromagnetism and its exceptional enhancement

From Positron annihilation lifetime measurements (PALS), we have observed that MgO-600 possess both Mg mono vacancy (either double or single charge) and di-vacancy clusters i.e. $2(V_{Mg}{}^{0} + V_{O}{}^{0})$, which upon annealing undergoes dissociation, forming mono vacancies of Mg and O along with the residual di vacancies. From EPR study we have observed that MgO-600 compound possess both singly negative charged Mg vacancies i.e. V_{Mg}^{-1} and singly positive charged oxygen vacancies i.e. V_O^{+1} or F^+ centres. At low annealing temperature the concentration of V_{Mg}^{-1} is very much low while and at higher annealing temperature a significant increase in intensity of the EPR signal due to V_{Mg}^{-1} was observed. Low temperature EPR study showed that the spins of both of these vacancies are ferromagnetically coupled. Photoluminescence study in Figure 3.12, showed that in MgO-600, both F^+ and F_2^{2+} centres are present with major contribution coming from the latter one. Upon increasing the annealing temperature, the percentage of F^+ centre was decreased while that of F_2^{2+} centres was increased to some extent. Since at higher temperature, the magnetically inert $2(V_{Mg}^0 + V_O^0)$ cluster vacancies undergo dissociation forming paramagnetic V_{Mg}^{-1} and V_O^{+1}, these newly V_O^{+1} may aggregate to F_2^{2+} centres. However, the newly born cationic vacancy V_{Mg}^{-1} now plays an addition role in the magnetization value. Thus, the increased magnetization value at higher annealing temperature is due to both increase in V_{Mg}^{-1} and F_2^{2+} centres population while at lower annealing temperature it was mainly due to the F_2^{2+} centres. Or in other way this change in magnetism can be linked to a transformation of one kind of cluster vacancy $(2V_{Mg}^0 + 2V_O^0)$ to another cluster vacancy (F_2^{2+}) via a dissociation and association mechanism [**163**].

3.3. Synthesis and Optical properties of $MgAl_2O_4$ (MAS) [180]:

3.3.1. Synthesis and characterization

3.3.1.1 Synthesis:

In this present sol-gel-combustion method, stoichiometric amounts of required Magnesium carbonate [$Mg(CO_3)_2$] (99%, AR grade) and Aluminum nitrate [$Al(NO_3)_3 \cdot 9H_2O$] (98%, AR grade) were used as starting materials while citric acid ($C_6H_8O_7 \cdot H_2O$) (99.7%, AR grade) was used as a fuel for the synthesis of MAS . $Mg(CO_3)_2$ and citric acid were taken in the molar ratio 1:10. At first, two different solution of the mentioned metal carbonate and metal nitrate were prepared by dissolving required amounts of the corresponding precursor material in quartz double distilled (QDD) water. $Mg(CO_3)_2$ salt was dissolved in QDD by slight addition of pure HNO_3. Then these two prepared solutions were mixed in a beaker and kept for stirring by a magnetic stirrer for 1 hour. When a clear solution was observed, citric acid solution (prepared in QDD water) was also added into the mixture under vigorous stirring. The final solution mixture was then heated at 80^{0}C with continuous stirring for 5 hours after which a highly viscous gel formation was observed. This viscous gel was then heated at 150ºC in a furnace for 3 hours and an ash-like product was obtained. The ash-like product was then removed from the furnace and ground in a agate mortar pestle. The obtained powder was then kept for annealing at 600º C in air atmosphere for 12 hr and finally a fine white powder (MAS-600) was obtained. To confirm the phase purity of this compound, X-ray diffraction (XRD) study was carried out. This compound was further annealed at different higher temperatures viz. 800ºC (MAS-800) and 1000ºC (MAS-1000) respectively in order to study the effect of annealing on PL properties. Small amount of MAS-600 compound was also annealed in vacuum atmosphere. In a different lot, two MAS compounds with different Mg/Al molar ratio viz. $\frac{0.98}{2.00}$ and $\frac{1}{1.96}$, were also prepared following the same procedure.

3.3.1.2. Phase purity: X-Ray Diffraction

Figure 3.24 represent the XRD patterns of MAS samples annealed at different temperatures which shows that all the patterns are very well consistent with the standard data ICSD-31373 of $MgAl_2O_4$ compound with space group $Fd\overline{3}m$ and thereby confirmed the formation of the pure spinel compound. Absence of impurity peaks in the XRD spectra confirmed the formation of a single phase spinel structure while the strong and sharp diffraction peaks of the annealed samples indicate crystalline nature of MAS samples. The two MAS compounds with different Mg/Al composition ratio $\frac{0.98}{2.00}$ and $\frac{1}{1.96}$ do not show any impurity peaks which indicate absence of any binary systems with these compositions.

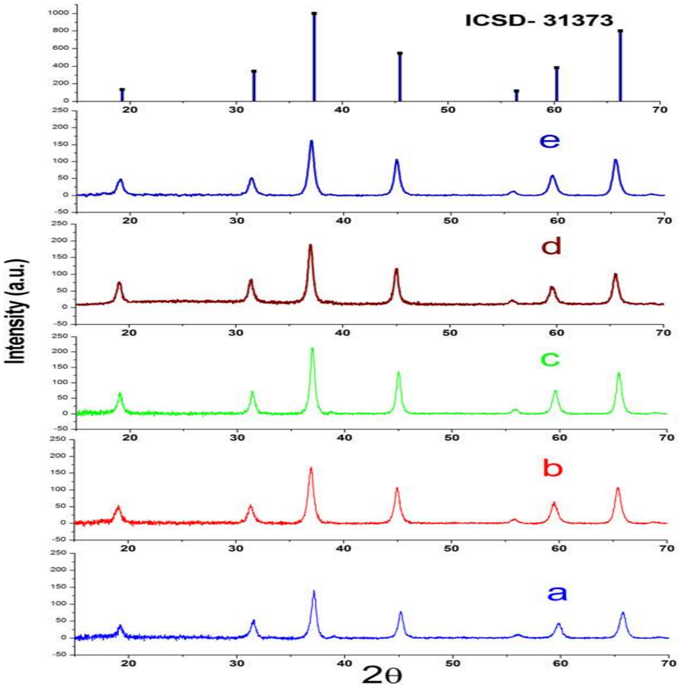

Figure 3.24. *XRD patterns of (a)MAS-600), (b) 800 ^{0}C (MAS-800) and (c) 1000 ^{0}C (MAS-1000) and with Mg/Al composition ratio (d)* $\frac{0.98}{2.00}$ *and (e)* $\frac{1}{1.96}$ **[180]**

3.3.2. Excitation, emission and life time spectroscopy

Figure 3.25 represents the excitation spectra of MAS-600 at different emission wavelength, which consist of different bands with λ_{max} at 230, 235, 245,250, 260, 273, 287, 298, 311 and 326 nm etc. This indicates presence of different electronic states inside the band gap of MAS. The peaks in the 230-245 nm regions are attributed to F^+ centre while those in the 250-260 nm regions are due to F centres **[180]**. The higher energy bands i.e. in the 270-298 nm regions are attributed to charge transfer between Al^{3+} at octahedral sites and its surrounding O^{2-} ions **[158].**

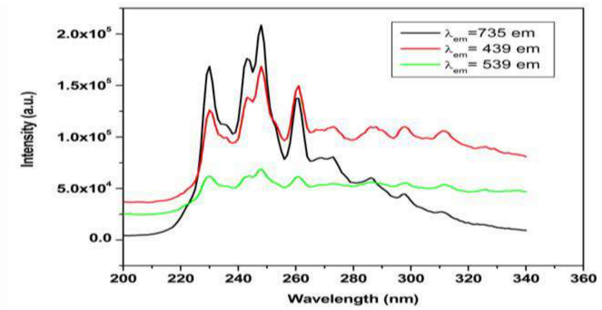

Figure 3.25*. Excitation spectra of MAS compound observed after annealing at 600^{0}C with different emission wave length* **[180]**.

Figure 3.26 represents the room temperature Gaussian fitted deconvoluted PL spectra of the MAS compounds prepared at different annealed temperatures. The figure showed ten different emission components in the ultraviolet-visible- near infrared region (UV-VIS-NIR). These colour components at different emission wavelength (nm) are represented in Figure 3.26 by P_1, P_2, P_3, P_4, P_5, P_6, P_7, P_8, P_9 and P_{10}, such as the UV component (P_1) at $\lambda_{max} \approx 375$ nm, violet (P_2) at $\lambda_{max} \approx 410$ nm, blue (P_3) at $\lambda_{max} \approx 460$ nm, bluish-green (P_4) at $\lambda_{max} \approx 490$ nm, green (P_5) at $\lambda_{max} \approx 530$ nm, yellow (P_6) at $\lambda_{max} \approx 570$ nm, orange (P_7) at $\lambda_{max} \approx 610$ nm, red (P_8) at $\lambda_{max} \approx 720$ nm and the NIR components at $\lambda_{max} \approx 780$ nm (P_9) and $\lambda_{max} \approx 850$ nm (P_{10}) respectively. Latter in this section, the existence of these emission components in the complex spectra will be further confirmed by the TRES study. This multi components emission characteristic indicates the presence of various defect states within the band gap of the material; where each colour arises due to a different electronic transition.

The major changes observed in the emission profile of the MAS compounds shown in Figure-3.26 are that, when the annealing temperature was increased from 600 $^{\circ}$C to 1000 $^{\circ}$C, the intensities of the red and near infrared (NIR) bands (P_8 & P_9) were increased drastically in comparison to that of the bands present in the blue-green-yellow regions. Now to specifically denote the colour characteristics of MAS compounds the CIE chromaticity coordinates were evaluated adopting standard procedures. In Figure 3.27, the values of x and y coordinates for different MAS samples are pictorially represented, where the colour point is denoted by an 'asterisk' which was found to change from bluish to bluish-white to orange-red, as the temperature is changed in the row 600 ^{0}C → 800 ^{0}C → 1000 ^{0}C. This observation renders this particular MAS compound as a potential candidate for optical thermometry. In particular, the drastic increase in the P_7 and P_8 band intensity for MAS-1000 also renders this material to be a potential NIR emitting material.

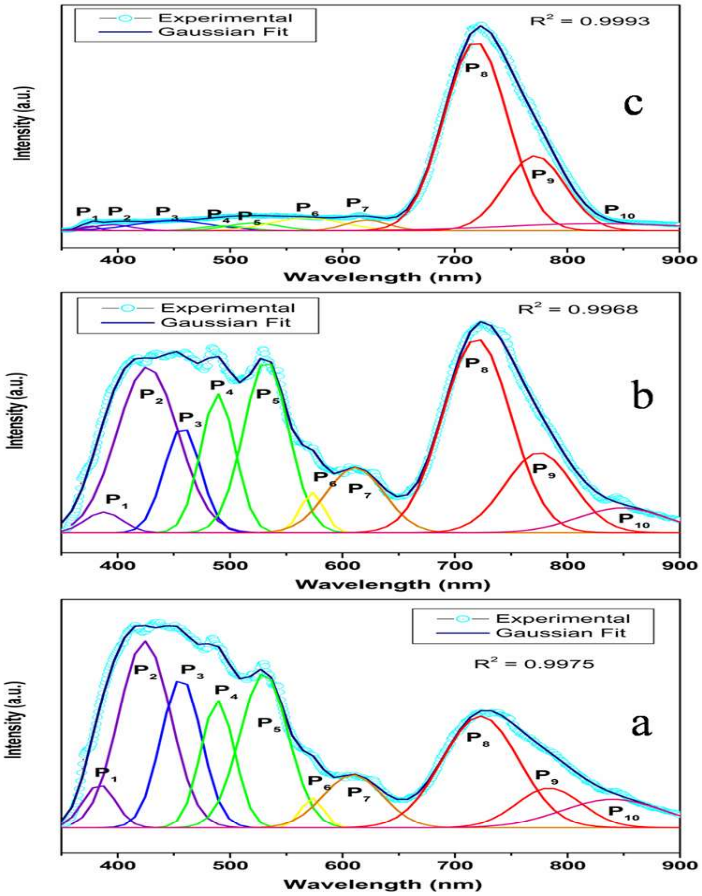

Figure 3.26. *Emission spectra of the MAS compounds obtained after annealed at a) MAS-600, b) MAS-800 and c) MAS-1000 temperature with* λ_{ex}*= 250 nm* **[180]**.

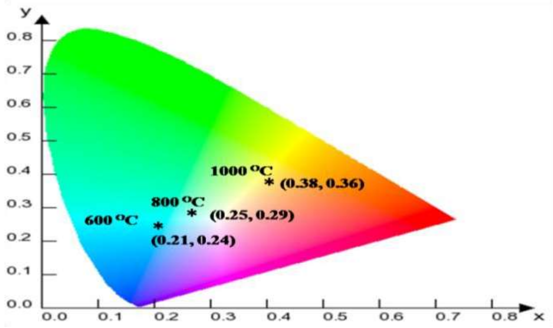

Figure 3.27: *CIE chromaticity diagram for the MAS phosphor at different temperature with* λ_{ex} *=250 nm***[180]**

Figure 3.28a shows the emission spectra for MAS-1000 at different excitation wavelength. Two observations can be marked from this figure. Firstly, when the excitation wavelength was tuned to λ_{ex} = 250 nm, the emission intensity in the red-NIR region has been found to increase sharply. The intensity of this red-NIR region, which is composed of two major bands viz. P_8= 720 nm and P_9 = 780 nm (at higher annealing temperature the P_{10} = 850 nm band was found to be disappear), has been found to increase continuously up to an excitation wavelength, λ_{ex} = 250 nm, beyond this wavelength, the intensity in red-NIR region started falling. The second interesting observation is that at higher excitation wavelength, the peak maxima at $\lambda_{max} \approx$ 720 nm, which was evident up to λ_{ex} = 280 nm, was red shifted to 760 nm at λ_{ex} = 320 nm as shown in Figure 3.28b. Emission spectra at different excitation for the MAS-600 and MAS-800 also followed similar trend **[180]**. Henceforth, it can be inferred that the peak at 720 nm disappears as the excitation wavelength was increased to 330 nm where the spectrum in the red-near IR region consists of only one peak i.e. ≈ 780 nm.

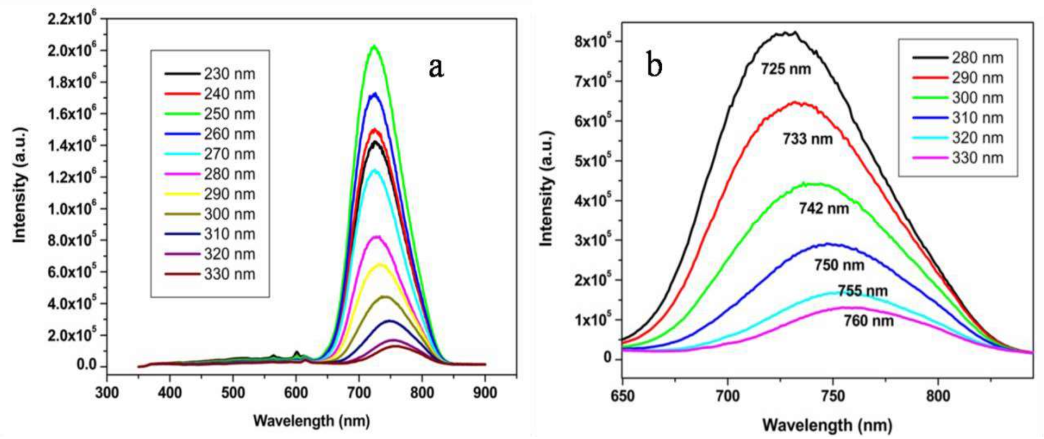

Figure 3.28: *Emission spectra of MAS -1000 at a) different excitation wavelengths and b) the enlarge version* **[180]**.

Figure 3.29 shows the low temperature (in the temperature range 77K-300K) emission spectra of MAS-1000. The overall intensity of the spectrum was found to increase upon decreasing the recording temperature. This is due to quenching of the non radiative pathways which are more efficient at higher temperatures. The lifetime values were also found to be increased accordingly. Interestingly the emission intensity of the red-NIR region (650-900 nm) was not affected strongly and slight decrease in intensity was observed as the temperature went down to 77 K. Thus the emission profile can be controlled by controlling the measurement condition and that the particular MAS compound can be used as a potential low temperature sensor material.

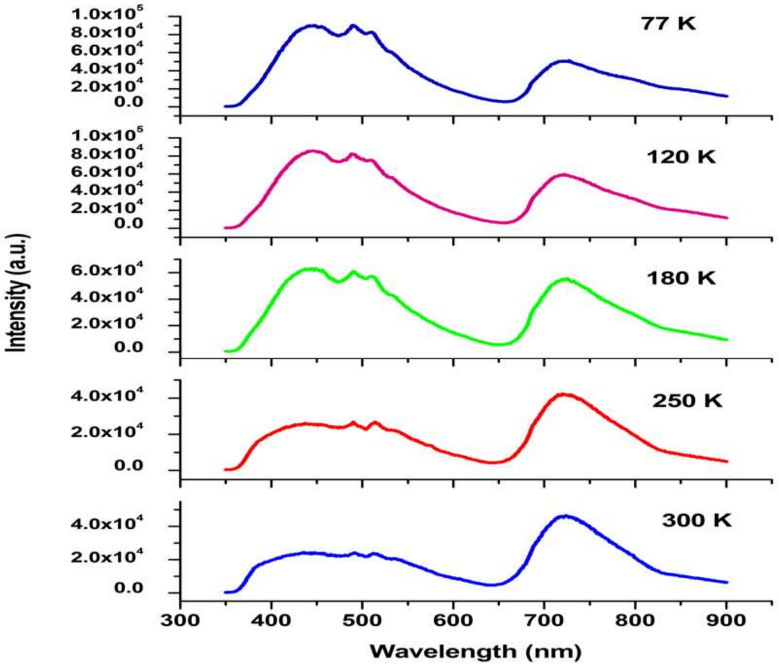

Figure 3.29. *Temperature variation Emission spectra of MAS-1000* **[180]**

Figure 3.30 represents the emission spectra of the two MAS compounds with Mg/Al composition ratio $\frac{0.98}{2.00}$ and $\frac{1}{1.96}$ respectively, prepared after annealing at 600^0C. It was found that for both of these compositions, there was an increase in intensity around 410, 530,720 and 780 nm regions (shown by black arrows) when compared to the ideal spinel composition $\frac{Mg}{Al} = \frac{1}{2}$. However with $\frac{Mg}{Al} = \frac{0.98}{2}$, the intensity in the 410 nm region was found to increase more compare to the other regions and with $\frac{Mg}{Al} = \frac{1}{1.96}$, the intensities of the 530, 720 and 780 nm region were found to increase more than the 410 nm region. The increase in intensity in the 720 and 780 nm regions (red-NIR region) was also found to be more with $\frac{Mg}{Al} = \frac{1}{1.96}$ compared to that with $\frac{Mg}{Al} = \frac{0.98}{2}$.

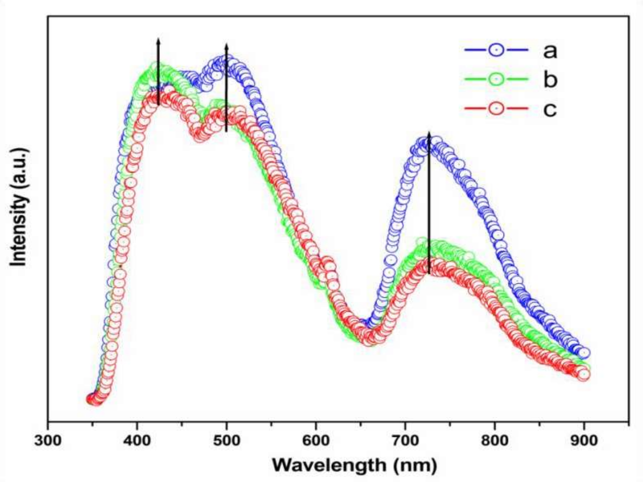

Figure 3.30. *Emission spectra of the MAS compounds with different Mg/Al composition (a)* $\frac{Mg}{Al}=\frac{1}{1.96}$, *(b)* $\frac{Mg}{Al}=\frac{0.98}{2}$ *and (c)* $\frac{Mg}{Al}=\frac{1}{2}$ *with* λ_{ex}*= 250 nm* **[180]**.

The emission behavior of the pure MAS compounds after annealing in air and vacuum atmosphere is shown in Figure 3.31. There is an overall increase in emission intensity (shown by black arrows) both in the blue-green-yellow and red-NIR region when the MAS compound was annealed in vacuum atmosphere.

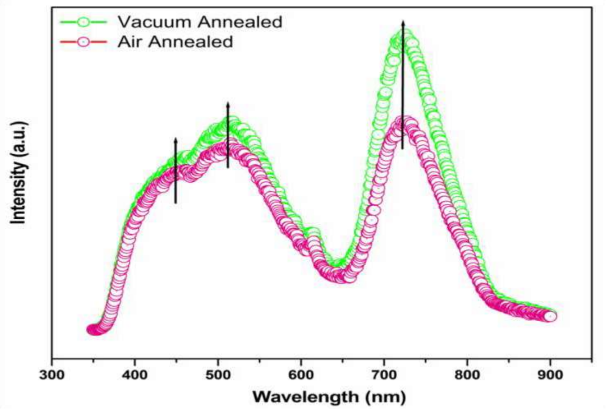

Figure 3.31. *Emission spectra of the MAS compounds observed after annealing in different atmospheres (vacuum and air)* **[180]**.

Figure 3.32 shows the luminescence decay profile of the MAS-600 compound at λ_{ex} = 250 nm and at different emission wavelengths viz., λ_{em} = 410, 460, 530 and 720 nm. Other decay curves recorded at 375,490, 560, 610, 780 and 850 nm emission peak are given in our report **[180]**. Most of the decay curves were found to be multi exponential and could be fitted into a sum of two or three exponentials following the decay equations 3.5,3.6 & 3.7. As in the case of MgO, the life time value, which has the maximum contribution among all, is assigned to the monitoring wavelength. Thus the lifetime values of the respective emission wavelengths can be given as 14.23 μs for P_1 (λ_{em} = 375 nm), 26.05 ms for P_2 (λ_{em} = 410 nm), 11.90 μs for P_3 (λ_{em} = 460 nm), 321.88 μs for P_4 (λ_{em} = 490 nm), 126 μs for P_5 (λ_{em} = 530 nm), 20 μs for P_6 (λ_{em} = 560 nm), 170 μs for P_7 (λ_{em} = 610 nm), 11.29 ms for P_8 (λ_{em} = 720 nm), 51 μs for P_9 (λ_{em} = 780 nm), 191 μs for P_{10} (λ_{em} = 850 nm) **[180]**. The lifetime values for MAS-1000 are included in Table-3.5.At low annealing temperature, few lifetime values were found to be in the order of several ms while at higher annealing temperature these life times values are significantly reduced to the order of μs. Later in $ZnAl_2O_4$ compound also we have observed similar trend in life time values with annealing temperature. We will explain there that this trend is due to presence of antisite defect centres which acts as a electron or hole trap and thereby delaying the recombination process. These antisite defects arise out due to inversion in the matrices, which is high at low annealing temperature while at high annealing temperature the major phase of the spinel is normal and inversion is less.

Table-3.5: Lifetime values of MAS compounds obtained at different annealing temperature

Annealing Temp.(in ^{0}C)	**T_1** (375 nm)	**T_2** (410 nm)	**T_3** (460 nm)	**T_4** (490 nm)	**T_5** (530 nm)	**T_6** (560 nm)	**T_7** (610 nm)	**T_8** (720 nm)	**T_9** (780 nm)	**T_{10}** (850 nm)
600	14.23 μs	26.05 ms	11.90 μs	321.88 μs	126.00 μs	20.00 μs	170.00 μs	11.29 ms	51.00 μs	191.00μs
1000	11.54 μs	13.25 μs	14.02 μs	91.74 μs	13.00 μs	9.28 μs	13.77 μs	5.5 ms	26.18 μs	13.02 μs

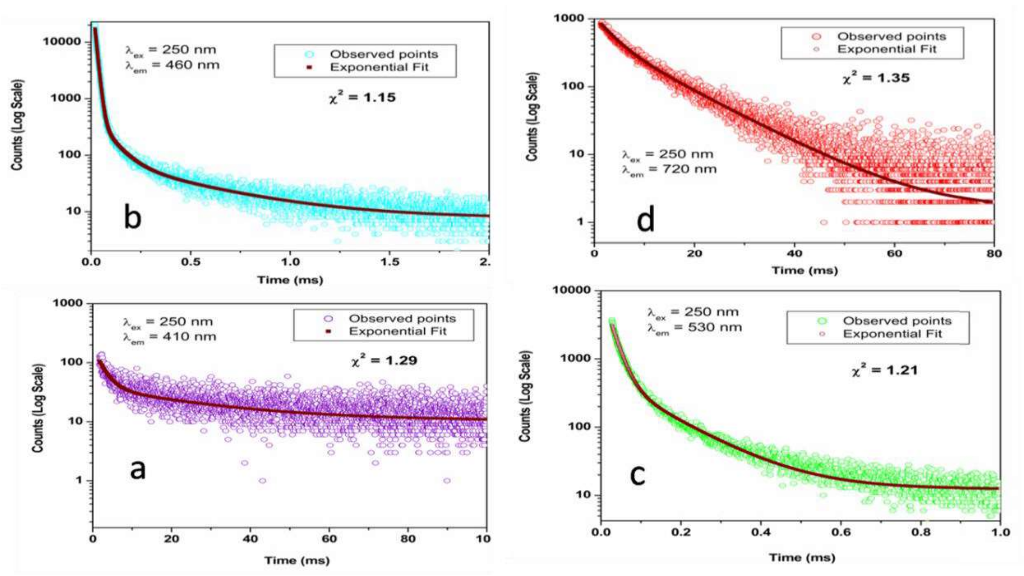

Figure 3.32. *PL decay curves of MAS compound prepared at 600^{0}C with λ_{ex} = 250 nm and λ_{em} = (a) 410, (b) 460, (c) 530 and (d) 720 nm* **[180]**

3.3.3 Time Resolved Emission Spectroscopy (TRES) [180]

Figure 3.33 shows the TRES spectra at different delay times viz. 2 μs, 100 μs ,200 μs, 400 μs, 600 μs ,1 ms, 5 ms, 10 ms and 50 ms with a constant integration time of 80 ms. As stated earlier,in case of MgO that most of the species fully decayed at an average time which is approximately three times of their respective life time (3τ).Thusat the very beginning of the decay time such as at 2 μs, all the emitting colours due to different defect states will be present in the spectra, since none of them have lifetime below 2 μs. The TRES spectra at 2 μs delay time is represented by Figure 3.33-I.However at higher time delay, such as at 100 μs; the species with lifetime values $\tau^{1}{}_{1}$= 14.23μs (at λ_{em} = 375 nm),$\tau^{1}{}_{3}$=11.90 μs (at λ_{em} = 460 nm) and $\tau^{1}{}_{6}$=20 μs (at λ_{em} = 560 nm) will be completely decayed as reflected by their decaying intensity at and around these wavelengths at100 μs delay timein Figure 3.33-II. Here the spectra consist of other species except those with above mentioned lifetime values. The other two species with higher lifetime values such as $\tau^{1}{}_{9}$=51 μs (at λ_{em} = 780 nm) and $\tau^{1}{}_{10}$=36 μs (at λ_{em} = 850 nm) also started decaying in this time region (100 μs) and at higher delay times such as 200 μs and 400 μs, they almost disappeared as seen in Figure 3.33-III & IV.The next component with comparably higher life time value is that with $\tau^{2}{}_{5}$= 126 μs (at λ_{em} = 530 nm) and at higher decay times such as at ~ 400 & 600 μs as shownin Figure 3.33-IV & V,a disappearance of the spectra in the 530 nm region was also observed. Therefore, it can be said that in the time region of 2 μs -

100 μs, the decaying species are with life time values $\tau^1{}_3$=11.90 μs, $\tau^1{}_1$= 14.23μs, $\tau^1{}_6$=20 μs, $\tau^1{}_{10}$=36 μs and $\tau^1{}_9$=51 μs and above 100 μs delay time and in the time region 200-400 μs, these species completely decayed and the new decaying species is $\tau^2{}_5$= 126 μs. Now if we subtract the TRES spectra at 2 μs delay time from that at 100 μs delay time, it will give a spectra mixed of emission at 375 nm, 460 nm, 530nm, 560 nm, 780 nm and 850 nm as shown in Figure 3.34-A. In the similar manner, if we subtract the TRES at 200 μs delay time from that at 400 μs delay time, the spectra obtained consists of emission at 530 nm as shown in Figure 3.34-B. It is to be noted that in this time region 200-400 μs, along with the 530 nm emitting species, another two species with higher life time values viz. $\tau^2{}_7$= 170.04 μs (at λ_{em} = 610nm) and $\tau^2{}_4$= 321.88 μs (at λ_{em} = 490nm) also started decaying as seen by their weak emission peak at 610 nm and 490 in Figure 3.34-B. When Figure 3.34-B was subtracted from Figure 3.34-A, a spectra consisting of emission at 375 nm, 460 nm, 560 nm, 780 nm and 850 nm was observed, as shown by Figure 3.34-C. Next two species are with relatively higher lifetime values i.e. $\tau^2{}_8$= 11.29 ms (at λ_{em} = 720 nm) and $\tau^2{}_2$=26.05 ms (at λ_{em} = 410 nm). As shown in Figure 3.33-VI, VII, VIII & IX, after a delay time of about 1 ms, all the TRES consists of two prominent peaks; one at 410 nm and other at 720 nm. However at higher delay time such as 10 ms, the intensity of the 720 nm peak kept on decreasing and disappeared at 50 ms delay time. After 50 ms delay, the spectra consists of a single component with $\tau^2{}_2$=26.05 ms emitting at 410 nm. Subsequently, Figure 3.33-IXrepresents the TRES of the species with lifetime, $\tau^2{}_2$=26.05 ms. At further higher delay time, the intensity kept on decreasing. When TRES at 5 ms delay time was subtracted from that at 50 ms, the TRES of the species with $\tau^2{}_8$= 11.29 ms was obtained as shown in Figure 3.34-D, emitting at 720 nm. Thus, TRES study confirmed the presence of all these emission components as observed from Gaussian fitted spectra in Figure 3.26**.**

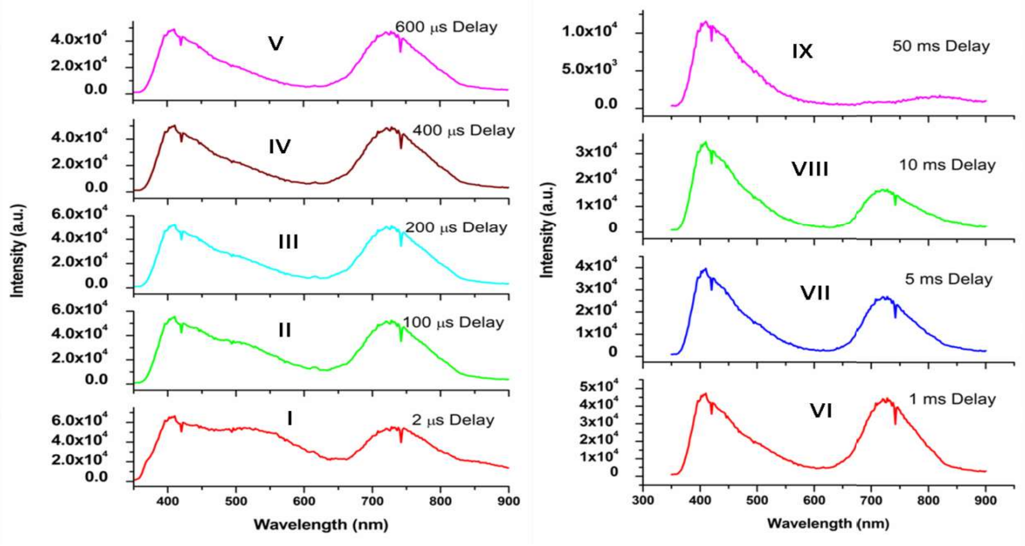

Figure 3.33. Time Resolved Emission Spectra (TRES) at different delay time **[180]**

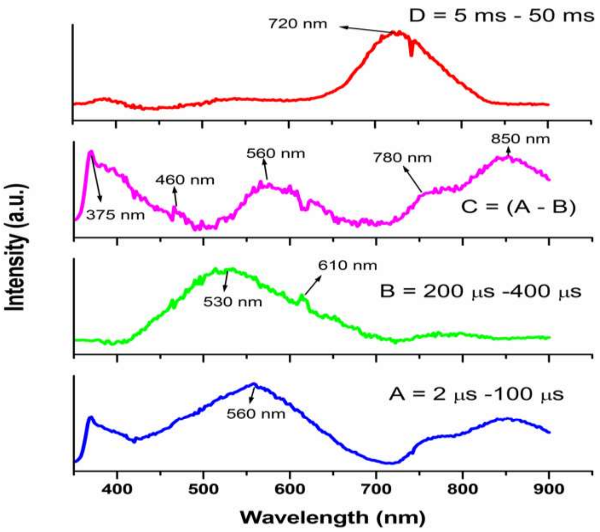

***Figure** 3.34. Time Resolved Emission Spectra of the respective species* **[180]**.

3.3.4. Electronic Structure and Band Gap Energy

The detail of the DFT calculation methodologies for various defect centres in MAS are given in our published report **[180]**. A pictorial summary is presented in Figure 3.35, observed from the density of state (DOS) analysis based on DFT calculations on both normal and inverse spinel, with different kind oxygen vacancies having different charges. As shown in Figure 3.35, both for normal and inverse phase, two filled states due to the neutral (V_O^{0}) and singly positive charge oxygen vacancies (OVs) (V_O^{+1}) have appeared above the valence bond. On the other hand two shallow vacant states (they are very close to each other and thereby showing a single band) just below the conduction band have also appeared due to the singly and doubly positive charged OVs. In the middle of the band gap two vacant deep defect states due to V_O^{+1} and V_O^{+2} are found to be exist in case of normal phase. In case of inverse phase, the deep states due to V_O^{+2} is found to be very close to the shallow states and almost merge with them, showing as a single broad band. This representation of defect states will be considered as basis to understand the PL profile.

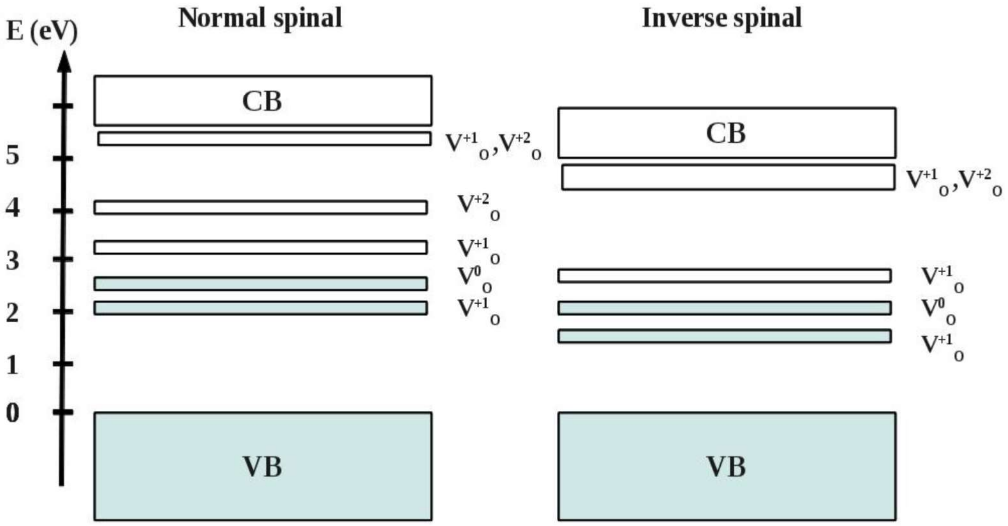

Figure 3.35. *Overall summary of the electronic structures inside the band gap due to V_O^0, V_O^{+1} and V_O^{+2} in the normal and inverse spinel of $MgAl_2O_4$. Light grey coloured bands are filled with electrons and white bands are empty* **[180]**.

3.3.5. Origin of the different colour components and their tunability with a proposed model:

3.3.5.1 Origins of different colour components.

In the present annealing temperature range during synthesis, MAS mostly used to be formed as a mixed spinel where both Al and Mg atoms have tetrahedral and octahedral co-ordination depending on the inversion rate. As reported earlier, a control over the inversion rate of the Mg^{2+} and Al^{3+} cations inside the spinel crystallographic network is possible by varying the synthesis condition and annealing temperature **[196]**. Now since in the mixed spinel, fraction of the Mg^{2+} ions are in octahedral co-ordination (inverse phase), it is interesting to compare the emission characteristics of MAS in the inverse phase with that of MgO; where all the Mg^{2+} have octahedral co-ordination as reported in our previous report on MgO **[161]**. This will certainly help in understanding the luminescence phenomenon, which occurs surrounding the Mg^{2+} coordination environment. On the similar lines, if we compare PL of α-Al_2O_3 with MAS normal phase, information related to emission behavior surrounding the octahedral Al atoms in the mixed spinel can be achieved [**132**]. The emission at 375 nm (P_1) is in close resemblance with the F^+ centre emission in MgO **[161]**. The lifetime ($\tau^1{}_1$= 14.23 μs) value also fall in same order as that of singly ionized oxygen vacancy ($V_O{}^{+1}$) or F^+ centre and therefore P_1 ($\lambda_{max} \approx 375$ nm) is attributed to the $^2T_{1u}$-$^2A_{1g}$ transitions of F^+ centre around the octahedral Mg atom. Similarly P_5 ($\lambda_{max} \approx 530$ nm) can be attributed to the F-centre surrounding the octahedral Mg atom as observed in case of MgO **[161]**. It is also clearly visible in Figure 3.35 that the filled states due to the neutral F centres ($V_O{}^0$) are placed above the states due to the singly charged F^+ centres ($V_O{}^{+1}$). The long lived decay $\tau^2{}_4$= 126 μs (at λ_{em} = 530 nm) of this F-centre compared to the F^+ centre at 375 nm can be explained in terms of forbidden transition of the F centres. The electronic structure of the F centre can be treated as a helium atom where the ground-state configuration $(ls)^2$ corresponds to the term ^1S_O and the excited states can be generated by promoting one electron into a 2s or a 2p state, resulting excited-state configurations 1s2s or 1s2p. These configurations correspond to both singlet and triplet states (^1S, ^3S, ^1P, and ^3P). The emission of F centre is due to ^3P -^1S transition which is forbidden **[197]**. The emission at 410 nm (P_2) can be attributed to the F centre associated with the distorted Al octahedral sites. The long lifetime value $\tau^2{}_1$=26.05 ms (at λ_{em} = 410 nm) is also very similar to the one observed by Itou *et al.,* in α-Al_2O_3 **[132]**. Since the co-ordination environment of the Al atoms in α-Al_2O_3 closely resemble with that in the normal phase of $MgAl_2O_4$ (where both of the Al atoms have octahedral co-ordination), the blue shifting of the F centre emission surrounding the Al-O_h (O_h = octahedral) compared to the Mg-O_h can be explained by considering the higher band gap energy of normal phase as compared to the inverse phase, shown in Figure 3.35. The emission at 560 nm (P_6) can be attributed to the $F_2{}^{2+}$ centres surrounding the octahedral Al^{3+} ions which are nothing but a pair of F^+ centres **[198, 199]**. The emission around 460 nm (P_3) is due to the charge transfer transition between Al^{3+} at octahedral sites and its surrounding O^{2-} ions **[198, 199]**. The green emission peaks at $\lambda_{max} \approx 490$ nm (P_4) can be assigned to transition of an electron to a hole trapped at Mg ion vacancy **[200]** while the yellow-orange emission peak (P_7) at λ_{em} = 610 nm can be assigned to the oxygen vacancies resulting from the existence of Mg_{Al} antisites **[160]**, respectively. The most important task is to assign the P_8 (720 nm), P_9 (780 nm) and P_{10} (850 nm) emission components. Since the P_{10} (850 nm) band was found to disappear at higher annealing temperature (Figure 3.26), this emission should originate from some kind of surface defect state which is annealed at higher annealing temperature. Obviously these longer wavelength (P_8 and P_9) emissions are associated with some kind of defects which exist deeply inside the band gap. Kim *et al.,* has also shown similar red emission at 680 nm in isostructural $ZnGa_2O_4$ **[201]**. They have shown that this emission with long decay time will only occur in case of distorted octahedral site (where there is an oxygen vacancy surrounding the Ga atom in octahedral site) and the electronic transition will be from O^{2-} ion to the singly charged oxygen vacancy ($V_O^{\cdot}$ or V_O^{+1}) confirmed by EPR spectroscopy. We have also observed an asymmetric signal at g ≈ 1.9967 in EPR spectroscopy as shown in Figure-3.36, due to paramagnetic $V_O^{\cdot}$. As stated earlier in the summary of DFT calculation (Figure-3.35), inside the band gap of the MAS compound, two vacant deep defect states and two vacant shallow defect states are present due to the singly and doubly positive charged oxygen vacancies. Electrons from the conduction band may also be trapped into these vacant shallow and deep states. Since the energy gap between these shallow and deep states are very close to the observed emission wavelengths in the red-NIR region, we believe transition between these states are responsible for the P_8 (720 nm) and P_9 (780 nm) bands. As seen in Figure-3.35, the vacant deep defect states due to V_O^{+1} (or $V_O^{\cdot}$) is placed below the vacant states due to V_O^{+2}. Therefore the P_8 (720 nm) band can be assigned to the transition of electron trapped at the shallow states to the vacant deep sates arising due to singly charged paramagnetic V_O^{+1}. On the other hand the P_9 (780 nm) band can be assigned to the transition of an electron trapped at the deep states of V_O^{2+} to the vacant deep sates of paramagnetic V_O^{+1}. In the next section, the annealing temperature effect on the emission profile of MAS compound will be explained.

3.3.5.2 Tunability with annealing temperature and atmosphere and with varying composition.

As shown in annealing temperature variation PL spectra in Figure 3.26, the intensity of the 720 nm and 780 nm band were enhanced when the annealing temperature was increased from 600 °C to 1000 °C. As stated in the earlier section that these two bands are linked to the paramagnetic singly charged oxygen vacancy, V_O^{+1} or ($V_O^{\cdot}$), hence the concentration of $V_O^{\cdot}$ also has to be more at higher annealing temperature leading to more intense peaks in the NIR region. In this context, Electron Paramagnetic Resonance (EPR) spectroscopy is a very useful technique to identify and quantify the paramagnetic species like $V_O^{\cdot}$ as shown in Figure 3.36. An asymmetric signal at g ≈ 1.9967 is shown by all the compounds which can be attributed to the paramagnetic singly charged oxygen vacancy ($V_O^{\cdot}$) **[161,163]**. The intensity of the signal was found to increase with increasing annealing temperature. It is worth to be noted here that all the positively charged defect centres will get stabilized through formation of a nearby negatively charged cationic vacancy such as V_{Mg}^{2-}, V_{Al}^{3-}, Mg_{Al}^{1-} and O_i^{2-} etc. This confirms that, this EPR signal which arise due to $V_O^{\cdot}$ surrounding the distorted Al -O_h & Mg -O_h sites must be responsible for the red-NIR emission [**201]**. As stated earlier that these spinel compounds synthesized at the mentioned annealing temperatures are mixed spinel in nature and at low annealing temperature (≈ 600 °C), percentage of inverse phase is more while at higher annealing temperature (≈ 1000 °C) percentage of normal phase is more. Now, since the sharing of the octahedral (O_h) sites by Al atom will be doubled in the normal phase than in the inverse phase, a transformation of inverse to normal form with annealing temperature will also be accompanied by a change in coordination of the tetrahedral (AlO_4) to octahedral [AlO_6]. Thus through this path of transformation, the co-ordination around Al^{3+} ions will be 4≤ Al-Coordination ≤6 and Al atoms which are newly placed at the octahedral sites, will not have perfectly octahedral symmetry or some of them will have distorted octahedral symmetry (as the co-ordination of Al will be ≤6). On the other hand for Mg atom, the reverse process i.e. a change in coordination of the octahedral [MgO_6] to tetrahedral (MgO_4) will happen and the perfectly octahedral [MgO_6] will now become distorted. Therefore the Al^{3+} and Mg^{2+}ions at distorted O_h sites will always be associated with some oxygen vacancy. Henceforth distortion around the Al-O_h and Mg-O_h sites will be increased as the temperature is increased from 600 °C to 1000 °C, which is reflected in the sharp increase in intensity of the red-NIR band at higher temperature and also in EPR signal intensity.Thus tuning of distortion around octahedral sites of the spinel of MAS compound might be responsible for the tuning of emission colour at higher annealing temperature.

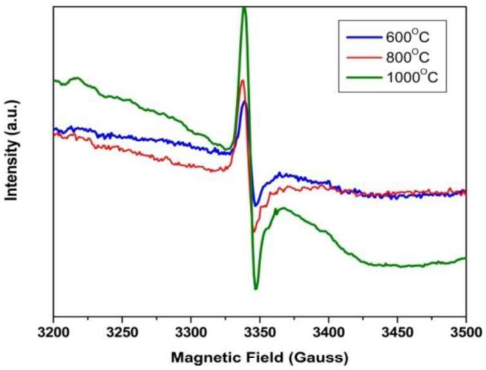

Figure 3.36*: EPR spectra of MAS samples at different annealing temperature* ***[180].***

Now on the basis of above conclusion , the explanation of emission behavior with different compositions and different annealing atmospheres can be given. Since different type of oxygen vacancies are responsible for the emission in the 410nm, 530 nm, 720 nm, 780 nm regions, annealing of the MAS samples in vacuum atmosphere will definitely lead to an increase the intensity around these regions as observed in case of the vacuum annealed MAS sample in Figure 3.31. Now the emission characteristics of the compounds with different Mg/Al molar ratio viz. 0.98/2.00 and 1/1.96 can be given on the basis of cationic vacancies. For these composition ratio, there will be negatively charged cationic vacancies such as V_{Mg}^{2-} or V_{Al}^{3-} which will lead to formation of positively charge oxygen vacancies for charge neutrality of the system. This is reflected in the increase in intensity in the 410nm, 530 nm, 720 nm, 780 nm regions for both Mg^{2+} (for 0.98/2.00) and Al^{3+} (for 1/1.96) cations deficient MAS compounds in Figure 3.30. Since these cationic vacancies may lead to formation of oxygen vacancies in their nearest neighbor because these oxygen atoms are shared by both Mg^{2+} and Al^{3+} ions for their co-ordination, a deficiency in Mg^{2+} ion from its lattice site will initiate the vacancy of the oxygen atoms from the Al^{3+} co-ordination and vice versa. The higher intensity at 410 nm with $\frac{Mg}{Al} = \frac{0.98}{2}$ in Figure 3.30, which is due to F centre emission surrounding the octahedral Al atom supports this argument. Similarly with $\frac{Mg}{Al} = \frac{1}{1.96}$, an enhancement in intensity at 530 nm, which is due to the F centre emission surrounding the Mg^{2+} atom was also observed in Figure 3.30. Again for both of the compositions the intensity in the red-NIR region is increased. This is due to red-NIR emission is linked to the V_O° surrounding the distorted Al -O_h & Mg -

O_h sites. Although a deficiency of Al atom with $\frac{Mg}{Al} = \frac{1}{1.96}$ is found to be more efficient in creating V_O°, compare to that with $\frac{Mg}{Al} = \frac{0.98}{2}$as reflected by the higher intensity.

3.3.5.3 Photo conversion of F to F$^+$ centres: Excitation tunable emission characteristics

The emission characteristic at different excitation wavelength indicates that the electrons might be involve with some kind of trapping and de trapping mechanism within the different electron trapped states inside the band gap. The continuous increase in intensity of the P_8= 720 nm band up to 250 nm excitation wavelength followed by a decay in Figure 3.28 indicates that the electrons started getting more and more trapped into the states responsible for P_8= 720 nm emission when excitation wavelength was increased to 250 nm where a maximum intensity was observed. Now the disappearance of the P_8= 720 nm band beyond 300 nm, where only P_9= 780 nm band exist indicates that de trapping of the electrons from the P_8= 720 nm states has been occurred, followed by re trapping of the same electrons into the states responsible for P_9= 780 nm band. The maximum intensity of these bands at 250 nm excitation wavelength indicated that a photo ionization process might be involved at this excitation where more free electrons are released and getting trapped into the different defect states in the band gap.

Now as in our previous work in MgO, we have observed a photo conversion process of F to F$^+$ centre at ~ 250 nm **[161]**, a parallel comparison can be drawn with emission properties MAS compound. At 250 nm excitation, the F centre will be converted to F$^+$ centres following the equation $F + h\upsilon \leftrightarrow F^+ + e^-$. Similarly in MAS we believe that the F centres surrounding the Mg atom (distorted octahedral) undergo a photo conversion at 250 nm excitation wavelength and the released electrons may be promoted to the conduction band or may be trapped into the vacant shallow and deep defect states arise due to V_O^{+1} and V_O^{+2}, as shown in Figure 3.35.

3.3.5.4 Proposed Model

Now to explain all these trapping- de trapping mechanism and the low temperature emission behavior, a model is proposed as shown in Figure 3.37, based on all the theoretical and experimental results observed till now. A photo ionization of the F to F$^+$ centre at 250 nm excitation wavelength following the equation $F + h\upsilon \leftrightarrow F^+ + e^-$ is shown in this model. The green bent arrows show that the released electron may either go to the conduction band or may be trapped into the shallow and deep trap levels. As shown in the model the P_8= 720 nm emission band arise due to transition of electron trapped at shallow states to the V_O^{+1} at distorted octahedral sites, while in case of P_9= 780 nm band, the transition is from a deep trap level. Now at 250 nm excitation, the population of these states will be maximum by trapping of electrons coming from the photo conversion of F centres and thereby sharply increasing the intensity in the red-NIR region. However when the excitation wavelength was tuned to 310 nm or above, the electrons which were trapped in the shallow states will de trapped followed by re trapping in the deep states responsible for 780 nm emission. This explains the presence of two emission band at 250 nm excitation wavelength where as at 310 nm excitation only one band is present.

This model can also explain the low temperature emission characteristic can. As seen from Figure 3.29 at room temperature the intensity of the red-NIR region is more compare to the blue-green region while at low temperature a reverse trend is observed. In our DFT summary in Figure 3.35, it has been shown that the conduction band and shallow sates are energetically very close. Thus at room temperature there is possibility of the electrons from conduction band to go to the shallow trap states and thereby increasing the red-NIR emission intensity. However, at low temperature this process become more difficult, which can explain the low temperature photoluminescence behavior.

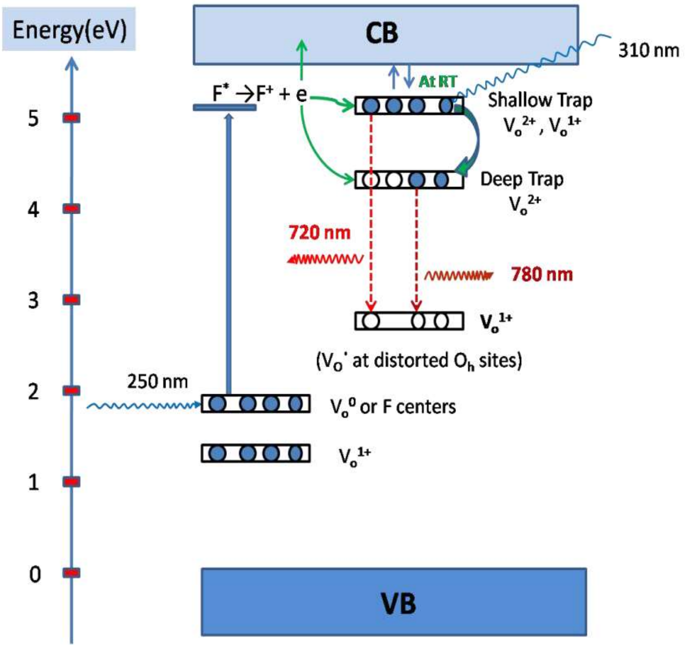

Figure 3.37: *Proposed model for trapping de trapping mechanism* ***[180]***.

3.4. Synthesis and Optical properties of $ZnAl_2O_4$ (ZA)

3.4.1. Synthesis and characterization of $ZnAl_2O_4$

3.4.1.2. Synthesis

Zinc nitrate [Zn $(NO_3)_2.6H_2O$] (99.0%, AR grade, s.d.fine-chem.ltd.), Aluminum nitrate [$Al(NO_3)_3.9H_2O$](98%, AR grade, S.d.fine-chem.ltd.), citric acid ($C_6H_8O_7\cdot H_2O$) (99.7%, AR grade, Chemico fine chemicals) (used as a fuel here) are the precursor materials and taken in the molar ratio 1: 2:10 for the synthesis of $ZnAl_2O_4$ compound**.** The procedure is similar to that of $MgAl_2O_4$.Initially separate solutions of the metal nitrates and citric acid were prepared by dissolving stoichiometric quantities in quartz double distilled (QDD) water. Then these solutions were mixed in a beaker with constant stirring with a magnetic stirrer for about 1 hour after which a clear solution was observed. The citric acid solution was then added to this mixed solution under vigorous stirring and left for heating at 80ºC for 5 hours after which a highly viscous gel formation was observed. The gel was then heated on a heating mantle at a temperature of 150^0C where the combustion took place after which an ash-like product was obtained. The ash-like product was then ground in an agate mortar and kept for calcining at 600ºC for 8 hours and then a fine white powder was obtained. The phase purity of the compound obtained at 600ºC was confirmed from X-ray diffraction (XRD) study. After confirmation of the pure product formation, the compound was further annealed at different higher temperatures viz.750ºC, 1000ºC, 1200ºC and 1300ºC respectively which were subjected to different physical characterization such as PL, PALS and EPR after each heating treatment.

3.4.1.2 Phase purity: X-Ray Diffraction

The Rietveld fittings of XRD patterns of $ZnAl_2O_4$ prepared at 750ºC is shown in Figure 3.38, which indicates formation of single-phase compound with space group Fd-3m by the present sol–gel-combustion study. The strong and sharp diffraction peaks of the compound indicate that it is well crystallized.

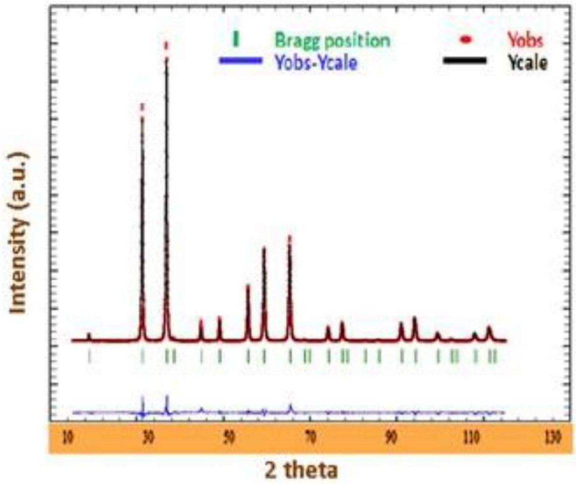

Figure. 3.38*: Rietveld fittings of XRD patterns of the* $ZnAl_2O_4$.

3.4.2. Emission and life time spectroscopy

Figure 3.39a & 3.39b represent the room temperature PL spectra of the ZA compounds prepared at different annealed temperatures and their respective CIE chromaticity coordinates. From Figure 3.39a, it is clearly visible that there are different emission components present in the spectra which in combination give rise to broad emission profiles. Now to specifically denote the colour characteristics of all the ZA compounds obtained after annealing at different temperature, the CIE chromaticity coordinates were evaluated adopting standard procedures **[202]**. In Figure 3.39b, the values of x and y coordinates for different thermally annealed ZA compounds are denoted by an 'asterisk', which was found to change from bluish to near white, as the annealing temperature was increased in the row 750^0C → 1000^0C → 1300^0C. This tunable colour characteristics at different annealing temperature renders this particular ZA as a potential phosphor material whose colour characteristics can be controlled or tune in between blue and white depending on annealing temperature. This observation also renders this particular ZA compound as a potential candidate for optical thermometry or optical based thermal sensor materials.

In the emission spectra (Figure 3.39a), different peaks or humps are visible at different wavelengths regions, starting from the Ultraviolet (UV) region to Visible to Near Infrared (NIR) region viz. UV (P_1) at $\lambda_{max} \approx 375$ nm, violet (P_2) at $\lambda_{max} \approx 410$ nm, blue (P_3) at $\lambda_{max} \approx 440$ nm, cyan (P_4) at $\lambda_{max} \approx 490$ nm, green (P_5) at $\lambda_{max} \approx 530$ nm, yellow (P_6) at $\lambda_{max} \approx 590$ nm, red (P_7) at $\lambda_{max} \approx 720$ nm and the NIR components at $\lambda_{max} \approx 780$ nm (P_8) and $\lambda_{max} \approx 850$ nm (P_9) respectively. These multicolour emissions indicate the presence of various electronic states inside the band gap; arising due to various defect centres present in the material. Each colour arises due to a different electronic transition. In Figure 3.40, the emission spectrum of ZA-750 was decomposed into the above nine emission peaks using Gaussian peak fitting. To confirm their (the emission components) existence in the complex spectra, their lifetime and TRES studies were carried out which is the best way to isolate each and individual emitting components from the complex broad emission spectrum as done earlier in case of MAS **[180]**.

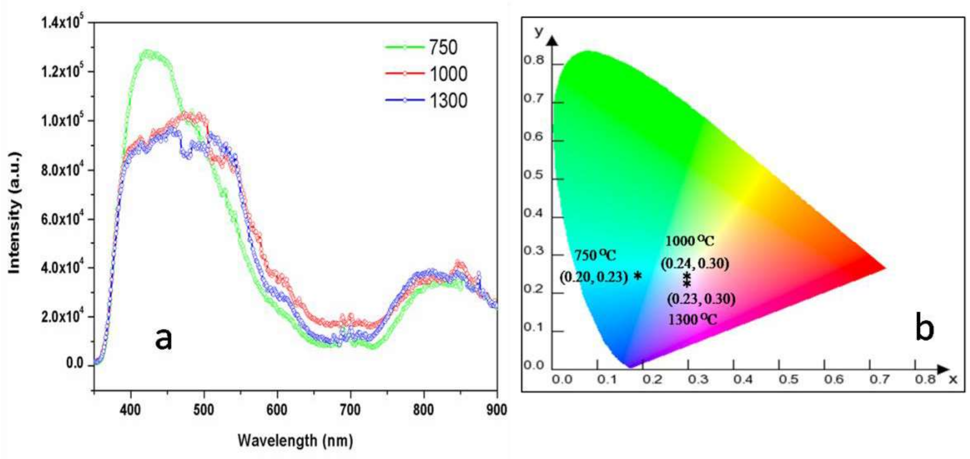

Figure 3.39. *(a)Emission spectrum of ZA annealed at different temperature with λ_{ex}=250 nm and (b) CIE chromaticity diagram for the ZA phosphor at different temperatures which show a tuning of colour coordinate from bluish to near-white*

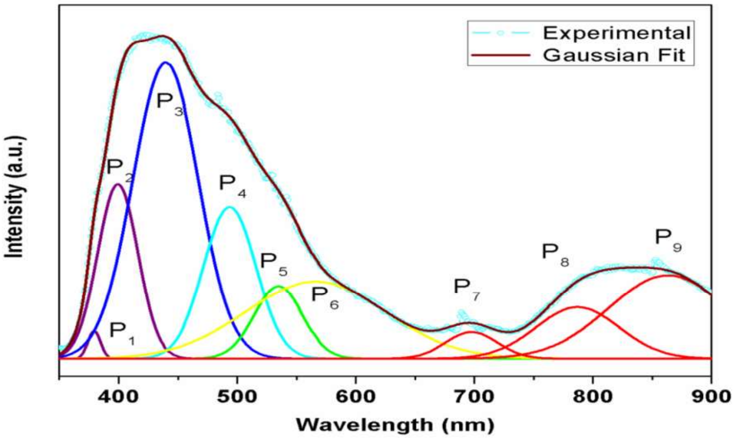

Figure 3.40. *Gaussian fitting of emission spectrum of ZA-750*

Similar to MgO and $MgAl_2O_4$, in ZA compound most of the bands are overlapped by either the preceding one or by the next band or by both. Thus instead of getting a single lifetime value at particular emission and excitation wavelength, here also multiple life time values were obtained at all the emission maximums. Among these values, the lifetime value, which has the maximum contribution among all is assigned to the monitoring wavelength (emission peak under consideration). Thus, the lifetime values with the highest contribution for each of the wavelength are included in Table 3.6 for different thermally annealed ZA compounds. At low annealing temperature the lifetime of the defect centres were found to be high (of the order of several ms) while at higher annealing temperature the life times are significantly reduced (of the order of μs). This observation suggest that at low annealing temperature the compound can be treated as long persistent phosphor materials while at high annealing temperature the compound can be treated as short persistent phosphors **[203]**. This is a very important observation since depending on the annealing temperature the decay kinetics of the luminescence can be changed

Table-3.6: Lifetime values for different emission components at 250 nm excitation wavelength.

Compound	**T_1** (375 nm)	**T_2** (410 nm)	**T_3** (450 nm)	**T_4** (490 nm)	**T_5** (530 nm)	**T_6** (600 nm)	**T_7** (730 nm)	**T_8** (780 nm)	**T_9** (850 nm)
ZA -750	14.23 μs	2.08 ms	13.99 ms	48.13 ms	1.643 ms	217.57 μs	-	424 μs	359.95 μs
ZA -1000	14 μs	90.17 μs	12.79	89.13 μs	204.48 μs	11.21 μs	3.5 ms	869.97 μs	23.83 μs
ZA -1300	12.81 μs	70.56 μs	11.80 μs	16.36μs	113.93 μs	10.72 μs	1.26 ms	287.56 μs	11.80 μs

3.4.3 Time Resolved Emission Spectroscopy (TRES)

TRES spectra of ZA-750 and ZA-1300 are shown in Figure 3.41a and 3.41bat different delay time. General approximation is that most the excited species fully decay at an average time, which is approximately three times of their respective lifetime (3τ). Since for both the compounds the lifetime values in Table-3.6are greater than 10 μs, it can be assumed that all the emitting colours due to different defect states will be present in the spectra at the very beginning of the decay time such as at 2 μs. The TRES spectra at 2 μs delay time is shown in Figure 3.41. For the low temperature annealed ZA-750 compound in Figure 3.41a, it can be observed that very little change is there when the delay time is increased from µs to ms. This is because for ZA-750, most of the emitting components are having lifetime in the ms region. The short lived components with lifetime in µs range will be decayed fast, whilethe long lived components with lifetime in ms range will be decayed late. Thus in the 5-500 µs range, if we subtract the TRES spectra at 5 µs delay time with that at 500 µs delay we will have those components in the decayed spectra as shown in Figure 3.42a,while in the 500 µs -5 ms range, the components are 420 nm and 850 nm as shown in Figure 3.42b. At higher delay time such as 60 ms two components with higher lifetime such as 450 and 490 still exist as shown in Figure 3.43a. Now in the time interval 5 ms-60 ms the P_3component i.e. 450 nm will decay faster than the P_4 component (490 nm) as shown by the TRES spectra in Figure 3.43b . The other two components which also decayed in this time interval are P_7 (690 nm) and P_8 (780 nm) components as predicted by their lifetime values from Table-3.6.

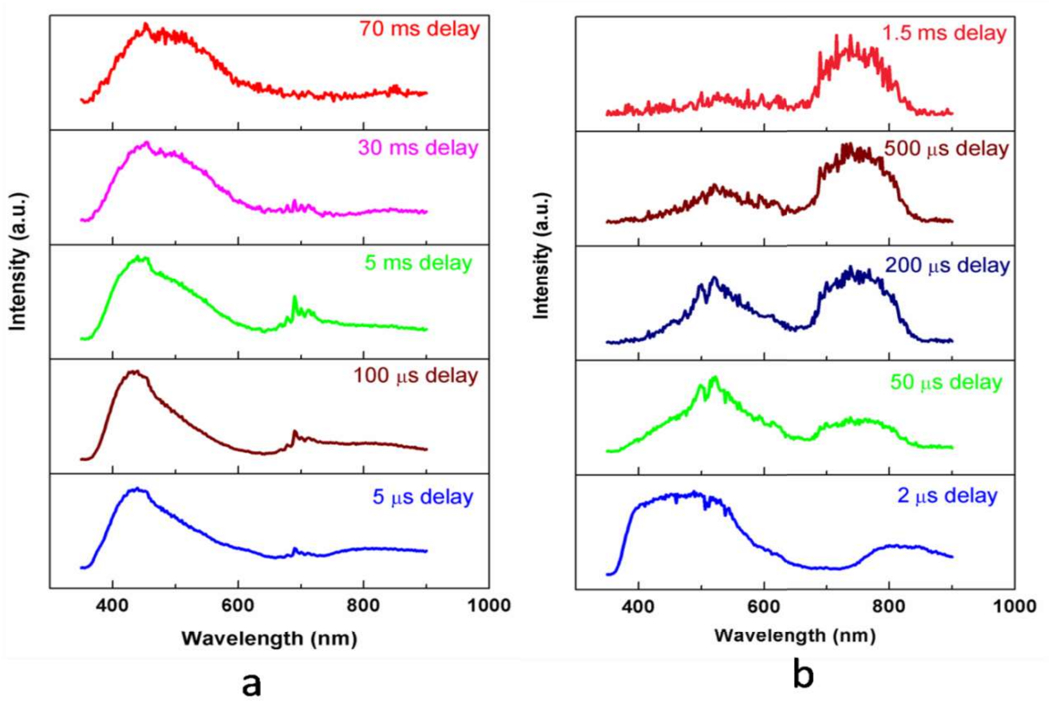

Figure 3.41. Time Resolved Emission Spectra (TRES) of (a) ZA-750 and (b) ZA-1300 at different delay time.

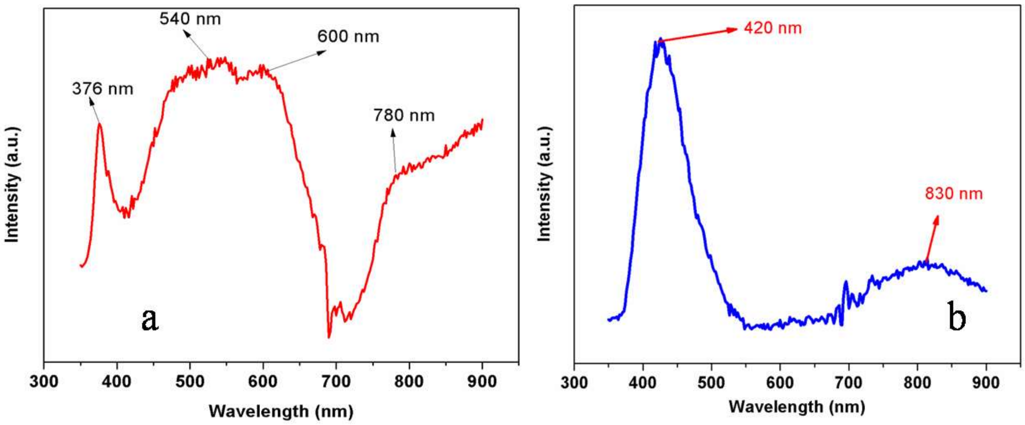

Figure 3.42. *Time Resolved Emission Spectra (TRES) of ZA-750 in (a) 5-500 µs region and b) 500 µs - 5 ms time interval*

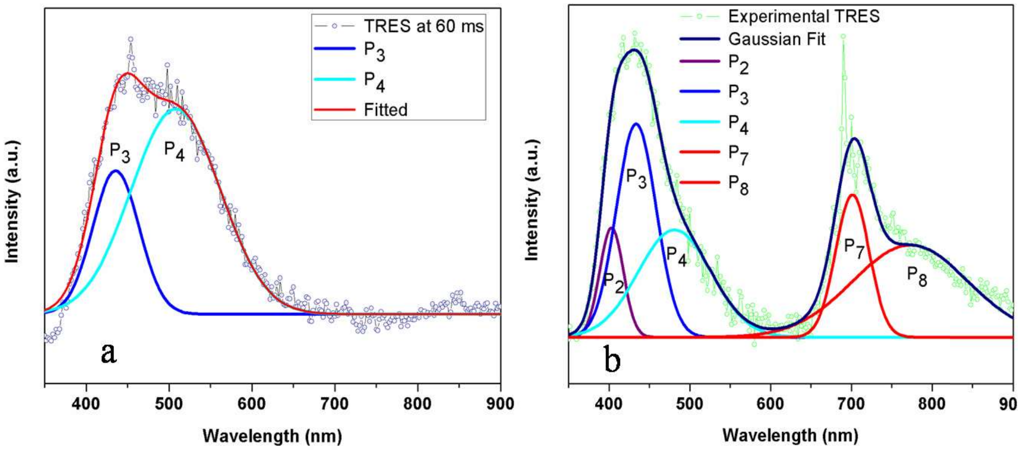

Figure 3.43. *Time Resolved Emission Spectra (TRES) for ZA-750 at a) 60 ms delay and b) in the 5ms -60 ms time interval*

Now when the compound is heated at higher temperature such as 1300^{0}C, the lifetime of most of the components decrease drastically from ms order to µs. From Figure 3.41, it is clearly visible that even in the µs delay time such as 500µs most of the components vanished. Another interesting observation for this compound annealed at higher temperature is that a new peak in the red region at 700-800 nm range was observed which was absent for the compounds annealed at low temperature. Since the lifetime values of the 400, 450,490, 600 and 850 nm components are in the 10-15 µs region they are decayed in the 2-75 µs interval as shown in Figure 3.44. While the components such as 530 (P_5), 720(P_7) and 780 (P_8) nm with higher delay time will be decayed at higher delay time. In Figure 3.45, two TRES at two different delay time viz. 400 µs and 1.7 ms are presented which found to be consisted of three components 530 (P_5), 720 (P_7) and 780 (P_8) nm. Among them, the 530 (P_5) component is having lower lifetime value and that is why at 1.7 ms delay time, the component was found to be almost decayed (Figure 3.45 b).

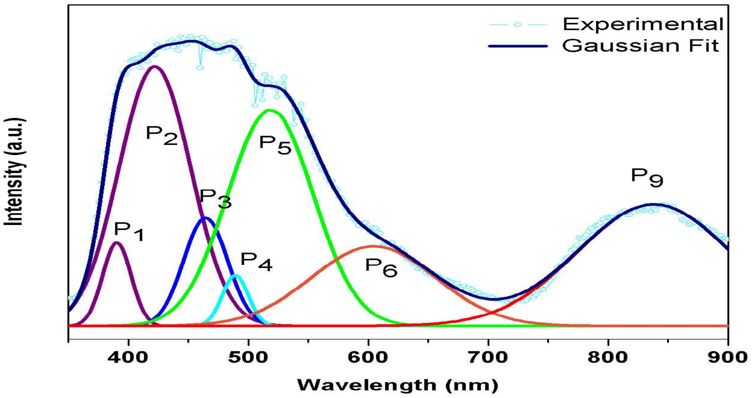

Figure 3.44. *Time Resolved Emission Spectra (TRES) of ZA-1300 in the 2μs-75 μs time interval*

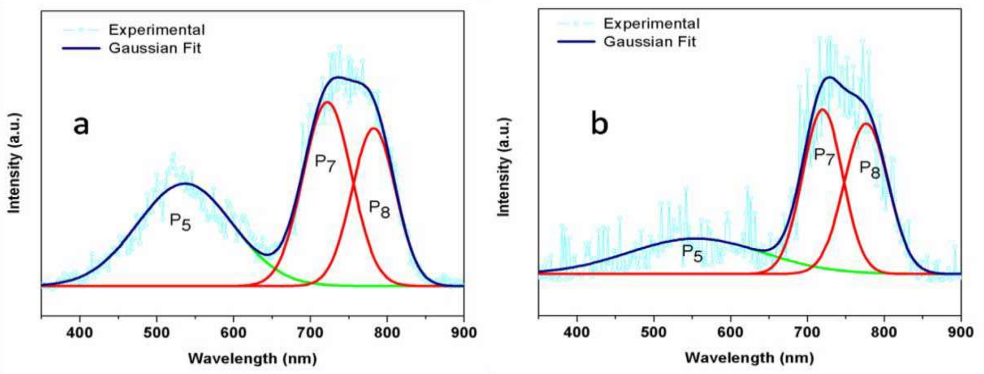

Figure 3.45. *Time Resolved Emission Spectra (TRES) of ZA-1300 at (a) 400 μs delay and (b) at 1.7 ms delay*

3.4.4 Positron annihilation lifetime spectroscopy (PALS)

PALS measurements have been carried out at room temperature using two BaF_2 scintillation detectors connected to a fast–fast coincidence system. The ^{22}Na positron source (~ 10 μCi) deposited in a thin Kapton foil was kept inside the powder sample in a aluminum vial and the vial was kept between two BaF_2 detectors. The resolving time measured with ^{60}Co source was 250 ps for the positron window settings and the time calibration was 12.5 ps/channel. The spectrum with approximately 2 x 10^6 counts was acquired for each measurement and data was analyzed using PALSFIT **[204]** analysis program. Figure 3.46 represents typical PALS spectra for ZA-750, ZA-1000 & ZA-1200.

The positron lifetime spectrum is a multi-exponential decay curve given as

$$F(t) = \sum_{i=1}^{k} \frac{I_i}{\tau_i} e^{-\frac{t}{\tau_i}}, \qquad (3.11)$$

where $F(t)$ represents the number of counts at time t, k is the number of exponential decay components, τ_i is the lifetime of the ith component, Ii is the corresponding intensity.

This multi-exponential function is convoluted with instrumental resolution function, *R(t)* (250ps). The lifetime spectra were fitted to four discrete components to obtain the best fit.

Results are shown in Table 3.7. The average lifetime τ_{av} and the bulk lifetime τ_B (given in Table-3.8) were calculated as follows:

$$\tau_{av}= (I_1\tau_1+I_2\tau_2)/(I_1+I_2) \qquad (3.12)$$

$$\tau_B=(I_1+I_2)/(I_1/\tau_1+I_2/\tau_2) \qquad (3.13)$$

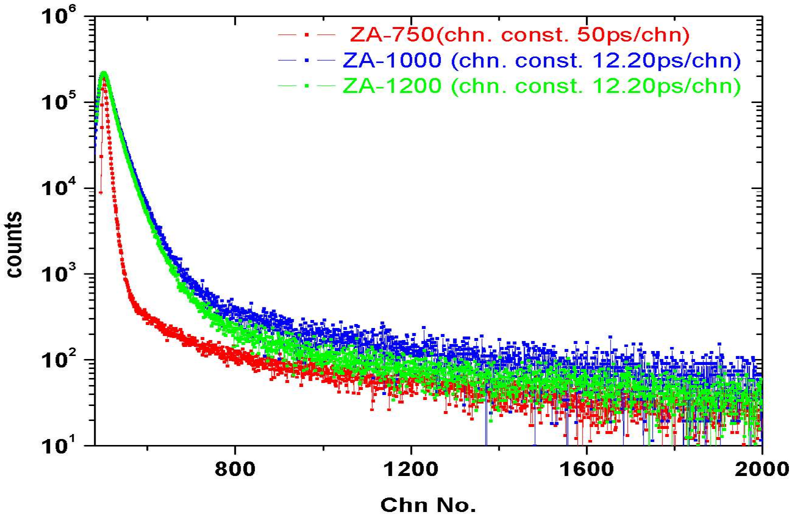

***Figure 3.46** : Typical PALS spectra for ZA-750, ZA-1000 and ZA-1200*

Table 3.7: Positron lifetimes of $ZnAl_2O_4$ (ZA) compounds annealed at different temperature.

Sample	τ_1 (ns)	I_1 (%)	τ_2 (ns)	I_2 (%)	τ_3 (ns)	I_3 (%)	τ_4 (ns)	I_4 (%)
ZA-750	0.254±.003	60.95±1.56	0.488±.007	32.25±1.54	5.21±.11	2.32±.03	56.88±.75	4.48±.03
ZA-1000	0.182±.003	46.89±1.67	0.400±.005	49.13±1.62	2.53±.18	1.46±.07	23.84±1.08	2.52±.03
ZA-1200	0.170±.002	52.69±0.94	0.388±.004	43.81±0.90	2.03±.08	1.69±.06	19.88±.52	1.80±.17

Table 3.8 : The average lifetime τ_{av} and the bulk lifetime τ_B for different ZA compounds

sample	τ_{av} (ns)	τ_B (ns)
ZA-750	0.335	0.304
ZA-1000	0.293	0.252
ZA-1200	0.269	0.228

The fitted τ_1 value in 750 °C annealed sample is very close to the theoretically calculated lifetime (254ps) in a try-vacancy constituting two Zn-vacancy plus one-oxygen vacancy ($2V_{Zn}$-V_o) in the lattice **[173,205]**. After annealing at 1000 °C the τ_1 reduces to around 182ps which lies very close to Zn as well as O mono vacancy. After annealing at higher temperature at 1200°C, it suggests that O vacancy population increases. The τ_2 value corresponds to the multi-vacancy or vacancy clusters in the grain boundary or inside the particle. The τ_2 value gets reduced after annealing at 1000 °C, but its intensity gets increased and it continues till annealing at even higher temperature 1200 °C which may indicate the de-clustering going on with the increase in annealing temperature. It is also interesting to see that $\tau_{av} > \tau_{B,}$ which is indicative of the presence of vacancy in the lattice even after annealing **[206]**. The second positron lifetime value (τ_2) might have then originated from Al-related vacancy and it must be a cluster vacancy. Literature survey on Al-doped ZnO samples showed that these compound are also consist various Al_{Zn} antisite defect related cluster vacancy such as $2Al_{Zn}$-V_{Zn} , Al_{Zn}-V_{Zn} , nAl_{Zn}-O_i **[206-209]**. These Al_{Zn} antisite defects are very much likely to exist in the spinel since they are directly linked with inversion of the spinel. Earlier report in ZA prepared through solution state method also showed that for ZA compound obtained at low annealing temperature, the inversion rate is high while at high annealing temperature the inversion rate goes down **[160]**. Theoretical calculation on various defects in ZA also showed that antisite defects have the lowest formation energy **[210]**. Thus, it is obvious that for ZA-750 the concentration of Al_{Zn} antisite defects will be more while for ZA-1200 they will be deactivated because the Al atom will occupy its own site and thereby lead to low inversion rate. Therefore, in present case it might be possible that in ZA-750 compound bigger cluster vacancies such as $2Al_{Zn}$-V_{Zn} are present which gives rise to higher life time value. Now upon thermal annealing they may reduce to smaller cluster such as Al_{Zn}-V_{Zn} since the Al in Zn-site will now move to its own site. For further confirmation EPR experiments were carried out,which can provide more evidence.The third (τ_3) and fourth (τ_4) lifetime components with very small intensity (1.5-4.5 %) correspond to the formation of *ortho*-positronium (*o*-Ps) may be in the large grain boundaries. The *pick-off* annihilation of *o*-Ps with the surrounding electrons from the grain boundaries gives the long lifetime components.

3.4.5 EPR study

Figure 3.47 represents respective EPR spectrum of ZA-750, ZA-1000, ZA-1200 and ZA-1300 compounds. From this figure it can be seem the EPR spectra of ZA-750 and ZA-1000 are different than that of ZA-1200 and ZA-1300 compounds. There is a huge change in intensity and a change in the resonance profile when ZA is annealed at higher temperature viz. 1200^0C and 1300^0C. Figure 3.48 represents the EPR spectrum of ZA-1000 and ZA-1200 with characteristics g values for different species. As seen from this figure only one paramagnetic signal at g = 2.02 is present for ZA-1000 while for ZA-1200 in addition to this signal, other signal such as g = 2.07, g = 2.14 and g = 2.30 also appeared in the spectrum. These signals therefore must be the results of thermal annealing of the samples. Some new defect centres must have formed in the compound at higher annealing temperature. The g = 2.02 signal can be attributed to electron trap at oxygen vacancy **[179-181]**.This signal exists among all the compounds and upon thermal annealing of ZA, the intensity was found to increase as shown in Figure 3.49. From positron lifetime study we have observed that the ($2V_{Zn}$ -V_o) vacancy dissociated into mono vacancies i.e. V_{Zn} and V_o . Thus it might be possible that ($2V_{Zn}$ -V_o) cluster was first reduced to (V_{Zn} -V_o) through deactivation of one Zn vacancy by one interstitial Zn_i and finally the (V_{Zn} -V_o) vacancy dissociated into mono vacancies i.e. V_{Zn}^- and V_o^+. The signal at g = 2.07 can be attributed to V_{Zn}^-.The signal was prominent for ZA-1200 and ZA-1300. This corroborates well with our assumption that at higher annealing temperature (V_{Zn} -V_o) vacancy dissociated into mono vacancies i.e. V_{Zn}^- and V_o^+ . The signal at g = 2.30 might have originated from spin exchange interaction, which was absent for ZA-750 and ZA-1000 since the concentration of paramagnetic mono vacancies V_{Zn}^- and V_o^+ were less. In ZA-750 most of the vacancies are in cluster form such as ($2V_{Zn}$ -V_o) and Al_{Zn}-V_{Zn} which are diamagnetic. Only g = 2.02 signal which is due to V_o^+ was present in ZA-750 suggesting that some mono oxygen vacancies V_o^+ were also present along with the cluster vacancies.

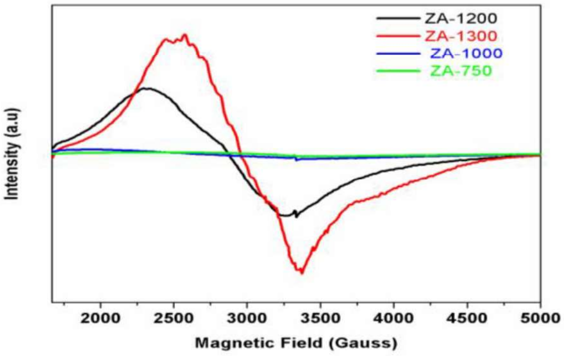

Figure 3.47 *: Room temperature EPR spectra for ZA-750, ZA-1000, ZA-1200 and ZA-1300*

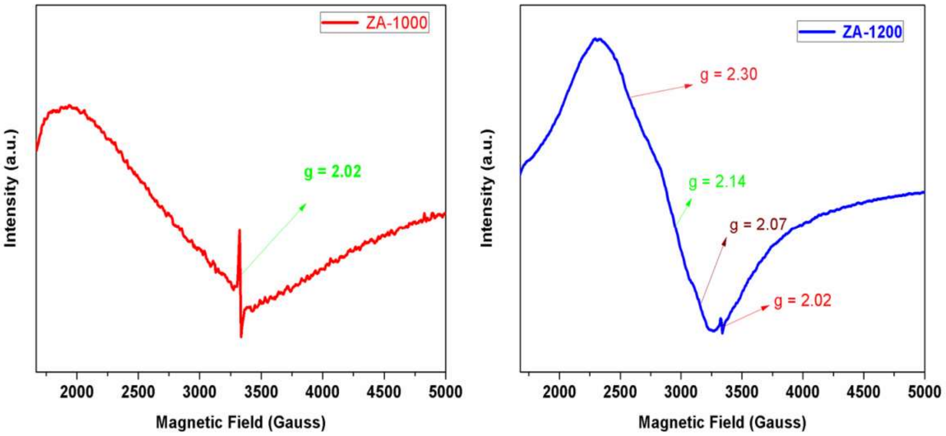

Figure 3.48 *: Room temperature EPR spectra for ZA 1000 and ZA-1200*

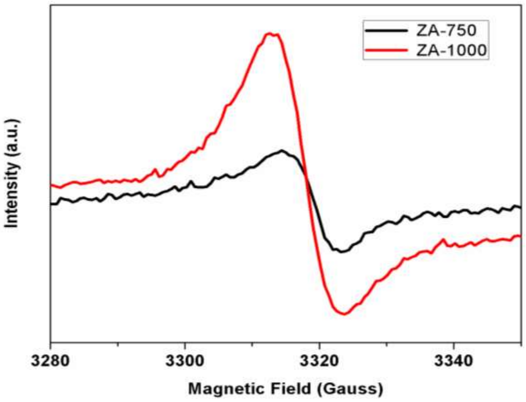

Figure 3.49*: Room temperature EPR spectra for ZA 750 and ZA-1000*

3.4.6 Electronic Structure and Band Gap Energy

Similar to the case of MgO and $MgAl_2O_4$, the multicolour emission of pure $ZnAl_2O_4$ compound indicates the presence of various electronic states within the band gap of the material. In present case the individual electronic states of various neutral and charged defect centres such as O vacancy (V_O^0, V_O^{+1} and V_O^{+2}), Al vacancy (V_{Al}^{3-}), Zn vacancy (V_{Zn}^0,V_{Zn}^{2-}), interstitial Zn (Zn_i^+), antisite defects (Al_{Zn}^+ & Zn_{Al}^-) etc. are calculated using DFT calculation. A detail explanation of the observed density of state from the DFT calculation will be given in our communicated report. The following summary from the density of states (DOS) for different kind charged and uncharged vacancies and vacancy cluster is pictorially represented in Figure 3.50.

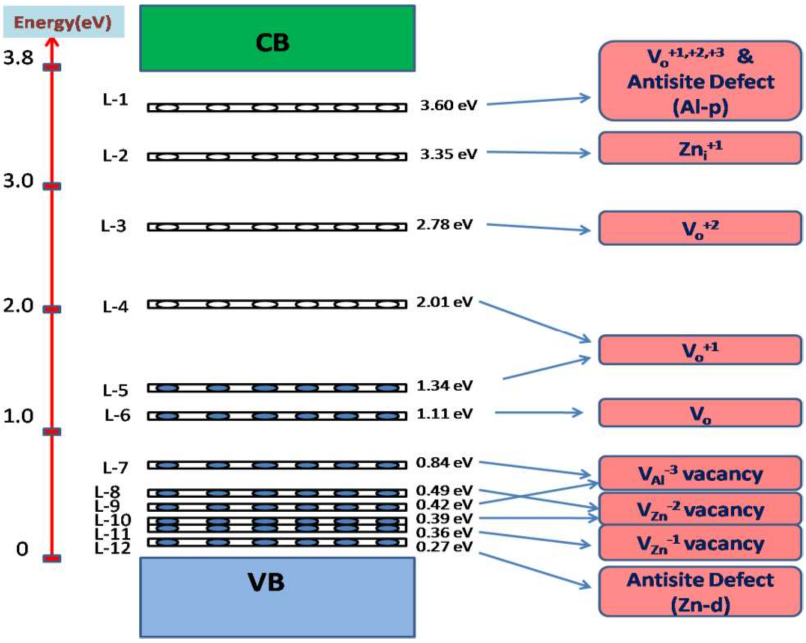

Figure 3.50: *Overall summary of the location of the defect states arises due as O vacancy (V_O^0, V_O^{+1} and V_O^{+2}), Al vacancy (V_{Al}^{3-}), Zn vacancy (V_{Zn}^0,V_{Zn}^{2-}), interstitial Zn (Zn_i^+), antisite defects (Al_{Zn}^+ & Zn_{Al}^-) etc in $ZnAl_2O_4$. Light gray coloured bands are filled with electrons and white bands are empty.*

3.4.7. Discussion:

From EPR and PALS study it can be confirmed that the following defects viz. O vacancy, Zn vacancy, antisite defects presents in ZA matrix either in the cluster form or single form. This cluster vacancy is nothing but a pair of two or three identical or different vacancies when they are neighbor to each other. Such as the cluster a cluster vacancy V_{Zn}-V_o can be formed when a pair of V_{Zn}^{2-} and V_o^{2+} exist side by each other. The similar vacancy can also be formed by a pair of V_{Zn}^{1-} and V_o^{1+} .In earlier report on ZA matrix, synthesised through the same sol-gel combustion method,various group including us concluded that at lower annealing temperature the percentage of inverse phase is more while its percentage decreases upon annealing the compound at higher temperature **[178,211]**. Various other groups also discussed that in this spinel compound it is possible to control the inversion rate by means of thermal annealing **[160]** which led to interesting optical properties. During thermal treatment, there is a reciprocal exchange of Zn^{2+} ions and Al^{3+} ions between octahedral and tetrahedral positions, which leads to inverse phase of the spinel. Now this reciprocal exchange of cations create the existence of $[Zn^{2+}{}_{Al}]^{-}$ or $[Al^{3+}{}_{Zn}]^{+}$ antisite defects. This negatively charge $[Zn^{2+}{}_{Al}]^{-}$ can acts as a hole trap while the positively charged $[Al^{3+}{}_{Zn}]^{+}$ act as electron trap **[212]**. Since Al^{3+} ions have low electron affinity, the captured electron may finally leave its trap and recombine with a trapped hole **[212]**.

Thus by trapping of electron these antisite defect centres delay the electron-hole recombination process, which is reflected in the lifetime value of the various emitting components for ZA obtained at low annealing temperature, where the rate of inversion is high. At higher annealing temperature since the spinel compound becomes more and more order and the rate of inversion is low, the concentration of these antisite defect centres become low. Therefore the electron and hole trapping process on this defect centres becomes less significant which is reflected in the drastic decrease in the lifetime values.

From the DFT summery in Figure 3.50 it can be seen that there are electronic states inside the band gap arising due to various defect centres. Some are filled by electron (states below the Fermi energy level) and some are unfilled (states above the Fermi energy level). Since the excitation energy (250 nm ~ 4.95eV) is more than the band gap energy (3.8 eV), the electron from valence band (VB) can be prompt into the conduction band (CB), leaving a hole in the VB. This hole can be trapped into the electronic states close to the VB such as L-9, L-10, L-11 etc. Similarly electron from the filled states such as L-5.L-6, L-7,L-8 etc. can also be prompted into the CB, leaving a hole in those states. The electrons from the conduction band can now be recombined with the holes in those levels or can be trapped into various vacant states such as L-1, L-2 & L-3. Now each and individual colour components due to various defects centres will be explained by considering their electronic structure observed from DFT calculation.

***P_1 (375 nm), P_2 (420 nm), P_3 (450 nm)& emission*:** As presented in the model (Figure 3.51) the 375 nm is very close to the energy gap between the L-1 and L-12 level which are arising out due to antisite defect centres. Since the energy of the emission375 nm (3.3 eV) is lower than the band gap (3.8 eV) there must be some shallow level. In earlier report too **[160]**, this band was observed where the authors attributed this band to the radiative recombination of a trapped electron below the CB with a hole in the valence band. Now in present case as observed from our DFT calculation these shallow states below the CB (L-1 and L-2) are contributed by antisite defect and O-vacancy defects (Figure 3.50). Thus we can attribute the 375 nm emission to be due to antisite defect states which creates some shallow vacant states below the CB and some filled state just above the VB as shown in Figure 3.50. On excitation electron may prompt into the CB or into the shallow states below the CB as shown in Figure 3.51-a, creating hole in the VB or L-12 level. The electron from CB can exchange into the L-1 followed by recombination with the hole in L-12.

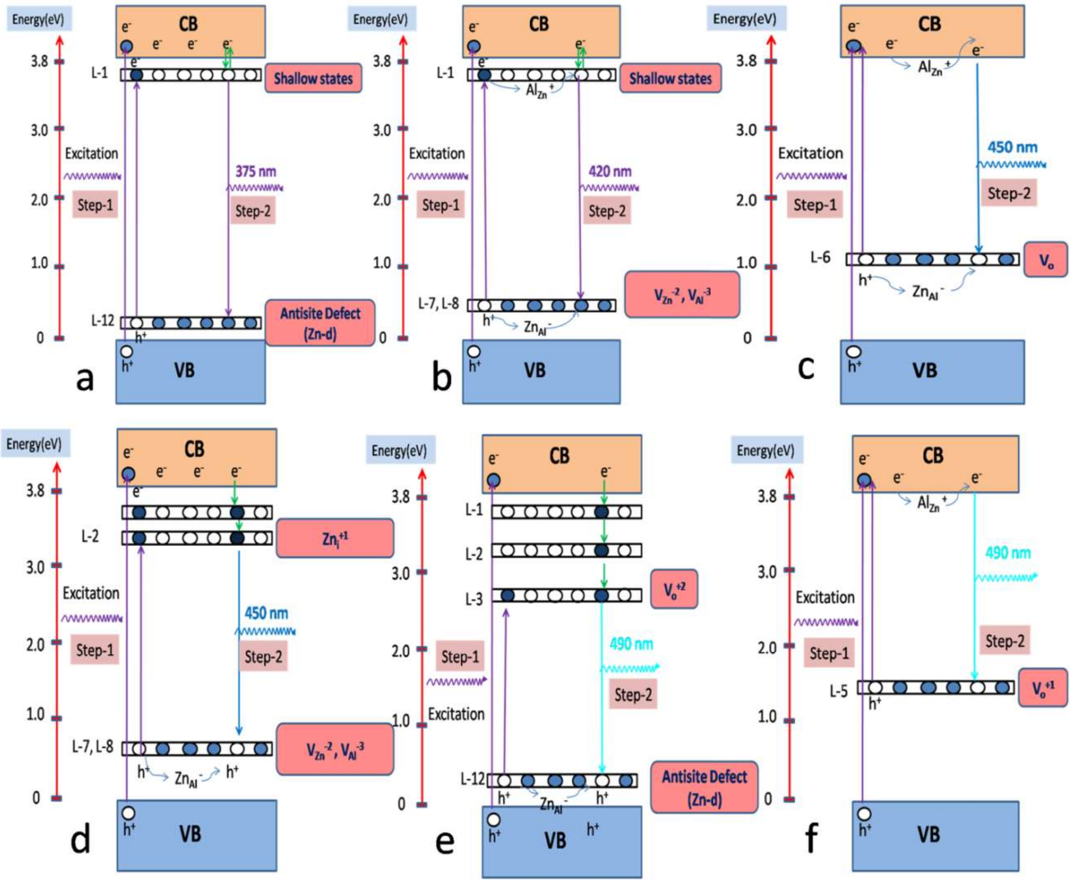

Figure 3.51: *Probable electron transition of various colour components a) 375 nm, b) 420 nm, c & d) 450 nm, e& f) 490 nm*

In earlier report **[159]** emission in 400-450 nm regions are attributed to oxygen vacancies although no clear understanding about the electronic transition involving these emissions have been presented there. In present case the 420 nm emission was found energetically close to the electronic transition L-1 → L-7, L-8 as shown in Figure 3.51-b. L-1 level is contributed from various oxygen vacancy related defect centres while L-7 and L-8 are contributed by cationic vacancies. For P_3 (450 nm) component, the transition from CB to L-6 level is energetically good match as shown in Figure 3.51-c. L-6 is contributed by the oxygen vacancy (V_o). Emission in the same region was also observed by Cornu *et al.,* and they have attributed it to interstitial Zn (Zn_i) **[160]**. We have also calculated the electronic structure due to Zn_i . From the energy matching criteria it was found that P_3 (450 nm) component can be linked to L-2 → L-7, L-8 transition where the L-2 is contributed by Zn_i as shown in Figure 3.51-d . Again since the antisite defect centres are also close to these level (in case of L-1 level the energy level of both oxygen vacancy defect centres and antisite defect centres are very close and thereby represented by a single level i.e. L-1), they may act as an electron and hole trap which will delay the electron hole recombination process. The 490 nm emission can be linked to transition of an electron trapped in a deep level such as L-3 to L-12 as shown in Figure 3.51- e where a hole has been created due to excitation. The 490 nm emission is also energetically close to the transition CB → L-5 as shown in Figure 3.51- f. In both cases, either the electron or hole is in the trapped state. The lifetime of this particular emission is the highest among others. Since the L-12 is directly contributed by the antisite defects, it might be possible that 490 nm emission is the result of L-3 →L-12 transition.

P_5 (530nm) and P_6 (600nm) emission : The 530 nm emission can be correlated to the transition from L-3 level to L-11 as shown in Figure 3.52-a . L-11 is contributed by V_{Zn}^{1-} while L-3 is linked to V_O^{+1} is involved. In the emission spectra in Figure 3.39a it can be found that with increasing the annealing temperature the intensity around this region is enhanced. In EPR spectra also, the resonance signal due to V_O^{+1} and V_{Zn}^{1-} were found to be more intense for the compound annealed at high temperature. In PALS study the cluster vacancies were found to be dissociated to mono Zn and O-vacancies. This established the fact the green at 530 nm are directly linked with the Zn and O-vacancy.

Earlier report **[160]** in ZA showed that this emission is probably associated with some oxygen vacancy related intermediate levels. Through our DFT calculation this 600 nm emission can be energetically linked to two transitions; i) L-2→L-5 and ii) L-4→VB as shown in Figure 3.52-b and Figure 3.52-c. Both L-4 and L-5 are linked to filled and unfilled O-vacancy related states. The enhanced intensity at higher annealing temperature can be explained on the basis of increase in free V_O^{+1} due to dissociation of cluster vacancy.

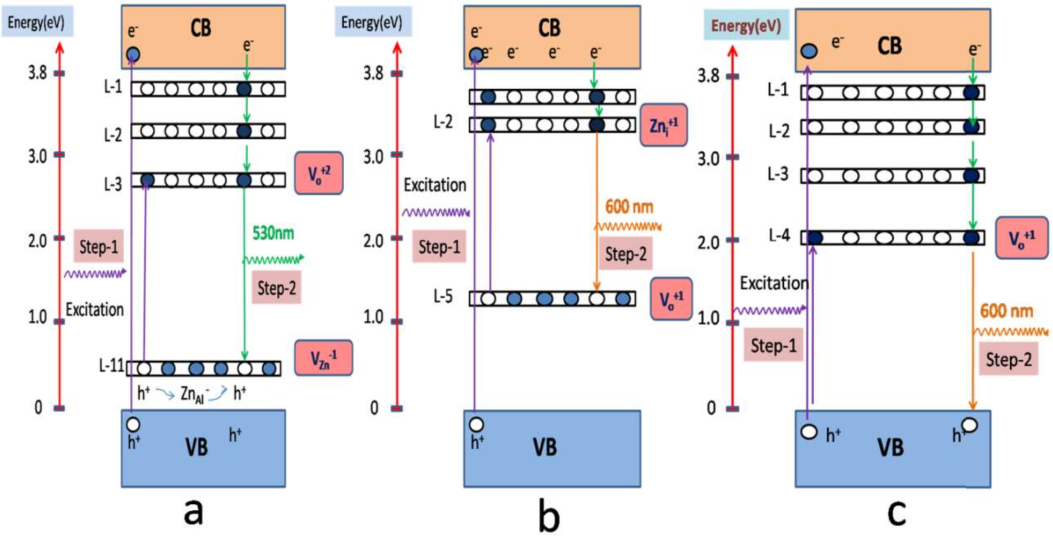

Figure 3.52: *Probable electron transition of various colour components a) 530 nm, b & c) 600 nm*

Red Near IR region: 720 nm (P_7) , 780 nm (P_8) and 850 nm (P_9)

From TRES study it was found that the 720 nm (P_7) emission was absent for ZA-750 compound. A group of lines with the most intense at around 690 nm were found for all heated samples, which might be due to Cr^{3+} ion **[160]**. However, a prominent peak around 720 nm was observed for ZA-1000, ZA-1350 compounds. Thus the transition might be associated with free O & Zn- vacancies which arise out only at higher annealing temperature. From DFT calculated electronic structure this emission can be linked to two transitions; i) L-3 →L-6 Figure 3.53-a and ii) L-4 →L-11 Figure 3.53-b. In first case the transition levels are associated with the oxygen vacancies while in 2nd case L-4 is linked V_O^{+1} and L-11 to V_{Zn}^{1-}. The seconnd case is found more sound, since from PALS and EPR study it was observed that the concentration of free V_O^{+1} and V_{Zn}^{1-} were more at higher annealing temperature.

The 780 nm (P_8) emission can be linked to L-1→L-4 transition as shown in Figure 3.53- c. On the other hand 850 nm (P_9) emission can be linked with L-3→L-5 transition (Figure 3.53- d). Both the transitions are linked with O-vacancy. Thus slight enhancement of the emission intensity in the near-IR region can be due to same region as that of 720 nm.

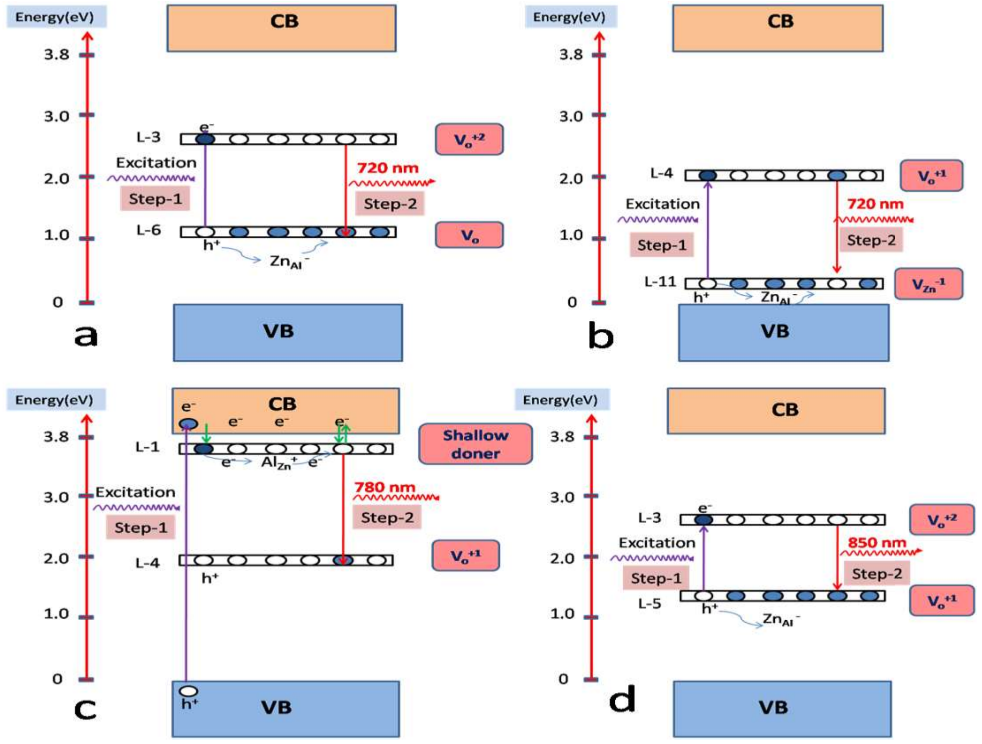

__Figure 3.53:__ Probable electron transition of various colour components a & b) 720 nm, c) 780 nm & d) 850 nm

Explanation of the change in colour co-ordinate from bluish to near white:

At low annealing temperature the blush emission characteristics is due to strong intense violet-blue emission as shown in Figure 3.39a, where the percentage of green and red emission was low. Now as the annealing temperature was increased the percentage of green and red colour was also increased due to increase in oxygen vacancy. On contrary a decrease in intensity of the blue region was observed. Thus in a balance of all the three colours viz. blue, green and red, the compound showed white emission characteristics as reflected in the colour co-ordinate in Figure 3.39b.

Chapter 4

Transition metal ions mediated optical properties in Fe^{3+}:$ZnAl_2O_4$, $Mn^{2+:}SrZrO_3$ & $LiZnVO_4$

4.1 Introduction:

In the past few decades,research on metal-ion doped phosphors has been carried out all over the world which covered almost all branches of luminescence. Various type of metal-ion doped phosphors have been synthesized in different forms such as crystals, powders and thin films, in which the activators control the luminescent properties of the phosphors **[213]**. Mostly two types of metal-ions are utilized as activators, which are transition-metal (TM) ions and lanthanide ions (Ln^{3+}). In case of TM ions the intra-shell d–d transitions are exploited while for Ln^{3+} ions, both parity-allowed 5d–4f (e.g. $Ce^{3+)}$ and parity-forbidden 4f–4f (e.g. Tb^{3+}) transition occurs. These TM and Ln doped luminescent materials have wide range of applications starting from optoelectronics to biomedicine, through to almost all aspects of human life **[214-220].** Among these activator based phosphors materials, d-block or transition metal doped phosphor possess certain advantages over the others due to the their crystal field dependent optical properties. Most of the TM ions have an incompletely filled d-shell (d^n, $0 < n < 10$). For example the 3d transition metal ions utilized in phosphors may have three electrons (Cr^{3+} and Mn^{4+}), or five electrons (Mn^{2+} and Fe^{3+}) occupying the outermost 3d orbitals which in contrast to lanthanide ions, are not shielded from the host lattice. This is why the optical properties can be influenced by the host lattice. Thus varying crystal field environment surrounding the transition metal ion in different host matrices, one can justifiably induce a large diversity of optical properties in the transition metal doped oxide materials. For example in case of d^5 ions such as for Fe^{3+} and Mn^{2+} ion, the emission is due to $^4T_1 \rightarrow {}^6A_1$ transition which is very much dependent on the crystal field strength **[221]**. Here since the 3d electrons of Mn^{2+} ion are not shielded by any outer orbitals, the energy difference between the excited state and ground state is modified by the host lattice. At higher crystal field strength, the transition energy gap is small while it is large for low crystal filed environment **[221]**. Thus with the increase of crystal field strength, the emission between $^4T_1$ and $^6A_1$ can shift from green to deep red. For example Mn^{2+}-doped ZnS (ZnS:Mn) is one of the most used phosphors in flat-panel displays and lighting sources **[222,223]**. Similarly, the luminescence of Cr^{3+} in Al_2O_3 was utilized for the first generation of solid-state lasers where the emission spectrum consists of two strong lines at 694.3 and 692.9 nm (the so-called R1 and R2 lines) **[213].** The luminescence of Cr^{3+} arises from the spin-allowed transition $^4T_2 \rightarrow {}^4A_2$ where $^4T_2$ level is sensitive to the crystal field. Thus, spectroscopic properties of Cr^{3+} ions depend strongly on the crystal field and the emission is characterized by a broad band with a short lifetime. The emissions of Cr^{3+} can be changed from red to green with altering the crystal field strength from high to low **[224]**. In most of the cases of TM doped host matrices, the luminescence is characterized by some broad and undefined features which is due to the strong coupling of electronic transitions with vibrational transitions of the host lattice. In present study, the luminescence properties of various TM ions such as Fe^{3+}, Mn^{2+} and V^{5+} in various matrices such as Fe:$ZnAl_2O_4$, Mn:$SrZrO_3$ and $LiZnVO_4$ have been investigated. In Fe:$ZnAl_2O_4$ and Mn:$SrZrO_3$, by varying the dopant site occupancy a change in crystal field environment was possible which led to tuneable emission characteristics.This tuneable emission characteristics were very much helpful in determining the local structure of the dopant ions, phase of the compound (in $ZnAl_2O_4$) and also defect structure of the host (in $SrZrO_3$).

$ZnAl_2O_4$ compounds have an ideal formula AB_2O_4 where, (A) represents the divalent metal ions (cations) occupying FCC tetrahedral sites and (B) represents trivalent metal ions (cations) occupying FCC octahedral sites of a cubic crystal structure **[178]**. Spinels have cubic symmetry with a space group Fd-3m and 8 formula units per unit cell. The unit cell contains 32 oxygen atoms in a cubic close packed system with 8 tetrahedral (A) and 16 octahedral (B) occupied sites. These spinel compounds are commonly divided into two kinds namely, 'normal' and 'inverse' spinels. Normal spinel structures are usually cubic close-packed oxides with one tetrahedral and two octahedral sites per oxide. The tetrahedral sites are smaller than the octahedral sites. B^{3+} ions occupy the octahedral holes because of a charge factor, but can only occupy half of the octahedral holes. A^{2+} ions occupy 1/8 of the tetrahedral holes. Inverse spinel structures however are different in the cation distribution, in that the entire A cations and half of the B cations occupy octahedral sites, while the other half of the B cations occupies tetrahedral sites. There is intermediate class also where the cation distribution can be described as $(A_{1-x}B_x)$ $[A_{x/2}B_{1-x/2}]_2O_4$, where parentheses () and brackets [] are used to denote tetrahedral and octahedral sites, respectively. The so-called inversion degree x adopts values between 0 (normal) and 1 (inverse), and it is x=2/3 for a fully random cation distribution. However, when an active dopant is introduced into these spinels, their optical and magnetic properties are dramatically changed depending on its distribution in the spinel. Studies of dopant ion distribution in spinels have attracted much attention because they may allow better understanding of the correlations between structure and properties such as colour, magnetic behaviour, catalytic activity, and optical properties, etc., which are strongly dependent on the occupation of these two sites by metals.

In present work,we have synthesised various $Zn_{1-X}Fe_X Al_2O_4$ (x = 0.005, 0.010, 0.025 or 0.050) compounds through sol-gel combustion route at different annealing temperature such as 700 ^{0}C, 800 ^{0}C & 900 ^{0}C. We have observed two different emission bands in the blue and red region respectively **[178]**. The blue band is attributed to the Fe^{3+} in tetrahedral geometry (low crystal field) while the red band is due to Fe^{3+} in octahedral geometry (high crystal field). Upon increasing the Fe^{3+} concentration, there was an enhancement of intensity of the red band while that of blue band remained almost constant. When these compounds were annealed at higher temperatures (such as 800 ^{0}C & 900 ^{0}C), a reverse trend in the two respective bands was observed. The intensity of the blue band was found to decrease while that of the red band to increase on increasing annealing temperature. Since in EPR spectroscopy also, Fe^{3+} shows different spectrum characteristics for different coordination geometry, these tunable emission behaviour on varying concentration and temperature was further supported by EPR study.These observations in combination with the calculated cell constants obtained from rietveld refinements of the XRD patterns suggested that at low annealing temperature the percentage of inverse spinel is more while at higher annealing temperature normal spinel is predominant. Thus there is a phase change of the spinel from inverse to normal upon thermal annealing.

The ABO_3 type of perovskite materials, which have various crystalline structures, show interesting physiochemical properties that offer potential hosts for chemical substitution. Substitution at both the A and B sites can lead to changes in symmetry and composition, and thus create various defects via cation or oxygen vacancies that can drastically influence band structures. Substitution then is the main factor in determining the electronic structures. In particular, these materials can accommodate both transition metal and lanthanide ions on the A or B site, and these doped oxides are not only used as probes to investigate local centres and energy but also to provoke changes in optical behavior. Moreover, doping foreign elements into a semiconductor with a wide band gap to create a new optical absorption edge is known to be one of the primary strategies for developing materials with optical-driven properties. However, the role of rare earth (RE) in the perovskite structure is not really clear and is still being discussed.

Further Mn doped $SrZrO_3$ compounds were synthesised through sol-gel route. Substitution of Mn^{2+} ion at Zr-site will face a strong crystal field environment while at Sr-site, it faces a week crystal field **[179]**. Thus at Sr-site, Mn^{2+} emits green colour while at Zr-site it gives red emission. We have also observed an enhancement of the red emission at higher doping level indicating more substitution of Mn^{2+} at Zr-site at higher concentration. Further this substitution at Sr & Zr- site was also linked with the shallow and deep defects of the $SrZrO_3$ as observed from DFT calculation. It was observed from the density of states (DOS) that the substitution of Mn^{2+} at Sr-sites leads to the generation of shallow defect states, whereas that at Zr-site, both shallow and deep defect states generated within the band gap of the material. A change in the corresponding emissions of these defect states with varied concentrations of Mn^{2+} was also observed. Thus Mn-substitution also helped in characterising shallow and deep defect related emission. In EPR spectroscopy, Mn^{2+} showed characteristic spectra due to substitution in the lattice site and surface of the particle. In addition a broad spectra due to oxygen vacancy was also observed which was found to increase at higher concentration of Mn^{2+}. This is due to more substitution of Mn^{2+} at Zr^{4+}-site, which will create more oxygen vacancies due to charge imbalance.

Alkali/alkaline earth vanadates have shown considerable interest by researchers due to their potential application in solid state lighting devices attributed to their better chromaticity **[225,226]**. In these compounds, the broad and intense oxygen to metal charge transfer (CT) band, usually observed in the near-UV region, are very efficient in transferring their energies to a luminescent centre of interest by non radiative pathways. Thus by playing with the composition of the vanadates and choosing a suitable luminescent centre, luminescence of choice can be generated. Specifically, the vanadate group, VO_4^{3-}, where the central metal ion is coordinated by four oxygen ions in tetrahedral (T_d) symmetry is known to be an efficient luminescent centre.

In $LiZnVO_4$ an intense green emission was observed due to oxygen vacancy and charge transfer transition of the VO_4^{3-} host **[177]**. The compound was synthesised through sol-gel combustion route and phosphor material obtained via this route often showed low quantum yield due to agglomeration of the particles at higher annealing temperature. In present case, since V exist as VO^{2+} ($3d^1$ and EPR active) in the sol and gel form during the synthesis procedure while in the final product $LiZnVO_4$, it exist as V^{5+} ($3d^0$ and EPR inactive), monitoring the EPR spectra at different annealing temperature confirmed that 600 ^{0}C is the optimum temperature for synthesis. Further the EPR parameters at different intermediate steps during heating procedure showed that there is a change in co-ordination surrounding the V from octahedral to tetrahedral geometry, which confirms that tetrahedral VO_4^{3-} is the main luminescence centres. Thus transition metal can be used for developing colour tuneable phosphors material and also as a structural probe to monitor synthesis of phosphor materials.

4.2 Synthesis and Optical properties of Fe^{3+} doped $ZnAl_2O_4$ [178]

4.2.1 Synthesis and Characterization

4.2.1.1 Synthesis

The starting materials for the synthesis of the desired compounds are Zinc nitrate [$Zn(NO_3)_2.6H_2O$] (99.0%, AR grade, s.d.fine-chem.ltd.), Aluminum nitrate [$Al(NO_3)_3.9H_2O$] (98%, AR grade, S.d.fine-chem.ltd.), citric acid ($C_6H_8O_7{\cdot}H_2O$) (99.7%, AR grade, Chemico fine chemicals) and $Fe(NO_3)_3$ (99.99%, ICP standard, Merck, Germany). For doped compounds viz. $Zn_{1-x}Fe_xAl_2O_4$, Zinc nitrate, Ferric nitrate, Aluminum nitrate, and citric acid were taken in the molar ratio (1-x) : x : 2 : 10 where x = 0.005, 0.010, 0.025 and 0.050 for 0.5, 1.0, 2.5 and 5.0 mol % Fe^{3+} doped compounds respectively. At first, stoichiometric quantities of the metal nitrates were dissolved in quartz double distilled (QDD) water; then the solutions were mixed in a beaker with constant stirring with a magnetic stirrer for 1 hour to get a clear solution. In another beaker, citric acid solution was made by dissolving it in QDD water. This citric acid solution was then added to the mixture of metal nitrate solution under vigorous stirring. This final solution mixture was then heated at 80ºC with continuous stirring for 5 hours after which a highly viscous gel formation was observed. Next the gel was heated at a temperature of 150 ºC placed on a heating mantle when a combustion process had taken place resulting an ash-like product. The ash-like product was then ground in an agate mortar and kept for calcining at different temperatures starting from 200 ºC to 600 ºC in air. Finally, at 600 ºC, a fine white powder of the desired compound was obtained followed by characterization using X-ray diffraction (XRD) study. In order to study the effect of annealing temperature, one of the doped compound (1 mol% Fe^{3+} doped $ZnAl_2O_4$) was further annealed at different higher temperatures viz. 700 ºC, 800 ºC and 900 º C respectively.

4.2.1.2 Phase purity: X-Ray Diffraction and Rietveld refinements

The XRD patterns for undoped and doped compounds in Figure 4.1a confirmed that all the patterns are consistent with the standard data of $ZnAl_2O_4$ with ICDD file No 5-669. This indicates the formation of pure compounds with space group Fd-3m and that the effect of Fe doping had no dominating impact on the crystallization behaviors. For higher mol % doped viz. 5.0 mol% Fe^{3+} doped $ZnAl_2O_4$, some impurity peaks due to β -alumina were observed and hence we did not synthesized more than 5.0 mol% Fe^{3+} doped $ZnAl_2O_4$. The strong and sharp diffraction peaks of the studied samples indicate that all the annealed samples were well-crystallized.

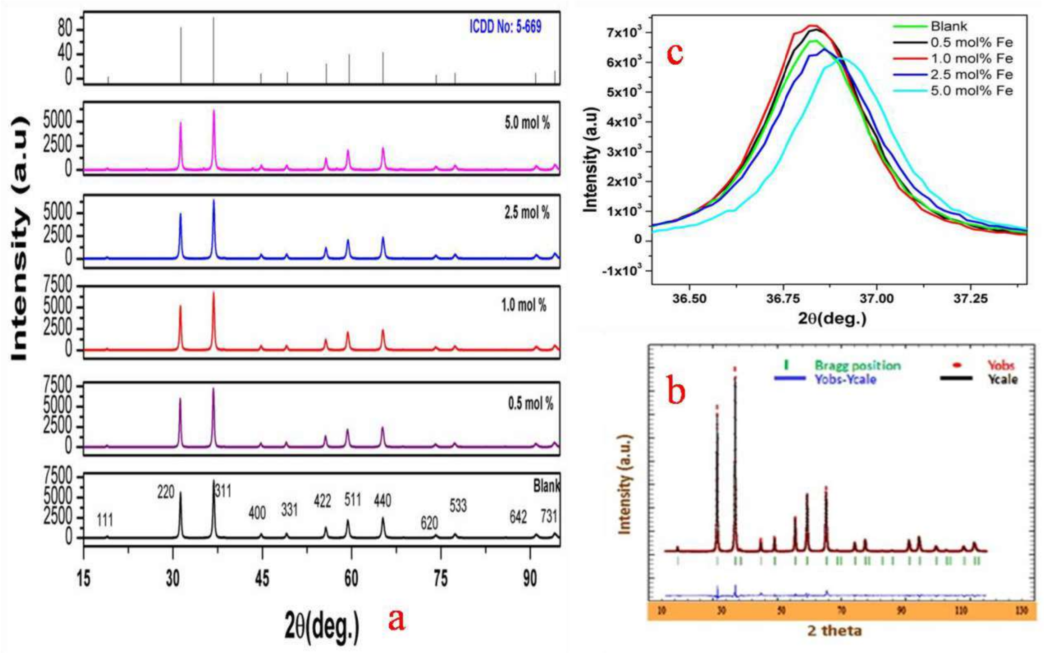

Figure 4.1: a) *XRD pattern of the $ZnAl_2O_4$ powder samples annealed at 600 ^oC and standard ICDD stick patterns with file No-5-669, b) Rietveld fittings of XRD patterns undoped $ZnAl_2O_4$ system & c) Expanded XRD pattern corresponding to 2θ value of 36.835**[178]***

Rietveld refinement of the undoped $ZnAl_2O_4$ compound obtained after annealing at 600^oC is shown in Figure 4.1b and the refinements of other compounds are given in reference **178**. The calculated cell constants values of the undoped and doped compounds obtained after refinement of the XRD patterns as listed in Table-4.1, which shows an initial increase up to 1.0 mol % dopant concentration and beyond that a reverse trend was observed. This observed trend is also supported by Figure 4.1c, which shows a shifting in the position of the diffraction peaks towards lower theta value w.r.t blank for lower concentrations of Fe^{3+} viz. 0.5 and 1.0 mol %;but as the concentration of Fe^{3+} increased beyond 1.0 mol %, same diffraction peak shifted towards higher theta side. This is because shifting in the position of the diffraction peak is inversely related with the lattice constant value. This trend in lattice constant can be understood on the basis of size of the dopant ion and the cations to be substituted. If we consider the respective ionic radii of the cations in the present systems, then Zn^{2+} ion has larger ionic radii than Fe^{3+} ion while Al^{3+} ion has smaller ionic radius than that of Fe^{3+} ion. Thus if Fe^{3+} ions were incorporated into the Al^{3+} sites (tetrahedral/octahedral); an increase in cell constant value would be observed as Fe^{3+} is larger in size than Al^{3+}. Similarly, if Fe^{3+} were incorporated into the Zn^{2+} site (tetrahedral/octahedral) there should be a decrease in cell constant.

Thus the present trend in lattice constant values in Table-4.1 suggests that at lower concentration fraction of Fe^{3+} (ionic radii 4-coordinated Fe^{3+} = 0.49 and 6-coordinated Fe^{3+} = 0.65 Å) residing at tetrahedral/octahedral Al^{3+} (0.39/0.535 Å) site is more than tetrahedral/octahedral Zn^{2+} site (0.60/0.74 Å) since an increase in lattice constant value w.r.t to blank sample was observed. However the decrease in cell constant value at higher doping concentration indicates that fraction of Fe^{3+} residing in tetrahedral/octahedral Zn^{2+} would be more. Therefore at lower doping concentration Fe^{3+} ions were preferentially substituting Al^{3+} site while at higher concentration they substituted at Zn^{2+} sites. This might be due to the charge compensation playing dominant role at lower concentration while at higher concentration the comparable size of substituting and substituted ions becomes dominant.

Table-4.1: Structural parameters of Fe doped $ZnAl_2O_4$ synthesized through the sol-gel-combustion route **[178]**

Mol% of doped Fe^{3+}	**Cell parameter (Å)**	**Reliability factors**		
		R_p	**Chi^2**	**Bragg R-factor**
0	8.0837	9.04	1.75	2.903
0.5	8.0849	11.5	2.71	2.990
1.0	8.0862	8.54	1.48	3.049
2.5	8.0803	10.2	1.86	3.427
5.0	8.0751	15.7	4.06	5.782

4.2.2. Emission, excitation and life time spectroscopy of Fe^{3+} doped $ZnAl_2O_4$

Figure 4.2 represents the excitation spectra of 0.5 mol % Fe^{3+} doped $ZnAl_2O_4$ where the sharp peak at 388 nm is due to the $^6A_1$ (^6S) - ^4E (^4D) transition while the peaks at 430 and 471 nm are due to the $^6A_1$ (^6S) -^4E, $^4A_1$ (^4G) transition **[227]**. The bands in the region 280 and 350 nm are probably associated with O^{2-}-Fe^{3+}charge-transfer processes **[228,229]**. The other excitation band in the region of 520 nm with doublet character can be assigned to $^6A_1$ (^6S) - $^4T_1$, (^4G) transition which is the inverse of the emission process. **[227,230]**

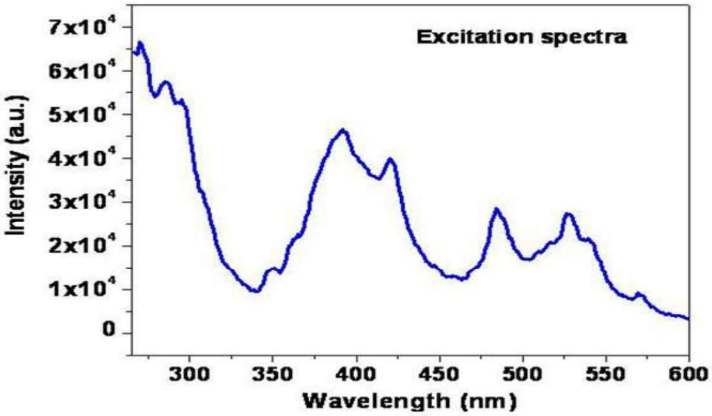

Figure 4.2: *Excitation spectra of 0.5 mol% Fe^{3+} doped $ZnAl_2O_4$ with λ_{em}= 693 nm***[178]**

Figure 4.3a & 4.3b represent the room temperature emission spectra of 0.5 % & 5.0 mol% Fe^{3+} doped $ZnAl_2O_4$ compounds respectively. For 0.5 % Fe^{3+} doped compound, the emission spectrum is characterized by a blue broad emission band with maxima at 445 nm and with vibronic sidebands at 665, 674, 684 and 693 nm (magnified image is shown in inset of Fig. 4.3a) having constant energy differences (~ 9-10 nm). While for higher doping level (5.0 mol %), in addition to the blue 445 band, another red band at 745 nm was also observed (Fig. 4.3b). Here the vibronic sidebands are not so clear as in 0.5 mol % since the spectrum is dominated by a broad emission in the range 660-790 nm. The red emission (~ 745 nm) is attributed to Fe^{3+} ions in octahedral coordination while the blue emissions (~ 445 nm) is due to Fe^{3+} in tetrahedral coordination **[229,230,231]**. The vibronic sidebands are mainly due to Fe^{3+} in tetrahedral coordination and their origin is attributed to local modes of a [FeO_4] centre **[229,233,234]**. As stated in our earlier chapter the emission peaks at 480, 520 and 530 nm are attributed to various intra band gap defects like oxygen vacancies etc. coming from the host $ZnAl_2O_4$ itself. For d^n ions situated in crystalline environments, the electric-dipole transitions to or from the ground state are normally both spin and parity forbidden. However, when configurations of opposite parity is mixed by odd components of the crystal field the transition may becomes partially allowed. This is why ions situated at tetrahedral sites which lacks inversion symmetry generally show strong emission than those at centrosymmetric octahedral coordinated sites

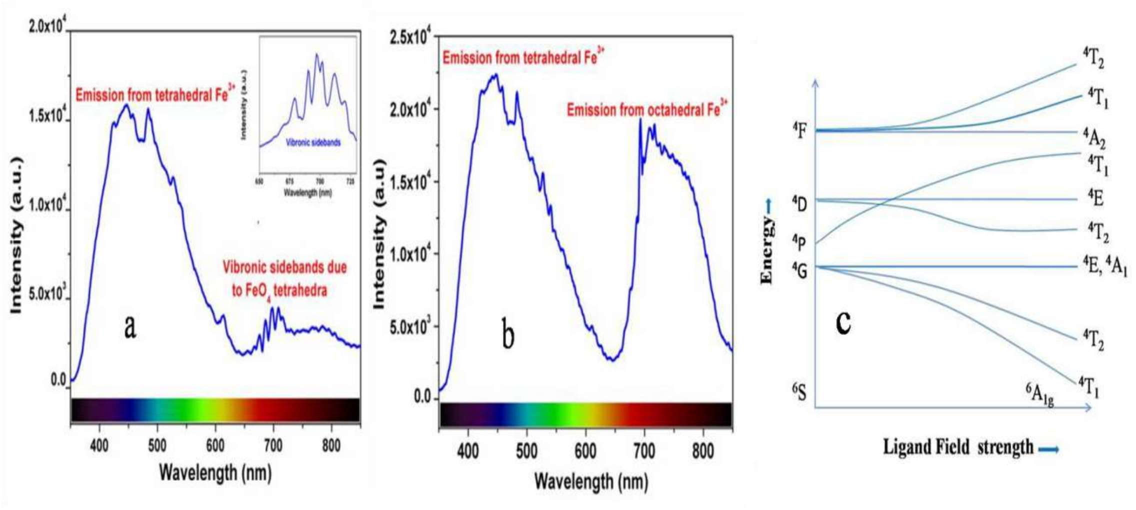

Figure 4.3: *Emission spectra of a) 0.5 mol% Fe^{3+} doped $ZnAl_2O_4$ where Inset shows vibronic sidebands FeO_4, b) 5.0 mol% Fe^{3+} doped $ZnAl_2O_4$with λ_{ex}= 280 nm and c) Energy level diagram of a d^5 configuration* ***[178]***

Figure 4.3c represents the energy level diagram of a d^5 configuration where the ground state terms of this d^5 configuration are $^{6}A_{1g}$ (^{6}S) for octahedral and $^{6}A_{I}$ (^{6}S) for tetrahedral coordination respectively. As can be seen that all the electronic transitions from the higher excited states are spin forbidden since ground state term is the only sextet of d^5 configuration. The first excited states for octahedral and tetrahedral coordination are $^{4}T_{Ig}(^{4}G)$ and $^{4}T_{I}(^{4}G)$ respectively. Emission of Fe^{3+} for octahedral coordination is attributed to the transition $^{4}T_{Ig}$ $(t_{2g}^{4},e_g) \rightarrow {}^{6}A_{Ig}(t_{2g}^{3},e_g^{2})$ while for tetrahedral coordination it is due to transition $^{4}T_{I}(e^{3}, t_2^{2}) \rightarrow {}^{6}A_{I}$ (e^{2}, t_2^{3}). The emission peaks are broadened due to difference in occupancy of e and t_2 orbitals both in ground and excited states. Thus the transition energies depend on the crystal field parameter 10 *Dq*. Again due to zero-point and thermal vibrations there will be fluctuation in the magnitude of 10*Dq* and thus in the emission wavelength **[235].** In a cubic field approximation the free electron term ^{4}G splits into $^{4}T_{1}(^{4}G)$, $^{4}T_{2}(^{4}G)$ and the degenerate $^{4}A_{1}$,$^{4}E(^{4}G)$. Generally those energy terms, which give horizontal lines, are independent of the crystal field splitting. The ground state free-ion term $^{6}A_{1}(^{6}S)$ is a horizontal line. Other terms giving horizontal lines are 4E (^{4}G), $^4A_1$ (^{4}G), ^{4}E (^{4}D) and $^4A_2$ (^{4}D) and hence their energies are independent of the crystal field. Thus transitions from ground state to these four states should give rise to sharp peaks. By the same reasoning the transitions from states, which slope appreciably, such as $^4T_1$ and $^4T_2$ give broader bands. The 693 nm emission band is from $^4T_1(^4G)$ - $^6A_1(^6S)$ transition and the weak side bands are due to the cooperative vibronic line because of the coupling with the AlO_4 or ZnO_4 vibration. The electronic transition and the vibronic transitions are spatially separated.

We have observed a constant increase in intensity of the octahedral peak's (~745 nm) when the concentration Fe^{3+} was increased from 0.5 to 5.0 mol% **[178]**. This observation suggests that at lower concentration, Fe^{3+} preferentially occupies the tetrahedral site whereas on increasing the concentration, its local site occupancy changes to octahedral site.

Since there are two lattice sites (tetrahedral and octahedral) available for the Fe^{3+} ions, PL decay time (lifetime) studies will be very much helpful about the nature of occupancy of the dopant ion. The decay curves of 0.5 mol % Fe^{3+} doped $ZnAl_2O_4$ compound with different emission wavelengths viz., λ_{em}= 445 and 693 nm at an excitation wavelength of λ_{ex}= 280 are shown in Figure 4.4.The decay curve with emission at 445 nm was fitted using the mono-exponential decay equation-4.1

$$\mathbf{I\ (t) = A_1 \exp (-t/\tau_1)} \tag{4.1}$$

While with emission at 693 nm a good fit was found to a bi-exponential decay using the following equation-4.2

$$\mathbf{I\ (t) = A_0 + A_1 \exp (-t/\tau_1) + A_2 \exp (-t/\tau_2)} \tag{4.2}$$

Where A_0, A_1 and A_2 are scalar quantities obtained from the curve fitting, t is the time and τ_1, and τ_2 are decay time values for exponential components respectively.

After analyzing the decay curve at λ_{em}= 693 nm, two different components were found to exist; one short lived and one long lived with respective life time value of ~ 39.5 μs (short component, τ_1) and ~170 μs (long component, τ_2) which can be indicative of the presence of two emitting species or states. While the decay curve at an emission wavelength of 445 nm showed the presence of single component with life time value ~ 40.2 μs.

Now it is assumed that for a given phonon energy, the relatively longer PL decay time can be attributed to a more symmetric site since the d-d transition becomes more forbidden in this case, whereas a shorter decay time is often linked with an asymmetric site due to relaxation in the selection rules. In $ZnAl_2O_4$ spinel structure, 4-coordinated site (S_1) is surrounded by four nearest neighbor oxygen ions in the form of tetrahedral, which is less symmetric structure than that of the 6-coordinated (S_2) site with regular octahedral. Species τ_1 (~40 μs) arises because of Fe^{3+} ions occupying S_1 site without inversion symmetry, whereas τ_2 (170 μs) can be ascribed to Fe^{3+} ions occupying S_2 site with inversion symmetry. The single component observed from decay curve at an emission wavelength of 445 nm is due to the unique emission of tetrahedral Fe^{3+} ion at that region while the observance of two components at an emission wavelength of 693 nm is due to presence of both Fe^{3+} tetrahedral sidebands and Fe^{3+} octahedral emission in that region.

In Table 4.2, the life time values and their respective population (in %) at two different sites for various concentration of Fe^{3+} are tabulated. From this table it can be observed that although with increase in concentration there is not much change in life time value however the percentage occupancy of Fe^{3+} ions for a specific life-time calculated using equation-4.3 changes drastically.

$$\textbf{\% of species (n)} = \left[\frac{(A_n \times \tau_n)}{\sum\limits_{n=1,2} A_n \times \tau_n} \right] \times 100 \tag{4.3}$$

The table shows that shorter lived species (~40 μs) predominates at lower concentration and the longer one (~170 μs) is dominant at higher concentration. Since the species τ_1 (~40 μs) is assigned to Fe^{3+} ions occupying S_1 site without inversion symmetry (tetrahedral), whereas τ_2 (170 μs) to Fe^{3+} ions occupying S_2 site with inversion symmetry (octahedral), these observation indicate the tuning of local site occupancy of Fe^{3+} ions from tetrahedral to octahedral with increase in concentration.

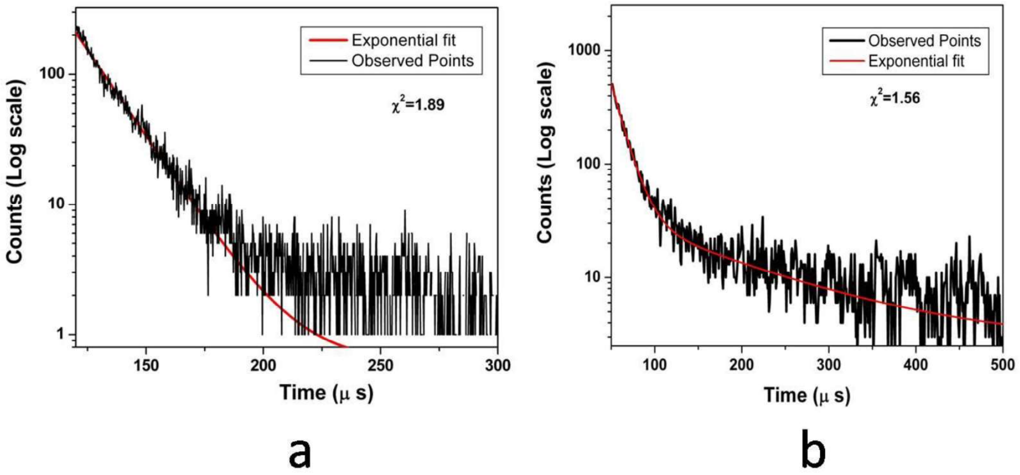

Figure 4.4: *Luminescence decay time profile of the 0.5 mol % Fe^{3+} doped $ZnAl_2O_4$ at λ_{ex}= 280 nm with a) λ_{em}= 445 nm and b) λ_{em}= 693 nm* ***[178]***

Table-4.2: Percentage and Lifetime values of τ_1 (Short lived) and τ_2 (Long lived) at different mol% of Fe^{3+} **[178]**

mol % of Fe^{3+}	**τ_1** (μs)	**τ_2**(μs)
0.5	39.5 (79.57 %)	170 (20.43%)
1.0	39.56 (82.5%)	169.19 (17.5 %)
2.5	42.17 (57.3 %)	173.25 (42.61 %)
5.0	39.73 (27.46%)	171.37 (72.54 %)

From X-ray diffraction studies, we have concluded that at at lower doping concentration Fe^{3+} ions are preferentially substituting Al^{3+} site while at higher concentration majority of them go to Zn^{2+} site. Hence combining XRD, PL and life time data, it is evident that at lower concentration, Fe^{3+} was substituting tetrahedral Al^{3+}, while at higher concentration it was substituting Zn^{2+} at octahedral site.

4.2.3. EPR studies of paramagnetic Fe^{3+} in $ZnAl_2O_4$ [178]

The room temperature EPR spectrum of 2.5 mol% Fe^{3+} doped $ZnAl_2O_4$ viz. $Zn_{0.975}$ Fe $_{0.025}$ Al_2O_4 consists of a number of signals at g ≈ 8.48, 6.66, 4.20, 4.01, & 1.99 and a broad signal at 2.20 respectively as shown in Figure 4.5a. In addition to these signals, the spectrum also consisted of five hyperfine lines with g ≈2.01 and A≈ 80G which are attributed to presence of Mn^{2+} as impurity ion. Fig. 4.5b and 4.6(a-g) shows the numerical simulation of the above experimental spectra and its simulated components. Fe^{3+} contains five unpaired electrons in its d orbital and with S=5/2 it should show a five line spectrum corresponding to the transitions: 5/2↔3/2, 3/2↔1/2, 1/2↔ -1/2,-

1/2↔-3/2, and -3/2↔-5/2. However, in the present case, since the crystal field splitting is large, the transition 1/2↔ -1/2 is only observed at the X-band frequency, while other are spaced wide apart. These multiple absorption lines in the EPR spectra indicate different environment of Fe^{3+}. The signals around g ≈ 4.20 & g ~ 8.48 are attributed to Fe^{3+} in tetrahedral sites while the broad signal at g≈2.20 is attributed to Fe^{3+} in octahedral sites **[236,237,238]**. The details of other signal are given in our published report **[178].**

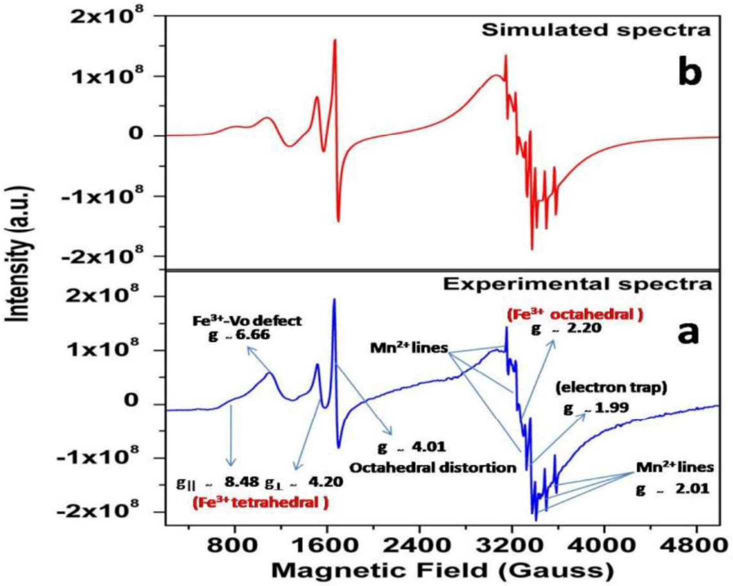

Figure 4.5: *a) Room-temperature X-band EPR spectra of* $Zn_{0.975}Fe_{0.025}Al_2O_4$ *(a) Experiment (blue) and (b) numerical simulation (red)* ***[178]***

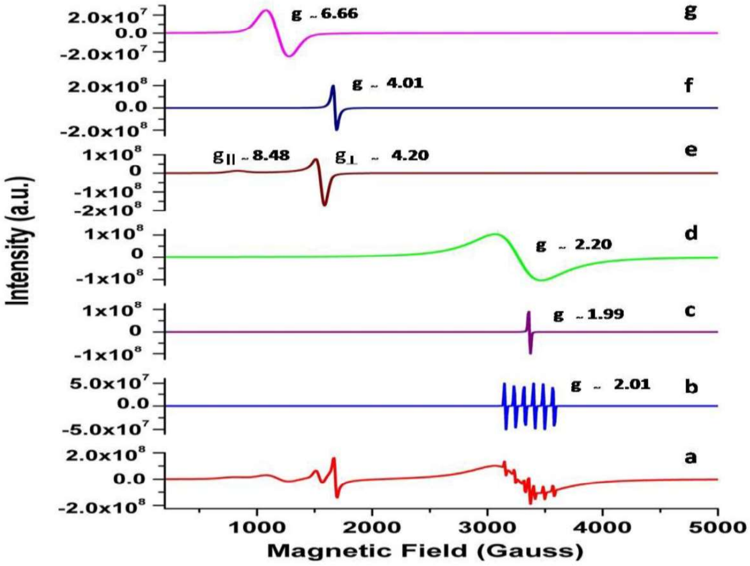

Figure 4.6: *a) Simulations (red) of experimental EPR spectra (a) and its components (b-g) for* $Zn_{0.975}Fe_{0.025}Al_2O_4$ ***[178]****.*

Figure 4.7 represents the EPR spectra of different mol % Fe^{3+} doped $ZnAl_2O_4$ compounds starting from 0.5 to 5.0 mol%, which shows that upon increasing the Fe^{3+} concentration the intensity of the peak at g~2.20 increases. The reduction in the resonance absorption of the tetrahedral Fe^{3+} (g ~ 4.20) and that of enhancement for the octahedral Fe^{3+} (at g~2.20) at higher concentration viz. 2.5 and 5 mol% is a clear indication for the transformation of lower symmetry (tetrahedral) to higher symmetry (octahedral).These observations are in concordance with the emission spectra at different dopant concentration.

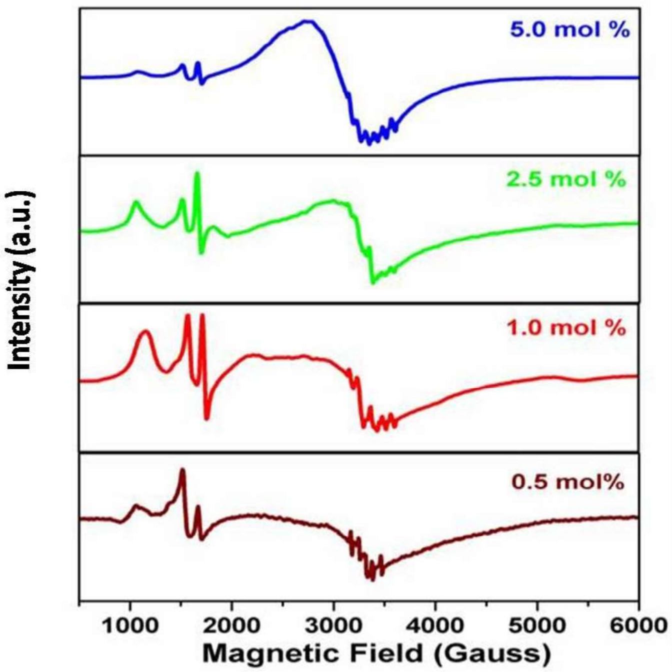

Figure 4.7: *EPR spectra of different mol % Fe^{3+} doped $ZnAl_2O_4$* ***[178]***.

Therefore, combining XRD, PL and EPR study, it can be concluded that at lower concentration Fe^{3+} was substituting tetrahedral Al^{3+} while at higher concentration it was substituting Zn^{2+} at octahedral site.

4.2.4 Transformation of inverse to normal phase: Tunable emission properties upon thermal annealing

From XRD data it has been concluded that for all the doped compounds prepared at 600 ^{0}C, at lower doping concentration Fe^{3+} is preferentially substituting Al^{3+} site while at higher doping level Fe^{3+} favourably going to Zn^{2+} site, as reflected in the continuous decrease in cell constant value upon increasing the dopant level. Further both PL and EPR studies of these compounds showed that Fe^{3+} prefers for tetrahedral site occupancy at lower concentration and the preference shifted to octahedral sites at higher concentration. These observations clearly indicate that at lower concentration Fe^{3+} is substituting tetrahedral Al^{3+} site while at higher concentration it substituting Zn^{2+} at octahedral site. Thus we can conclude that it is the inverse phase of zinc aluminate spinel which is forming as majority at 600°C as in inverse spinel the tetrahedral coordination is fully occupied by Al^{3+} while the octahedral is shared by both Al^{3+} and Zn^{2+}. It was reported in earlier work on zinc aluminate by Mathur *et al.,* **[211]** that in $ZnAl_2O_4$ the percentage of inverse structure is more when the synthesis temperature is <900°C .

Figure 4.8a & 4.8b represent the Emission and EPR spectra of 1.0 mol% Fe^{3+} doped $ZnAl_2O_4$ at different annealing temperature respectively. In the emission profile, an increase in the luminescence intensity of the octahedral Fe^{3+} and that a decrease for tetrahedral Fe^{3+} ion was observed for the compounds obtained at higher annealing temperature. Similarly the EPR spectra showed an increase in intensity of the signal at around $g=2.20$ (Octahedral Fe^{3+}) and a reduction in the resonance absorption at around $g = 4.20$ (Tetrahedral Fe^{3+}), upon annealing the compound at higher temperature. These observations clearly signify a tuning of local coordination around Fe^{3+} ions in $ZnAl_2O_4$ i.e. from tetrahedral FeO_4 to octahedral FeO_6 with increase in annealing temperature. Now there are two possible explanations for this behavior. The first one is that at low annealing temperature charge compensation of Al^{3+} by Fe^{3+} plays an important role and thereby substituting Al^{3+}, though it is smaller in size. While at higher annealing temperature the system could overcome that charge compensation barrier and occupying more favorable octahedral Zn^{2+}site in view of larger size of Zn^{2+} and more coordination number of octahedral sites. This explanation is favorable only if we assume that the system remains in inverse phase even at higher temperature. But if that is so, there should be a decrease in cell constant value. We have also observed that there is no appreciable change in cell constant value at higher temperature from rietveld refinement **[178]**. So there is no change in local site occupancy of Fe^{3+}; only thing which is taking place at higher temperature is, a change in the site of Al^{3+} to octahedral and Zn^{2+} to tetrahedral i.e. the formation of normal spinel. These observations clearly indicate a transformation of inverse phase to normal phase of $ZnAl_2O_4$ with higher annealing temperature and formation of normal spinel at temperature around 900 °C.

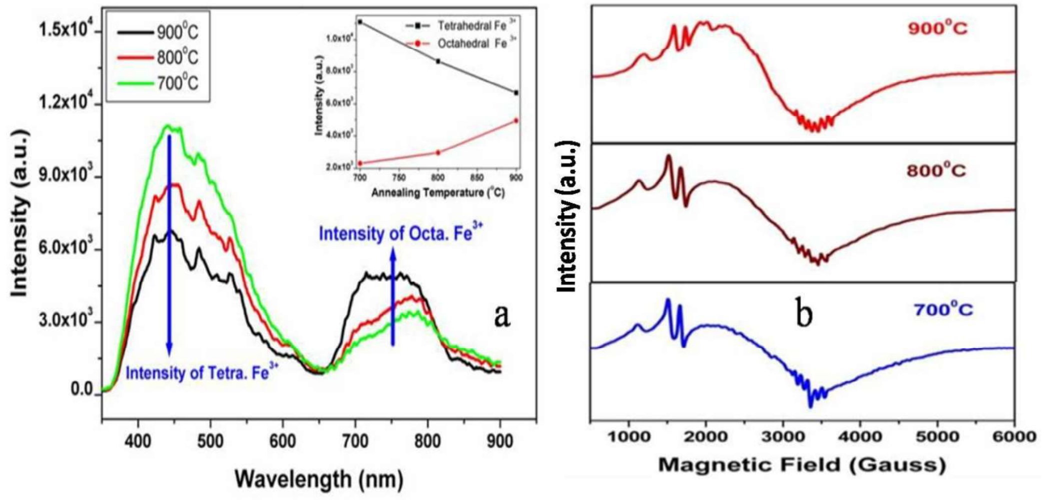

Figure 4.8: *(a) Emission and (b) EPR spectra of 1.0 mol% Fe^{3+} doped $ZnAl_2O_4$ at different annealing temperature* ***[178]***

4.3. Synthesis and Optical properties of Mn doped $SrZrO_3$ [179]

4.3.1. Synthesis and characterization

4.3.1.1. Synthesis

All the reagents used in the preparation of doped and undoped $SrZrO_3$ compounds were of analytical reagent grade and procured from Sigma Aldrich. For synthesis of undoped compound, zirconyl oxychloride ($ZrOCl_2$) (reagent grade, 98%), strontium nitrate $Sr(NO_3)_2$ (99.99% trace metals basis), ammonium nitrate (NH_4NO_3) (99.99% trace metals basis), and citric acid ($C_6H_8O_7 \cdot H_2O$) (ACS reagent, ≥99.5%) were taken in the molar ratio 1 : 1 : 10 : 1.25. Separate solutions of all these reagents were prepared by dissolving them in quartz double-distilled (QDD) water in separate beakers. Initially two different solution of $Sr(NO_3)_2$ and (NH_4NO_3) were mixed with constant stirring for 30 minutes in a separate beaker followed by addition of $ZrOCl_2$ solution. Under vigorous stirring, citric acid solution (2 M) was poured into the mixed solution which resulted in an opal gel. This gel was then dried at 100 ^{0}C for 10 h under an IR lamp followed by transfer to a quartz beaker. The quartz beaker along with the gel was then kept in a muffle furnace at 300 ^{0}C for 10 min which resulted in formation of an ash-coloured fluffy substance. In this step, the actual combustion reaction using citric acid as the fuel had taken place. The ash-like product was then calcined at 600 ^{0}C for 1 h resulting in a white powder. For the preparation of Mn doped compound varied concentrations of $MnCO_3$ (≥99.9% trace metals basis) (0.1, 0.5, 1.0, 2.5 and 5.0 mol %) in HNO_3 solution were used.

4.3.1.2. Structural analysis: XRD

Figure 4.9-i represents the XRD patterns of both $SrZrO_3$ and Mn doped $SrZrO_3$ samples annealed at 600 ^{o}C where all the diffraction peaks match very well with the standard values of orthorhombic phase of $SrZrO_3$ (ICDD file no 44-0161). Absence of other phase in the spectra revealed that the doped manganese ions are incorporated into the host lattice and that incorporation of manganese in $SrZrO_3$ has not distorted the crystal structure. The XRD data was indexed into space group *Pnma*. The cell constants were calculated from indexing program for the undoped and doped compounds as listed in Table-4.3.

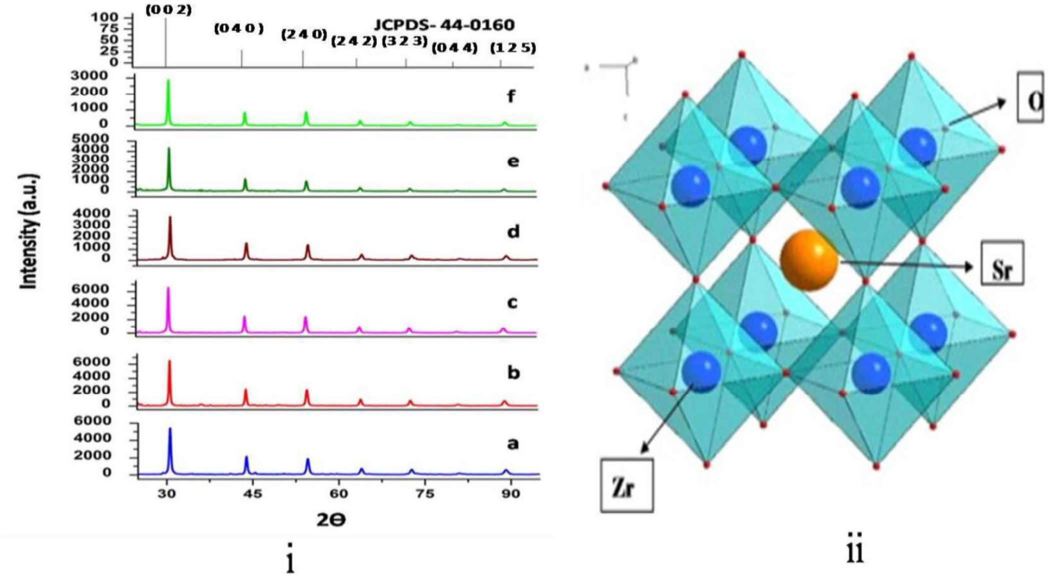

Figure 4.9. (i) *XRD pattern of the undoped and Mn doped $SrZrO_3$ powder samples annealed at 600 °C with dopant mol % of (a) 0, (b) 0.1, (c) 0.5, (d) 1.0, (e) 2.5, (f) 5.0 and the standard ICDD stick patterns with file no. 44-0160 and (ii) Schematic crystal structure of $SrZrO_3$* ***[179]***.

From this table it can be seen that the cell constant values for all the doped compounds are less than that of the undoped compound. This observed trend is also in accordance with the shifting of the diffraction peaks, which is inversely related with the lattice constant **[179].**

Table 4.3: Structural parameters of manganese doped $SrZrO_3$ synthesized through the sol–gel-combustion route. **[179]**

Mol% of Mn^{2+}	Cell constants (Å)			Cell volume $(Å)^3$ ($a*b*c$)
	a	***b***	***c***	
0 (Blank)	5.8207	8.2077	5.8006	277.1211
0.1	5.8170	8.2040	5.7970	276.6483
0.5	5.8153	8.2035	5.7950	276.4551
1.0	5.8137	8.2031	5.7937	276.3036
2.5	5.8153	8.2035	5.7954	276.4742
5.0	5.8155	8.2036	5.7956	276.4966

The structure of an ABO_3 ideal perovskite can be described as an association of $[AO_{12}]$ and $[BO_6]$ groups where the BO_6 octahedra forms a network by sharing corners, in combination with A^{2+} ion, which fills the hole in between the octahedra. A schematic of the crystal structure for the $SrZrO_3$ is presented in Figure 4.9-ii. In $SrZrO_3$, the size of Sr^{2+} ion is smaller than the hole which leads to a distorted structure. The incorporation of a smaller ion such as Sr^{2+} ion in the perovskite structure is accompanied by rotation of the octahedra leading to the lowering of the symmetry with respect to an ideal perovskite in which the coordination numbers of Sr cations & Zr cations are reduced. Tilting of the ZrO_6 octahedra reduces the coordination of an undersized Sr cation from 12 to as low as 8. Conversely, off-centreing of an undersized Zr cation within its octahedron allows it to attain a stable bonding pattern. This is why $SrZrO_3$ is considered to be pseudo cubic or orthorhombic at room temperature **[239,240]**.

Now the observed trend in lattice constant in Table 4.3 can be understood on the basis of the respective sizes of the cations. If we consider their ionic radii then 8-coordinated Mn^{2+} has a smaller ionic radius (0.96 Å**)** than the same coordinated Sr^{2+} ion (1.26 Å**)**; while 6-coordinated Mn^{2+} (0.83 Å**)** is larger than the same coordinated Zr^{4+} ion (0.72 Å**)** **[241]**. Thus if manganese ion occupies Sr^{2+} sites, a decrease in the cell constant value would be expected and if it occupies Zr^{4+} site, the cell constant value would be increased. Two interesting observations could be highlighted in Table 4.3; (i) the lattice constant values at all concentration is lower than undoped sample and (ii) it shows a decreasing trend up to 1 mol % followed by an increasing trend. This suggests that, for the entire range of concentration, the fraction of manganese ions residing at the Sr^{2+} site is more than that at octahedral Zr^{4+} site. However at higher doping level viz. 2.5 & 5.0 mol%, there is a considerable increase in the fraction of Mn^{2+} ions residing at octahedral Zr^{4+} site. This is probably due to the fact that at higher concentration, charge compensation gets relaxed and size matching plays the dominating role.

4.3.2. Photoluminescence: Emission, excitation and life time spectroscopy of Mn^{2+} doped $SrZrO_3$

The excitation spectrum of undoped $SrZrO_3$ (SZO) is represented by Figure 4.10a which shows a peak at around 250 nm which is attributed to host absorption band (HAB) arising due to O to Zr charge transfer **[242]**. Figure 4.10b represents the excitation spectrum of 0.1 mol % manganese ion doped $SrZrO_3$ where similar to the undoped compound a broad peak in the low wavelength region was observed. This is attributed to the overlap of the charge transfer (CT) bands from oxygen to manganese (O–Mn) and the host band (O-Zr). In addition to these host absorption bands, the excitation spectrum also consisted of few peaks at around 375, 438 and 489 nm which are characteristics excited bands of Mn^{2+} **[243]** due to transitions involving $^6A_1$ (^6S) $\rightarrow {}^4T_2$ (^4D), $^6A_1$ (^6S) $\rightarrow {}^4T_2$ (^4G) and $^6A_1$ (^6S) $\rightarrow {}^4T_1$ (^4G) of Mn^{2+} levels respectively.

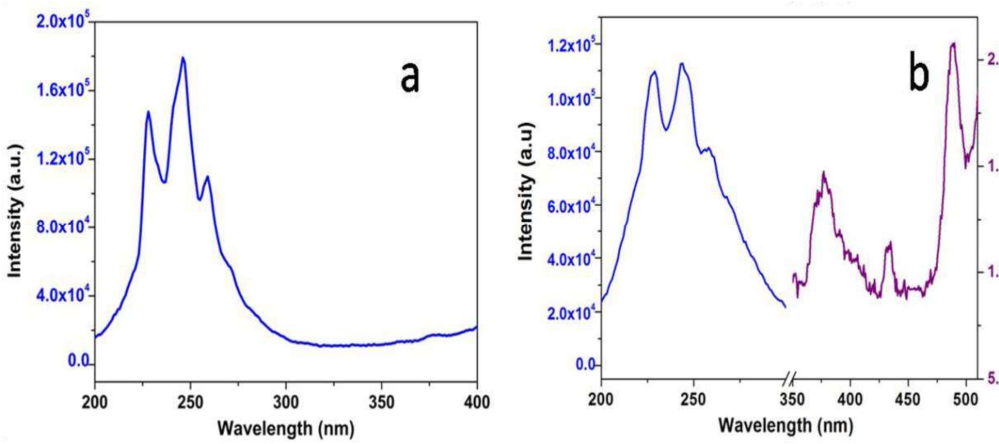

Fig. 4.10. *Excitation spectra of a) Pure SZO and b) 0.1mol% Mn^{2+}doped SZO with λ_{em} =430 nm* ***[179]***.

Fig. 4.11a & 4.11b show the room temperature emission spectra of undoped and 0.1 mol% manganese ion doped SZO. Based on the Gaussian line broadening mechanism for luminescence processes, the PL curves of the undoped and doped samples were deconvoluted using Gaussian fitting. The emission spectrum in Figure 4.11a for undoped SZO shows three PL components after deconvolution, namely violet-blue at $\lambda_{max} \approx 430$ nm (P_1), blue-green at $\lambda_{max} \approx 490$ nm (P_2) and yellow –

orange at $\lambda_{max} \approx 600$(P_4). The sharp peak around 600 nm might be due to unintensional Eu^{3+} ion impurity in the sample holder.This multicolour components are attributed to the presence of various defect states which create various electronic states within the band gap of materials. As reported in earlier literature, violet-blue emission (P_1) can be attributed to shallow defects, yellow-orange emission (P_4) (and also red) to deeper defects and the blue-green emission (P_2) is associated to surface defects. **[242,243,245]**

For the Mn-doped samples, in addition to host emission, two additional peaks at 540 nm (P_3) and 680 nm (P_5) were observed. Mn can be stabilized in host lattice in divalent, trivalent or tetravalent oxidation state. Mn^{4+} ion exhibits its characteristics emission band between 600 and 700 nm with four sharp peaks occurring at about 643, 656, 666, and 671 nm due to the ^2E-$^4A_2$ transition **[246-249]**. Absence of such peaks eliminates the possibility of Mn existing as Mn^{4+} in the present matrix. In addition size mismatching does not permit the stabilization of Mn as Mn (IV) (Ionic radios of 6 coordinated Mn^{4+}= 0.53 Å) on either at Sr^{2+} (1.26 Å) or Zr^{4+} (0.72 Å) site. Again if at all Mn gets stabilized in +4 oxidation state, in XRD a continuous decrease in the cell constant values would have been observed upon Mn doping since Mn^{4+} ions is smaller in size compared to both Sr^{2+} and Zr^{4+} ions. Therefore based on four analogy i.e. (i) spectral features in excitation spectra and in emission spectra, (ii) size matching assumption, (iii) cell constant values and (iv) low combustion temperature; we can propose that it is Mn^{2+} which is getting stabilized in $SrZrO_3$ lattice and not Mn^{4+}.

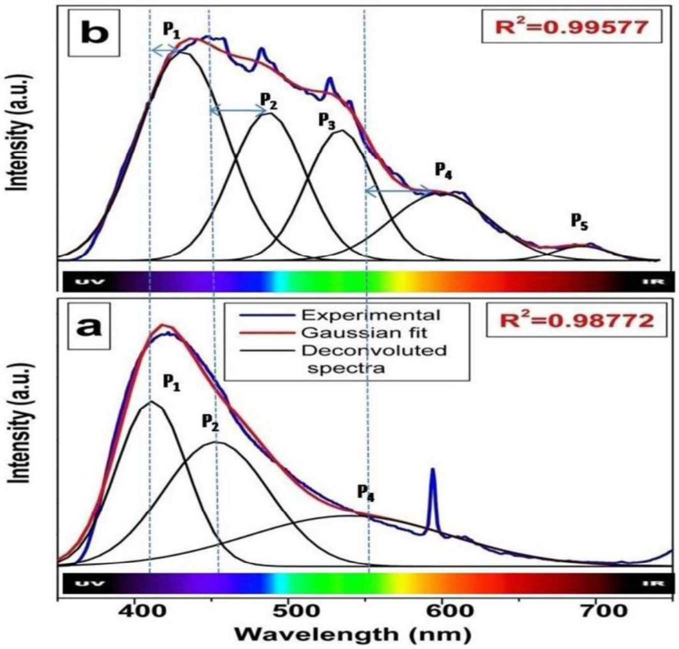

Figure 4.11. *Room temperature emission spectrum of a) pure SZO and b) 0.1 mol% Mn^{2+}doped SZO with λ_{ex} =255 nm* ***[179]****.*

Similar to Fe^{3+} in $ZnAl_2O_4$ **[178],** tetrahedrally coordinated Mn^{2+} ions (in weak crystal field) exhibit a green emission while the octahedrally coordinated Mn^{2+} ions (in strong crystal field) emit in the orange to red region **[250-253]**. In present case, observation of two different Mn^{2+} emission bands (green band at 540 nm; P_3 and red band at 680 nm; P_5) suggests that two different kind of crystal field environments are being experienced by the Mn^{2+} ions. In $SrZrO_3$, the mean bond Zr–O bond length is 2.10 Å which is much shorter than that of the Sr–O bond length is 2.96 Å **[250]**, which suggests that crystal field effect at Zr^{4+} site is stronger than at Sr^{2+}. Thus, the P_5 emission band at the longer wavelength can be attributed to the luminescence of Mn^{2+} ions staying in Zr^{4+} sites (characterized by a stronger crystal field and nephelauxetic effect), while the P_3 emission band at the shorter wavelength is due to Mn^{2+} ions located at Sr^{2+} sites.

Now to investigate the effect of doping level/concentration, the variation of intensity ratios of P_5/P_3 and P_4/P_1 with various concentration of Mn^{2+} viz. 0.1, 0.5, 1.0, 2.5 and 5.0 mol% were calculated as shown in Figure 4.16. It can be seen that at all concentrations, intensity of P_3 is more than that of P_5 justifying XRD results that Mn preferentially occupies Sr^{2+} site.With increasing Mn concentration, ratio of P_5/P_3 increases. In other words, emission due to Mn^{2+} at Zr^{4+} site increases i.e. at higher concentration, proportion of Mn ion occupying Zr^{4+} site is more than that at lower concentration, which is in concordance with the XRD results.

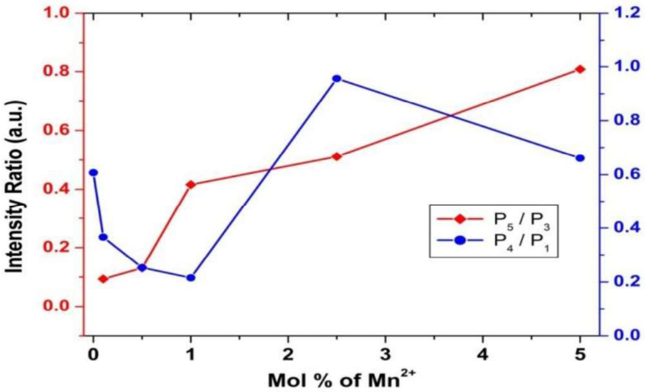

Figure 4.12: *Variation of intensity ration of peak P_5 to P_3 and P_4 to P_1 with different mol % of Mn^{2+} ion* ***[179]***.

The Figure 4.12 also reveals that at all concentration emission intensity of the P_1 band is more than that of P_4 ($P_4/P_1 < 1$). As stated earlier, P1 & P_4 bands are linked to shallow and deep defect states respectively. Thus an initial decrease in P_4/ P_1 ratio indicates increase in the population of shallow defect states while the increasing value of P_4/ P_1 ratio indicates increase in the population of deep defect states. In our report **[179]** from DFT calculated total and partial density of state (DOS) of Mn doped SZO, it was shown that Mn^{2+}substitution at Sr-site is linked to shallow defect states while that at Zr-site is linked to both deep and shallow defect states in the band gap . Thus the emission (P_4) coming from deep defect states will be influenced by substitution at Zr site only while emission (P_1) coming from shallow defect states will be influenced by substitution at both Sr & Zr sites. The current trend in P_4/ P_1 ratio implies that at all concentrations, fraction of Mn^{2+} ions occupying Sr^{2+} site are more than that at Zr^{4+} site. Initially at lower concentration (uo to 1.0 mol%) fraction of Mn^{2+} ions substituting Sr^{2+} ions increases, thereby increasing the P_1 emission intensity. However at higher concentration (beyond 1.0 mol %), there is a site swapping of Mn^{2+} ions towards Zr^{4+} site which leads to an increase in P_4 emission intensity. For better understanding about the origin of different components in the emission curve of $SrZrO_3:Mn^{2+}$and their respective change at different doping level, a pictorial representation is given in Figure 4.13.The higher intensity of P_2 band at higher doping level might be due to more number of surface defects of the SZO particles at higher Mn^{2+} ion concentration.

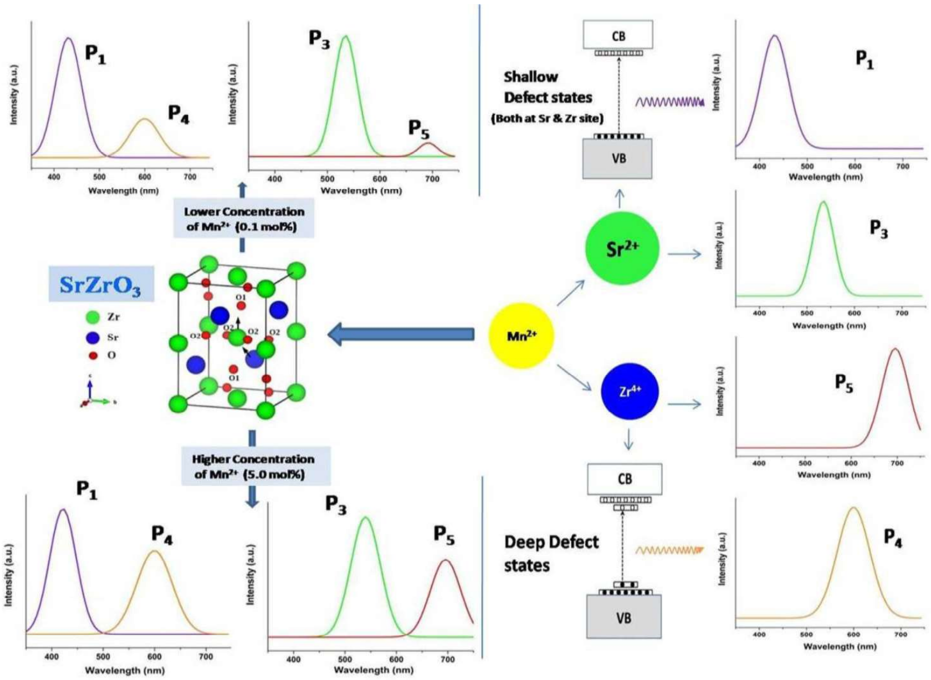

Figure 4.13: *Pictorial representation for the origin of the different peaks of SrZrO$_3$:Mn^{2+} and their variation with doping level* ***[179]****.*

Figure 4.14a shows the PL decay curves for undoped SrZrO$_3$ at emission wavelength λ_{em} = 480 nm and at excited wavelength λ_{ex} = 250 nm. The curve was best fitted on a 100 μs scale using the bi-exponential decay equation 4.**2**. The average lifetime values of slower decaying species is 12.0 μs, whereas for fast decaying species the values are around 2.0 μs. As explained in earlier section, there are shallow and deep defects within the band gap of SrZrO$_3$ nanoparticles. Faster decaying species is therefore attributed to radiative recombination process from deep defects whereas slower decaying species is attributed to similar phenomenon from shallow defects **[242, 254]**.

For 0.1 mol % Mn^{2+} doped SrZrO$_3$, the decay curve (λ_{em} = 540 nm and λ_{ex} = 250 nm) is shown in Figure 4.14b and a good fit was found on an 800 μs scale using the tri-exponential equation 4.**3**.

$$\mathbf{I\ (t) = A_0 + A_1 \exp(-t/\tau_1) + A_2 \exp(-t/\tau_2) + A_3 \exp(-t/\tau_3)} \qquad (4.3)$$

where A$_0$, A$_1$, A$_2$ and A$_3$ are scalar quantities obtained from the curve fitting, t is the time and τ_1, τ_2 and τ_3 are decay time values for exponential components respectively. The three lifetime values are of the order 1.5 μs (τ_1), 14 μs (τ_2) and 69 μs (τ_3). $\tau_1$and τ_2 are the contribution from host lattices itself whereas τ_3 is because of Mn^{2+} in SrZrO$_3$ matrix. It is difficult to resolve the lifetime value for Mn at Sr^{2+}-site and Mn at Zr^{4+}-

site due to strong host contribution in the doped sample also. Much change in the values of τ_1 and τ_2 was not observed while varying the concentration of Mn^{2+}, however the value of τ_3 first increased uo to 1.0 mol %, beyond which concentration quenching had taken place, resulting in decrease in τ_3 value **[179]**.

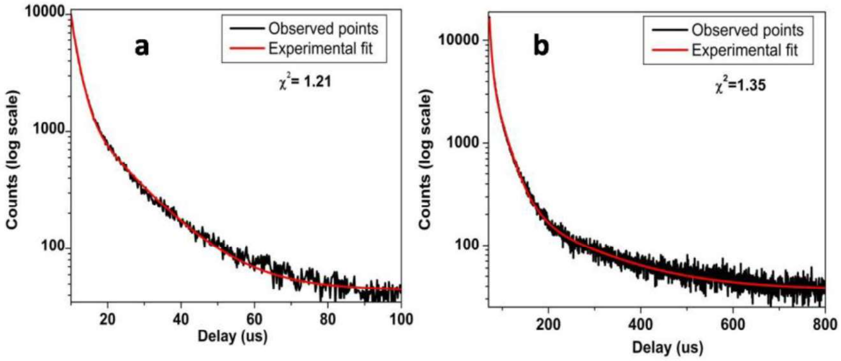

Figure 4.14: *Luminescence decay time profile of the a) SZO and b) 0.1 mol% Mn^{2+}doped SZO* ***[179]***

4.3.3. EPR study [179]:

The EPR spectrum of pure SZO (Figure 4.15a) shows an intense and asymmetric signal (g= 1.976) of the spin Hamiltonian at room temperature indicating the presence of some kinds of intrinsic defects in the as prepared material. This signal corresponds to singly ionized oxygen vacancies $V_O^{\bullet}$ and vacancy-related defects, **[255-257]** with the g-value in the range of 1.9560–2.0030. The change in the value of g for $V_O^{\bullet}$ in different system are related to differences in the method employed for synthesis, chemical environment, and heat treatment conditions. The broad line width of signal indicates a certain degree of heterogeneity (several species differ slightly in spectral parameters) typical of disordered environments, such as those found at the surface of nanostructured crystals. Such broad signal is also found in case of nanocrystallineTitania, which has attributed by the authors to species formed at the surface of TiO_2 **[258]**.

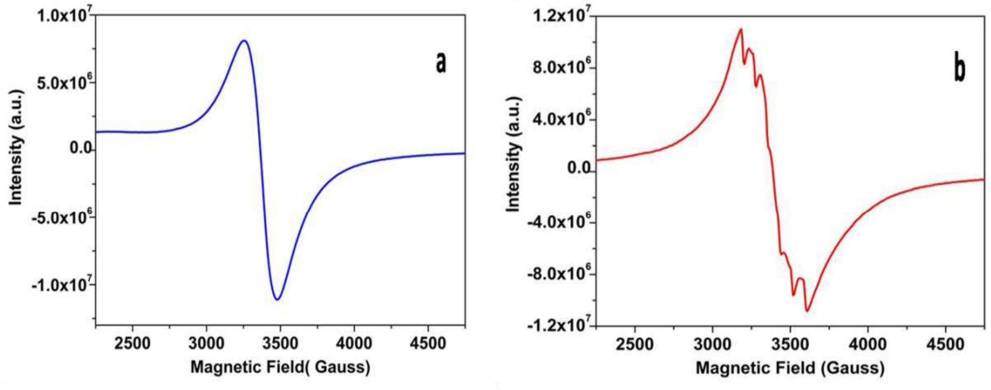

Figure 4.15: *Room-temperature EPR spectra of a) SZO & b) 0.1 mol% Mn^{2+} doped SZO* ***[179]***.

Matta *et al.,* **[259]** employed EPR to understand the phase transition from tetragonal to monoclinic zirconia and observed a signal *g* =2.0018, which was attributed to trapped single electrons located in oxygen vacancies of ZrO_2. Lin *et al.,* **[260]** reported that the EPR signal at *g*=1.9800 is related to oxygen vacancy. In the disordered ZrO_2, these $V_O^{\bullet}$ are linked to ZrO_5 clusters, called $[ZrO_5.V_O^{\bullet}]$ oxygen complex clusters **[261]**.

The powder EPR spectra corresponding to 0.1 mol% Mn^{2+} doped SZO is shown in Figure 4.15b, which shows six line patterns. In SZO lattice containing 0.1 mol % Mn ion, hyperfine transitions are possible due to the resonance associated to the dipole-allowed $\Delta M_S = \pm1$ with $\Delta M_I = 0$ that is ±5/2↔±3/2, ±3/2↔±1/2 and +1/2↔ -1/2 transitions. But the random orientations cancel out the anisotropic contributions from ±5/2↔±3/2 and ±3/2↔±1/2 transitions. Thus, only +1/2↔-1/2 transition shows six line pattern. These signals are attributed to Mn^{2+} incorporation inside the lattice sites (Sr^{2+}/Zr^{4+}) of SZO particles. In addition, it is possible to observe weaker kinks in the spectrum, which are produced by fine and hyperfine resonance from Mn^{2+} ions located on the surface. The substituted Mn^{2+} magnetic ions inside the lattice sites (Sr^{2+}/Zr^{4+}) of SZO particles generated an EPR signal S_I (g ≈ 1.993) and the ions located near the surface produced a low intensity EPR signal S_{II} (g ≈ 2.013) as shown in the simulated spectra for both 1st and 2nd harmonic EPR spectra of 0.1 mol% Mn^{2+} doped SZO in Figure 4.16 a & b. Our PL data has also shown an increase in surface defect related emission intensity (P_2) with increasing Mn ion concentration. This was probably due to increase in surface defects with increase in Mn ion concentration on the surface of the particle. In addition to S_I and S_{II}, the EPR spectrum also includes another broad signal S_{III} due to single-electron trapped oxygen vacancies for all the doped compounds. Kar *et al.,* has also reported surface defect-related luminescence properties of SnO_2 nanorods and nanoparticles in the visible region and also observed similar type of EPR signal (S_{III}) **[128]**. They have also shown that greater the surface defects greater is the intensity of S_{III} signal in EPR spectroscopy. The simulated S_I, S_{II} and S_{III} EPR signals as well as their combined effects S_{Total} for dipole-allowed transitions $\Delta M_S = \pm 1$ with $\Delta M_I = 0$ were compared to the experimental spectrum recorded for the 0.1 mol% Mn^{2+} doped SZO.

Figure 4.16a & b shows excellent agreement between the experimental and the simulated (S_{Total}) spectra which indicates the stabilization of divalent Mn^{2+} ions in the lattice **[262]** and further justifying our luminescence data to support the stabilization of Mn(II) in SZO lattice. It can also be observed from our EPR spectra, that broad signal (S_{III}) is more intense than the fine structure embedded in it, confirming strong host contribution even in doped sample. The simulation parameters (given in ref 179) agree reasonably well with the values reported in the literature for Mn^{2+} doped different nanocrystals having both surface and core Mn^{2+} ion **[263-265]**.

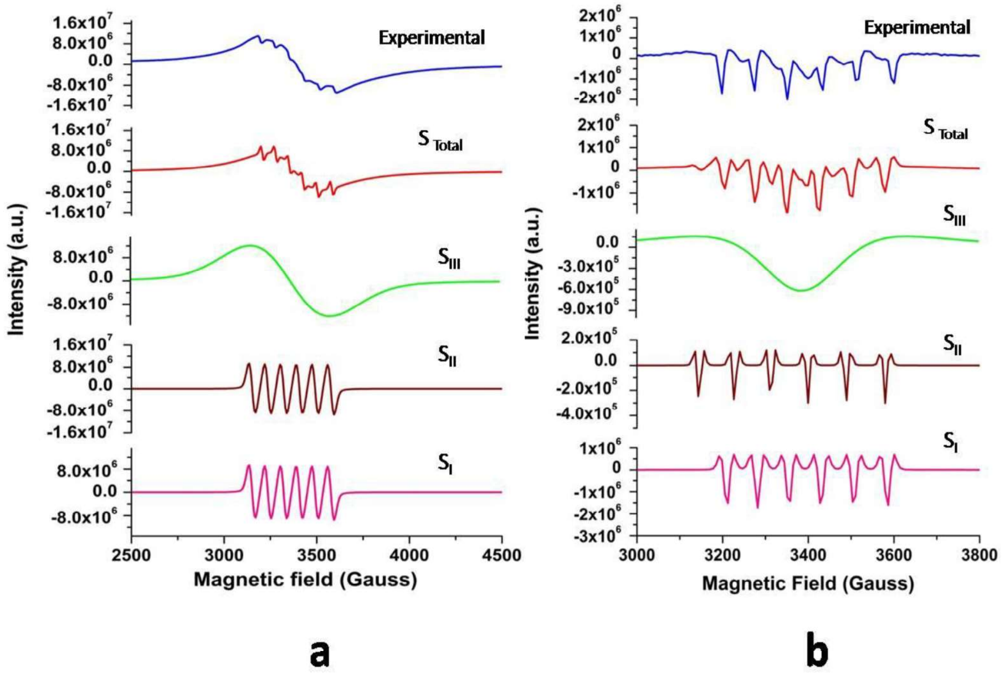

Figure 4.16: *(a) First & (b) Second harmonic EPR spectra of 0.1 mol% Mn^{2+} doped SZO samples (blue) and their simulated signals S_I, S_{II}, S_{III} and S_{Total}= S_I+ S_{II}+ S_{III}* **[179]**.

Figure 4.17 shows the dependence of EPR spectra on dopant ion concentration. At high Mn^{2+} ion concentration the hyperfine splitting completely disappears and the spectrum merges to one broad signal with slight decrease in line width. There are two contributions to the EPR signal coming from Mn^{2+} ions with concentration up to 1.0 mol%; (i) a broad resonance line of Lorentzian shape arising from spin–spin interactions between different Mn^{2+} centres in the core of the particles or the undiluted adsorbed Mn^{2+} ions as MnO on the surface of the particle in a cluster-like assembly such that the hyperfine structure collapses to a single line, and (ii) a set of six hyperfine lines from isolated Mn^{2+} centres (six allowed hyperfine transitions on the central Ms= 1/2 ↔ -1/2). With increasing dopant concentration, contributions from dipolar interactions between Mn centres become dominant, such that only one single line is detected for the samples with the highest Mn content. The initial increment in the line width can be attributed to Mn–Mn energy transfer and prevalence of exchange interactions over the hyperfine interactions. For the heavily Mn^{2+} doped samples (5 mol%), both fine and hyperfine structures are too weak and result in only a broad EPR spectrum reassembling a free-like state for S=1/2 and magnetic spin quantum number $M_S = \pm 1/2$. The disappearance of hyperfine lines and the observation of a single broad EPR line suggest that the Mn^{2+} ions are not completely diluted and strong dipole–dipole interactions persist in between them, both in core and surface of the particles at higher concentration of Mn. On increase of Mn concentration to 5 mol.% there is an exchange narrowing effect between the Mn^{2+} ions and as a result a decrease in the singlet line width is observed. Again the line broadening corresponding to the heavily doped $Mn^{2+:}$ SZO particles may not be only due to dipole–dipole interaction between paramagnetic Mn^{2+} ions, but may also be due to dipole–dipole interaction in between the paramagnetic single-electron trapped oxygen vacancies $[V^{\bullet}_{O}]$. Since S_{III} is contributing more to the S_{Total} value as shown in Fig. 4.16, any change in S_{III} value will be reflected in the value of $S_{Total.}$ Thus the increase in intensity of the EPR spectra at higher doping level is not only due to increase in concentration of paramagnetic Mn^{2+} ions but also due to increase in S_{III} value. This suggests an increase in the concentration of paramagnetic single-electron trapped oxygen vacancies $[V^{\bullet}_{O}]$. This is possible only when Mn^{2+} ions are either adsorbed on surface and thereby creating surface defect oxygen vacancies or substituting Zr^{4+} ions and thereby creating oxygen vacancies due to charge compensation. This also suggests that at higher concentration the number of Mn^{2+} ions substituting Zr^{4+} ions or present on the surface of the particles are also increased. Thus, both the explanations are supported by our earlier observed photo luminescence data and vice versa.

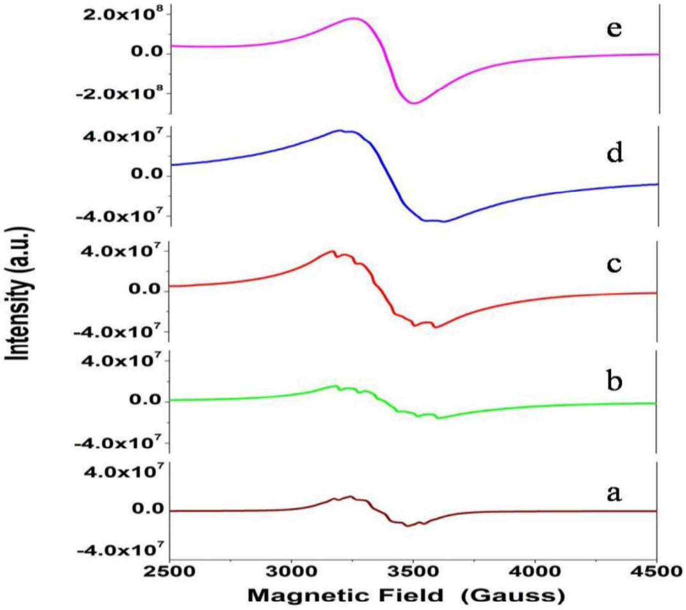

Figure 4.17: *The EPR spectra recorded for the $Sr_{1-x}Mn_xZrO_3$ samples with concentration: a) x = 0.001, b) x = 0.005, c) x = 0.01, d) x= 0.025 and e) x = 0.05* ***[179]***

4.4. Synthesis and optical properties of $LiZnVO_4$ [177]

4.4.1 Synthesis, characterization and morphology

4.4.1.1. Synthesis

In sol-gel-combustion method, stoichiometric amounts of lithium carbonate (98 %, Merck), zinc acetate (99 %, Lobachemie), ammonium metavanadate (99 %, Qualigens fine chemicals) and Citric acid and as a fuel were used. At first, ammonium vanadate was made soluble in quartz double distilled (QDD) water by adding few drops of concentrated nitric acid under IR lamp where a clear yellow colour solution was observed. In another beaker, solution of Lithium carbonate was prepared by dissolving it in QDD water with addition of few drops of concentrated nitric acid. This solution was then added to the ammonium vanadate solution. Separately prepared Citric acid and zinc acetate solutions by dissolving the reagents in ODD water were added to the mixed solutions under vigorous stirring. It was found that on addition of zinc acetate solution the colour was changed from yellow to blue via an intermediate green colour. The explanation of this interesting colour changing is given in the next section. The bluish solution was then heated at 70 ^{0}C with constant stirring on a magnetic stirrer for

5 hours until gel formation had taken place following a chemical reaction. The gel was then heated at a temperature of 100 ^{0}C placed on a heating mantle and a combustion reaction had taken place resulting an ash-like product. The ash-like product was then ground in an agate mortar and kept for calcination at different temperatures, starting from 200ºC to finally at 600ºC when a white powder was formed. At each heat treatment, from solution state to solid white powder during the course of reaction, EPR spectrum has been recorded. This white powder was then characterized by XRD and SEM techniques followed by PL measurements.

4.4.1.1.a Explanation of colour changing during the solution chemistry

Vanadium exhibits various oxidation states of +2, +3, +4 and +5 under different conditions among which +4 is the most stable one. The various oxidation states of vanadium are characterized by their different colours in acidic solution. It shows pale yellow colour at +5 state, blue at +4 state, green at +3 state and purple–violet at +2 states. Here in the present synthesis procedure,$NH_4VO_3$was taken as a starting material along with Zinc acetate and Li_2CO_3. Thus, the yellow colour of acidic NH_4VO_3 solution was due to formation of VO_2^+ ion. Now the colour change from yellow to blue via an intermediate green colour on addition of Zinc acetate solution was due to change of oxidation state from +5 to +4 (in the form of VO^{2+}) via an intermediate oxidation state +3. The systematic changes of oxidation states and their relative stability in this acidic medium can be explained in a proper way by considering the Latimer diagram of the species involved and the Electrode potential values of the following red-ox reactions.

i. $VO_3^{1-}{}_{(aq)} + 6H^+{}_{(aq)} \rightleftharpoons VO_2^+{}_{(aq)} + 3H_2O_{(l)}$ [an acid–base reaction]

ii. $VO_2^+{}_{(aq)} + 2H^+{}_{(aq)} + e^- \rightleftharpoons VO^{2+}{}_{(aq)} + H_2O_{(l)}$
$E^{\varnothing}_{\text{half–cell potential}} = +1.00V$, pale yellow to the blue oxovanadium (IV) ion

iii. $VO^{2+}{}_{(aq)} + 2H^+{}_{(aq)} + e^- \rightleftharpoons V^{3+}{}_{(aq)} + H_2O_{(l)}$
$E^{\varnothing}_{\text{half–cell potential}} = +0.34V$, blue to green vanadium (III) ion

iv. $2VO_2^+{}_{(aq)} + 4H^+{}_{(aq)} + Zn_{(s)} \Longrightarrow 2VO^{2+}{}_{(aq)} + 2H_2O_{(l)} + Zn^{2+}{}_{(aq)}$
$E^{\varnothing}_{\text{reaction}} = E^{\varnothing}_{\text{reduction}} - E^{\varnothing}_{\text{oxidation}} = +1.00 - (-0.76) = +1.76V$

v. $2VO^{2+}{}_{(aq)} + 4H^+{}_{(aq)} + Zn_{(s)} \Longrightarrow 2V^{3+}{}_{(aq)} + 2H_2O_{(l)} + Zn^{2+}{}_{(aq)}$

$E^{\varnothing}_{\text{reaction}} = +0.34 -(-0.76) = +1.10V$,where $E^{\varnothing}_{Zn(s)/Zn2+(aq)}$ is $-0.76V$

Thus the redox reactions (i-v) explained the existence of VO^{2+} in the mother solution giving steady blue colour while the intermediate green colour is due to less stable V^{3+} in this medium. Latimer Diagram (Figure 4.18) also explains the same.

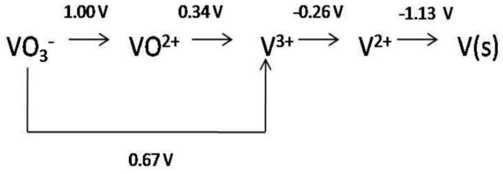

Figure 4.18: *Latimer Diagram* ***[177]***

4.4.1.2. Phase purity and structure: X-Ray Diffraction

Figure 4.19a represents the XRD patterns of $LiZnVO_4$ which matches well with rhombohedral phase of $LiZnVO_4$(ICDD file no 38-1332). Pure $LiZnVO_4$ could be obtained on annealing the samples at and above 600°C. The XRD data was indexed on a rhombohedral system with space group *R3* having cell parameters a = 14.18 Å and c=9.487Å.

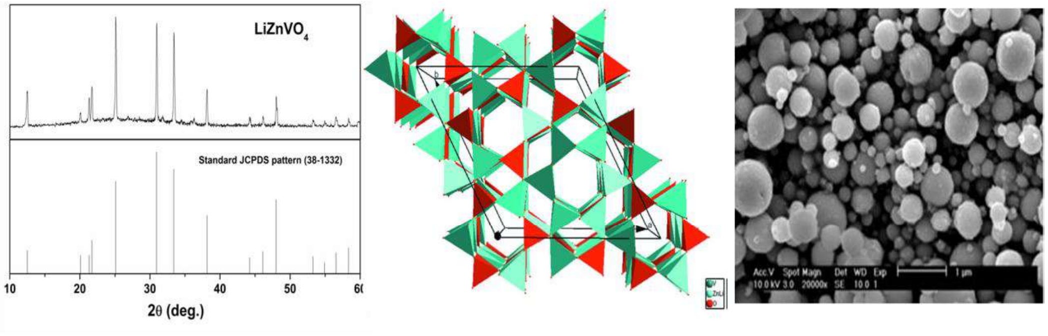

a b c

Figure 4.19: *(a) XRD pattern of the lithium zinc vanadate (LZV) powder samples annealed at 600°C and Standard ICDD stick patterns with file No-38-1332 , (b) Crystal structure of* $LiZnVO_4$ *and (c)SEM image of LZV*

Figure 4.19b shows the phenacite structure of $LiZnVO_4$ which could be described as three dimensional arrangement of $[MO_4]$ tetrahedra (M= Li/Zn or V) sharing apices. The arrangement concerns three different types of tetrahedra $[VO_4]$ and two disordered sites $[Li/ZnO_4]$, which give rise to an overall disordered phenacite structure. When viewed along the c axis, the packing of $[MO_4]$ tetrahedra results in two types of tunnels: large hexagonal tunnels surrounded by six lozenge like channels (rings of four tetrahedra). Similar description has recently been reported by Capsoni*et al* **[266]** using a powder X-ray diffraction data of $LiZnVO_4$.

4.4.1.3. Morphology and particle size: Scanning electron microscopy

SEM studies showed that the particles are uniformly distributed and mostly of spherical morphology as can be seen from Figure 4.19c. Moreover the LZV nanosphere shows 100-200 nm size grains, which were highly uniform and monodisperse in nature. Most of the particles have same morphology. These image shows homogeneous aggregates with a sphere-like aspect, which are composed of large number of small grains.

4.4.2 EPR study at various intermediate steps during synthesis

EPR spectra were recorded at different interval during the course of this synthesis procedure. This technique is a powerful tool which provides information about the elemental composition, nuclearity, and electronic structure of a paramagnetic state. In the present case, since VO^{2+} is a paramagnetic species ($3d^1$), it can be used as a spin probe to monitor the progress of reaction during the formation of $LiZnVO_4$ via sol-gel combustion route. Figure 4.20a shows the EPR spectrum recorded at various stages of the reaction. In the solution stage of the reaction (after stirring for 2 hours of the mixed solution), the EPR spectrum had shown a set of 8 lines with different intensities which is due to existence of VO^{2+}. The set of 8 lines arise due to interaction of the electron spin ($S = 1/2$) with the ^{51}V nucleus ($I = 7/2$). Here the g-values for vanadium complexes are smaller than that for free electrons ($g_e = 2.0023$). An octahedral site with a tetragonal compression would give $g_{||} < g_{\perp} < g_e$ and $A_{||} > A_{\perp}$ with A_{iso} generally larger than 100 G **[267]**. As stated earlier that g is the g-factor (Landé g-factor) and A is hyperfine coupling constant, which is the characteristic of the molecular environment and is parameterized by the A_{iso} where the 'iso" emphasizes that this is the isotropic value. A_{iso} is calculated using the equation:

$$A_{iso} = (A_{||} + \mathbf{2}\, A_{\perp})/3 \tag{4.4}$$

The g and A values obtained (Table-4.4) in the solution state agree with this relationship and are close to those reported for octahedral vanadyl complexes containing oxygen as an equatorial ligand **[267]**. It is therefore confirmed that the vanadium ions in solution state of the reaction exist as VO^{2+} ions in octahedral coordination with a tetragonal compression and have C_{4v} symmetry. The intensities of these lines were decreased, when the ash-like product was heated at different temperatures. Finally the set of 8 lines completely disappeared in the white powder obtained after calcination at 600 ^{0}C. This is due to complete oxidation of the VO^{2+} ions to EPR inactive V^{5+} (3d^0) ion. In the intermediate states, the intensities decreased due to partial conversion of the VO^{2+} ions to EPR inactive V^{5+}. Up to 400 ^{0}C, there was a clear existence of VO^{2+} ion in small concentration and above 400 ^{0}C, the concentration was too low to be detected by EPR technique and at 600 ^{0}C the spectrum showed a flat line. Thus EPR technique in this case can be used to monitor the change of oxidation states and to optimize the final calcination temperature for the formation of LiZnVO$_4$ via sol-gel-combustion route.

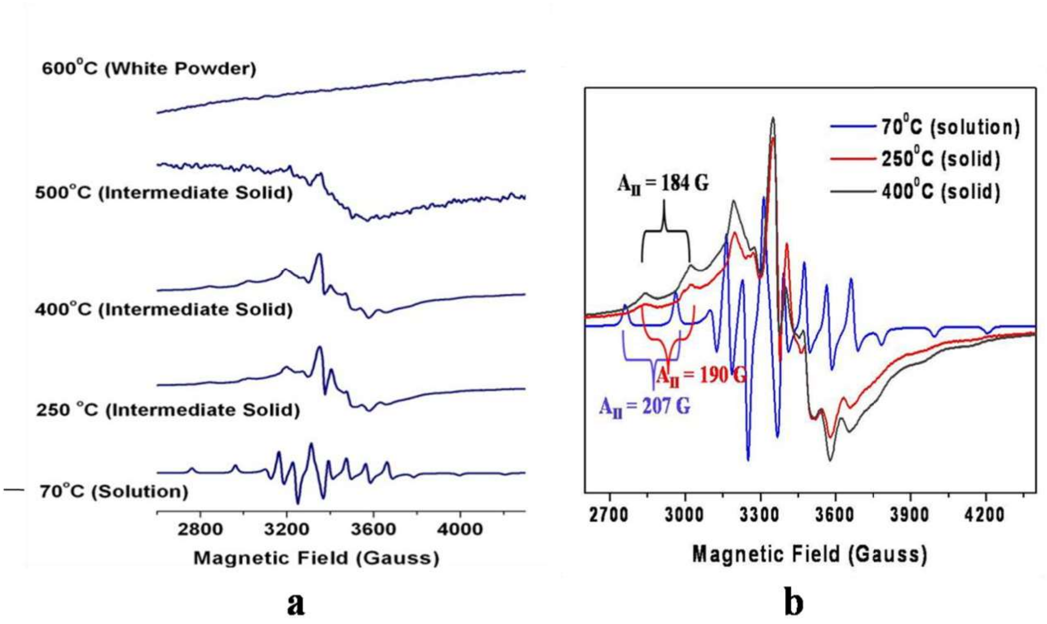

Figure 4.20: *(a)EPR spectra of vanadium at different stages during sol-gel chemistry and (b) Comparison of $A_{//}$ value of VO^{2+} in different stages of annealing* ***[177]***

The results in Table-4.4 also show a continuous decrease of A_{iso} values from the solution to solid state at different heating temperatures. The decrease in A_{iso} indicates the change in symmetry around vanadium from octahedral to tetrahedral. The axial ESR spectra of tetrahedral vanadium complexes are characterized by $g_\perp > g_{||}$ and $A_{||} > A_\perp$ but with A_{iso} value (80-100 G) smaller than that for octahedral complexes **[267].** Figure 4.20b shows the comparison of $A_{||}$ value for VO^{2+} in solution (70 ^{o}C), intermediate (250 ^{o}C) and solid state stage (400 ^{o}C). It is to be noted here that g and A values were calculated uo to 400^{o}C and after that the spectrum started disappearing as most of the

VO^{2+} present were converted to EPR inactive V^{5+}. These changes of coordination around vanadium ion also support the existence of VO_4 tetrahedra as concluded from XRD data shown in Figure 4.19.

Table-4.4: Principal values of g and hyperfine (A) tensors for paramagnetic vanadyl complexes at different temperatures. **[177]**

Physical State	$g_{\|\|}$	$g_{\perp}$	g_{iso}	$A_{\|\|}$ (G)	$A_{\perp}$ (G)	A_{iso}(G)
Solution (freeze at -70 ^{0}C)	1.9345	1.9818	1.9660	207.14	80.28	122.56
Solid at 250 ^{0}C	1.9273	1.9685	1.9547	190	60.71	103.80
Solid at 400 ^{0}C	1.9355	1.9630	1.9538	184.28	57.53	99.78

4.4.3. Photoluminescence spectroscopy: Excitation and Emission spectroscopy, colour coordinates and lifetime study

The excitation spectrum of $LiZnVO_4$ phosphor with λ_{em}= 543 nm is shown in Figure 4.21a which exhibits a broad band in the UV region with maximum intensity at 375 nm ($^1A_1 \rightarrow {}^1T_1$). This absorption band (excitation peak) is mainly because of the charge transfer from the oxygen ligands (O^{2-}) to the central vanadium atom (V^{5+}) **[268]**. The emission spectrum of $LiZnVO_4$ phosphor at λ_{ex} =375 nm is shown in Figure 4.21b. In $LiZnVO_4$, VO_4^{3-} ion is in T_d symmetry where the V^{5+} ion has a closed-shell electronic structure with no d electron. The excitation and luminescence phenomenon results from the one electron charge transfer process from the oxygen 2p orbital to the 3d orbital of the V^{5+}. Here in LZV, the bright green luminescence at 543 nm is due to the ($^3T_2 \rightarrow {}^1T_1$) transition and it is allowed due to spin–orbit interaction [**269,270]**. In compounds like tungstates and vanadates, the most common defects are found to be oxygen vacancies. These defects also act as radiative centres in the luminescence processes by creating different electronic states inside the band gap. Thus these vacancies might also be responsible for the bright green emission in the prepared $LiZnVO_4$ ceramic phosphor.

The decay curve for LZV prepared at 600°C is shown in Figure-4.21c at excitation wavelength of 375 nm and emission wavelength 543 nm and fitted using the mono-exponential decay equation 4.1 and the decay time obtained is 8.3 µs.

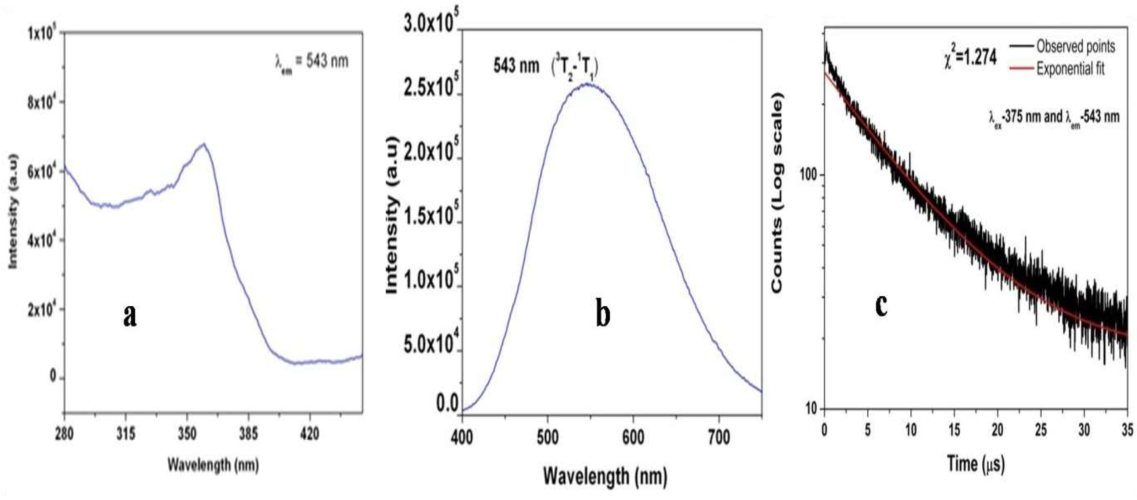

Figure 4.21: *(a) Excitation and(b) Emission spectra of* $LiZnVO_4$ *(c) and its decay profile* ***[177]***

Evaluation of colour coordinates:

CIE chromaticity coordinates were evaluated adopting standard procedures for the system **[202]**. The values of x and y coordinates of the present phosphor system were calculated to be 0.31 and 0.41 respectively. This is pictorially represented in Figure 4.22, where the point is denoted by an 'asterisk'. As evident from Figure 4.22, the CIE index for the phosphor system is very close to the 'greenish' line. Thus, it can be inferred that the particular lithium zinc vanadate can be potential green phosphor material.

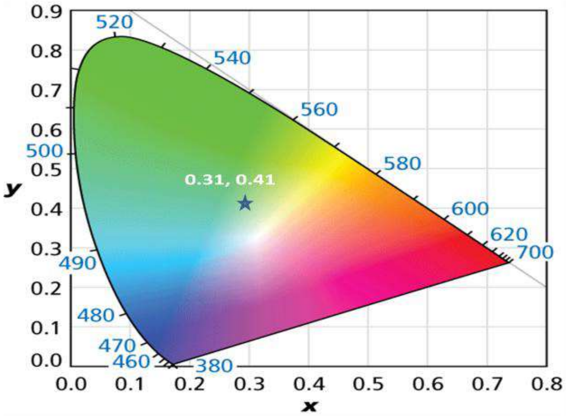

Figure 4.22 *: CIE chromaticity diagram for the* $LiZnVO_4$ *phosphor at 359 nm excitation* ***[177]***

Chapter 5

Lanthanide and Actinide ions mediated optical properties in Sm^{3+}:$BaZrO_3$, Eu^{3+}:$BaZrO_3$, $Bi_{1.96}Eu_{0.04}UO_6$ & U:$MgAl_2O_4$

5.1 Introduction:

The lanthanide series which comprises of 15 metallic chemical elements, starting from lanthanum (atomic numbers 57) through to lutetium (atomic numbers 71) along with the scandium and yttrium are known as the rare-earth (RE) elements. In most cases, the informal chemical symbol Ln is used to refer any lanthanide for any kind of general discussions of lanthanide chemistry. These elements are characterized by an incompletely filled 4f shell which is shielded from their surroundings by the filled $5s^2$ and $5p^6$ orbitals. This shielding results in sharp and narrow lines of the emission spectra of transitions within the 4f configuration **[271,272]** because the 4f electrons are not influenced by the surroundings. In contrast, the transition involving d-electrons such as the emission spectra arising from 5d–4f transitions (e.g. Ce^{3+}) are broad because the unshielded 5d electrons are heavily influenced by their surroundings in this case **[271]**. In addition to the sharp emission characteristics of the Ln elements, the forbidden character of the f–f transitions in 4f configuration also leads to substantially long lifetimes values (mostly in the range of milliseconds). However, for parity allowed transitions, such as for 5d–4f transitions, a much faster luminescence lifetime ($\sim 10^{-5}$ s) is observed. Lanthanide ions have been extensively studied as activators for luminescent materials due to the ladder like energy levels. Optical materials doped with rare earth elements are of great relevance in science and technology. In modern solid state optical technology, lanthanide doped materials have tremendous applications ranging from solid state lasers for industry, medicine and environmental monitoring, to active optical fibers for telecommunication purposes and phosphors for cathode ray tubes, displays, plasma monitors and lightning applications. Lanthanide ions are also extensively used as local probes for identifying local structures in crystalline material. This will help in understanding the effect of chemical and thermal treatment on catalysts and probing the structure of biological molecules. In this context Eu (III) ion is most appropriate as luminescent structural probe for the determination of the number of metal ion sites in a compound, their symmetry, and their respective population **[273-275]**. This is because of the relative simplicity of Eu energy-level structure and the fact that it possesses non-degenerate ground ($^7F_0$) and excited ($^5D_0$) states, and because the absorption and emission spectra of this ion show marked dependence on its site symmetry in the host material. The orange emission (590–600 nm) of Eu^{3+} ,which is due to the magnetic dipole (MD) transition $^5D_0 \rightarrow ^7F_1$ is not affected much by the site symmetry since it is parity-allowed, while the red emission (~610–630 nm) due to the electric dipole (ED) transition of $^5D_0 \rightarrow ^7F_2$, being hypersensitive, is affected by the site symmetry of Eu^{3+} ion **[273-275]**. Now in a crystal site with inversion symmetry the MD transitions are usually the dominant emission lines and the ED transtions are strictly forbidden. On the contrary, in a site without inversion symmetry (ED) of $^5D_0 \rightarrow ^7F_2$ transition is usually the strongest emission line, because transition with $\Delta J = \pm 2$ is hypersensitive to small deviation from inversion symmetry. In this way, the symmetry around the lanthanide ion can be determined from the shape of the emission spectrum of Eu^{3+} ion. Luminescence spectrum of Dy^{3+} consists of two relatively intense bands in the visible spectral region that correspond to the $^4F_{9/2}$–$^6H_{15/2}$ (blue) and $^4F_{9/2}$–$^6H_{13/2}$ (yellow) transitions, respectively. The yellow emission of Dy^{3+} is especially hypersensitive to the local environment, while its blue emission is not sensitive. Generally, when Dy^{3+} is located at a low symmetry (without an inversion centre), the yellow emission is dominant, whereas the blue emission is stronger, when Dy^{3+} is located at a high symmetry (with an inversion centre) **[276,277]**. In case of Sm^{3+}; $^4G_{5/2}$-$^6H_{7/2}$ ($\Delta J = \pm 1$) transition is partly magnetic dipole (MD) and partly electric dipole (ED) nature, whereas $^4G_{5/2}$-$^6H_{5/2}$ is purely MD in nature and $^4G_{5/2}$-$^6H_{9/2}$ is purely ED in nature **[278]**. The magnetic dipole (MD) transition $^4G_{5/2} \rightarrow ^6H_{5/2}$ does not depend on chemical surroundings of the luminescent centre and its symmetry. However, the hypersensitive $^4G_{5/2} \rightarrow ^6H_{9/2}$ transition is magnetic-dipole forbidden and electric-dipole allowed. Its intensity increases as the environmental symmetry become lower.

Recently lot of research interests have been focused on luminescence studies pertaining to ABO_3 type distorted perovskite oxide like $SrTiO_3$ **[279]**, $PbZrO_3$ **[280]**, $PbTiO_3$ **[281]**, $CaTiO_3$ **[282]**, $MgTiO_3$ **[283]**, $SrZrO_3$ **[178, 242, 284, 285]** etc., where local defects in the perovskite structure is mostly responsible for photoluminescence in visible region. The local defects in such cases are mostly oxygen vacancies (OV); which can be neutral (V_O), singly ionized V_O^{+1} or doubly ionized V_O^{+2} depending upon the thermal treatment and synthesis condition and methodology. The advantage of such perovskite-based materials is their ability to stand out from the other as far as luminescence study is concerned. Because they are very robust host and are sufficiently conductive to release the accumulated charges on the surface of phosphor particles, which makes them suitable candidate for field emission display (FED) and plasma display panel (PDP) devices **[286]**. They are also reported to be highly resistant to high-density electron irradiation because of which thermal stability and luminescence efficiency is maintained even with prolonged columbic loading **[287]**.

Among the materials evaluated as host for lanthanide ions in this work, our attention was mostly focused on alkaline zirconate such as Eu^{3+} and Sm^{3+} doped $BaZrO_3$ (BZO). These materials are characterized by good transmission properties in the visible part of the electromagnetic spectrum with relatively low phonon energies. They can be efficiently doped with lanthanide ions, due the similarity between the ionic radius of the alkaline earth and the lanthanide ions. Barium zirconate is one such perovskite which is an excellent luminescence host and used in various rare earth doped phosphor such as Eu:BZO **[288]**, Eu,Ti:BZO **[289]**, and Yb,Tm :BZO **[290]** etc. Undoped BZO is reported to give visible light emission in blue-green region which is attributed to presence of oxygen vacancy or other structural defect produced during the synthesis **[261,291-294]**. As far as literature is concerned there is no report on luminescence of Sm^{3+} in BZO and there is only report by Hano-Gonzalez *et al.,* which explains the site occupancy of Eu^{3+} in $BaZrO_3$ **[295]**. In the present study, time resolved photoluminescence (TRPL) spectroscopy was used as a tool to probe the local site of Eu^{3+} and Sm^{3+} in BZO. Understanding the local site of lanthanide ion in doped host, where multiple sites are available for occupancy is very important to have better understanding of structure-property correlation to optimize its performance.

Another work, where special emphasis was given in the present thesis, is the local site occupancy of La in $Bi_{2-2x}La_{2x}UO_6$ (x=0-0.05).This compound is reported to show two regimes of conductivities with respect to temperature, having a change in conductivity at 550 °C **[296]**. In both regimes, O^{2-} ions are the charge carriers. The ionic conductivity of these solid solutions is due to the migration of oxide ions through the oxygen vacancies. Since the ionic sizes of La^{+3} and Bi^{+3} are similar (1.032 Å and 1.030Å respectively), La^{+3} can replace Bi^{+3} to form La doped Bi_2UO_6 solid solutions, with almost similar cell volume and structure. Such solid solutions shall be an interesting class of compounds having same cell volume and structure but different properties e.g. magnetic, ionic and thermal. Since La^{+3} is a non activator ion, PL study is not possible to probe the local structure around La in $Bi_{2-2x}La_{2x}UO_6$ solid solutions. However, in case of isostructural compound such as $Bi_{1.96}Eu_{0.04}UO_6$, with good activator Eu^{3+} (7 co-ordinated Eu^{3+}= 1.03Å) ion, which shows similar behavior as

La^{+3}, PL study might be very much helpful to probe the local structure. In a previous study on double perovskite compounds with the formula $BaA'LaTeO_6$ (A' = Na, K, Rb), the La site occupancy was supported by the characteristic PL emission of Eu^{3+} ion when it was doped in the matrix in place of La^{3+} ion **[297]**. Similarly in present case, proof of La site occupancy in $Bi_{2-2x}La_{2x}UO_6$ solid solutions can be obtained indirectly by preparing an isostructural solid solution $Bi_{1.96}Eu_{0.04}UO_6$ followed by its PL study. Again since both U (VI) and oxygen vacancies give emission in the visible region, PL technique will also give information regarding speciation of U(VI) and doping induced defect such as oxygen vacancies. The preparation and local structure investigation of $Bi_{2-2x}La_{2x}UO_6$ solid solution using PL and EPR technique is being reported for the first time to the best of our knowledge.

Similar to the lanthanides, actinides are good candidates as activator ions in electro-optic materials due to the numerous sharp emissions covering a broad spectral region. For example, crystals of uranium doped alkali fluorides, alkaline earth fluorides, and lanthanide fluorides have shown emission spectra containing many narrow lines and sharp bands associated with uranium as luminescent centre **[298-301]**. As stated earlier in Chapter 1 that compared to 4f electron in lanthanides; 5f-electrons are relatively less shielded by outer lying electrons. As a result they are more perturbed by local crystal field which results in broad emission and absorption spectrum. Oscillator strength of 5f-5f transition is relatively larger than in iso-electronic lanthanide ion. Actinide chemistry is gaining new interest day by day because of stabilization of various unusual oxidation states, unique magnetic properties and chemical reactivity. Among all the actinides, most of the research is focused on uranium, in particular in the form of UO_2^{2+} ion because it is the most dominant form of natural and spent uranium. The fact that U (+3), U(+4), U(+5) and U (+6) are all luminescence active ion and stabilizes under different conditions; time resolved photoluminescence (TRPL) is used extensively in uranium speciation in doped solid. In most of the cases U (+3), U (+4), U (+5) stabilize in single crystal while U (+6) is most likely to get stabilized in solid powder. Some of the recent results from our laboratory suggested similar trends e.g. Uranium stabilizes as UO_2^{2+} in Sr_2SiO_4, $Sr_2P_2O_7$, ThO_2 **[21, 302, 303]** whereas as octahedral uranate UO_6^{6-} in $SrZrO_3$, SrB_4O_7 **[304, 305]** etc. In some of the matrix uranium simultaneously stabilizes as U(IV) and U(VI) such as $Gd_2Zr_2O_7$ **[306]**.

In present work, special emphasize has been given on photoluminescence properties of uranium in $MgAl_2O_4$. $MgAl_2O_4$ is proposed candidate for minor actinide transmutation; because of its favorable high temperature properties and high radiation stability **[307].** It has been used extensively as a host for lanthanide luminescence like Ce^{3+} **[308]**, Eu^{3+} **[309]**, Tb^{3+} **[310]**, Dy^{3+} **[311]**, Gd^{3+} **[312]**, Yb^{3+} **[313]** etc. But actinides as dopant in $MgAl_2O_4$ ion have never been explored. Considering the fact that $MgAl_2O_4$ is one of the probable candidates to be used for transmutation of actinide; speciation study of uranium ion in this particular matrix holds high significance for nuclear scientist. 1.0 mol % of uranium ion was doped in combustion synthesized $MgAl_2O_4$ and its local site occupancy, valence state and coordination geometry behavior were probed using TRPL spectroscopy.

5.2. Synthesis and Optical properties of Sm^{3+} and Eu^{3+} doped $BaZrO_3$ nanocrystals [314]

5.2.1. Synthesis, characterization and morphology

5.2.1.1 Synthesis

Analytical grade chemicals of $ZrO(NO_3)_2.xH_2O$ (AR Grade, Loba Chemie), $Ba(NO_3)_2$ (AR Grade, Merck), NH_4NO_3 (AR Grade, Chemico Fine Chemicals) and citric acid (AR Grade, Chemico fine Chemicals $C_6H_8O_7{\cdot}H_2O$) Eu_2O_3 (Sigma-Aldrich $\geqslant$ 99.99%) and Sm_2O_3 (Sigma-Aldrich $\geqslant$ 99.9%) were used as starting reagents for the synthesis of barium zirconate nanoparticles. Initially dilute solution of $Ba(NO_3)_2$, $ZrO(NO_3)_2.xH_2O$, NH_4NO_3, Eu_2O_3 , Sm_2O_3 and citric acid were prepared in separate beakers by dissolving them in QDD water or dilute nitric acid .Then the solutions of ammonium nitrate was transferred to the beaker containing barium nitrate solution followed by addition of zirconyl nitrate solution under vigorous stirring. Solutions of Eu_2O_3 and Sm_2O_3 in dilute niric acid were added separately to two different slotion mixtures. Next 2M citric acid (acting as a fuel) was added to these mixtures. These entire solution resulted in the formation of an opal gel after few minutes; which on subsequent heating at 100 °C for 10 hr under Infrared (IR) lamp lead to complete dehydration. These dehydrated products were then subjected to heating at 300 °C for 10 min in muffle furnace, which resulted in an ash-coloured voluptuous mass. The ash-like products were ground in an agate-mortar pestle and then subjected to slow calcination at 600 °C for 2-3 hour, which resulted in formation of crystalline white powder.

5.2.1.2 Phase identification and structure

Figure 5.1 represents the X-ray diffraction (XRD) pattern of $BaZrO_3$ (BZO) host and 1 mol % Ln^{3+}($Ln^{3+} = Sm^{3+} / Eu^{3+}$) doped $BaZrO_3$ samples. All the diffraction peaks can be indexed to the pure cubic phase of $BaZrO_3$ (JCPDS 06-0399). No traces of any other impurities diffraction peaks (BaO, Eu_2O_3 or Sm_2O_3) were observed in the doped sample which indicates formation of a single phase solid solution of $BaZrO_3$ and Eu^{3+}/Sm^{3+}. Thus it can be said that doping of lanthanide ion i.e. Sm^{3+} or Eu^{3+} ions into the BZO hosts did not cause any significant distortion or changes in the host crystal structure.

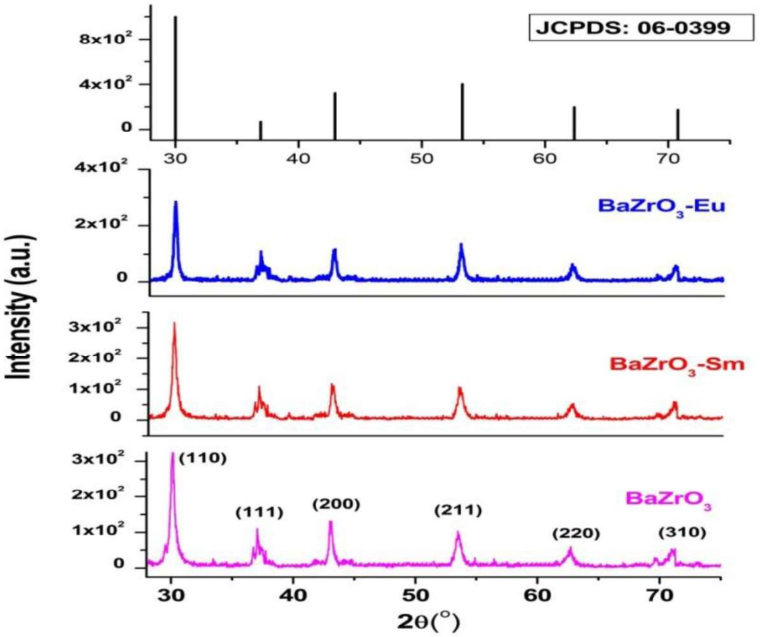

Figure 5.1: *XRD Pattern of undoped and Sm and Eu doped $BaZrO_3$ nanocrystal. This figure also consists of standard pattern corresponding to JCPDS No: 060399* ***[314].***

$BaZrO_3$ belongs to ideal cubic type perovskite structure, where Ba sits at cube corner position (000), Zr atom sits at body centre position (1/2, 1/2, 1/2) and oxygen atoms sit at face centred positions (1/2, 1/2, 0). It belongs to Pm3m space group (SG) O_h point symmetry. The coordination number of zirconium atom which is referred as lattice former is 6, oriented in the form of ZrO_6 octahedra, whereas that of barium which is called as lattice modifier is 12 in the form of BaO_{12} cuboctahedral. Its unit cell can be visualized as corner linked ZrO_6 octahedra embedded inside a cube formed by Ba atoms.

5.2.1.3 Morphology and particle size: Transmission electron microscopy

Figure 5.2a shows the TEM image of $BaZrO_3$ particles. The image shows agglomerated particles having smaller particles dispersed in BZO matrix. The nanoparticles are typically of the size of 20-30 nm; however, some large particles having size of 60–100 nm can also be seen. Figure 5.2b shows the high-resolution TEM image where lattice fringe could be observed. Figure 5.2c shows the selected area electron diffraction (SAED) pattern of BZO nanoparticles. The pattern shows that BZO nanoparticles are well crystalline in nature.

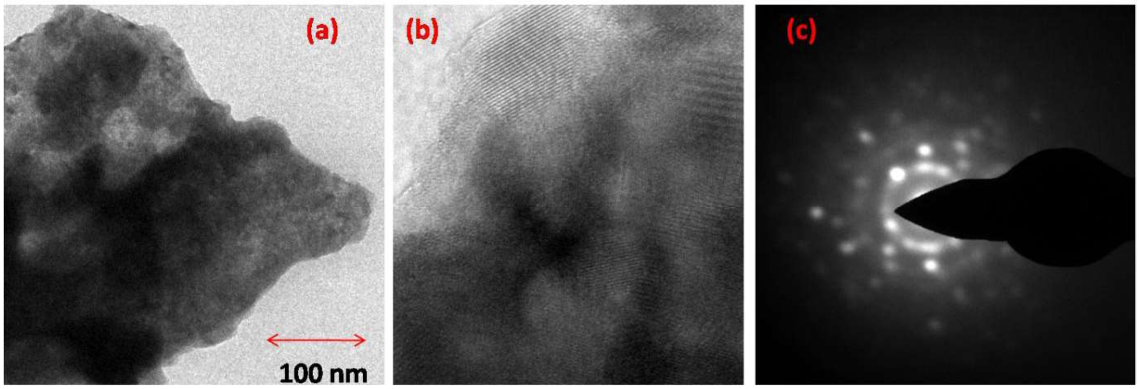

Figure 5.2: *(a) TEM (b) HRTEM image and (c) SAED pattern of BZO nanoparticles* ***[314].***

5.2.2. Defects induced photoluminescence in $BaZrO_3$

Figure 5.3a represents the photoluminescence spectrum of undoped $BaZrO_3$ at an excitation wavelength of 270 nm. In the emission spectrum there are two broad bands, centred at around 440 nm and 515 nm. This kind of multicolour emission indicates that the relaxation takes place via various pathways and there exists large number of states within the band gap of materials **[285]**. Again the excitation wavelength used for recording the emission spectrum 270 nm (~ 4.59 eV) is less than the experimental band gap of BZO (~ 5.3 eV) **[315]** which indicates presence of certain localized energy states within the band gap of the material otherwise direct transition from valence to conduction band will be forbidden in this case. This type of emission in nanostructure can be because of local defects which arise during heating treatment of the sample. It is reported that local defect can mainly get invoked in perovskite nanostructure due to different types of oxygen vacancy (OV) namely; neutral, singly ionized and doubly ionized **[316]**.

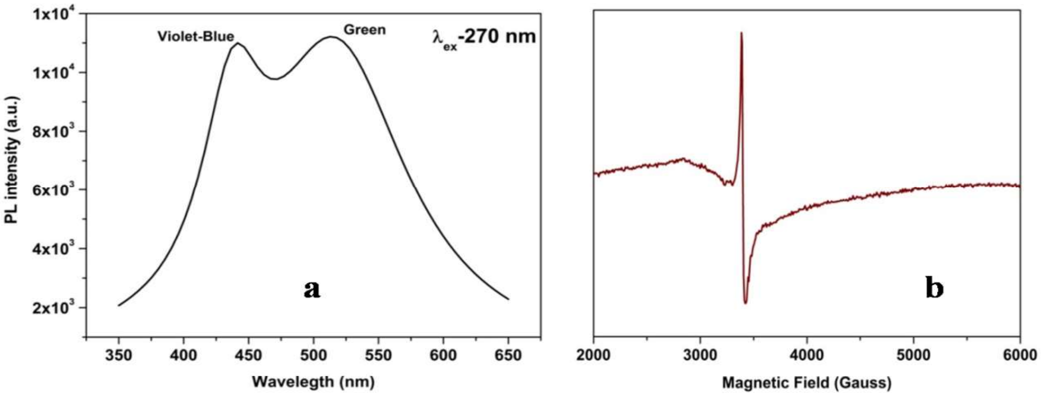

Figure 5.3: *(a) PL and (b)EPR spectra of* $BaZrO_3$ *at room temperature* ***[314]*.**

Now as mentioned in the earlier chapter, EPR is an efficient tool for characterizing paramagnetic defects. Since $BaZrO_3$ is a non-magnetic (no unpaired electron in Ba^{2+}, Zr^{4+} or O^{2-}), it will not have an EPR signal of its own. In present case $BaZrO_3$ is showing an intense room temperature EPR signal in Figure 5.3b at around 3400 Gauss with g ~ 1.9567. This signal is typical of singly ionized oxygen vacancy ($V_{\dot{O}}$) **[317]**. Thus it is the oxygen vacancy, which creates intermediate energy states within the band gap of BZO nanostructures where electron-hole recombination takes place leading to intense blue-green photoluminescence.

Further, since the violet-blue emission is more energetic than green emission, the intense violet-blue emission (Figure 5.3a) can be attributed to shallow defects while the green emission can be linked to deep defects. This is because the energy gap from the valence band to deep defect related electronic state is less than that with the shallow defect state. Thus, emissions involving shallow defects are generally in the higher energy region while that due to deep defects are in the low energy region. There are reports which show that presence of such deep and shallow defect generates energy dependent localized state which forms electron traps within the band gap of material during excitation with highly energy UV light **[318]**. In such case emission originates from recombination process wherein an excited electron of the conduction band (CB) loses its energy and re-occupied the energy levels of an hole in the valence band (VB) through the localized defect levels.

5.2.3. Photoluminescence spectroscopy of Sm^{3+} doped $BaZrO_3$: Excitation and emission spectroscopy, colour coordinates and lifetime study.

Sm^{3+} ion gives bright photoluminescence in the visible and near infrared (NIR) region and the characteristics emission bands are due to transitions between the energy levels in the $4f^5$ electron configuration. The excitation spectrum at λ_{em}= 643 nm is shown in Figure 5.4a wherein the broad band in the range of 200 – 270 nm with λ_{max} at 240 nm was attributed to the charge transfer band $O^{2-}\rightarrow Sm^{3+}$ (CTB). In the 320–550 nm wavelength region, several excitation peaks are observed such as 348 nm ($^6H_{5/2}$-$^6H_{13/2}$), 367 nm ($^6H_{5/2}$-$^4D_{3/2}$), 382 nm ($^6H_{5/2}$-$^6P_{7/2}$), 405 nm ($^6H_{5/2}$-$^4F_{7/2}$), 421 nm ($^6H_{5/2}$- $^6P_{5/2}$), 435 nm ($^6H_{5/2}$-$^4G_{9/2}$), 460 nm ($^6H_{5/2}$-$^4I_{9/2}$), 469 nm ($^6H_{5/2}$-$^4I_{11/2}$), 473 nm ($^6H_{5/2}$-$^4I_{13/2}$) and 488 nm ($^6H_{5/2}$-$^4I_{15/2}$) which are attributed to f–f transitions of Sm^{3+}. Figure 5.4b showed the emission spectrum of Sm^{3+} ions doped $BaZrO_3$ at an excitation wavelength of 240 nm (CTB). It was found that the emission characteristics remains similar on excitation with both 240 nm (charge transfer) and 405 nm (f-f band), except for significant difference in their intensity. The intensities at λ_{ex} = 405 nm were found to be quiet low compared to that obtained with λ_{ex} = 240 nm which might be because of the fact that the Sm^{3+} absorption bands corresponding to the f-f transitions are electronically forbidden and exhibit poor absorption in UV region. The high intensities of emission bands with CTB excitation are due to the intramolecular energy transfer (IMET) process, which mainly occurs in the UV region. Since there is no host emission in the Sm^{3+} doped sample, we can assume that there is a complete energy transfer from host to dopant.

The emission spectrum consists of sharp emission lines starting from 550 to 725 nm, which are characteristic lines of the Sm^{3+} ions. The peaks at 561, 597, 643 and 701 nm are attributed to the $^4G_{5/2}$-$^6H_{5/2}$, $^4G_{5/2}$-$^6H_{7/2}$, $^4G_{5/2}$-$^6H_{9/2}$ and $^4G_{5/2}$-$^6H_{11/2}$ transitions of the Sm^{3+} ions. Among them, the red emission at 643 nm ($^4G_{5/2}$-$^6H_{9/2}$) is having the maximum intensity. As stated earlier in the introduction part that for Sm^{3+} ion the transition $^4G_{5/2}$-$^6H_{7/2}$ at 597 nm ($\Delta J = \pm 1$) is a partly magnetic dipole (MD) and partly electric dipole (ED) in nature emission band. On the other hand, the transition at 561 nm ($^4G_{5/2}$-$^6H_{5/2}$) is purely MD in nature and the 643 nm ($^4G_{5/2}$-$^6H_{9/2}$) transition is purely ED natured, which is sensitive to crystal field. In general, the intensity ratio of ED and MD transition, which is known as asymmetry ratio, has been used to measure the symmetry of the local environment of the trivalent 4f ions. Higher intensity of the ED transition is linked with the more asymmetry surrounding the Sm^{3+} ion. In the present study, the 643 nm ($^4G_{5/2}$-$^6H_{9/2}$) transition of Sm^{3+} ions is much more intense than $^4G_{5/2}$-$^6H_{5/2}$ (MD) transition, which indicates that Sm^{3+} occupied highly asymmetric site in $BaZrO_3$. CIE chromaticity coordinates were also evaluated for

BZO: Sm phosphor adopting standard procedures in order to evaluate the material performance for phosphor application. The position of the coordinates is represented as the point ‘*’ in Figure 5.4c, which shows that BZO:Sm emits in orange-red region.

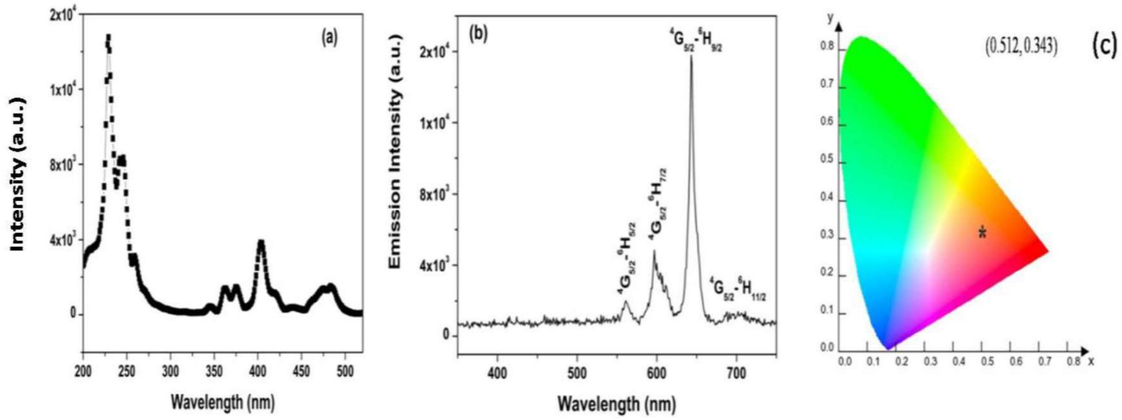

Figure 5.4: *(a) Excitation ,(b) Emission spectra of* $BaZrO_3:Sm^{3+}$ *under 643 nm* (λ_{em}) *and 240 nm* (λ_{ex}) *(c) CIE diagram showing the co-ordinates and representing the colour emitted by* $BaZrO_3:Sm^{3+}$ ***[314]****.*

The coordination numbers of Ba and Zr ions in BZO are 12 and 6 respectively in cubic perovskite structure. Now since the ionic size difference between 12-coordinated Sm^{3+} (124 pm) and 12-coordinated Ba^{2+} (161 pm) ion is more, if Sm^{3+} ions occupy the Ba^{2+} sites, it will lead to a large distortion inside the lattice. Further, if the associated defect due to charge difference is also at a nearby distance then the local site symmetry will be having non-inversion symmetry. On the other hand size difference between 6-coordinated Sm^{3+} (ionic size 96 pm) and 6-coordinated Zr^{4+} (ionic size 72 pm) is small and hence Sm^{3+} ions occupying the Zr^{4+} sites will not lead to a large distortion in the lattice. If the associated defect due to charge difference is at a large distance then the local site symmetry will be having inversion symmetry. Thus from the observed spectra where $^4G_{5/2}$-$^6H_{9/2}$ (ED) transition of Sm^{3+} ions is much more intense than $^4G_{5/2}$-$^6H_{5/2}$ (MD) transition, it can be inferred that majority of Sm^{3+} ions are occupying Ba^{2+} site without inversion symmetry and also oxygen vacancies are introduced in vicinity to ensure local charge compensation. The presence of relatively less intense allowed MD transition at 561 nm suggests that some of the Sm^{3+} ions also occupy Zr^{4+} site with symmetric environment.

Lifetime spectroscopy of Sm^{3+} doped $BaZrO_3$:

To get an idea about the nature of the dopant ion occupancy in these lattice sites, PL decay time (lifetime) studies were conducted. The decay curves corresponding to the $^4G_{5/2}$ level of Sm^{3+} ions in the 1.0 mol % Sm^{3+} doped $BaZrO_3$ are shown in Figure 5.5a at excitation wavelength of 240 nm, monitoring emission at 643 nm. The decays were correctly fitted by using a bi-exponential equation 4.2 as given in previous chapter. Broadly, the analysis showed the presence of two components; short-lived components (τ_1) and long-lived (τ_2). The lifetime values are 20 μs (τ_1) and 67 μs (τ_2) indicative of the presence of two different environments for Sm^{3+} in $BaZrO_3$ as is also evident from emission spectroscopy. Assuming a given phonon energy (same host for the lanthanide ions), a relatively longer PL decay time should be attributed to a more symmetric site, as the f-f transition becomes more forbidden, whereas a shorter decay time is often associated with an asymmetric site due to relaxation in the selection rules. Species τ_1 (20 μs) arises because of Sm^{3+} ions occupying 12-coordinated Ba^{2+} site without inversion symmetry whereas τ_2 (67 μs) can be ascribed to Sm^{3+} ions occupying 6-coordinated Zr^{4+} with inversion symmetry. These results are in agreement with our emission studies, where it was observed that majority of Sm^{3+} ions occupy Ba^{2+} sites without inversion symmetry.

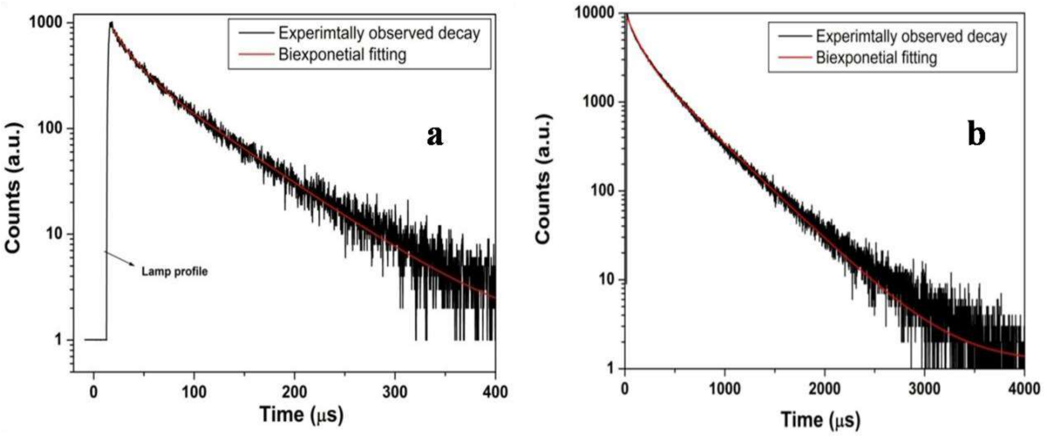

Figure 5.5: *PL decay profile for (a) Sm^{3+}:$BaZrO_3$ under excitation of 240 nm and emission of 643 nm and (b) for Eu^{3+}:$BaZrO_3$ under excitation of 255 nm and emission of 616 nm* ***[314]****.*

5.2.4. Photoluminesence spectroscopy of Eu^{3+} doped $BaZrO_3$: Excitation and emission spectroscopy, colour coordinates, Stark splitting pattern, lifetime study and calculation of Ω_λ (Judd-Ofelt) parameters

Figure 5.6a represents the PL excitation spectra of 1.0 mol % doped Eu^{3+} doped $BaZrO_3$ by monitoring emission at 616 nm corresponding to $^5D_0\rightarrow{}^7F_2$transition of Eu^{3+} ion. The spectrum consists of a broad band centered at 255 nm, which is assigned to charge transition band (CTB) arising due to transfer of electron from filled 2p shell of oxygen to partially filled 4f shell of Eu^{3+} ion. The other weaker peaks at 321, 365, 386 and 396 nm are due to to $^7F_{0,1}\rightarrow{}^5H_{3,6}$, $^7F_{0,1}\rightarrow{}^5D_4$, $^7F_{0,1}\rightarrow{}^5G_3$ and $^7F_0\rightarrow{}^5L_6$ transitions of Eu^{3+}, respectively. Since the f→f transitions are forbidden in nature, these peaks have relatively weak intensity compared to Eu–O charge transfer band absorption.

Figure 5.6b represents the emission spectrum of 1.0 mol % Eu^{3+} doped $BaZrO_3$ on excitation with 255 nm corresponding to CTB. The spectrum consists of many sharp peaks due to the direct excitation of the Eu^{3+} ions from the ground state to higher levels of the 4f-manifold. As stated earlier in this chapter, the two major peaks viz. 594 ($^5D_0\rightarrow{}^7F_1$) and 616 nm ($^5D_0\rightarrow{}^7F_2$) corresponds to magnetic dipole transition (MDT) and electric dipole transition (EDT), respectively. Apart from these prominent peaks, some weak emission peaks are also observed at 655 and 698 nm correspond to $^5D_0\rightarrow{}^7F_3$ and $D_0\rightarrow{}^7F_4$ transitions, respectively. In addition to these allowed transitions, small peak at $^5D_0\rightarrow{}^7F_0$ could also be observed which is normally forbidden both by electric dipole as well as magnetic dipole transition. Absence of broad host emission due to oxygen vacancy in emission spectra of Eu^{3+}:$BaZrO_3$ indicates complete energy transfer at 1.0 mol % of Eu^{3+} ion concentration. The fine splitting of emission peaks can be seen in the spectral features of $^5D_0$–$^7F_{1,\,2,\,3,\,4}$ which implies that the final $Ba_{1-x}Eu_xZrO_3$ perovskite samples prepared using gel-combustion method have been well crystallized **[319]**.

As seen in the emission spectrum, among all the transitions mentioned above, the hypersensitive electric dipole transition $^5D_0\rightarrow{}^7F_2$ at 616 nm transitions is the strongest and is characterized by intense red emission, whereas magnetic dipole transitions $^5D_0\rightarrow{}^7F_1$ at 594 nm is relatively very weak. As stated earlier that in a crystal site with centre of inversion (C_i), the EDT are strictly forbidden while the MDT is allowed and it is the most intense emission peak. . On contrary in a site without inversion symmetry, it is EDT which is usually the strongest emission line, because transition $\Delta J= \pm 2$ is hypersensitive to small deviation from inversion symmetry. The more sensitive parameter for understanding symmetry is asymmetry ratio (I), which is described as ratio of integral intensities of EDT ($^5D_0 \rightarrow ^7F_2$) to MDT ($^5D_0 \rightarrow ^7F_1$). The fact that in $Ba_{1-x}Eu_xZrO_3$, EDT is much more intense than MDT; asymmetry ratio is found to be much greater than unity ($I >> 1$) indicating majority of Eu^{3+} ions are at site without inversion symmetry in $BaZrO_3$ perovskite.

Normally 12 coordinated Eu^{3+} ions do not exist **[241],** which means most of Eu^{3+} ions occupy 6-cordinated Zr^{4+} site, because stabilization of Eu^{3+} in BaO_{12} is difficult. However the ionic size difference between 6-coordinated Zr^{4+} (72 pm) and 6-coordinated Eu^{3+} (95 pm) is more. Hence, Eu^{3+} ions occupying the Zr^{4+} sites will lead to a large distortion in the lattice and if the associated defect due to charge difference is at a nearby distance, the local site symmetry will be having non-inversion symmetry. This is the reason for enhanced EDT compared to MDT in the emission spectrum (Figure 5.6b). The appearance of $^5D_0 \rightarrow ^7F_0$ transition at 578 nm in Figure 5.6b also confirm that that the surrounding environment of Eu^{3+} is asymmetric in nature since this transition normally appears when the point symmetry around Eu^{3+} is very low. This is in agreement with reported data **[320]** that emission spectrum of europium doped BZO consists of intense EDT and presence of $^5D_0 \rightarrow ^7F_0$ transition. They have also observed two lifetimes value for Eu doped BZO which they have attributed to presence of (i) Eu at Zr^{4+} site with no oxygen vacancy and (ii) Eu at Zr^{4+} with presence of charge compensating oxygen vacancy. This fully supports our experimental finding.

The CIE chromaticity coordinates for Eu^{3+}:$BaZrO_3$phosphor were calculated, which is represented as the point '*' in the CIE diagram shown in Figure 5.6c. The CIE chromaticity coordinates show that Eu^{3+}:$BaZrO_3$phosphor is a strong red emitter.

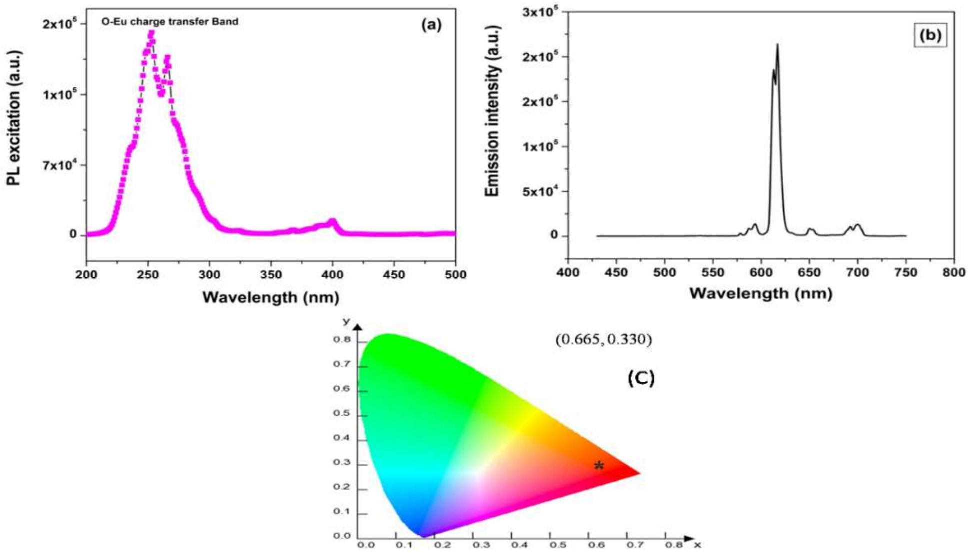

Figure 5.6: *(a) Excitation, (b) Emission spectra of Eu^{3+}:BaZrO$_3$ under 616 nm (λ_{em}) and 255 nm (λ_{ex}) and (c) CIE diagram showing the co-ordinates and representing the colour emitted by Eu^{3+}:BaZrO$_3$* ***[314].***

When the Eu^{3+} ion is inserted into any chemical/ligand environment (crystal field) under the influence of inorganic host, the (2J + 1)-degenerate J-energy levels split into the so-called Stark sub-levels by ligand field effect and the number of such levels depends on the local site symmetry around Eu^{3+} ion. The substitutions of either Zr^{4+} with Eu^{3+} may results in significant lattice distortion due to ionic size as well as charge mismatching.

Radiative transitions from $^5D_0$ to levels with $J = 0$ or odd J ($J = 3, 5$) are both ED and MD forbidden, and only weak transitions from $^5D_0$ to these levels are observed due to CF induced *J*-mixing effect. Moreover, the $^5D_0 \rightarrow {}^7F_0$ transition is only allowed in the following 10 site symmetries: C_s, C_1, C_2, C_3, C_4, C_6, C_{2V}, C_{3V}, C_{4V}, and C_{6V}, according to the ED selection rule **[321].**

From stark splitting pattern shown in Figure 5.7, One lines for $J = 0 \rightarrow J = 0$ transition, two lines for $J = 0 \rightarrow J = 1$ transition, two lines for $J = 0 \rightarrow J = 2$ transition, two lines for $J = 0 \rightarrow J = 3$ transition and two lines for $J = 0 \rightarrow J = 4$ transition of Eu^{3+} were resolved for Eu^{3+} :BaZrO$_3$. According to the branching rules of various point groups **[322, 323],** it infers that the actual site symmetry of Eu^{3+} in BaZrO$_3$ is C$_6$.

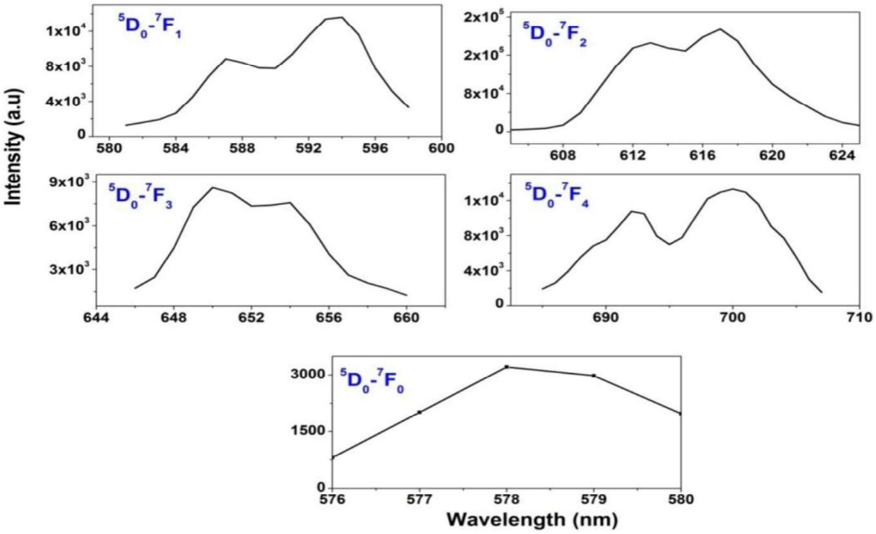

Figure 5.7: *Stark splitting pattern of* Eu^{3+}*emission peak in* $BaZrO_3$ ***[314]***

Lifetime spectroscopy of Eu^{3+} doped $BaZrO_3$:

The decay curve corresponding to the $^4G_{5/2}$ level of Eu^{3+} ions in the 1.0 mol % Eu^{3+} doped $BaZrO_3$ is shown in Figure 5.5b at excitation wavelength of 255 nm, monitoring emission at 616 nm. The decays were correctly fitted by using a bi-exponential temporal dependence similar to Sm^{3+} doped $BaZrO_3$. The two lifetimes are 114 µs and 406 µs respectively, which indicate the presence of Eu^{3+} ions in two different environments. Both these species are present in 6-coordinated Zr^{4+} sites since twelve-coordinated Eu^{3+} at Ba^{2+} site is not possible. The species which is having relatively lower life time value might be nearer to the charge compensating defects and thereby induce more asymmetry surrounding the Eu^{3+}ion, while the other one which is having higher lifetime is far off from charge compensating defects. The charge compensating defects can be schematically represented using Kroger-Vink notation as

$$BaZrO_3 \longrightarrow V_O^{\cdot} + {Eu^{3+}}'_{Zr} \qquad (5.1)$$

where $V_O^{\cdot}$ represents oxygen vacancy having two positive charges and ${Eu^{3+}}'_{Zr}$ represent Eu^{3+} occupying Zr^{4+} site with extra negative charge.

Calculation of Ω_λ (Judd-Ofelt) parameters, radiative properties and quantum efficiency of the $^5D_0$ level:

Judd-Ofelt (JO) intensity parameters, Ω_J (J = 2, 4) calculated using Judd-Ofelt theory **[324,325]** provide information about local environment and bonding in the proximity of lanthanide ion. Ω_2 generally known as short range parameter gives the measure of degree of covalence and polarizability of the chemical environment experienced by the Ln^{3+} ion while Ω_4 called as long range parameter is related to the bulk measurable such as viscosity and rigidity of the inorganic matrices **[275]**. The application of JO theory to the quantitative analysis of Eu^{3+} emissive properties in matrix is nicely presented by Werts *et al.,* **[326]**, and also by our group **[275,327]** and can be summarized as follows. There is a close relationship between radiative emission rates and integral PL intensity for transition between two manifolds $^5D_0$ and ^7F_J (J = 2, 4) can be written as:

$$A_{0-J} = A_{0-1}\frac{I_{0-J}}{I_{0-1}}\frac{h\nu_{0-1}}{h\nu_{0-J}} \tag{5.2}$$

where I_{0-J} and I_{0-1} are integral intensities for $^5D_0 \rightarrow {}^7F_J$ and $^5D_0 \rightarrow {}^7F_1$ (pure magnetic dipole) transitions and $h\nu_{0-J}$ and $h\nu_{0-1}$ are their energies (in cm^{-1}), respectively. Since $^5D_0 \rightarrow {}^7F_1$ transition which is known as magnetic dipole transitions is not affected much by environmental effect its transition rate is constant with the approximate value of 50 sec^{-1} **[328]**. The $^5D_0 \rightarrow {}^7F_J$ (J = 2, 4, and 6) transitions are an electric dipole transition and can be expressed as follow:

$$A_{0-J} = \frac{64\pi^4 e^2 k^3}{3h\,(2J+1)}\frac{n\,(n^2+2)^2}{9}\sum_{\lambda=2,4,6}\Omega_\lambda \langle \Psi J \| U^\lambda \| \Psi' J' \rangle^2 \tag{5.3}$$

where n is the refractive index of the medium, e is the electric charge, k is the transition energy of electric dipole transitions in cm^{-1}, Ω_λ is the J-O intensity parameter, and $\langle \Psi J \| U^\lambda \| \Psi' J' \rangle^2$ values are the squared reduced matrix elements, whose values are 0.0032 and 0.0023 for J' =2 and 4, respectively. For $BaZrO_3$ we have adopted value for the index of refraction of 2.07. Emission quantum efficiency of the emitting $^5D_0$ level is written as

$$\eta = \frac{A_R}{A_R + A_{NR}} = \tau \sum_{J=1-4} A_J \tag{5.4}$$

where the A_R rate was obtained by summing over the radiative rates for each $^5D_0 \rightarrow {}^7F_J$ (J = 1-4). The JO parameter and other photophysical values are mentioned in Table 5.1.

It is well known that the parameter Ω_2, is an indication of the dominant covalent nature and/or structural changes in the vicinity of the Eu^{3+} ion (short range effects), while Ω_4 intensity parameters are long range parameters that can be related to the bulk properties such as viscosity and rigidity of the inorganic matrices. The Ω_2 parameter is related to the degree of covalence and polarizability of the chemical environment experienced by the Eu^{3+} ion; higher Ω_2 values point to more covalent and polarizable environments. In case of BZO:Eu; Ω_2 value was found to be greater than Ω_4 indicating high covalency and low symmetry around Eu^{3+} ion which is also supported by our point symmetry calculations, which comes out to be C_6. This is well in agreement with high asymmetry value of Eu^{3+} in $BaZrO_3$ (6.23). The calculated τ_R for the excited $^5D_0$ level of Eu^{3+} ion is found to be 0.523 ms, which is larger than the τ_{exp} (0.365 ms). This difference in τ_{exp} and τ_{cal} can be attributed to nonradiative decays. The trend in branching ratio- suggests most of radiative energy goes in the $^5D_0 \rightarrow {}^7F_2$ transition. The Judd-Ofelt parameter and other properties calculated for Eu^{3+} in $BaZrO_3$ is mentioned in Table 5.1.

Table 5.1: J-O intensity parameters and radiative properties for Eu^{3+} in $BaZrO_3$ **[314]**

Transition	A_{Red} (s^{-1})	A_{Rmd} (s^{-1})	Ω_J (10^{-20} cm^2)	β_J (%)	η (%)	A_R (s^{-1})	A_{NR} (s^{-1})
$^5D_0 \rightarrow {}^7F_1$	0	147	-	17.3	69.1	1052	762
$^5D_0 \rightarrow {}^7F_2$	723	0	5.52	62.9			
$^5D_0 \rightarrow {}^7F_4$	216	0	2.68	18.3			

5.3 Synthesis and Local structure determination of $Bi_{2-2x}La_{2x}UO_6$ and $Bi_{1.96}Eu_{0.04}UO_6$ [181]

5.3.1. Synthesis

The solid solutions $Bi_{2-2x}La_{2x}UO_6$ (x= 0-0.08) were prepared by heating stoichiometric amount of Bi_2O_3 (AR grade), U_3O_8 (nuclear grade) and $La(OH)_3$ (AR grade). The reactants in powder forms were mixed in a pestle mortar. The powder mixture of reactants were transferred in different platinum boats and heated at 750°C for about 48 hours in steps of twelve hours. After each heating cycle, the products obtained were ground and XRD pattern was recorded to check the progress of the reaction and formation of the compound. Similarly Eu_2O_3 (AR grade), Bi_2O_3 and U_3O_8 were mixed in stoichiometric ratios and heated up to 750°C to prepare $Bi_{1.96}Eu_{0.04}UO_6$.

5.3.2. XRD measurements and Rietveld refinement

All the structural refinements were performed using Rietveld refinement program FULLPROF **[329]**. In all refinement procedure, the background was defined by a sixth ordered polynomial in 2θ. A pseudo Voigt function (linear combinations of Gaussian and Lorenzian function) was chosen to define the profile shape of X-ray diffraction peaks. Except for the occupancies of the atoms, all other parameters *i.e.*, scale factor, zero correction, background and half-width parameters along with mixing parameters, lattice parameters, positional coordinates and thermal parameters were refined.

The X-ray diffraction pattern of the Bi_2UO_6 prepared in this study indicates that it is a single phase compound. All the reflections could be indexed by the cell parameters of low temperature monoclinic phase of Bi_2UO_6, having C_2 space group as reported in literature **[330]**. The XRD pattern of Bi_2UO_6 along with its Rietveld profile fitting is shown in Figure 5.8a. Vesta software has been used to obtain the crystal structure of Bi_2UO_6 from the CIF file generated after rietveld refinement.

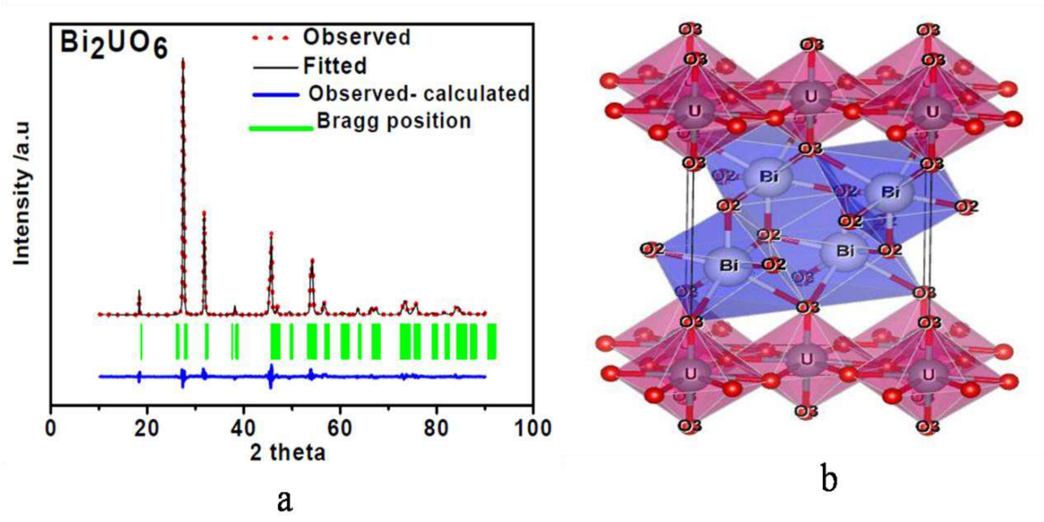

Figure 5.8: *(a) Rietveld fitting of XRD pattern of Bi_2UO_6 (dotted line, observed pattern; continuous line, best fitted theoretical curve after Rietveld refinement) and (b) Crystal structure of Bi_2UO_6* ***[181]***

The structure of Bi_2UO_6 obtained on the basis of this refinement is shown in Figure 5.8b. The XRD patterns of the products obtained during attempt to prepare $Bi_{2-2x}La_{2x}UO_6$ (x=0.02, 0.05, 0.06 and 0.08) were found to be similar to that of Bi_2UO_6 for x values up to 0.05. Figure 5.9a shows the XRD patterns of these products and Figure 5.9b shows enlarged part of the XRD patterns in the 2θ range of 14°-24°. It can be seen from the XRD patterns, that the position of the peaks remain almost unchanged compared to the undoped compound and no additional peak was observed up to x=0.05. However for x > 0.05, two extra peaks appeared in the 2θ range of 21-23º. On careful examination of the XRD patterns, it was found that these two additional peaks arising at 21.4º and 22.8º correspond to 100% XRD line of U_3O_8 and Bi_2O_3 respectively. Rietveld profile fittings were carried out to determine the cell parameters of the solid solutions. The reliability factors (chi-square, R-factor) obtained after the Rietveld refinement are shown in Table 5.2. It was found that good fitting is obtained when we assume that La^{+3} ions are replacing Bi^{+3} ions in Bi_2UO_6 lattice to form the solid solutions. The cell parameters determined from the Rietveld fitting is listed in the Table 5.2. It can be seen from the table that the cell parameters do not change appreciably in $Bi_{2-2x}La_{2x}UO_6$ solid solutions since the size of La^{+3} (1.032 Å) and Bi^{+3} (1.030Å) are similar. This observation suggests that during formation of the solid solutions, La^{+3} ions occupy the Bi^{+3} positions in the lattice. From the XRD data, the bond distances of Bi-O and U-O at different doping concentration level were determined and are given in Table 5.3. The table shows that, Bi is coordinated to two types of oxygen atoms; Bi-O2: in plane oxygen and Bi-O3: out of plane oxygen as shown in Figure 5.8b. Average Bi-O3 bond distance is found to be greater than Bi-O2 type bond distance. On the other hand, U has two type of bonding; U-O1 type and U-O3 type. U-O1 type bonds are greater than U-O3 type bonds. All the U-O1 type bonds are situated in a plane where they remain slight up and down compared to each other. U-O3 type bond is basically U=O bonds (uranyl i.e. UO_2^{+2} type), which is perpendicular to the plane of U-O1 type bonds. From the XRD data, no significant change in the bond distance was observed with La doping, as XRD gives average crystallographic data and cannot probe any local distortion in the crystal structure.

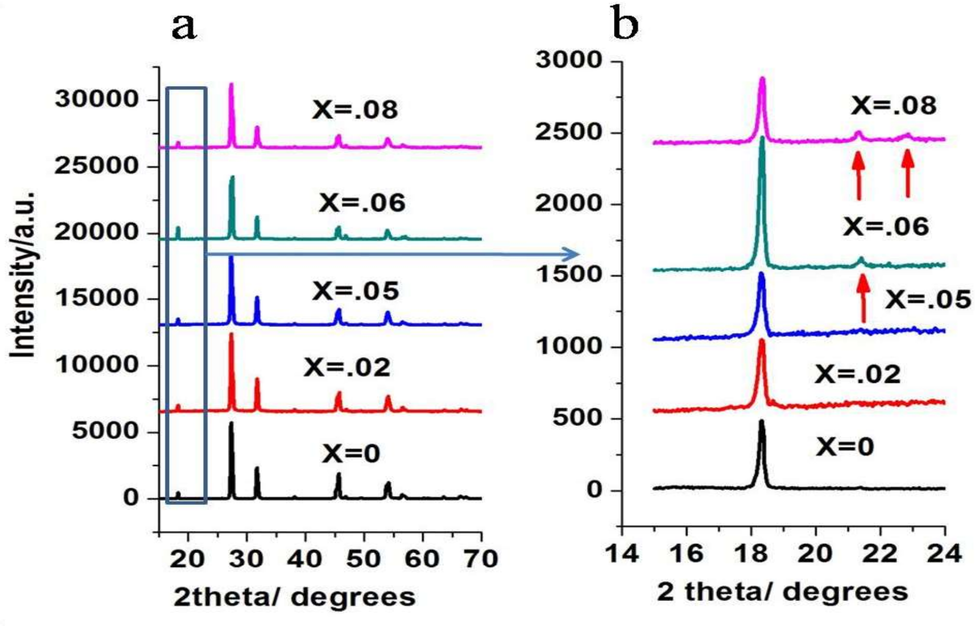

Figure 5.9: *(a)XRD patterns of* $Bi_{2-2x}La_{2x}UO_6$ *with X= 0.00, 0.02, 0.05, 0.06, 0.08 respectively and (b) XRD patterns of the enlarged portion of Fig.5.9a (in the 2 theta range of 14-24°) as shown above* ***[181]***

Table.5.2: Cell parameters and reliability factors (chi-square, R-factor) obtained after the Rietveld refinement **[181]**.

Sample	Cell parameters				Reliability factors		
	a (Å)	b (Å)	c (Å)	β (θ)	Rp	Bragg-R factor	Chi square
Bi_2UO_6	6.8796(4)	4.0047(2)	9.6903(5)	90.123(5)	12.3	5.099	2.12
$Bi_{1.96}La_{.04}UO_6$	6.8830(6)	3.9951(4)	9.6680(7)	90.075(9)	15.6	5.536	2.14
$Bi_{1.90}La_{.10}UO_6$	6.8865(7)	4.0004(4)	9.6752(9)	90.09(1)	17.7	7.725	2.42
$Bi_{1.88}La_{.12}UO_6$	6.9120(3)	3.984(2)	9.6812(6)	90.03(6)	18.5	11.33	3.57
$Bi_{1.84}La_{.16}UO_6$	6.8876(7)	4.0042(4)	9.6785(7)	90.23(1)	22.8	9.729	3.49

Table. 5.3 : Bond distances at different doping concentration

Sample	Bi-O bond	distances(Å)	U-O bond	distances(Å)
Bi_2UO_6	Bi-O2	2.194	2x U-O1	2.340
	Bi-O2	2.290	2x U-O1	2.603
	Bi-O2	2.308	2x U-O1	2.013
	Bi-O2	2.520	2x U-O3	1.909
	Bi-O3	2.800		
	Bi-O3	2.683		
	Bi-O3	2.867		
$Bi_{1.96}La_{.04}UO_6$	Bi-O2	2.189	2x U-O1	2.341
	Bi-O2	2.290	2x U-O1	2.598
	Bi-O2	2.304	2x U-O1	2.010
	Bi-O2	2.516	2x U-O3	1.905
	Bi-O3	2.798		
	Bi-O3	2.678		
	Bi-O3	2.863		
$Bi_{1.90}La_{.10}UO_6$	Bi-O2	2.191	2x U-O1	2.342
	Bi-O2	2.292	2x U-O1	2.601
	Bi-O2	2.307	2x U-O1	2.012
	Bi-O2	2.519	2x U-O3	1.906
	Bi-O3	2.800		
	Bi-O3	2.681		
	Bi-O3	2.865		
$Bi_{1.88}La_{.12}UO_6$	Bi-O2	2.192	2x U-O1	2.347
	Bi-O2	2.296	2x U-O1	2.601
	Bi-O2	2.307	2x U-O1	2.012
	Bi-O2	2.519	2x U-O3	1.908
	Bi-O3	2.803		
	Bi-O3	2.682		
	Bi-O3	2.866		
$Bi_{1.84}La_{.16}UO_6$	Bi-O2	2.191	2x U-O1	2.343
	Bi-O2	2.293	2x U-O1	2.604
	Bi-O2	2.308	2x U-O1	2.013
	Bi-O2	2.520	2x U-O3	1.907
	Bi-O3	2.802		
	Bi-O3	2.682		
	Bi-O3	2.867		

We have also carried out EXAFS analysis which is reported in our published literature **[181]**, where it was found that the coordination number of La is close to 7 (6.3 to 6.7); this also suggests that La is going at the position of Bi in Bi_2UO_6 lattice. The La-O bond distances calculated are smaller than the Bi-O bond distances. For 2 at% La doped solid solutions, there are two types of La-O distances and from 5 at% onwards, there is only one type of La-O bond distance, which is around 2.2Å. As we know, Bi has one stereochemically active lone pair in Bi_2UO_6; this lone pair is very much responsible for the different Bi-O bond distances around Bi atom**.** When La replaces Bi atom in Bi_2UO_6; all the La-O bond distances will become almost same, as La do not have any lone pair. This observation establishes the fact that La is going at Bi sites up to 5 at% La doping. This hypothesis receives further confirmation from PL and EPR studies as discussed below.

5.3.3. EPR study

Figure 5.10 shows the EPR spectrum of $Bi_{2-2x}La_{2x}UO_6$ (x=0.02 to 0.08) samples recorded at room temperature. All the compounds showed an asymmetric signal at g ≈ 2.12. Since U^{6+}, Bi^{3+} and La^{3+} cations do not contribute to EPR signals due to absence of any unpaired electron, these strong intense resonance signals must have been due to some type of intrinsic defects, such as oxygen vacancies. The oxygen vacancies can exist in three possible states as represented by Kröger–Vink notation; (i) The doubly positively charged vacancies without trapping of any electron, which are assigned as V_O^{2+} or $V_O^{\circ\circ}$ and are diamagnetic, since no unpaired electron is left there. Therefore, V_O^{2+} centres are not observed by EPR technique. (ii) The single positively charged vacancies with trapping of one electron, which are assigned as V_O^{+} or V_O°. They are paramagnetic and hence EPR sensitive. This defect centre is same like F^+ centre in alkali halides and is formed when the F^{2+} centres trap an electron from the conduction band. (iii) Finally the singly charged centres ($V_O^{\cdot}$) may become a neutral centre by capture of another electron forming the neutral F or V_O^{x} centre. However it must be noted that the introduction of the F^{2+} or F^+ centre must be accompanied by simultaneous introduction of some negatively charged centres such as negatively charged cationic vacancies $V^{///}_{Bi}$ or $V^{///}_{La}$. The F^{2+} centre can trap one or two electron from it's nearest negatively charged cationic vacancies ($V^{///}_{Bi}$ or $V^{///}_{La}$) leading to the formation of F^+ and F centre. If the spins of two trapped electrons in F or V_O^{x} centre somehow compensate each other, the F or V_O^{x} centre will result as a diamagnetic one. However, if the spins do not compensate, we may expect the existence of a triplet state, which is EPR active and will show two fine transitions. In present case,only one fine transition is seen in all of the doped compounds, which suggest, that the resonance signal must be due to paramagnetic oxygen vacancies V_O°. From Figure 5.10, it is also clear that, there is an increasing trend of EPR signal intensity up to 5 at % La, beyond which decay in intensity was observed. This can be explained only in terms of doping of La, as confirmed by XRD and EXAFS data, up to 5 at % La doping. When La is going to the Bi site forming a single phase; an increasing concentration of the $V_O^{\cdot}$ is usually expected. But after 5 at % of La doping, since some impurity phases (e.g. U_3O_8 and Bi_2O_3) are formed as shown in XRD pattern, there will be decay in EPR signal intensity. This also indirectly supports the La site occupancy mentioned above .

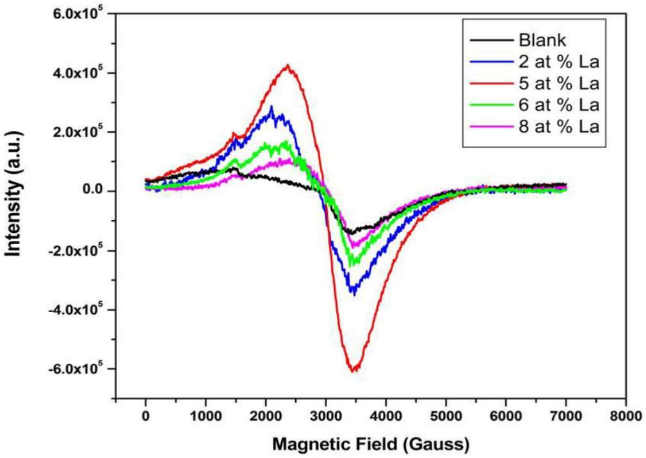

Figure 5.10: *EPR spectra of* $Bi_{2-2x}La_{2x}UO_6$ *(x=0.02 to 0.08) recorded at room temperature.*

There are several possible ways to understand the creation of oxygen vacancies due to substitution of Bi^{+3} by La^{+3}, having similar charge and size. As discussed earlier, Bi^{+3} has one stereo chemically active lone pair and because of which it has irregular co ordination around it **[331]**. One group of coordination has shorter Bi-O bond distances and another group of coordination has longer bond distances. This type of irregular coordination is also observed in Bi_2UO_6 compound, where one group of coordination has shorter Bi-O distances (2.1 Å -2.3 Å) and another group of coordination has longer Bi-O distances (2.5 Å -2.9Å). But when Bi^{+3} is replaced by La^{+3} ion, this type of irregular co ordination around La atom will not be present as La^{+3} does not possess any stereo chemically active lone pair, as seen from the EXAFS data at La L_3 edge. From EXAFS study **[181]**, we have seen that the La-O bond distances in the La-O3=U link in $Bi_{2-2x}La_{2x}UO_6$ matrix are in the range of 2.1-2.25Å which is very much shorter than the Bi-O3 bond distances (2.5 Å -2.9Å) of the Bi-O3=U link in pure Bi_2UO_6 (Figure 5.8b). Therefore, on La doping, the $Bi_{2-2x}La_{2x}UO_6$ lattice will always show a tendency to rearrange the oxygen atoms (O3) linked between La/Bi and U atoms. Again, since it is difficult to move an oxygen atom of the O3=U link towards the La atom (in order to reduce the La-O bond), the lattice will be always a distorted or it will be structurally disordered. This type of distortion or disorder may create oxygen vacancies. Observation of such oxygen vacancies due to lattice distortion/disorder are reported in several matrices. **[261, 332].** This distortion might be the reson of getting impurity phases when the doping level of La is more than 5 at % .

As stated earlier that these doubly positive charged oxygen vacancies (V_O^{2+} centres) can trap one electron from the negatively charged cationic vacancies and thereby forming the EPR active V_O° centres (or V_O^{1+} centres), the system will contain both V_O^{2+} and V_O^{1+} centres. These positively charged oxygen vacancies will be balanced by negatively charged Bi vacancies such as V_{Bi}''' and V_{Bi}'' (hole trap at Bi vacancies) and forming Bi_2O_3. Therefore, the new charge balance equation can be written as

$$2Bi_{Bi}^{*}+3O_O^{*}= V_{Bi}''' + V_{Bi}'' + 2\ V_O^{\circ\circ} + V_O^{\circ} + Bi_2O_3 \qquad (5.7)$$

Now the increase in EPR signal intensity can be explained in terms of doping of La. As explained in our XRD and EXAFS data, up to 5 at% doping level, La is going to the Bi site forming a single phase. Therefore, an increase in distortion in the system is also expected with increasing doping level of La, which is reflected in the increasing intensity trend of the EPR signal due to the paramagnetic V_O^{1+}. On the other hand, there are two possible reasons for observing decay in the EPR signal at La concentration levels more than 5 at %. Since out of the two different oxygen vacancies (V_O^{2+} and V_O^{1+}) only V_O^{1+} is EPR active and give rise the EPR signal, at higher La concentration i.e. at x= 0.06 & 0.08, obviously the concentration of the paramagnetic species (V_O^{1+}) will be less. This indicates that at higher La concentration, the conversion of V_O^{2+} to V_O^{1+} by an electron capture from the negatively charged cationic vacancies become less prominent and at this concentration the Bi_2O_3 separated phase shall be so appreciable that it may prevent the formation of Bi vacancies in the solid solutions. The other possible reason is that, since at higher La concentration the mixture contains the un reacted U_3O_8, Bi_2O_3 and La_2O_3 along with the $Bi2_{-2x}La_{2x}UO_6$ solid solutions, the concentration of the paramagnetic species (V_O^{1+}) will get diluted as it belongs to the $Bi_{2-2x}La_{2x}UO_6$ system only. This was not the case for the solid solution with x up to 0.05, where the synthesized product was mostly $Bi_{2-2x}La_{2x}UO_6$ matrix.

5.3.4. Photoluminescence study: Excitation and emission spectroscopy, lifetime study and time resolve emission spectra

Figure 5.11a & b show the excitation spectra at λ_{em} = 615 nm and 530 nm respectively for 2 at % Eu^{3+} doped Bi_2UO_6 ($Bi_{1.96}Eu_{0.04}UO_6$). Two broad band with λ_{max}= 245 nm and λ_{max} = 270 nm are attributed to the $O^{2-}\rightarrow U^{6+}$ and $O^{2-}\rightarrow Eu^{3+}$ charge transfer band (CTB) (Figure 5.11a), since the degree of covalency of Eu^{3+}– O^{2-} bond is weaker than U^{6+}– O^{2-}due to the larger electro negativity and smaller size of U^{6+}. These bands arise due to charge transfer transition from oxygen (2p) orbital to uranium (6d) orbitals and to 4f shells of Eu^{3+} ions. The sharp lines in between 350–500 nm in Figure 5.11b in case of λ_{em} = 615 nm are attributed to intra-configurational 4f–4f transition of Eu^{3+} in host lattice. The peaks at 320, 360, 380, 395, 420, 460 and 480 nm are assigned to electronic transitions of $^7F_0 \rightarrow {}^5H_3$, $^5L_9$, $^5L_7$, $^5L_6$, $^5D_4$, $^5D_3$ and $^5D_2$ of Eu^{3+} respectively **[333]**, whereas, in case of λ_{em} = 530 nm, the excitation peaks at 326, 362, 392, 412, 424, 445 and 487 nm are due to hexavalent uranium **[305,334]**. The peaks in between 285 and 330 in Figure 5.11a are due to Bi^{3+} ions **[335-337]**. Thus, the absorption bands due to Bi^{3+} are overlapped with the existing charge transfer bands.

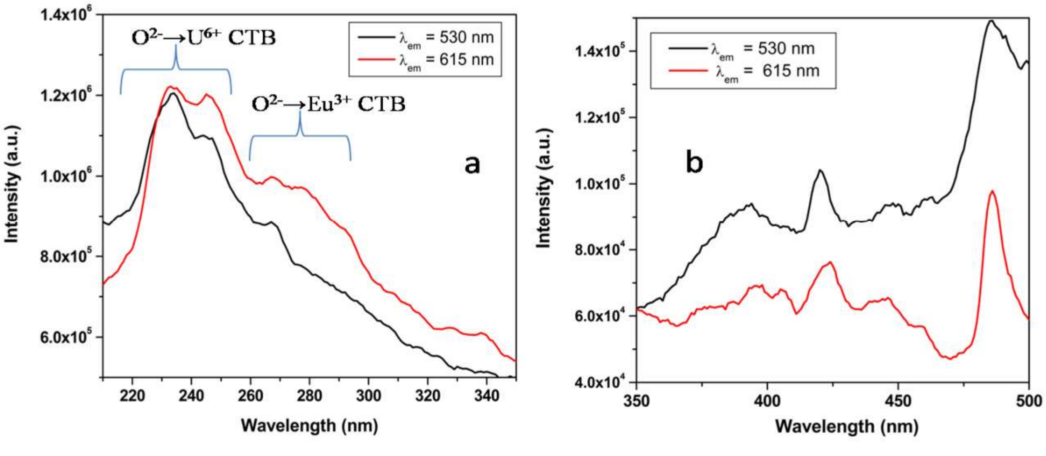

Figure 5.11: *PL excitation spectra of $Bi_{1.96}Eu_{0.04}UO_6$ at different emission wavelengths (530 nm & 615 nm): a) Charge Transfer Bands (CTB) and b) Different characteristic excitation lines of Eu^{3+} and U^{6+}*

Emission spectra for 2 at % Eu $^{3+}$ doped Bi_2UO_6 at λ_{ex} = 245 nm & 270 nm (charge transfer band, CTB) are shown in Figure 5.12a & b. It was observed for both the excitation wavelengths, that there is a broad band in the range 350–460 nm with maxima at 430 nm. This emission at 430 nm is assigned to paramagnetic oxygen vacancies $V_O^{\cdot}$ **[178,179]**. The spectra also consists of vibronic structure due to UO_2^{2+}

as reported in the literature **[305,334]** along with characteristic transitions of Eu^{3+} such as $^5D_0 \rightarrow {}^7F_1$ (593 nm), $^5D_0 \rightarrow {}^7F_2$ (615), $^5D_0 \rightarrow {}^7F_3$ (652 nm) and $^5D_0 \rightarrow {}^7F_4$ (700 nm) arising due to transition from the excited $^5D_0$ state to ^7F_J (J= 0–4) levels. As seen from these two figures, for λ_{ex} = 245 nm, the characteristic emission lines of UO_2^{2+} are very clear while that of Eu^{3+} ion are very low intense and not visible clearly (Figure 5.12a) while for λ_{ex} = 270 nm, the characteristic emission lines of Eu^{3+} ion are more intense and more clear compared to UO_2^{2+} (Figure 5.12b). From the characteristic lines of Eu^{3+} ion in Figure 5.12b, it is also clearly seen that $^5D_0 \rightarrow {}^7F_2$ (615 nm) is the most intense one among all. If one carefully sees these two figures (5.12 a & b), a broad background feature with maxima at 520 nm is also found to be present which is attributed to the $^1S_O \leftrightarrow {}^3P_1$ transition of Bi^{3+}. Generally, U (VI) in the form of UO_6^{6-} also shows emission in this region **[333]**. However, as Bi_2UO_6 does not contain this moiety, the presence of UO_6^{6-} emission can be ruled out completely. The emission due to Bi^{3+} ions is generally observed in the spectral range 470-670 nm depending on the covalence; crystal field and co-ordination number **[335-337]**. A combined PL decay and Time Resolve Emission Spectra (TRES) study was performed to resolve all the components, which is discussed below.

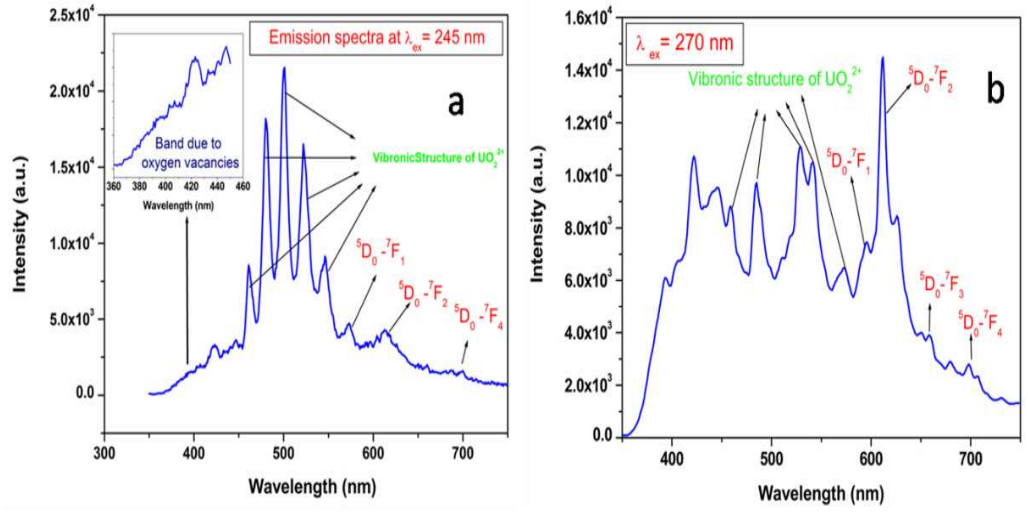

***Figure 5.12**: PL emission spectrum of $Bi_{1.96}Eu_{0.04}UO_6$ at a) λ_{ex}=245 nm and b) λ_{ex}=270 nm*

The PL decay curves corresponding to the 2 at % Eu^{3+} doped Bi_2UO_6 ($Bi_{1.96}Eu_{0.04}UO_6$) with different emission wavelengths viz., λ_{em} = 430, 520 and 615 nm at an excitation wavelength of λ_{ex} = 245 nm are shown in Figure 5.13. The decay curve at 430 nm was fitted using the mono-exponential decay equation; while the other two decay curves at 540 and 615 nm were fitted using the bi-exponential decay equation. The details of this equation are given in previous chapters.

The lifetime values (**τ_1** and **τ_2)** corresponding to the emission wavelengths 430 nm, 540 nm and 615 nm are tabulated in Table 5.4. The life time values at λ_{em} = 430 nm ($\tau^1{}_1 \approx 14$ μs) is attributed to oxygen vacancies since the emission is associated with electron hole recombination process as observed in our previous cases **[179]**. In case of λ_{em} = 540 nm, the two lifetime values obtained from the bi-exponential equation are $\tau^2{}_1 \approx 20$ μs and $\tau^2{}_2 = 95$ μs. Since both uranyl 'UO_2^{2+}' and Bi^{3+} generally show emission in the same region, the two life time values are due to these two species only**.** The origin of uranyl group's emission is charge transfer transition, which is allowed while that of Bi^{3+} ion is due to $^1S_O \leftrightarrow {}^3P_1$, which is forbidden due to triplet to singlet transition. Therefore the shorter lifetime i.e. $\tau^2{}_1 \approx 20$ μs is assigned to the uranyl 'UO_2^{2+}' group while the longer one i.e. $\tau^2{}_2 = 95$ μs is assigned to the Bi^{3+} ion. The lifetime values observed from the bi-exponential decay curve at λ_{em} = 615 nm are $\tau^3{}_1 \approx 50$ μs and $\tau^3{}_2 \approx 400$ μs. Since EXAFS and XRD studies have indicated that La^{+3} is going at Bi^{+3} site in Bi_2UO_6, these two life time cannot be assigned to Eu^{3+} ion at two different sites (Bi^{3+} and U^{6+} site). As the f-f transition of Eu^{3+} ion is a forbidden one, obviously the longer lifetime $\tau^3{}_2$ is due to Eu^{3+} ion at Bi^{3+} site. Emission spectrum shows that there are defects like oxygen vacancies in the solid solutions. These defect centres provide some non-radiative pathways to the activator in the excited state to come back to the ground state. Therefore we attribute the shorter lifetime $\tau^3{}_1 \approx 50$ μs to Eu^{3+} ion at Bi^{3+} site which is in the vicinity of oxygen vacancies, while the longer one i.e. $\tau^3{}_2 \approx 400$ μs is due to Eu^{3+} ion at Bi^{3+} site which is far from oxygen vacancies.

In Figure 5.14: I, II, III, IV and V, TRES spectra at λ_{ex}= 245 nm and at different delay times viz. 20, 200, 400 & 800 μs with constant integration time of 1 ms, have been shown. In general, all the species fully decayed at an average time of 3 times of their respective life time (3τ). Assuming that, at 20 μs delay time, all the species will be present. Figure 5.14-I represents a mixture of all the emissions from these species. However at higher time delay such as 200 μs, the species with $\tau^1{}_1 \approx 14$ μs will be completely decayed and the spectra Figure 5.14-II will consist of other species except that one with life time $\tau^1{}_1$. Therefore A=(I-II) represents the

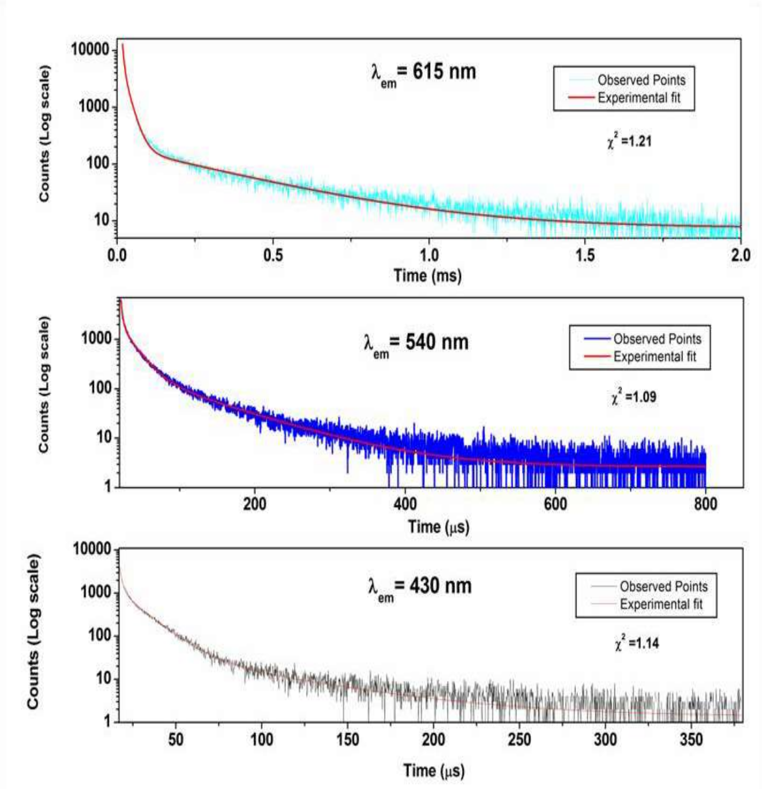

Figure 5.13: *PL decay curves corresponding to 2 atom % Eu* $^{3+}$ *doped* Bi_2UO_6 $(Bi_{1.96}Eu_{0.04}UO_6)$ *with different emission wavelengths (* λ_{em} *= 430, 537 and 615 nm) at an excitation wavelength of* λ_{ex} *= 245.*

Table 5.4 : Lifetime values at different emission wavelength

Wavelength (nm)	$\tau^{1,2,3}_1$ **(μs)**	$\tau^{1,2,3}_2$ **(μs)**
430	τ^1_1= 13.96 (100%)	-
540	τ^1_2=19.81 (44.78%)	τ^2_2=95.03 (55.22.27%)
615	τ^1_3=49.39 (28.20 %)	τ^2_3=398 (71.80%)

TRES spectra due to the species $\tau^1_1 \approx 14$ μs as shown in Figure 5.14 A, with a maxima peak at 430 nm, which is assigned to oxygen vacancies. Similarly the TRES spectra of uranyl ($\tau^2_1 \approx 20$ μs) and Bi^{3+} ($\tau^2_2 = 95$ μs) species can be represented by B= (II-III) and C= (III-IV). At 800 μs delay time, the spectrum will be mostly contributed by the long lived component of Eu^{3+} as represented by IV in Figure 5.14. Since both the Eu^{3+} species with $\tau^3_1 \approx 50$ μs and $\tau^3_2 \approx 400$ μs occupy the same symmetry and same co-ordination, their TRES spectra will be same. The orange emission (590–600 nm) of Eu^{3+} is due to the Magnetic Dipole Transition (MDT) $^5D_0 \rightarrow {}^7F_1$, which is not affected appreciably by the site symmetry while the red emission (610–630 nm) is due to the Electric Dipole Transition (EDT) $^5D_0 \rightarrow {}^7F_2$ which is sensitive to local site symmetry as stated in our earlier case in Eu:BZO. Hence, the intensity ratio of $^5D_0 \leftrightarrow {}^7F_2$ to $^5D_0 \leftrightarrow {}^7F_1$ will provide information about the site symmetry of Eu^{3+}. Strong intensity of $^5D_0 \leftrightarrow {}^7F_2$ line at 614 nm (EDT) in comparison to $^5D_0 \leftrightarrow {}^7F_1$ line at 594 nm (MDT) from Figure 5.12b, 5.14-III & 5.14-IV, indicates that Eu^{3+} occupy asymmetric environment without inversion symmetry. As stated earlier, Bi ions possess more asymmetric environment compared to U in Bi_2UO_6; it can be easily concluded that Eu^{3+} ions are substituting Bi^{+3} ions in Bi_2UO_6 lattice to form $Bi_{1.96}Eu_{0.04}UO_6$. Since both Eu^{3+} and La^{3+} have similar size and charge, they will also follow similar behavior during formation of $Bi_{2-2x}La_{2x}UO_6$ solid solutions. Hence, La^{3+} will also substitute Bi^{3+} in Bi_2UO_6 to form $Bi_{2-2x}La_{2x}UO_6$ solid solutions.

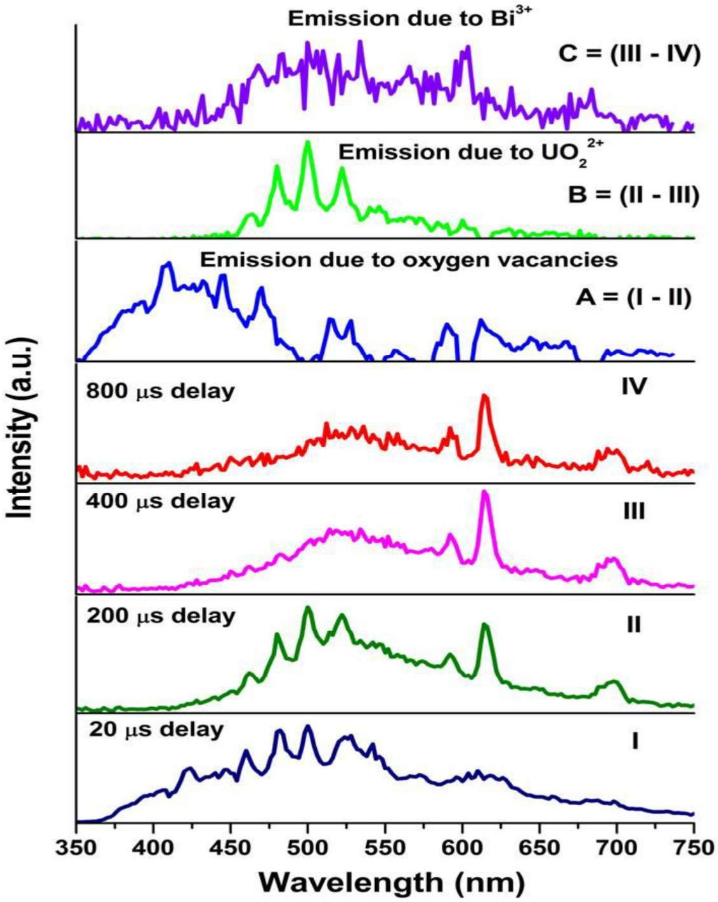

Figure 5.14: *TRES spectra of 2 atom % Eu^{3+} doped Bi_2UO_6 ($Bi_{1.96}Eu_{0.04}UO_6$) at two different delay time (20 & 200 μs).*

5.4. Synthesis and optical properties of U:$MgAl_2O_4$ [338]

5.4.1. Synthesis and Characterization

U:$MgAl_2O_4$ has been synthesized using gel-combustion method employing citric acid as combustion fuel. The raw materials used in this synthesis are citric acid ($C_6H_8O_7 \cdot H_2O$) (99.7%, AR grade), Magnesium Carbonate [$MgCO_3$] (99%, AR grade), Aluminium nitrate [$Al\ (NO_3)_3 \cdot 9H_2O$] (98%, AR grade) and U_3O_8 (Spectroscopic Grade, 99.999 %). At first required amount of magnesium carbonate and uranium oxide were converted into their respective nitrate form by dissolving their appropriate amounts in dilute nitric acid (4M).In a separate beaker, required amount of Aluminum nitrate salt was dissolved in QDD water. The magnesium and aluminum nitrate solutions were then mixed in a beaker under constant stirring for half an hour and a transparent solution was obtained. The uranium nitrate solution was then mixed to this mixed solution. Citric acid solution, which was prepared in a separate beaker by dissolving its required amount in QDD water, was subsequently added to the nitrate solution mixture. The entire mixing process was done at room temperature under vigorous stirring at magnetic stirrer and kept as such for 1 hour. The solution mixture was then heated at 80^0C with continuous stirring for 5 hours, until a highly viscous gel is formed. The gel was then heated under infrared lamp for 10-12 hours after which a brown ash-like voluminous product was formed. The ash like mass was then grounded and kept for calcining at 800º C in a muffle furnace under air atmosphere for 12 hr, after which a fine white powder was obtained.

Figure 5.15 shows the XRD patterns of as-prepared 1.0 mol % U doped $MgAl_2O_4$ (U:MAS). XRD patterns of the compound are in close agreement with reported cubic pattern of $MgAl_2O_4$ spinel (MAS) with JCPDS No. 77-0435. The XRD patterns do not show any signature of impurity phase diffraction peaks such as MgO, Al_2O_3 or U_3O_8 phase which is an indication of homogeneous solid solution of $MgAl_2O_4$ and U, which further confirms the occupancy of uranium ions at the lattice sites of MAS. It can also be seen from the XRD pattern that all peaks are sharp and well defined, indicating a high degree of crystallization in U:MAS sample. We have synthesized the pure phase at 800^oC and in comparison to reported literature our samples mostly stabilizes in normal spinel form with octahedral Al^{3+} and tetrahedral Mg^{2+} sites **[339]**.

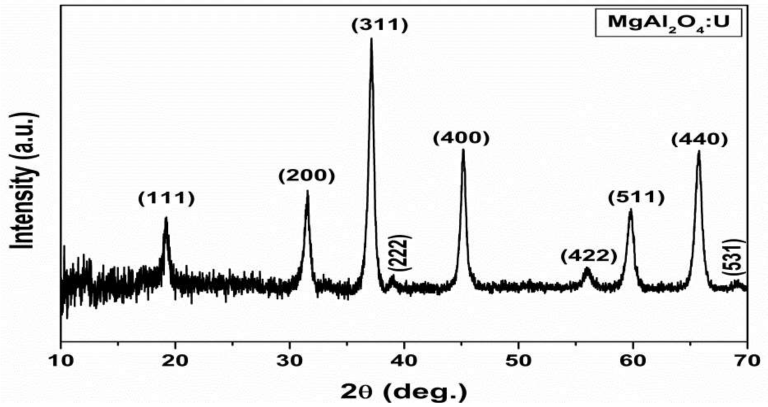

Figure 5.15: *Powder X-ray diffraction pattern of U:MAS*

5.4.2. Excitation and Emission Characteristics, lifetime, local site occupancy, energy transfer and TRES study

Figure 5.16 shows the emission spectrum of MAS undoped sample under 230 nm excitation. The emission can be seen in the visible bluish green region, which was attributed to presence of shallow and deep defect in band gap of materials. Since the excitation wavelength used in this case is less than the band gap of MAS, direct band-to- band transition is not possible. There must be some defect states (cation or oxygen vacancies) which are aiding the hole-recombination process. The origin and role of various defects is explained in our earlier work **[178, 179]**.

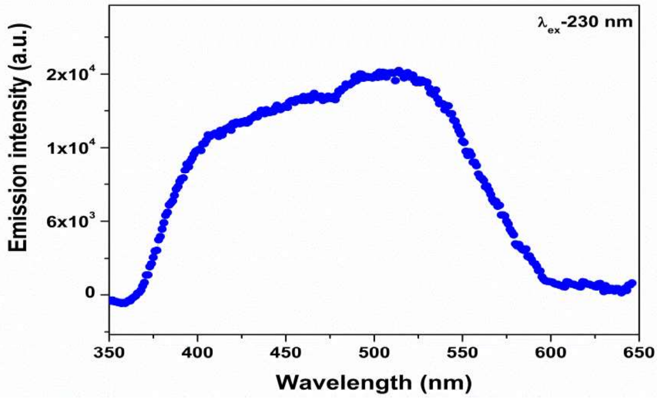

Figure 5.16: *Emission spectrum of* $MgAl_2O_4$ *under excitation of 230 nm.*

Figure 5.17 depicts the excitation spectrum of U:MAS under emission at 501 nm. There are two main features; one is a broad band at around 260 nm and there are cluster of peaks at around 422 nm. Broad peak at 260 nm has been attributed to a U–O charge transfer transition corresponding to the presence of U ions at the Mg^{2+} or Al^{3+}

sites. The peak at 422 nm is typical of uranium in the form of uranyl ion. It is reported **[340]** that the absorption band at 420 nm is typical of ligand-to-metal charge transfer (LMCT) electronic transition of uranyl (VI) salts, consisting vibrational fine structure of which maximum of twelve transitions can be resolved.

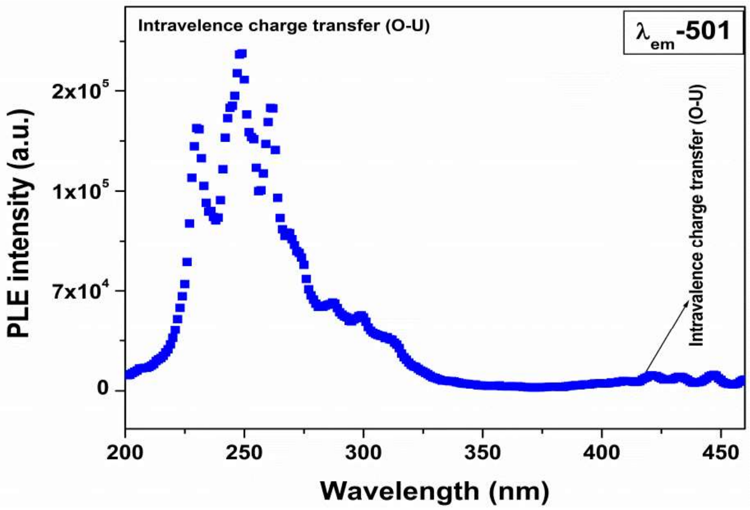

Figure 5.17: *Excitation spectrum of U:MAS (λ_{em}-501 nm)*

Figure 5.18a shows the emission spectrum of U:MAS under excitation range from 230 to 300 nm. The spectral feature remains same as a function of excitation wavelength but they do differ in terms of intensity; 250 nm excited sample gives the maximum emission output. The fluorescence spectrum has six characteristic bands at 460, 480, 500, 520, 546 and 572 nm. The four main peaks (460, 480, 500, and 520 nm) have a full width at half maxima (FWMH) of around 20 nm (Figure 5.18a). Complete disappearance of defect induced host emission of MAS in emission spectrum of U:MAS is an indication of the fact that complete energy transfer takes place at 1.0 mol % of uranium ion concentration. This has also been explained using DFT calculation, which is given in details in our published report **[338]**. From DFT calculation, it was observed that d and f-states of U contribute strongly in the lower part of CB as well as in the defect states generated due to oxygen vacancies. In our previous study **[179],** it was shown that photo-luminescence properties of the $MgAl_2O_4$ are dominantly governed by the presence of oxygen vacancies (neutral and charged). As a result, photon energy transfer from host MAS to dopant U is easy and preferable.

The vibronic progression with constant spacing in the emission spectrum is specific signature of uranium in +6 oxidation state in the form of UO_2^{2+} **[21]**. Such uniformly distributed vibrational progression arises from strong interaction of the ground state Raman active O=U=O symmetric stretching mode with the $^3\Pi_u$ electronic triplet excited state (generally observed between 780 and 900 cm^{-1}). These characteristic emission peaks of U:MAS (Fig. 5.18a) is due to LMCT involving electronic transition from bonding oxygen orbital (σ_u, σ_g, π_u and π_g) to a non-bonding uranium $5f_\delta$ and $5f_\phi$ orbital **[22]**. U-O in uranyl ion (UO_2) has partial triple bond character and relatively shorter bond length compared to single U-O bond in uranate ion (UO_6). The position of first vibrational band (υ_{0-0}) is most confirmatory signature in deciding the number of oxygen around uranium and bond order of U-O and it is termed as zero phonon band (ZPB). ZPB for UO_2^{2+} can vary from 440-520 nm and the fact in our spectrum it is observed at 460 and the subsequent vibrational progression can be seen at room temperature is an indication of the fact U (+6) stabilizes as UO_2^{2+}.

Figure 5.18b shows the emission spectra for the uranium incorporated $MgAl_2O_4$ samples as a function of excitation wavelength, from 300-400 nm. It can be seen from the figure that as the excitation wavelength increases and reach the limit of 330 nm, the fine uranyl structures vanishes and a broad band was observed centered at around 525 nm which is the signature of uranate ion in octahedral coordination (UO_6^{6-}). This indicates that minor amount of U (+6) may also be stabilized in the form of UO_6^{6-} .

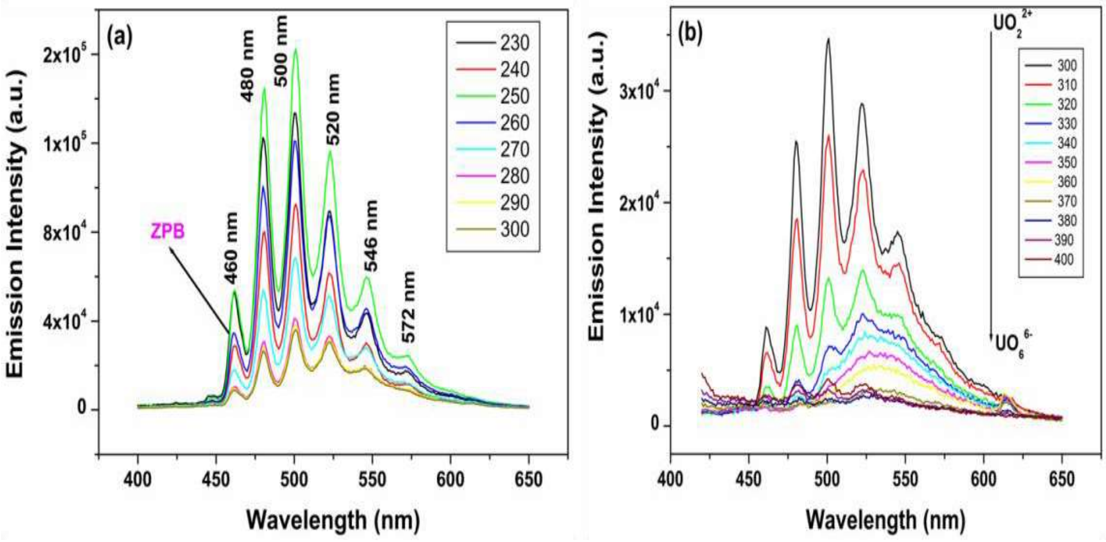

Figure 5.18: *Emission spectra of U:MAS in the excitation range (a) 230-300 and (b) 300-400*

Local site occupancy of Uranium in MAS

In order to compare the emission profile of uranyl ion in a magnesium aluminate spinel and that of pure uranyl ion compound, the fluorescence spectrum of uranyl fluoride, available in our laboratory, was recorded. Figure 5.19 shows the comparative emission spectra of uranyl fluoride crystal systems and that of U:MAS. The emission spectrum of U:MAS exhibits broad spectral features compared to uranyl fluoride crystal; this is typical of uranyl ion in disordered chemical surrounding. Secondly, the emission bands in U:MAS are blue shifted with respect to peak position of uranyl fluoride, which also indicates a distorted chemical environment for the uranyl ion in magnesium aluminate compared to pure uranyl compound. This indicates that majority of UO_2^{2+} occupies relatively asymmetric Mg^{2+} sites (tetrahedral) in magnesium aluminate.

To get better insight into local structure and site of uranyl ion in MAS, luminescence lifetime measurements were conducted. The decay curve corresponding to U:MAS is depicted in Figure 5.20a under excitation wavelengths of 250 nm and emission wavelength 501 nm. The PL decay curve was fitted using bi-exponential model using equation4.2 as given in previous chapter. The decay curve shows two different lifetime value 15μs (T1) and 119 μs (T2) with magnitudes 22% and 78 % respectively. Bi- exponential decay indicates different chemical environment of uranyl ion in $MgAl_2O_4$.

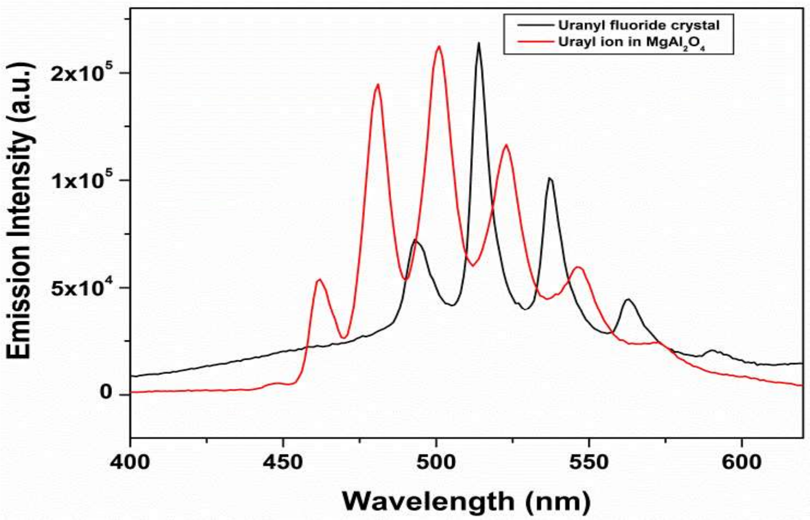

Figure 5.19: *Emission spectra of U:MAS and uranyl fluoride crystals under identical conditions*

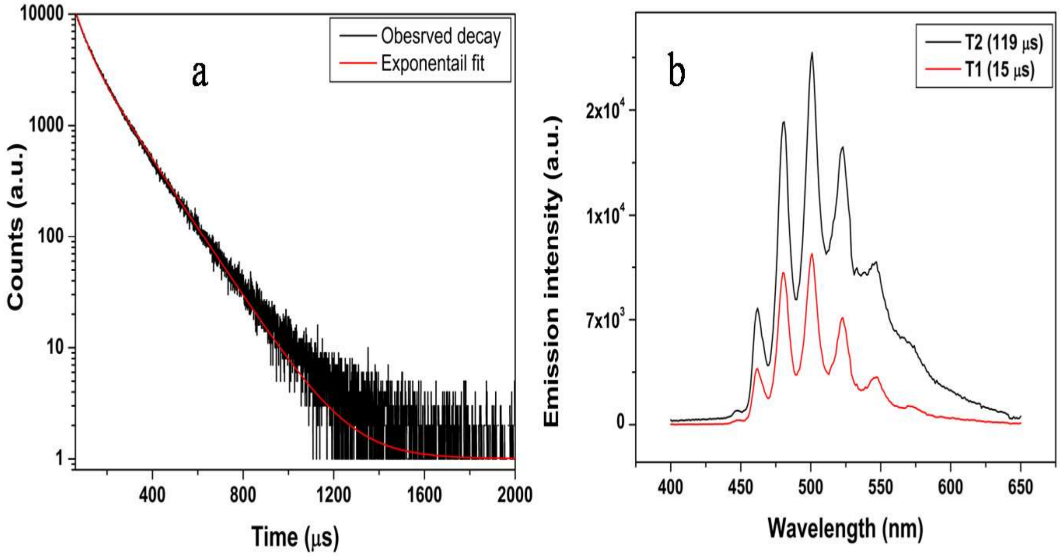

Figure 5.20: *(a)Luminescence decay profile of Uranyl ion in $MgAl_2O_4$ under λ_{ex}-250 nm and λ_{em}-501 nm & (b) Time resolved emission spectra of short and longer lived uranyl ion in MA*

Time resolved emission spectroscopic analysis:

To get information about emission characteristics of T1 and T2, TRES measurement was carried out on U:MAS. On applying suitable delay and selecting appropriate gate width, one can get emission spectral information for T1 (15 µs) and T2 (119 µs). The emission profile obtained for shorter and longer-lived species is shown in Figure 5.20b. It can be seen from the spectra that the emission peaks corresponding to the slow decaying species are blue shifted by 3–5 nm and both the species differ in their emission output. This observation clearly confirmed the presence of the uranyl ion at two different chemical environments in MAS.

Chapter 6

Conclusions and future scope

The present thesis describes a detail investigation on defects and dopant mediated optical properties in various oxide based matrices (both doped and undoped) e.g. magnesium oxides (MgO), zinc and magnesium aluminates ($ZnAl_2O_4$, Fe:$ZnAl_2O_4$, $MgAl_2O_4$ & U:$MgAl_2O_4$), zirconate ($SrZrO_3$, Mn:$SrZrO_3$, $BaZrO_3$, Sm:$BaZrO_3$ & Eu:$BaZrO_3$), uranate ($Bi_{2-2x}La_{2x}/Eu_{2x}UO_6$) and vanadate ($LiZnVO_4$), which were synthesised through either solid state or sol-gel combustion method. Structural and optical properties of these materials have been investigated using XRD, SEM, TEM, PAS, EPR and PL techniques. In Chapter 1, a brief introduction to various defects and dopant related optical materials, different luminescence centres and their luminescence properties are given and discussed. In chapter 2, basic principles of different experimental and instrumentation techniques used for synthesis and the characterization of the luminescent materials are discussed. Subsequent chapters (chapters 3-5) deal with the various defects and dopant mediated fascinating optical properties of the mentioned oxide matrices.

MgO was synthesized by the thermal decomposition of magnesium oxalate precursor at different temperatures viz. 600°C, 800°C and 1000°C .Various defect centres such as oxygen vacancies (different F centres), cationic vacancy, interstitial oxygen, etc. are responsible for multi component emission characteristics. DFT based calculations were performed for these defect centres to characterize their electronic states inside the band-gap. In MgO, a photo ionization process viz. $F + h\upsilon \leftrightarrow F^+ + e$ was observed, where the released electron becomes free after prompting into the conduction band. Being free, the electron may recombine with different types of positively charged defect centres in addition to the newly formed F^+ centres. Thus, different electronic transitions from the conduction band (CB) to the empty ground electronic states of positively charged F and F_2-type centres were correlated with the respective colour components. Recombination of a hole in the valence band (VB) with a filled electron in the electronic states may also be responsible for some emission behaviors in the near infrared (NIR) region. These recombination processes lead to observation of different emitting colours. Study on magnetic measurements showed a low temperature weak ferromagnetic ordering with a T_C (Curie temperature) around 65 K (±5 K). The saturation magnetization (M_s) was found to increase with increasing annealing temperature during the synthesis. A combined EPR and Positron annihilation lifetime study suggested that both oxygen and Mg vacancies are responsible for the ferromagnetism behavior and the observed higher magnetic value at higher annealing temperature was due to dissociation of cluster vacancy to mono vacancies.

Both $MgAl_2O_4$ and $ZnAl_2O_4$ compounds were synthesized using sol-gel combustion method at different annealing temperatures. In $MgAl_2O_4$, two broad emission bands; one in the blue-green-yellow and other in the red-near infrared (NIR) regions were observed. Tuning of emission profile from blue-green-yellow to red-NIR region was possible upon thermal annealing of the as prepared compound. Multiple defect centres, such as F, F_2, F^+, and F_2^{2+} and different shallow and deep defects were found to be present inside the band gap, as confirmed by the lifetime and time-resolved emission spectroscopy (TRES) studies. The tunable emission characteristic at different annealing temperatures could be linked with the phase behavior of the spinel. Excitation wavelength variation suggested that a photo conversion process of F to F+ centres was involved with λ_{ex} = 250 nm, followed by a trapping−de-trapping mechanism of the released electrons within different trap states. An exchange mechanism of electrons in between conduction band and shallow states was also observed at room temperature, which was absent at low temperature, as indicated by the emission profile. These observations render $MgAl_2O_4$ to be a potential optical based thermal sensor material.

In $ZnAl_2O_4$, a broad emission peak in the blue-green region was observed which is due due to presence of oxygen vacancies, interstitial defect and anisette defect centres. No prominent emission in the red-NIR regions was observed like $MgAl_2O_4$. However TRES study showed that at higher temperature, there is an existence of a low intense red-NIR peak. Unlike $MgAl_2O_4$, no photo conversion of F centres and tuneable emission characteristics on excitation wavelength variation was observed. For both $MgAl_2O_4$ and $ZnAl_2O_4$, when the compounds were synthesised at lower annealing temperature the lifetime of the defect centres were found to be high (of the order of ms) while annealing them at higher temperature, the life times are significantly reduced (of the order of μs).This observation can be attributed to the presence of antisite defect centres such as Al_{Zn}^+ or Al_{Mg}^+ which act as an electron trap, thereby delaying the electron-hole recombination. For these compounds obtained at lower annealing temperature, the percentage of inversion is more while at higher annealing temperature it is less. In both cases of the compounds, DFT-based calculations were carried out for both pure and various oxygen-vacancy-introduced spinel phases in order to characterize the different defect related electronic states inside the band gap.

In Fe:$ZnAl_2O_4$, which was synthesised through sol-gel combustion method, two different emission profiles in the blue and red region were observed. With changing concentration, there was an increase in the red emission due to Fe^{3+} substituted Zn^{2+} at octahedral site. At higher annealing temperature, a reverse trend in both the colour was observed. The blue emission kept on reducing, while the red emission kept on increasing as the doping level was increased. In EPR study also, Fe^{3+} showed two characteristics spectra in the tetrahedral and octahedral site and their variation with concentration and annealing temperature was in concordance with the results in PL spectroscopy. These observations suggest that at low temperature the percentage of inverse phase in $ZnAl_2O_4$ spinel is more, while at higher annealing temperature normal phase exists in majority.

In Mn:$SrZrO_3$, which was synthesised through sol-gel combustion method, Mn^{2+} at Zr-site experiences strong crystal field environment, while at Sr-site it faces low crystal field environment. At Sr-site it gives green emission and at Zr-site it gives red emission. A tuning of emission colour to the red region could be observed at higher Mn concentration, due to increase in Mn^{2+} ion substitution at Zr-site. Further this substitution at Sr- & Zr-site was also linked with the shallow and deep defects of the $SrZrO_3$ as confirmed by DFT calculation. Thus Mn -substitution also helped in characterising shallow and deep defects of the host emission. In EPR investigation, Mn^{2+} showed characteristic spectra due to substitution at the lattice site and on surface of the particle. In addition, a broad spectrum due to oxygen vacancy was also observed; this was found to increase at higher concentration of Mn^{2+} due to more substitution at Zr-site.

In $LiZnVO_4$, an intense green emission was observed due to oxygen vacancy and charge transfer transition of the VO_4^{3-} host. The compound was synthesised through sol-gel combustion route. Generally phosphor material synthesised through this route shows low quantum yield due to agglomeration of the particles at higher annealing temperature. In this case during synthesis, in the starting solution, V exists as VO^{2+} ($3d^1$) which is EPR active, while in $LiZnVO_4$, V exist as V^{5+} ($3d^0$) which is EPR inactive. Thus monitoring the EPR spectra at different annealing temperatures, it was observed that 600 ^{0}C is the optimum temperature for synthesis. Further the EPR parameters at different steps showed that there is a change in co-ordination surrounding the V from octahedral to tetrahedral, which confirmed that tetrahedral VO_4^{3-} is the main luminescence centre in $LiZnVO_4$. Thus on a general note, we can say that transition metal ions can be used for developing colour tunable phosphors materials, as a structural probe and to monitor synthesis of phosphor materials.

$BaZrO_3$ nanoceramics were synthesized using gel-combustion route. Intense blue and green emission was observed in undoped sample due to the presence of oxygen vacancy. Both Sm^{3+} and Eu^{3+} doped $BaZrO_3$compounds were found to be red emitting phosphors. Based on PL spectroscopy, it was inferred that majority of Sm^{3+} ion stabilize at Ba^{2+} site without inversion symmetry, whereas majority of Eu^{3+} ions occupy Zr^{4+} site. The actual site symmetry for Eu^{3+} ion in barium zirconate was also evaluated based on stark splitting pattern and was found to be C_6.

In $Bi_{2-2x}La_{2x}UO_6$ in order to understand the site occupancy of La, Eu^{3+} had doped in place of non-activator ion La^{+3}. The compounds were synthesized through solid state method. In iso-structural $Bi_{1.96}Eu_{0.04}UO_6$, it was observed that majority of Eu^{3+} ions were occupying the Bi^{3+} site. Thus Eu^{3+} can be used as a spectroscopic probe for site occupancy of La^{3+} having similar charge and size. Emission due to oxygen vacancy was also observed in this compound, which in a combined study with EXAFS was concluded to be due to La substitution at Bi site, which leads to distortion in the matrix. These oxygen vacancies are responsible for the conductivity of the material. In $Bi_{1.96}Eu_{0.04}UO_6$, uranium stabilizes in +6 oxidation state in the form of UO_2^{2+} ion giving a vibronic structure in the emission profile. With the help of TRES study, the five line vibronic structure was isolated from the complex emission spectra.

Uranium doped $MgAl_2O_4$ was synthesized through gel-combustion method. It is very important to know the exact state of U, since the physical properties associated with the U based compound is very much dependent on its state of existence. From excitation and emission spectroscopy, it was observed that uranium stabilizes in +6 oxidation state in the form of UO_2^{2+} ion. On doping uranium in $MgAl_2O_4$, complete energy transfer from host to uranium ion was observed, which was explained using DFT. Bi-exponential decay indicated two different chemical environments for uranyl ion in $MgAl_2O_4$.TRES obtained after suitable delay time showed the emission characteristics of two different uranyl ions.

Future scope:

As a natural continuation of this work the following issues should be investigated

1) Theoretical and EXAFS measurements to reach a deep understanding about the defect structure in $ZnAl_2O_4$ and $BaZrO_3$
2) Defect induced emission characteristics in other aluminates such as $BaAl_2O_4$, $CaAl_2O_4$ and comparing their PL properties with $MgAl_2O_4$ and $ZnAl_2O_4$.
3) Exploring defects and dopant induced optical properties in double perovskite materials.
4) Photocatalysis study of these materials will also be very an interesting research area.

References:

1.B. Raveau*, J. Am. Ceram. Soc.* **2005**,*25*, 1965.

2.P.H.C. Camargo, K. G. Satyanarayana and F. Wypych, *Mater.Res.,***2009**,*1*,12.

3.C. Feldmann, T. Ju¨stel, C. R. Ronda and P. J. Schmidt, *Adv. Funct. Mater.,* **2003**,*13*,511.

4.V. P. Tuyen, T. Hayakawa, M. Nogami *et al., J. Solid State Chem.,* **2010**, *183*, 2714.

5. P. A. Tanner, Z. Pan, N. Rakov and G. S. Maciel, *J. Alloys Compd.,* **2006**, *424*, 347.

6.W. C. Ke, C. C. Lin, R. S. Liu and M. C. Kuo, *J. Electrochem. Soc.,* **2010**, *157*, 307.

7.W. Luo, C. Fu, R. Li, Y. Liu, H. Zhu and X. Y. Chen, *Small,* **2011**, *7*, 3046.

8.L. X. Yu and M. Nogami, *Mater. Lett.,* **2010**, *64*, 1644.

9. C. H. Zheng et al., *Cryst Eng Comm,* **2010**, *12*, 3277.

10.C. Zhang and J. Lin, *Chem. Soc. Rev.,* **2012**, *41*, 7938.

11.W. H. Green, K. P. Le, J. Grey, T. T. Au and M. J. Sailor, *Science*, **1997**, *276*, 1826.

12.K. P. Loh, Q. Bao, G. Eda and M. Chhowalla, *Nat. Chem.,* 2010, 2, 1015–1024.

13.V. Bekiari and P. Lianos, *Chem. Mater.,* **1998**, *10*, 3777.

14.S.D. Haa and S. Ramanathan, *J. Appld. Phys.,* **2011**, *110*, 071101.

15.M. Godlewski and M. Leskelä, *CRC Critical Reviews in Solid State and Materials Sciences,* **1994**,*19*,199.

16. S. K. Gupta, "Synthesis, characterisation and photoluminescence spectroscopy of lanthanide ion doped oxide material", Thesis submitted to the Homi Bhabha National Institute for the award of the degree of Doctor of Philosophy in Chemistry.

17.S. K. Gupta, C. Reghukumar and R. M. Kadam, *RSC Adv.,***2016**,*6*, 53614.

18.S. K. Gupta, P. S. Ghosh, N. Pathak and R. M. Kadam, *RSC Adv.,***2016**,*6*, 42923 .

19.M. Sobczyk *et al., J. Lumin.,***2008**,*128*, 185.

20.B. Ordejon, V. Vallet, J.P. Flament, L. Seijo and Z. Barandiara, *J. Lumin.,* **2007,** *126*, 779.

21.S. K. Gupta et al., *Spectrochim. Acta A,* **2015**, *151*, 453.

22.L.S. Natrajan, *Coord. Chem. Rev.,***2012**, *256*, 1583.

23.J.Chen *et al., Sensors*, 2**012**, *12*, 2414.

24.N. Jain *et al., RSC Adv.,* **2016**, *6*, 4960.

25. M. Nirmal and L. Brus, *Acc. Chem. Res.,* **1999**, *32*, 407.

26.S. Angelov *et al., J. Phys. Chem. Solids*, **1986**, *47*, 409.

27.W. H. Green, K. P. Le, J. Grey, T. T. Au and M. J. Sailor, *Science,* **1997**, *276*, 1826.

28.D.Y. Inamdar *et al., J. Phys. Chem. C,* **2010**,*114*, 1451.

29.E. Tirosh and G. Markovich, *Adv. Mater.*,**2007**, *19*, 2608.

30.D. Gao *et al., J. Phys. Chem. C*, **2010**, *114*, 11703.

31.J. I. Beltran *et al., Solid State Comm*., **2009**, *149*, 1654.

32.Y. Ohno *et al., Nature,* **1999**, *402*, 790.

33.A. Sundaresan *et al., Phys. Rev. B*, **2006**,*74*,16106.

34.C. Madhu, A. Sundaresan and C.N.R. Rao, *Phys. Rev. B* , **2008**, *77*, 201306.

35.M. Venkatesan, C. B. Fitzgerald and J. M. D. Coey, *Nature* , **2004**, *430*, 630.

36.N. H. Hong, J. Sakai, N. Poirot and V. Briz, *Phys. Rev. B*, **2006**, *73*, 132404.

37.J. Hu, Z. Zhang, M. Zhao, H. Qin and M. Jiang, *Appl. Phys. Lett.,* **2008**, *93*, 192503.

38.N. Kumar *et al., Chem. Phys. Lett.* **2009**, 477,360-364.

39.C. Mart´ınez-Boubeta, *et al., Phys. Rev. B*, **2010**, *82* , 024405.

40.C. Attaccalite, L. Wirtz, A. Marini, A. Rubio, *Scientific Reports*,**2013**, *3*, 2698 .

41.https://www.ndeed.org/EducationResources/CommunityCollege/Materials/Structure/point_defects.htmM. Zawadzki

42.Ben Meir Maoz, "Synthesis and Properties of Highly Defective MgO Nanosheets", Thesis submitted to School of Chemistry, Tel Aviv University, for the award of M.Sc Degree.

43.A. Gibson, R. Haydock and J. P., Lafemina, *Physical Review B,* **1994**,*50*, 2582.

44.W. Hayes *et al., Defects and Defect Processes in Nonmetallic Solids,* **1985**, 472.

45.M. Zawadzki, *Solid State Sci.,* **2006**, *8*, 14.

46.R. J. Twiss and E. M. Moores, *Structural Geology*. W. H. Freeman publisher,**2006**,532.

47.D. R. Vij and N. Singh, *Luminescence and Related Properties of II-IV Semiconductors*, Nova Publishers, New York, **1997**,169.

48. S. Ekambaram, K.C Patil and M. Maaza, *Synthesis of lamp phosphors, Facile combustion approach*, Purdue University, USA. **2005**.
49. J. C. Whitaker, *The Electronics Hand Book*, CRC Press, USA, **1996**, 469.
50. C. R Ronda, *Luminescence from Theory to Applications*, Willy-VCH, Germany, **2008**, 3.
51. J.G Sole, L.E Bausa and D. Jaque,*An Introduction to the Optical spectroscopy of Inorganic Solids*, ISBN 0-470-86886-4,John Wiley and Sons,Ltd,**2005**,17.
52. B. M. Mothudi, "Synthesis and characterization of Strontium (Sr), Barium (Ba) and Calcium (Ca) Aluminate phosphors doped with rare earth ions", Thesis submitted to University of the Free State for the award of the degree of Doctor of Philosophy in Physics.
53. S. Boggs and D. Krinsley, *Application of Cathodoluminescence imaging to the study of sedimentary rocks*, Cambridge University Press, England, **2006**.
54. R.D. Blackledge, *Forensic analysis on the cutting edge*, John Willey & Sons Publications, USA, **2007**.
55. W.M Yen and S. Shionoya, *Fundamentals of phosphors,* CRC Press, USA, **2007**.
56. J. Ball and A. D. Moore, *Essential physics for radiographers,* Blackwell Publishing, First edition, Oxford, **1979.**
57. S. Shionoya and W.M. Yen, *Phosphors Handbook,* CRC Press,USA, **1998**, 95 .
58. W. Martienssen and H. Warlimont, *Handbook of Condensed Matter and Data Materials, Springer*, USA, **2005**
59. G. Blasse and B. C. Grabmaier, *Luminescent Materials*. Springer Verlag, Berlin Heidelberg, **1994**.
60. B. Henderson and G. F. Imbusch. *Optical Spectroscopy of Inorganic Solids*, Claren-don Press, Oxford, **1989**.
61. P. D. Fleischauer and P. Fleischauer, *Chem. Rev.,***1970**, *70*,199.
62. B. Henke, "Structure Sensitive Investigations on Mn-activated Perovskites and Rare-Earth-doped Aluminates" Thesis submitted by to University of Paderborn for the award of the degree of Doctor of Philosophy in Physics.
63. K.A. Gschneider and L. Eyring, *Handbook on the Physics and Chemistry of Rare earths,* North Holland Publishing Company, Amsterdam, 1979.

64.I.K. Hemmilä, *Applications of Fluorescence in Immunoassays*, Wiley and Sons, New York, 1991.

65.(a) F.J. Steemers *et al., J. Am. Chem. Soc.* **1995**, *117*, 9408. (b) F.J. Steemers *et al., J. Org. Chem.,***1997***, 62*, 4229.

66.R. Moncorge, L.D. Merkle and B. Zandi, *MRS Bull*, **1999**,*24*,21

67.E. Desurvire, *Phys. Today*, **1994**, *97*, 20.

68.M. Karplus and R.N. Porter, *Atoms and Molecules*, The Benjamin-Cummings Publishing Company, Amsterdam,1970.

69.W.T. Carnall, G.L. Goodman, K. Rajnak and R.S. Rana, *J.Chem. Phys.* **1989**,*90***,** 3443.

70.S.V. Eliseeva and J.C.G. Bunzli, *Chem. Soc. Rev.*, **2010**,*39***,**189.

71.F. Auzel. *Chem. Rev.*, **2004**,*104*,139.

72.(a)B. R. Judd, Phys. Rev.,**1962**,*127*,750. (b) G. S. Ofelt, J. Chem. Phys.,**1962**, *375*,11.

73.M.H.V. Werts, R.T.F. Jukes and J.W. Verhoeven, *Phys. Chem. Chem. Phys.,***2002**,*4*,1542.

74.R.T. Wegh, H. Donker, K.D. Oskam and A. Meijerink, *Science*,**1999**, *283***,** 663.

75.M.J. Weber, *Phys. Rev. B*,**1973**, *8***,** 54.

76.Y. Haas and Y. G. Stein, *J. Phys. Chem*.,**1972**,*76***,** 1093.

77.W.D. Horrocks Jr. and D.R. Sudnick, *Acc. Chem. Res*.,**1981**,*14*,384.

78. A. Beeby *et al., J. Chem. Soc., Perkin Trans.,***1999**, *2***,** 493.

79.(a) Y. Haas and Y. G. Stein, *J. Phys. Chem*., **1971**,*75***,** 3668 (b) Y. Haas and Y. G. Stein, *J. Phys. Chem*., **1971**, *75***,** 3677.

80.V.L. Ermolaev and E.B. Sveshnikova, *Russ. Chem. Rev.,***1994**, *63*,905.

81.M.P.O. Wolbers *et al., J. Am. Chem. Soc.* **1997**, *119*,138.

82.I. Hemmilä, V.M. Mukkala and H. Takolo, *J. Fluorescence*, **1995**, *5* ,159.

83.B.L. Cushing, V.L. Kolesnichenko and C. J. O'Connor, *Chem. Rev*.,**2004**,*104*,3893.

84.J. Livage, M. Henry, C. Sanchez and C, *Prog., Solid State Chem*., **1988,** *18***,** 259.

85.L.L. Hench and J.K. West, *Chem. Rev*., **1990**,*90*,33.

86.R.C. Mehrotra and A. Singh, *Prog. Inorg. Chem*., **1997**,*46***,** 239.

87.H. Fang, H. Binyuan and L. Wang, *Front. Chem. China*, **2008**,*3*,193.

88.C. Cannas, A. Musinu, D. Peddis and G. Piccaluga, *J. Nanopart. Res.*, **2004**,*6*,223.

89.R. D. Purohit and A. K. Tyagi, *J. Mater. Chem*.,**2002**, *2* ,312.

90.S. V. Chavan and A. K. Tyagi, *J. Mater. Res*., **2004**,*19*,3181.

91.W. Eric and R. Cawson, *Elsevier Health Sciences*, 2002,15–20. ISBN 0-443-07027-X.

92.X-RayGeneration, Available from: http://xrayweb.chem.ou.edu/notes/xray.html

93.B.D. Cullity, *Elements of x-ray diffraction,* (Reading: Addison Wesley) (1956) 16.

94.Powder X-ray Diffraction, [online]. Available from http: // chemwiki.ucdavis.edu/Analytical_chemistry/instrumental_Analysis/Diffraction/Powder_X-ray_Diffraction.

95.R.W. Seigel, *Ann. Rev. Mater. Sci.,* **1980**,*10***,** 393.

96.R.N. West*, Adv. Phys*.,**1974**,*22***,** 263.

97.V.I. Grafutin and E.P. Prokop'ev, *Phys. Usp*., **2002**,*45*,59.

98.B. A. Dupasquier, *Positron Solid State Physics*, North-Holland, Amsterdam, 1984.

99.M. J. Puska and R.M. Nieminen, *Rev. Mod. Phys*.,**1994**, *66***,** 841.

100.E. Zavoisky, "Paramagnetic Absorption in Perpendicular and Parallel Fields for Salts, Solutions and Metals", Thesis submitted to the Kazan State University for the award of the degree of Doctor of Philosophy (1944).

101.W.R. Hagen, *Dalton Trans.,* **2006**, 4415–4434.

102.http://en.wikipedia.org/wiki/File:EPR_methyl.png

103.http://en.wikipedia.org/wiki/File:EP...hoxymethyl.png

104.http://en.wikipedia.org/wiki/File:EPR_lines.png

105.J.R. Lakowicz, *Principles of fluorescence spectroscopy*, Springer Science Business Media LLC, New York, USA, **2006**.

106.Edinburgh Photonics, Technical note, TN/2012/02.

107.Z. Ning *et al., Nature*, **2015**, *523*, 324.

108.I. Villa *et al., Chem. Mater*.,**2016**, DOI: 10.1021/acs.chemmater.5b03811.

109.M. Altmeyer *et al., Phys. Rev. Lett.,* **2016**,*116*, 157203 .

110.J. Nowotny *et al., Chem. Soc. Rev.,* **2015**, *44*, 8424.

111.L. Kong, C. Wang, H. Zheng, X. Zhang and Y. Liu, *J. Phys. Chem. C,* **2015**, *119*, 16623.

112.M. Sterrer, T. Berger, O. Diwald and E. K. Zinger, *J. Am. Chem. Soc*., **2003**, *125*, 195.

113.X. Y. Yu *et al.,J. Phys. Chem. C,* **2011**, *115*, 22242.

114.A. J. Haes *et al., J. Phys. Chem. B,* **2004**, *108*, 109.

115.S. W. Bian *et al., J. Mater. Chem.,***2010**, *20*, 8705.

116.T. Bak *et al., J. Phys. Chem. A,* **2015**, *119*, 9465.

117.J.W. Gonzalez *et al., Phys. Chem. Chem. Phys*., **2015**, *17*, 24707.

118.Y. Ito *et al., J. Am. Chem. Soc*., **2015**, *137*, 7678.

119.N. Chaudhari *et al., ACS. Appl. Mater*., **2015**, *7*, 17671.

120.N.J. Kramer, K.S. Schramke and U.R. Kortshagen, *Nano. Lett*., **2015**, *15*, 5597.

121.E. Sachet *et al., Nat. Mater*., **2015**, *14*, 414.

122.R. M. Amisse *et al., Chem. Mater*., **2015**, *27*, 4261.

123.C. Ji *et al., J. Phys. Chem. C,* **2015**, *119*, 13841.

124.P. K. Chow et al, *ACS Nano*,**2015**, *9*, 1520.

125.U.K. Gaur, A. Kumar and G.D. Verma, *J. Mater. Chem. C,* **2015**, *3*, 4297.

126.C. Park, J. Lee and W.S. Chang, *J. Phys. Chem. C*, **2015**, *119*, 16984.

127.J. Li, Z. Wang *et al., J. Phys. Chem. C* ,**2015**, *119*, 17848.

128.A. Kar, S. Kundu and A. Patra, *J. Phys. Chem. C,* **2011**, *115*, 118.

129.S. Saha *et al., J. Mater. Chem. C,* **2015**, *3*, 6786.

130. S. Ikeda and T. Uchino, *J. Phys. Chem. C,* **2014**, *118*, 4346.

131.P. V. Pikhitsa *et al., Appl. Phys. Lett*., **2015**, *106*,183106.

132.M. Itou, A. Fujiwara and T. Uchino, *J. Phys. Chem. C,* **2009,** *113,* 20949.

133.K.H. Lee and J.H. Crawford, *Phys. Rev. B,* **1977**, *15*, 4065.

134.B.G. Draeger and G.P. Summers, *Phys. Rev. B,* **1979**, *19*, 1172.

135.K. W. White and G. P. Kelker,*J. Am. Ceram. Soc*., **1991**, *74*, 1732.

136.N. Jain *et al., RSC Adv*., **2016**, *6*, 4960.

137.J. Hu, Z. Zhang, M. Zhao, H. Qin and M. Jiang, *Appl. Phys. Lett.,* **2008**, *93*, 192503 .

138.B. M. Maoz, E. Tirosh, M. B. Sadan and G. Markovich, *Phys. Rev. B,* **2011**, *83*, 161201**.**

139.G. H. Rosenblatt *et al., Phys. Rev. B,* **1989**, *39*, 10309.

140.B. Choudhury, P. Basyach and A. Choudhury, *J. Lumin.,* **2014**, *149*, 280.

141.R. C. Whited and W. C. Walker, *Phys. Rev. Lett.,* **1969**, *22*, 1428.

142.B. Choudhury and A.Choudhury, *Mater. Res. Express*, **2014**, *1*, 025026.

143.T. Uchino and D.Okutsu, *Phys. Rev. Lett.*, **2008**,*101*, 117401.

144.R. T. Williams *et al., Phys. Rev. B* ,**1979**, *20*, 1687.

145.A. Gibson, R. Haydock and J. P. LaFemina, *Phys. Rev.* B, **1994**, *50*, 2582.

146.P. Rinke *et al., Phys. Rev. Lett.,* **2012**, *108*, 126404.

147.W. Park and G. Yi, *Adv. Mater.,* **2004**, *16*, 87.

148.H. K. Fu, C. L. Cheng, C. H. Wang, T. Y. Lin *et al., Adv. Funct. Mater.,* **2009**, *19*, 1.

149. Y. H. Yang, X. Y. Chen, Y. Feng and G. W. Yang, *Nano. Lett.,* **2007**, *7*, 3879.

150. N. W. Wang, Y. H. Yang and G. W. Yang, *J. Phys. Chem. C,* **2009**, *113*, 15480.

151.F. H. Leiter *et al., Phys. B*, **2003**, *201*,340.

152.D. Das and P. Mondal, *RSC Adv.,* **2014**, *4*, 35735.

153.D. Das and P. Mondal, *RSC Adv.,* **2016**, *6*, 6144.

154.H. Zeng, G. Duan, Y. Li, S. Yang, X. Xu, and W. Cai, *Adv. Funct. Mater.,***2010**, *20*, 561.

155.K. Morita, B.N. Kim, H. Yoshida, K. Hiraga and Y. Sakka, *Acta Mater*. **2015**, *84*, 9.

156.C.J. Tang and H.Y. Lu, *J. Am. Ceram. Soc*., **1999**, *82*, 841.

157.U. Schmocker, H.R. Boesch and F. Waldner, *Phys. Lett. A*, **1972**, *40*, 237.

158.S. Sawai and T. Uchino, *J. Appl. Phys*., **2012**, *112*, 103523.

159.S-F. Wang *et al., Sci. Rep.,***2015**, *5*, 12849.

160.L. Cornu, M. Gaudon and V. Jubera, *J. Mater. Chem. C*, **2013**, *1*, 5419.

161.N. Pathak,P. S. Ghosh, S. K. Gupta, R. M. Kadam and A.Arya, *RSC Adv.,* **2016**,*6*,96398.

162.H. P. Klug and L. E. Alexander, *X-ray diffraction procedures for polycrystalline and amorphous materials, 2nd ed*., John Wiley & Sons: New York, 1974.

163.N. Pathak *et al., Phys. Chem. Chem. Phys.,***2017**, *19*, 11975.

164.L. A. Kappers *et al., Phys. Rev. B,* **1970**, *1*, 4151.

165.A.I.; Popov *et al.,* J. *Nucl. Instrum. Methods Phys. Res. Sect. B,* **2013**, *310* ,23.

166.V.A. Shvets *et al., J. Chem. Soc., Faraday Trans.* 1, **1985**, *81*, 2913.

167.Y. Chen, R.T. Williams and W.A. Sibley, *Phys. Rev.*,**1969**, *182* , 960.

168.Y. Chen, J. L. Kolopus and W. A. Sibley, *Phys. Rev.,* **1969,***186*, 865.

169.A. Kumar, S. Thota, S. Verma and J. Kumar, *J. Lumin.,* **2011**, *131*, 640.

170.R. R Nair *et al., Nature physics,* **2012**, *8*, 199.

171.M. Sepioni *et al., Phys. Rev Lett.,* **2010**, *105*, 207205.

172.L. Chen *et al., Scientific Reports*, **2013**, *3*, 2599.

173.S.K. Sharma *et al., Solid State Comm*., **2009**, *149*, 550.

174.M. J. Puska, Positron Annihilation, edited by L. Dorikens-Vanpraet, M. Dorikens, and D. Segers (World Scientific, New Jersey, 1988), p. 101.

175.M. Forster *et al., Mater. Sci. Forum*, **1992**,*1005*, 105 .

176.J. Xu *et al., Phys. Rev. Lett.,* **1999**, *83*, 4586.

177.N. Pathak *et al., J. Mol. Struct.,* **2014**, *121*, 1056.

178.N. Pathak *et al., Dalton Trans*., **2014**, *43*, 9313.

179.N. Pathak *et al., RSC Adv.,* **2015**, *5*, 17501.

180.N. Pathak *et al., J. Phys. Chem. C,* **2016**, *120*, 4016.

181.K. Sanyal *et al.,Dalton Trans.,* **2016**, *45*, 7650.

182.S. K. Gupta, P. S. Ghosh, N. Pathak and R. Tewari, *RSC Adv.,* **2015**, *5*, 56526.

183.M. Chiesa, E. Giamello and M. Che, *Chem. Rev*., **2009**, *110*, 1320.

184.A. J. Tench and M. J. Duck, *J. Phys. C: Solid State Phys,***1973**, *6*,1134.

185.L. Chen *et al., Scientific Reports*,**2016**, *6* , 14.

186.S. B. Oseroff *et al., Phys. Rev. B,* **1996**, *53,* 6521.

187.J. Yang, X. Rong, D. Suter and Y. P. Sun, *Phys. Chem. Chem. Phys.,* **2011**, *13*, 16343.

188. S. K. Gupta *et al., J. Magn. Magn. Mater.,* **2015**, *391*, 101.

189.R. M. Kadam *et al., Chem. Phys. Lett***.,** **2002**, *357*,457.

190.D. Karmakar *et al., Phys. Rev. B,* **2007**, *75*, 144404.

191.D. Toloman *et al., J. Alloy. Compd*., **2013**, *551*, 502.

192.N. Jedrecy, H. J.von Bardeleben, Y. Zheng and J-L.Cantin, *Phys. Rev. B,***2004**,*69*, 41308.

193.A. B. Mahmoud *et al., Phys. Rev. B,* **2006***,74*, 115203.

194.F. J. Owens, *J. Phys. Chem. Solids*,**2003**, *64*, 2289.

195.V.V. Srinivasu *et al., J. Appl. Phys.,* **1999**, *86*, 1067.

196.D. Dwibedi, M. Avdeev and P. Barpanda, *J. Am. Ceram. Soc*., **2015**, *98*, 2908.

197.K. H. Lee and J. H. Crawford, *Phys. Rev. B* , **1979**, *19*, 3217.

198.M.J. Springs and J.A. Valbis, *Phys. Stat. Sol. B ,***1984**, *123*, 335.

199.B.D. Evans and M. Stapelbroek, *Solid State Commun.* **1980**, *33*, 765.

200.C.M.Boubeta *et al., Solid State Commun*. **2011**, *151*, 751.

201.J. S. Kim *et al., Appl. Phys. Lett*. **2003**, *82*, 2029.

202.Publication CIE no 17.4, International Lighting Vocabulary, Central Bureau of the Commission Internationale de L'E´ Clairage, Vienna, Austria, 1987.

203.Phosphor Handbook, edited by Shigeo Shionoya, William M. Yen, Hajime Yamamoto, CRC press.

204.P. Kirkegaard, N. J. Pedersen, M. Eldrup, PATFIT-88. RisΦ- M-2740; RisΦ National Laboratory, Roskilde, Denmark, 1989.

205.Sreetama Dutta *et al., Progress in Materials Science,* **2009**, *54* ,89.

206. F. Tuomisto *et al., Phys. Rev. Lett.* **2003**, *91*,205502.

207.J. T-Thienprasert *et al.,Phys. Rev. Lett.***, 2013**,*110*, 055502.

208.R. Maller, *et al., J. Mater. Chem. C,* **2016**, *4*, 5953.

209.J. E. Stehr *et al., J. Appl. Phys.,* **2016**, *119*, 105702.

210.H. Dixit *et al., Phys. Rev. B* **2013**, *88*, 059905.

211.S. Mathur *et al., J. Am. Ceram. Soc.,* **2001**, *84*, 1921.

212.T. A. Bazilevskaya *et al., J. Nucl. Mater.,* **1998**, *253*, 133.

213.Y. Zhang and J. Hao, *J. Mater. Chem. C,* **2013**, *1*, 5607

214.C. M. Zhang *et al., J. Mater. Chem.,* **2011**, *21*, 717.

215.F. Wang *et al., Nature,* **2010**, *463*, 1061.

216.S. J. Zeng *et al., Biomaterials,* **2012**, *33*, 9232.

217.C. H. Dong and F. C. J. M. van Veggel, *ACS Nano,* **2009**, *3*, 123.

218.H. T. Wong *et al., J. Mater. Chem.,* **2011**, *21*, 16589.

219.Z. L. Wang, J. H. Hao and H. L. W. Chan, *J. Mater. Chem.,***2010**, *20*, 3178.

220.D. T. Tu *et al., Angew. Chem., Int. Ed.,* **2011**, *50*, 6306.

221.P. D. Fleischauer and P. Fleischauer, *Chem. Rev.,* **1970**,*70*,199.

222.V. Wood *et al., Nano Lett.,* **2009**, 9, 2367.

223.Y. Zhang *et al., Adv. Mater.,* **2012**, *24*, 1729.

224.K. K¨ompe *et al., Angew. Chem., Int. Ed.,* **2003**, *42*, 5513.

225.S. Cao *et al., J. Alloys Compd.*, **2009**,*487*, 346.

226.X. Wu, Y. Huang, L. Shi and H. J. Seo*, Mater. Chem. Phys.,* **2009**, *116*, 449.

227.G.T. Pott and B.D. McNicol, *J. Chem. Phys*., **1972**, *56*, 5246.

228.M. Nayak and T.R.N. Kutty, *J. Alloys Compd*., **1998**, *269*, 75.

229.F. de S. Barros, P. J. Viccaro, and J. O. Artman, *Phys. Rev. B*, **1972**, *5*, 3377.

230.N. T. Melamed, P. J. Viccaro, J. O. Artman and F. de S. Barros, *J. Lumin*.,**1970**, *348*, 1.

231.G. T. Pott and B. D. McNicol, *Chem. Phys. Lett*.,**1970,** *6*, 623.

232.T. Abritta and F. de S. Barros, *J. Lumin*.,**1985**, *33*,141.

233.J. M. Neto, T. Abritta and F. de S. Barros, *J. Lumin*., **1981**, *22*,109.

234.M. V. Klein and C. B.Pierce, *Phys. Rev*., **1964**, *83*,135.

235.L. E. Orgel, *J. Chem. Phys*., **1955**, *23*, 1004.

236.R.W. Kidzie, D.H. Lyons, M. Kestigian, *Phys. Rev*.,**1965**, *138*, 918.

237.T. Castner Jr, G. S. Newell, W.C. Holton and C.P. Slichter, *J. Chem. Phys*.,**1960**, *32*,668.

238.Y.J. Li , Y.Y. Maa, S. Ye , G.P. Hub and Q.Y. Zhang, *Mater. Res. Bull.,* **2014**, *51***,** 1.

239.S.K. Gupta *et al., J. Lumin*., **2015**,*164*,1.

240.JAM, Van Roosmalen at al., *J Solid State Chem*., **1992**,*101*, 59

241.R. D. Shannon, *Acta Crystallogr.,***1976**, *32*, 751.

242.S.K. Gupta *et al., RSC Adv*., **2014**, *4* , 29202.

243.W. J. Yang, L. Y. Luo, T. M. Chen and N. S. Wang, *Chem. Mater*., **2005**, *17*, 3883.

244.A. E. Souza *et al., Cryst. Growth Des.,* **2012**, *12*, 5671.

245.L.F. Silva *et al., J. Nanomater.,* 2012, DOI: 10.1155/2012/890397.

246.T. Murata, T. Tanoue, M. Iwasaki, K. Morinaga and T. Hase, *J. Lumin*., **2005**, *114* , 207.

247.L. Bo, S. Chao-Shu, Q. Z. Ming, T. Ye, *Chin. Phys. Lett.* **2005**, *22*, 2677.

248.K. Dunphy and W. W. Duley, *J. Phys. Chem. Solids*, **1990**, *51*, 1077.

249.A. Bergstein and W. B. White, *J. Electrochem. Soc.,***1971**, *118*, 1166.

250.M. Yoshino, H. Yukawa and M. Morinaga, *Mater. Trans*., **2004**, *45*, 2056.

251.M.M. Shang *et al., J. Mater. Chem.,* **2012**, *22*, 19094.

252.D.L. Geng *et al., J. Mater. Chem.,* **2012**, *22*, 14262.

253.Y. Liu, X. Zhang, Z. Hao, X. Wangc and J. Zhang, *Chem. Commun.,* **2011**, *47*, 10677.

254.U. Soni *et al., ACS Nano*, **2014**, *8*, 113.

255.K. Vanheusden *et al., J. Appl. Phys*., **1996**, *79*, 7983.

256.P. H. Kasai, *Phys. Rev.* **1963**, *130*, 989.

257.M. Z. Z. Jin *et al., J.Mol. Catal. A: Chem.,* **2004**, *217*, 203

258.S. Livraghi *et al., J. Phys. Chem. C,* **2011**, *115*, 25413.

259.J. Matta *et al., Phys. Chem. Chem. Phys.,* **1999**,*1*, 4975.

260.C. Lin, C. Zhang, and J. Lin, *J. Phys. Chem. C*, **2007**, *111*, 3300.

261.L. S. Cavalcante *et al., J. Appl. Phys.,* **2008**, *103*, 63527.

262.D. Capsoni *et al., Chem. Mater*., **2008**, *20*, 4291.

263.F. C. Romeiro *et al., J. Phys. Chem. C*, **2013**, *117*, 26222.

264.R. Viswanatha *et al., J. Phys. Chem. B*, **2004**, *108*, 6303.

265.Z. Wang *et al., Chem. Phys. Lett*., **2012**, *524* ,73.

266.D. Capsoni *et al., J. Phys. Chem. B.* **2006**,*110*, 5409.

267.A. Davidson and M. Che, *J. Phys. Chem.,* **1992**, *96*, 9909.

268.T. Nakajima, M. Isobe, T. Tsuchiya, Y. Ueda and T. Kumagai, *J.Lumin.,***2009**,*129*, 1598.

269.X.Wu, Y. Huang, L. Shi and H. J. Seo, *Mater. Chem. Phys.,* **2009**,*116*, 449.

270.V.G. Zubkov *et al., Sol. State Sci.,***2009**,*11***,** 726.

271.Y. Zhang and J. Hao, *J. Mater. Chem. C*, **2013**, *1*, 5607.

272.F. Wang and X. G. Liu, *Chem. Soc. Rev.,* **2009**, *38*, 976.

273.S. K. Gupta *et al., J. Mater. Sci.,* **2012**, *47*, 3504.

274.S. K. Gupta *et al., J .Lumin*. **2012**, *132***,** 1329.

275.S. K. Gupta, M. Mohapatra, V. Natarajan and S.V.Godbole, *RSC Adv.,* **2013**,*3*, 2004.

276.S. K. Gupta *et al., Int. J .App. Ceram. Tech.,***2013**, *10* **,**593.

277. S. K. Gupta, M. Kumar, V. Natarajan and S.V. Godbole, *Opt. Mater.*, **2013**, *35***,**2320.

278.S. K. Gupta, R. Gupta, V. Natarajan and S.V. Godbole, *Mater. Res. Bull.,* **2014**, *49*, 297.

279.A. E. Souza *et al., Cryst. Growth. Des.*, **2012**,*12*,5671.

280.S. Parida *et al., Ceram. Intl.*, **2012**, *38*, 2129.

281.R. I. Eglitis at al., *J. Phys.: Condens. Matter*, **2002**, *14*, 647.

282.M. L. Moreira *et al., Acta Mater.*, **2009**, *57*, 2174.

283.E.A.V. Ferri *et al., Mater. Chem. Phys.*, **2009**, *117*, 192.

284.V.M. Longo *et al., Acta Mater.,* **2008**, *56*, 2191.

285.V. M. Longo *et al., Appl. Phys. Lett.,* **2007**, *90*, 091906.

286. P. Barik, T.K. Kundu and S. Ram, *Philos. Mag. Lett.,* **2009***, 89*, 545.

287.Y. Pan *et al., J. Solid State Chem.,***2003***, 174,* 69.

288.L. Guo, X. Wang, C. Zhong and L. Li, *J. Am. Ceram. Soc.*, **2011,** *94*, 3175.

289.D. Sun, D. Li, Z. Zhu, J. Xiao, Z. Tao, W. Liu, *Opt. Mater.*, **2012**,*34*, 1890.

290.R. Borja-Urby *et al., Mater. Sci. Eng. B* , **2010**,*174*, 169.

291.K. Dhahria *et al., Chem. Phys. Lett.*, **2014**, *610*,341.

292.V.H. Romero at al., *J. Solid State Chem.,***2012***, 196***,** 243.

293.L.S. Cavalcante *et al., Opt. Comm.*,**2008**, *281*, 3715.

294.L.S. Cavalcante *et al., J. Alloy Compd.*, **2009**, *471*, 253.

295.P. Haro-González at al., *Solid State Ionics,* **2013**, *94*,247.

296.M.G. Lazarraga *et al., Solid State Ionics.,* **2005**, *176*, 2313.

297. R. Phatak *et al., Dalton Trans.* **2014**, *43*, 3306.

298.S. Gernot *et al., J.Appl. Phys.*, **1990**,*67*, 2040.

299. G. H. Karras. G. Koetitz. and R. Lehmann, *Phys. Status Solidi*, **1965**,*8*,385.

300.A. Runciman. B. Thangavadivel and N. B. Manson, *J. Lumin.,***1981**, *209, 24125*.

301.W. T. Carnall, H. Crosswhite, and K. Rajnak, *Rare Earths Spectroscopy,* edited by B. Jezowska·Trzebiatowska, J. Legendziewicz. and W. Strek (World Scientific. Philadelphia, PA, 1985).

302.M. Mohapatra *et al., Chem. Phys. Lett.*, **2014**, *601***,** 81.

303.S.K. Gupta, N. Pathak and R.M. Kadam, *J. Mol. Struct.*, 2015**, 1102,** 81.

304.M. Mohapatra *et al., J. Alloys. Compd.*, **2014**, *611***,** 74.

305.S.K. Gupta *et al., J. Mol. Struct.*, **2014,** *1068***,** 204.

306.D. J. Gregg *et al., J. Nucl. Mater.*, **2014**, *452***,** 474.

307.Y. Yang *et al., Nucl. Instrum. Methods Phys. Res., Sect. B* , **2014**, *326***,** 260

308.W.A.I. Tabaza, H.C Swart and R.E. Kroon, *Physica B*, **2014**, *439***,** 114.

309.S.J. Yoon, D.A. Hakeem and K. Park, *Ceram. Intl*., **2016**, *42***,** 1261.

310.W.A.I. Tabaza, H.C Swart and R.E. Kroon, *J. Lumin*, **2014**, *148***,** 192.

311.I. Omkaram and S. Buddhudu, *Opt. Mater*, **2009**, *32***,** 8.

312.V. Singh, G. Shivaramaiah, J.L. Rao and S.H. Kim, *J. Lumin*, **2013**, *143***,** 162.

313.R.J. Wiglusz *et al., Dalton Trans*. **2014**, *43***,** 7752.

314.S. K. Gupta, N. Pathak and R.M. Kadam, *J. Lumin*, **2016**,*169*, 106.

315.J. Robertson*, J. Vac. Sci. Technol., B*, **2000**,*18*, 1785.

316.K. Dhahria *et al., Chem. Phys. Lett*., **2014**,*610*, 341.

317.Z. L. Wang *et al., J. Phys. Chem. B*, **2006**,*110*, 9469.

318.T. Ye *et al., Cryst. Engg. Comm.*, **2011**,*13*, 3842

319.M. Yu, J. Lin, J. Fu, H.J. Zhang and Y.C. Han, *J. Mater. Chem.*,**2003**, *13*, 1413.

320.P. Haro-González *et al., Solid State Ionics,* **2013**, *94*, 247.

321.S. K. Gupta *et al., J. Am. Ceram. Soc.*, **2014**, *97*, 3694.

322.S. V. Eliseevaa and J.C.G Bunzli, *Chem. Soc. Rev*., **2010**, *39***,** 189.

323.Q. Ju, Y. Liu, R. Li, L. Liu, W. Luo and X. Chen, *J. Phys. Chem. C*, **2009**, *113*, 2309.

324.B.R. Judd, Phys. *Rev.*,**1962**, *127*, 750.

325.G.S. Ofelt, *J. Chem. Phys*., **1962**, *37*, 511.

326.M.H.V. Werts *et al., Phys. Chem. Chem. Phys*., **2002**, *4***,**1542.

327.R. Shukla *et al., Dalton Trans. 2015,* DOI: 10.1039/C4DT02717E

328.G. F. de Sa *et al., Coord. Chem. Rev*., **2000**,*196*, 165.

329.R. J. Carvajal, *An introduction to fullproof 2000 program*; version July, **2001**.

330.D. White and S. Ramdas, *Ultramicroscopy*, **1989**, *31*, 124.

331.N. Kumada and N. Kinomura, *Journal of Solid state Chemistry*, **1995**, *116*, 281.

332.V.M. Longo *et al., J. Appl. Phys.*,**2008,** *104*, 1.

333.S.K. Gupta *et al., J. Am. Ceram. Soc*. **2014**, *97*, 3964.

334.S.K. Gupta *et al., Spectrochim. Acta Mol. Biomol. Spectrosc.,* **2014**, *117*, 204.

335.M. Ilmer, B.C. Grabmaier, G. Blasse, *Chem. Mater.,* **1994**,*6*, 204.

336.F. Kang *et al., J. Mater. Chem. C.* **2014**, *2*, 6068.

337.H. Zhou, Y. Jin, M. Jiang, Q. Wang and X. Jiang, *Dalton Trans*., **2015**, *44*, 1102.

338. S. K. Gupta, N. Pathak, P.S. Ghosh and R.M. Kadam, *J. Alloys Compd.*, **2017**, *695*, 337.
339. R.J. Wiglusz *et al., Dalton Trans.*, **2014**,*43*, 7752.
340. K. Ohwada, *Spectrochim. Acta A*, **1978**, *35*, 99.